UNIVERSITÉ DU LUXEMBOURG

PhD-FSTM-2024-056
The Faculty of Science, Technology and Medicine

DISSERTATION

Defence held on 09/07/2024 in Luxembourg

to obtain the degree of

DOCTEUR DE L'UNIVERSITÉ DU LUXEMBOURG

EN BIOLOGIE

by

Lorraine RICHART

Born on the 11th of August 1990 in St.Mandé (France)

IMPLICATION OF DNA METHYLATION PATTERNS IN MOUSE MICROGLIAL CELL IDENTITY

Dissertation defence committee

Pr. Dr. Michel Mittelbronn, Dissertation Supervisor
Professor, University of Luxembourg, Luxembourg

Pr. Dr. Paul Heuschling, Chairman
Professor, University of Luxembourg, Luxembourg

Pr. Dr. Barbara Klink, Vice Chairman
Professor, University of Luxembourg, Luxembourg

Pr. Dr. Julia Schulze-Hentrich
Professor, Saarland University, Germany

PD Dr. Pia Zeiner
Professor, Goethe University, Germany

IMPLICATION OF DNA METHYLATION PATTERNS IN MOUSE MICROGLIAL CELL IDENTITY

Dissertation by

Lorraine RICHART

DOCTOR OF PHILOSOPHY

University of Luxembourg

Doctoral School in Science and Engineering (DSSE)
Doctoral Program in Systems and Molecular Biomedicine

Luxembourg 2019-2024

Funded by

Fonds National de la Recherche Luxembourg

Affidavit

I hereby confirm that the PhD thesis entitled “Implication of DNA Methylation Patterns in Microglial Cells Identity” has been written independently and without any other sources than cited. Ethical approvals for mouse experimentation have been obtained in accordance with the “Règlement grand-ducal du 11 janvier 2013 relatif à la protection des animaux utilisés à des fins scientifiques” adapted from and in line with the European Directive 2010/63/EU.

Luxembourg, 18.04.2024

Lorraine Richart

Acknowledgements

I would like to start this section by acknowledging the institutions without which this phD could not have been realized. I would like to thank the University of Luxembourg for providing the frame of this PhD and allowing me to learn and develop my skills, he Luxembourg Institute of Health (LIH) for welcoming me and offering me a place and tools to perform the art of biology, together with the Laboratoire National de Santé (LNS) for giving me the opportunity to use the epigenetic platform and finally the Luxembourg Centre for System Biomedicine (LCSB) for providing the necessary equipment for primary cell culture. This PhD could also not have been done without the funding from the Luxembourg National Research Fund and the participation from the Rotary Club of Luxembourg for which I am extremely thankful.

I must also acknowledge my PhD supervision team, my CET members Dr. Barbara Klink and Dr. Lasse Sinkkonen for the feedbacks and guidances they have been providing all along those 5 years, but especially my PhD co-supervisor Dr. Ann-Christin Hau, for the patience with all the tutorials she taugh me, for all the statistical lessons and the bio-informatic tools. Beyond the pure disciplinary knowledge you provided me, interacting with you made me a stauncher scientist and a stronger person on the workplace and this is the best gift every PhD student could ever received as it will last for my entire career. Thank you.

I would now like to express my sincere and deepest gratitude to my PhD supervisor Pr. Michel Mittelbronn that trusted me with this PhD project and gave me the opportunity to try, fail and grow without any form of blaming during those past 5 years. It was an amazing experience to watch you work and the transparency, dedication and kindness you are constantly exhibiting towards your teams, really was inspiring. I am very lucky I could benefit from your advices and I can say without a doubt that I am a better professional, a better scientist and a better person thanks to you. Thank you.

The next person I need to thank is colleague and former internship supervisor, Dr. Tony Heurtaux, for well…basically everything ! I did not know what to do before you appeared out of knowhere with tiny mindblowing microglial cells and now, like 7 years later, I still want to know everything there is to know about microglia, I guess I have to thank you for giving me passion to pursue. But on top of that, by being so authentic, joyful and caring, you really are one of the foundation holding the LCNP group, and I am really happy I could work not that far from you. Thank you.

Talking about the LCNP, I do know how to sum up my appreciation for everything you represent. It was an honor to be part of such an extraordinary group. Alessia, Beatriz, David, Felicia, Felix, Gael, Irati, Jay, Katrin, Kris, Maitane, Mélanie, Michel (Valmi), Monica, Oihane, Redouane, Sergio, Sonja, Sophie, Tanja, Uxue, Victoria, Ziad, that was an amazing journey thanks to all of you. I am really going to miss you.

Of course the picture would not be complete if I forgot to thanks the amazing colleagues from LIH and LNS, starting with Valérie and Fred, I am so grateful that you ended up sharing the office, our discussions made this end of PhD feels like a beginning and, I needed that so : Thank you.

Next would be Reka and Arnaud, you saved the day so many times for me, you took the time to explain and explain and explain again and I really owe you. I also want you know how much I appreciated feeling the passion you have for biology and research, every discussion with you left me with joy and excitement for my project even at the worse parts of it. I can even admit now that the tiny part of me that still dream about academia exists because of passionate people like you. Thank you.

And it goes without saying that I am extremely grateful for all the persons that made me smile, gave me pep talks at coffee break or just the ones that I was crossing in corridors and got inspired by, Amandine, Alexandros, Alice, Andrea (♀), Andrea (♂), Céline, Chantal, Chloé, Denise, Eric, Frida, Lars, Ludo, Max, Monica, Nadine, Patrick, Sabrina, Steffy, Takhouie. Thank you.

Et, of course, the one and only magnificent mermaid : Camille Cialini.

Comme j'ai pas les mots et que t'façon t'es un caillou :

Pour ta force, ton courage, ta lucidité, ta bienveillance et ta sincérité,

Mlle Camille Cialini, cette thèse t'est dédiée.

(Ça rime)

Je ne vois pas qui d'autre pourrait comprendre autant que toi ce que cette thèse représente pour moi, les difficultés, les erreurs et la solitude, mais aussi, les joies et les petites réussites du quotidien, et enfin, la fierté d'avoir été jusqu'au bout, et puis tout le reste. C'est tout ça que je te dédie aujourd'hui parce que tu as tout vécu avec moi, des crises d'angoisses aux crises de rires en passant par les brainstorming scientifiques ou philosophiques, tu étais là, au labo ou en dehors. Je n'aurais pas pu devenir ce que je suis aujourd'hui sans toi, et franchement, je me trouve plutôt cool. Et comme t'es mon role model ça veut dire que toi aussi t'es cool, mais hey, tu le savais déjà. Bref, merci.

You are the Ann to my Leslie.

Du fond du cœur, merci.

Et big up a Xavier, Francis et Volga.

Enfin, je tenais à remercier mes proches, mamie Lucie, papa Francois et maman Christine, Vincent et Coline, Raphaël, Arthur et Robin, Ingrid et Philippe, et enfin, Cyril.

Merci pour tout, y pas de mots pour decrire les gestes, les attentions, les non dits et les dits tout court, les repas toujours trop copieux, les livres pretés et les coups de téléphone impromptus, les silences pas si genants, les rires et les larmes, le temps qui passe et qu'on regarde passer tous ensemble, certains que rien nous arrivera parce que finalement on sera là les uns pour les autres. Donc merci d'avoir été là pendant ces 5 ans et pendant toute ma vie et merci d'avoir été vous, vous êtes fantastiques.

Je vous aime.

Et, bien evidemment, Pipette, AKA Pips, mon amour, ma belette, mon astre, je t'aime.

(C'est un chat et y peut pas lire, mais quand les AI auront gouverné le monde et que son esprit sera dans le cerveau positronique d'un robot surdeveloppé, vous ferez moins les malins)

« *There is absolutely nothing to be afraid of.* »

INZO

Table of contents

List of Figures

List of Tables

List of Annexes

List of Abbreviations

5caC	5-Carboxycytosine
5fC	5-Formylcytosine
5hmC	5-Hydroxymethylcytosine
5mC	5-Methylcytosine
Aβ	Amyloid Beta
AC	Adenyl Cyclase
ACAMP	Apoptotic-cell associated molecular patterns
AD	Alzheimer's Disease
ADHD	Attention Deficit Hyperactivity Disorder
ADP	Adenosine Di-Phosphate
AKT	Protein kinase B
ALS	Amyotrophic Lateral Sclerosis
AP-1	Activator protein 1
AR	Actin Remodeling
Arp2/3	Actin Related Protein 2/3
ASD	Autism Spectrum Disorder
ATAC-seq	Assay for Transposable-Accessible Chromatin sequencing
ATP	Adenosine Tri-Phosphate
BACE1	Beta secretase 1
BBB	Blood Brain Barrier
BDNF	Brain Derived Neurotrophic Factor
BSA	Bovine Serum Albumine
C1q	Complement component 1
Ca^{2+}	Calcium
cAMP	Cyclic adenosine monophosphate
CCL2	Chemokine (C-C motif) Ligand 2
CD	Cluster of Differentiation
CDC42	Cell division control protein 42
C/EBP	CCAAT/enhancer binding proteins
CFL1	Cofilin 1
ChIP-seq	Chromatin Immunoprecipitation sequencing

CK	Cytokine
Cl^-	Chloride
CM-GL261	GL261 conditionned media
CNS	Central Nervous System
CNTF	Ciliary Neurotrophic Factor
CORO1A	Coronin 1
COX	Cyclooxygenase
CP	Cortical Plate
CR3	Complement Receptor 3
CRKII	Proto-oncogene c-CRK II
CSF1R	Colony Stimulating Factor 1 Receptor
CXCL (-)	Chemokine C-X-C motif ligand (-)
CXCL10	Chemokine Interferon-ɣ inductible protein 10 kDa
CXCR (-)	Chemokine C-X-C motif receptor (-)
DAM	Disease-Associated Microglia
DAMP	Damage-associated molecular pattern
DAP12	DNAX-activating protein of 12 kDa
DAPI	4',6-diamidino-2-phenylindole
DEG	Differentially Expressed Gene
DMEM	Dulbecco's Modified Eagle Medium
DMEM Full	DMEM with 10% FBS and 1% Penicillin Streptomycin
DMG	Differentially Methlated Gene
DML	Differentially Methylated Loci
DMR	Differentially Methylated Region
DMS	Differentially Methylated Site
DNA	Desoxyribo Nucleic Acid
DNMT	DNA Methyltransferase
DOCK180	Dedicator of cytokinesis protein 1
E	Embryonic day
ECM	Extracellular matrix
EEA1	Early Endosome-Associated protein 1
EGF	Epidermal Growth Factor
ELISA	Enzyme Linked ImmunoSorbent Assay

ELMO	Engulfment and Cell MOtility
EMP	ErythroMyeloid Progenitor
ENCODE	Encyclopedia of DNA Elements
En-Pd	Enhancer, Poised TSS-distal
En-Pp	Enhancer, Poised TSS-proximal
En-Sd	Enhancer, Strong TSS-distal
En-Sp	Enhancer, Strong TSS-proximal
En-W	Enhancer, Weak
ER	Endoplasmic Reticulum
ERK1/2	Extracellular signal-regulated protein kinases 1 and 2
EtoH	Ethanol
FACS	Fluorescent Activated Cell Sorting
F-actin	Filamentous actin
FADD	Fas-Associated protein with Death Domain
FBS	Fetal Bovine Serum
FC	Fold Change
FCRL	Fc-receptor like molecules
FDR	False Discovery Rate
FGF	Fibroblast Growth Factor
G-actin	Globular actin
GAM	Glioma Associated Macrophages
Gas6	Growth arrest specific 6
GB	Glioblastoma
GBM-CM	Glioblastoma Conditioned Media
G-CSF	Granulocyte colony-stimulating factor
GDNF	Glial cell line-derived neurotrophic factor
GFAP	Glial Fibrillary Acidic Protein
GM-CSF	Granulocyte-Macrophage Colony Stimulating Factor
GO	Gene Ontology
GP130	Glycoprotein 130
GPCR	G protein-coupled receptor
GPR56	G protein-coupled receptor 56
GSDMD	Gasdermin D

Hc-H	Heterochromatin, H3K9me3-associated
Hc-P	Heterochromatin, Polycomb-associated
HDAC	Histone deacetylase
HIF	Hypoxia-Inductible Factor
HRP	Horseradish peroxidase
Iba1	Ionized calcium-binding adapter molecule 1
IF	ImmunoFluorescence
IFN-ɣ	Interferon Gamma
IGF-1	Insulin-like Growth Factor 1
IKK	IkappaB kinase
IL	Interleukin
IL-1βR	Interleukin 1 Beta Receptor
IL-4	Interleukin 4
IL-13	Interleukin 13
iNOS	Inductible Nitric Oxide Synthase
IRAK	IL-1R associated kinase
IRF	Interferon Regulatory Factor
IRF8	Interferon Regulatory Factor 8
IZ	Intermediate Zone
JAK	Janus Kinase
JNK	c-Jun N-Terminal Kinase
KCNK13 (THIK-1)	K+ channel subfamily K member 13
KEGG	Kyoto Encyclopedia of Genes and Genomes
KLF6	Krueppel-like factor 6
KO	Knock-Out
LAMP	Lysosome-Associated Membrane glycoprotein
LDTF	Lineage Determining Transcription Factor
LIF	Leukemia Inhibitory Factor
LPS	Lipopolysaccharide
LXR	Liver X Receptor
MACS	Magnetic-Activated Cell Sorting
MAPK	Mitogen-activated protein kinase
MCP	Monocyte Chrmoattractant Protein

M-CSF	Macrophage colony-stimulating factor
MDB	Methyl Binding Domain
MEF2C	Myocyte-specific enhancer factor 2C
MEK1/2	Mitogen Activated Protein Kinase Kinase
MHC I - II	Major Histocompatibility Complex class I – II molecules
MIA	Maternal Immune Inflammation
mIL6R	Membrane IL-6 receptor
MIP1	Macrophage Inflammatory Protein
miRNA	Micro RNA
MLKL	Mixed Lineage Domain-Like Pseudokinase
MMP	Matrix Metalloproteinase
MRTF	Myocardin-related transcription factor
MS	Multiple Sclerosis
MZ	Marginal Zone
NCBI	National Center for Biotechnology Information
ND	Neurodegenerative Disease
NDD	NeuroDevelopmental Disorders
NFκB	Nuclear Factor Kappa-light-chain-enhancer of activated B cells
NFT	NeuroFibrillary Tangles
NGF	Nerve Growth Factor
NLR	Nucleotide Oligomerization Domain Like Receptor
NLRP3	NOD-like receptor family, pyrin domain containing 3
NO	Nitric Oxide
NPC	Neural Progenitor Cell
NRP1	Neuropilin 1
NS	No significant
NSC	Neural Stem Cell
OPC	Oligodendrocyte progenitor cell
P	Post-natal day
P53	Tumor protein 53
PAMP	Pathogen-associated molecular pattern
PBS	Phosphate Buffered Saline
PC	Principal Component

PCA	Principal Component Analysis
PCR	Polymerase Chain Reaction
PD	Parkinson's Disease
PDGF	Platelet Derived Growth Factor
PFA	ParaFormaldehyde
PiP_3	Phosphatidylinositol (3,4,5)-trisphosphate
PI3K	Phosphoinositide 3-kinase
PKA	Protein kinase A
PLC	Phospolipase C
PPARɣ	Peroxisome proliferator activated receptor gamma
Pr-A	Promoter, Active
Pr-B	Promoter, Bivalent
Pr-F	Promoter, Flanking Region
PRR	Pattern Recognition Receptor
Pr-W	Promoter, Weak
P/S	Penicillin-Streptomycin
PS	Phosphatidylserine
PTM	Post-Translational Modifications
RAF	Rapidely Accelerated Fibrosacrcoma
RAS	Rat sarcoma virus
RhoA	RAS homolog family member A
RIPK3	Receptor-interacting serine/threonine-protein kinase
RNA	Ribo Nucleic Acid
RNA-seq	RNA sequencing
RNS	Reactive Nitrogen Specie
ROCK	Rho-associated kinase
ROI	Region Of Interest
ROS	Reactive Oxygen Specie
RUNX1	Runt-related transcription factor 1
RXR	Retinoid X Receptor
SALL1	Spalt Like Transcription Factor 1
SAM	S-Adenosyl Methionine
SASP	Senescence-Associated Secretory Phenotype

SDTF	Signal Determining Transcription Factor
SEM	Standard Error of the Mean
sIL6R	Soluble IL-6 receptor
SIRPα	Signal-regulatory protein alpha
SMAD	Mothers against decapentaplegic
SNARE	Soluble N-ethylmaleimide-sensitive-factor attachment protein receptor
SOCS	Suppressor of cytokine signaling
SR	Scavenger Receptor
SRF	Serum response factor
SVZ	Sub-Ventricular Zone
SWI/SNF	Switch/Sucrose Non-Fermentable
SYK	Spleen tyrosine kinase
SZ	Schizophrenia
TβRI-II	Type I and II TGF beta receptors
TAK1	Transforming growth factor-β activated kinase 1
TAM	Tyro3/Axl/MerTK receptors
TDG	Thymine ADN glycosylase
TET	Ten-Eleven Translocation
TF	Transcription Factor
TFEB	Transcription Factor EB
TGF-β	Transfroming Growth Factor beta
TLR	Toll Like Receptor
TLR4	Toll Like Receptor 4
TNFα	Tumor Necrosis Factor Alpha
Tp	Timepoint
TRAF	TNF receptor-associated factor
TRAM	TRIF-related adaptor molecule
TRIF	TIR domain-containing adapter-inducing interferon-β
Tr-I	Transcription, Initiation
TREM2	Triggering receptor expressed on myeloid cells 2
Tr-P	Transcription, Permissive
Tr-S	Transcription, Strong
TSP1	Thrombospondin 1

TSS	Transcription Start Site
Tt	Treatment
TUNEL	Terminal deoxynucleotidyl transferase dUTP nick end labeling
UCSC	University of California, Santa Cruz
UV	Ultra Violet
VASP	Vasodilator-stimulated phosphoprotein
vATPases	Vacuolar ATPases
VEGF	Vascular Endothelial Growth Factor
VZ	Ventricular Zone
WASP	Wiskott-Aldrich Syndrome protein
WHO	World Health Organization
YS	Yolk Sac

List of contributions

Dr. Ann-Christin Hau gave multiple trainings on statistical analysis, bio-informatic tools and data visualization, supervised the completion of the DNA methylation experiments and interpretation of the first part of the project.

Dr. Tony Heurtaux gave trainings on pup dissection, MACS isolation and culture of primary microglial cells and supervised the successful completion of the first part of the project (part 1 of the results chapter).

Dr. Reka Toth realized the analysis of the DNA methylation raw data for the first part of the project (part 1 of the results chapter).

Nathalie Nicot and Arnaud Muller from LuxGen platform generated and analyzed the RNA sequencing data, respectively.

Master trainee, Michel Valtey realized partly the experimental part for the collection and treatment of mouse primary microglial cells (part 2 of the results chapter).

Technical laboratory specialist Camille Cialini participated to the experimental part for the collection and treatment of mouse primary male and female microglial cells (part 3 of the results chapter), treated the Incucyte raw data for the entire project and reviewed the Materials and Methods section of this manuscript.

Summary

Microglial cells, the resident immune cells of the brain parenchyma, are responsible for the establishment and maintenance of the brain homeostasis. Belonging to the macrophage lineage, they function first as a part of the innate immune system and thus, have to execute immune related roles. However, microglial cells are also involved in a plethora of central nervous system (CNS) related roles, from synaptic pruning to oligodendrocyte maturation and clearing of myelin. In order to fulfil those roles, microglial cells can adapt in the best way to a specific situation without harming the delicate CNS environment. Microglial cells are constantly monitoring the environment by displaying surface receptors, phagocytosis can be modulated to clear debris or apoptotic cells, but also synapses; cytokine secretion can be cytotoxic or neurotrophic. Microglial cells are highly plastic, capable of reacting to any stimulation that could hamper the proper functioning of the brain. There is emerging evidence that microglial plasticity is related to chromatin modulation, orchestrated by epigenetic mechanisms, such as non coding RNAs, histones modifications and DNA modifications. DNA methylation is one of the most studied epigenetic mechanisms and yet, little is known about its involvement in microglial identity. Regarding the variety of functions realized by microglia, the involvement of microglial misfunction in a various range of neurodegenerative diseases, neurodevelopmental disorders and brain tumors, amongst others, is not surprising. As such, they do represent a promising target for innovative therapeutic approaches, but in order to achieve an efficient exploitation of microglial functions without hampering brain homeostasis, a deep understanding of the microglial core identity and how it can be influenced by the environment, is required. In this thesis, we hypothesized that mouse microglial identity was modulated by DNA methylation pattern reorganization, and, to test that hypothesis, we induced a reprogramming of microglial cell identity and explored genome-wide DNA methylation patterns. We characterized identities generated by treatments with Lipopolysaccharide (LPS), Interferon gamma (IFN-ɣ), Interleukin 4 (IL-4) and a glioma-based conditioned medium within a time frame between 1 and 48 hours. We observed changes in morphology, secretome composition and gene expression, in line with previously characterized inducible features of microglial reprogramming. We further performed Illumina MethylMouse methylation arrays and observed significant variations in DNA methylation patterns by both treatments and time of exposure, especially in the pro-inflammatory conditions. Then, we performed RNA-sequencing (RNA-seq) to explore gene expression modulation by LPS and IFN-ɣ treatments, however no unequivocal link between DNA methylation changes and gene expression could be established. We could nevertheless witness that DNA methylation changes induced by the treatments and associated with microglial reactivity were not only affecting gene promoters, thereby highlighting the meaning of DNA methylation in different

parts of the genome such as the distal intergenic regions. In summary, DNA methylation plays an important part in the reprogramming of microglial cells, however further exploration of other epigenetic mechanisms, such as histone modifications and the chromatin accessibility is necessary to unravel the potential innovative therapeutic options targeting microglia cells in neurological diseases.

Part I. Introduction

1. Introduction to microglial cell research

The story of glial cell research began in 1856, when Rudolf Virchow coined the term “neuroglia” to describe one single entity that was distinctively embedding neuronal elements[1]. The cellular content of neuroglia was clarified by Michael Von Lenhossek with the emergence of the term “astrocyte”[2], and with the development of a gold chloride sublimate staining method, Ramòn y Cajal was able to stain astrocytes and decipher another component of neuroglia that he named “the third element”[3]. Finally, Pio Del Rìo-Hortega, with an ammoniacal silver carbonate staining method, was able to identify the composition of the third element, oligodendrocytes and microglia.

In 1919, in a series of four papers, Pio Del Rìo-Hortega described intensively microglial morphologies in the normal brain of different species and “transformation” in pathologies, reporting “rod cells” and “granuloadipose bodies”, already highlighting the polymorphism of microglia[4,5]. He also explored the ontogeny of microglia, stating a mesodermal origin against the current view pointing out an ectodermal one, arguing that microglial cells were sharing more features common to leukocytes than astrocytes, emphasized by his functional observation that microglia were capable to proliferate, migrate and most importantly, to phagocytose. He characterized microglia as the “voracious macrophages” of the brain parenchyma [6]. By also identifying oligodendrocytes in 1921, Pio Del Rìo-Hortega was the first who identified distinctive and functional features of neuroglia’s third element and started the era of modern glial research[7].

However, the field of microglial research stagnated for many decades, microglia regarded as “docile spectator” of the brain parenchyma[8]. It was only in the late 20’s that the field started to emerge with the experiments of G.Kreutzberg on microglia stripping of synapses (1968)[9], the development of the Adenosine triphosphate (ATP) staining on microglia by Ibrahim and his team (1974)[10] and the first microglia *in vitro* culture system by D.Giulian and T.Baker (1986)[11]. This time point of microglial research was indeed essential, opening the gates of visualization and functional analysis of microglial behavior and leading to the first conclusions on their immune roles with the production of cytokines (CK) and the expression of Major Histocompatibility Complex class I molecule (MHC-I), substantially attracting more and more neuroscientists. Ultimately, the field took off in 1990 with the constitution of the first mouse microglial cell line BV2[12] and in 1998, the isolation of the now gold standard for microglia staining, ionized calcium-binding adapter molecule 1 (Iba1)[13]. Since then, microglial research

exponentially increased, and improving models and technologies led to an accumulation of knowledge proving implication of microglia in vital physiological functions of the CNS and in nearly all brain pathologies[14,15], witnessing an outstanding cellular plasticity of microglia[16]. With the technical advances in imaging and genetics, multifunctional aspects could be attributed to microglial subpopulations, thereby addressing the concept of microglial heterogeneity[17] and paving the way of one of the biggest branch of microglial study concerning the elaboration and evolution of its core identity[18].

Nearly 100 years later, at the era of single cell transcriptomics and epigenomics, and regardless of the incredible efforts made by a large community of scientists, the mechanisms orchestrating microglia's identities remain nevertheless mysterious[19].

2. Microglial ontogeny and maturation

The first step towards a clear view of microglial identity is to understand their complex origin and as mentioned above, it was subject of debate since their first description, opposing a mesodermal[5] to a neuroectodermal origin[20]. It was only in 2010 that Ginhoux and colleagues, by conducting an *in vivo* fate mapping study, proved that the mesodermal origin of microglial cells predicted by Pio Del Rio-Hortega in 1919 was true[21].

Indeed, we now know that in mouse embryogenesis, during the first wave of primitive hematopoiesis, erythro-myeloid precursors (EMPs) emerge in blood islands of the yolk sac (YS) at embryonic day (E) 7, navigate through the newly formed blood stream and enter the brain rudiment from E9.5[22]. Even though it is still not entirely clear, the main entry routes of microglia are thought to be the meninges, the lateral ventricles and blood vessels, constituting "hot spots" for microglial precursor's initial populations in the brain[23]. It is worth noticing that a small subset of Hoxb8^{+} microglia enter the brain later on, at E12.5[24] together with another subset of CD206^{+} macrophages that are subjected to a fate conversion into microglia[25], depicting slight variations of ontogeny within the final pool of microglial cells. At E13, the Blood Brain Barrier (BBB) starts to close, limiting the infiltration of other immune cells and isolating microglial progenitors[26] in the brain parenchyma that then migrate and colonize the entire brain, first by a tangential migration within the cortex, followed by a radial migration towards the cortical plate (CP)[27].

At the end of their intense migration process around E18, microglial cells proliferate intensively and migrate locally to reach their final localization around post-natal day (P)14[28]. From there, microglial

cells self-renew without any contribution from circulating monocytes during the entire lifespan of the individual in physiological conditions[29]. Interestingly, microglial niche is maintained through cycles of apoptosis and proliferation characterized by a very slow turn-over, making microglia very long lived cells[30]. Indeed, in the murine cortex, microglia have a median lifetime of more than 15 months with approximately 50% of these cells surviving the entire lifespan of the individual[31]. Once the brain colonization is complete, microglia are distributed regularly throughout the CNS ranging from 5 to 20% of the total glial cells of the brain parenchyma[32] with variations in density relative to brain localization[33]. In physiological conditions, the finalization of their maturation confers to microglia a highly ramified morphology[34], and by extending their processes, microglia cover the maximum area of brain tissue and are able to perceive any homeostasis disturbance within the CNS[35].

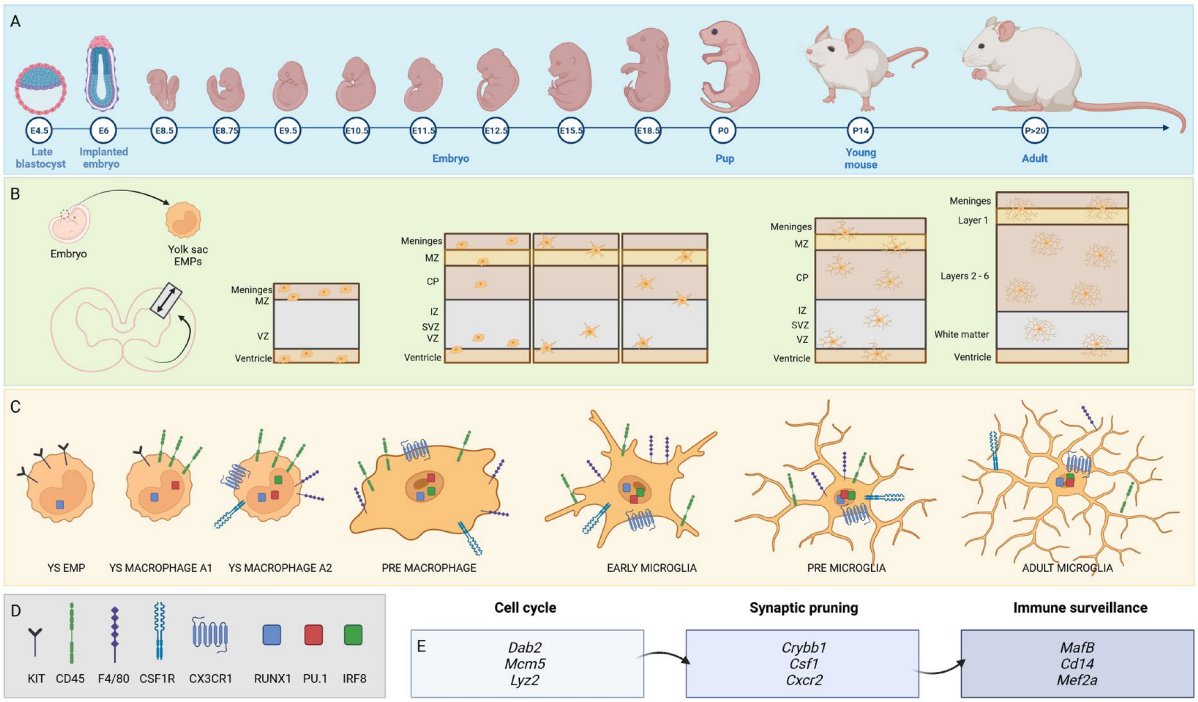

Figure 1. Microglial ontogeny and development in mouse:

Early YS EMPs, characterized by being dependent of the Runt-related transcription factor (RUNX1) but independent of Myb, emerge from the YS at E8.5 and follow the newly formed bloodstream while maturing into YS A1 macrophages through the action of PU.1, followed by an Irf8 dependent step to give rise to YS A2 macrophages. Initially, YS EMPs express tyrosine kinase receptor c-Kit but lack the expression of CD45. As they differentiate into YS macrophage A1 then A2, the expression of c-Kit progressively decreases while CD45 increases. YS macrophages enter the brain rudiment around E9.5 under the influence of neuronal progenitor cells (NPCs) expression of IL-34 recognized by the CSF1R, present on A2 YS macrophages[21,36], the chemokine CXCL12 released from pallial NPCs through its binding on CXCR4[37] and the chemokine CX3CL1 on CX3CR1 receptor (C)[38]. Maturation from embryonic

to mature microglia also depends on the Matrix Metalloproteinases MMP8 and MMP9[22]. Those environmental stimulations will dictate a tangential migration of microglia throughout the entire cortex and participate to the acquisition of microglial maturation program[39], followed by a radial migration towards the CP through a meningeal and SVZ initiated gradient of CXCL12, binding to microglial CXCR4 and leading to the absence of microglia within the CP from E15 to E16[40] (B). The finalization of microglial migration is characterized by an high proliferation rate and local migration to cover the entire brain in an allometric fashion[28]. The transcriptomic developmental program of microglia is developed in three steps that have been linked to microglial function, namely, a proliferative step (Expression of *Dab2*, *Mcm5*, *Lyz2*) followed by a specific synaptic pruning program in accordance with the development and maturation of NPCs (*Crybb1*, *Csf1*, *Cxcr2*) and finally, immune surveillance of the adult CNS (*MafB*, *Cd14* and *Mef2a*)[41]; this developmental maturation program is accompanied by a change in microglial morphology from an amoeboid to highly ramified shape. In the mouse adult homeostatic brain, microglia is characterized by an high expression of F4/80 and CD11b macrophage markers, and the receptors necessary for maintenance of microglial survival and identity, depending on IL-34[42] , TGF-β1[43] , CSF1R and cholesterol[44] signaling pathways, stimulated by neurons and astrocytes secretions [45]. From a transcriptomics point of view, mature microglia is recognized by the induction of the so called microglial homeostatic signature, characterized by the expression of *Tmem119*, *P2ry12*, *Sall1*, *Hexb*, *Gpr34* and *SiglecH*[39].

Created with Biorender, from[22,46,47,48,41]. Panel A: developmental timeline of the mouse embryo; panel B: microglial colonization of the cortex; panel C: microglial maturation in neurodevelopment; panel D: legend; panel E: transcriptional program of microglial maturation. CD11b: Cluster of Differentiation molecule 11b, CP: Cortical Plate, CSF1R: Colony Stimulating Factor 1 Receptor, CX3CL1: Fractalkine, CX3CR1: Fractalkine receptor, CXCL12: C-X-C Motif chemokine ligand 12, CXCR4: C-X-C chemokine receptor type 4, E: Embryonic day, F4/80: EGF-like module-containing mucin-like hormone receptor-like 1, IL-34: Interleukine 34, IZ: Intermediate Zone, MMP: Matrix metalloproteinases, MZ: Marginal Zone, P: Post-natal day, SVZ: Sub-Ventricular Zone, TGF-β: Transforming Growth Factor Beta, VZ: Ventricular Zone, YS: Yolk Sac.

3. Microglial roles

The semantics behind biological “roles” and “functions” has been a matter of debate for decades[49] and a consensus amongst all scientific fields has not yet been reached, especially since the arising of molecular biology[50]. For the purpose of this thesis, biological roles will be defined as the responsibility that a cell population has to assume in a larger structure, namely the tissue. The functions, on the other hand, will be defined as specific tasks performed by a cell to fulfill that biological role.

In that sense, microglial cells exert immunocentric and neurobiological roles fulfilled through a vast combination of individual functions such as phagocytosis or CK secretion.

3.1. Immunocentric role

As resident macrophages, microglial cells are the first line of immune defense of the CNS. In the healthy adult brain, microglial cells are not quiescent as previously thought but are highly motile and constantly monitoring their microenvironment by extending and moving their protrusions[51,35].

Disturbance in CNS homeostasis can be originated from viral[52], fungal[53] or bacterial infection[54], sterile inflammation[55] or protein aggregation[56], or anything else that can be considered as a real or potential danger to the CNS. Following the detection of the disturbance, microglial cells redirect their protrusions towards its source[51] and start migrating *via* the recognition of chemokines and extracellular ATP with G-protein coupled purinergic receptors (P2Y12, P2X4)[57] and through the acquisition of an differential morphology facilitating microglial movement[58,59].

Under the influence of CKs such as IL-6[60] and TNFα[61] emerging from injury induced damages, microglia proliferate in close vicinity to the pathological stimuli[62]. Identification of the stimulation causing the disturbance is realized *via* microglial sensome[63], a vast ensemble of surface receptors comprising pattern recognition receptors (PRRs)[64], phosphatidylserine receptors[65] and opsonic receptors[66], amongst many others. The recognition of the stimulus by its binding to surface receptors will allow microglia to integrate it and quickly initiate an appropriate response to restore cerebral homeostasis.

Facing an infectious challenge, the interaction between a set of PRRs and microbial components will pilot the recruitment and activation of other immune cells through chemokines and CKs secretion, stimulation of phagocytic activity and initiation of cytotoxic functions to remove the foreign pathogen causing homeostasis disturbance[67,54]. The execution of chemotaxis by microglial cells towards peripheral immune cells is a crucial part of a successful immune response within the CNS[68]. Trans-endothelial migration of peripheral immune cells can only be realized after the perturbation of the BBB integrity through microglial release of MMPs[69] or Cyclooxygenases (COXs)[70]. Once opened, chemotactic mediators, such as CCL2[71], MIP-1α[72] and MCP-1[73] can be directed to lymphocytes T[74], bone marrow derived monocytes[75] or perivascular macrophages[76] to support microglial cells facing the disturbing challenge[77].

The presence of various primed peripheral immune cells, apoptotic cells and cellular debris progressively induces a shift in microglial microenvironment and increases its inflammatory status, stimulating even more microglia into performing phagocytosis of the pathogen or apoptotic cells, through Toll-like Receptors (TLRs)[78] and Tyro3/Axl/Mer[79] signaling cascades, thus leading to the destruction of the engulfed material through phagolysosomal maturation[80].

The overall environment also leads to the deployment of microglial cytotoxic functions, comprising the secretion of pro-inflammatory CKs, Reactive Nitrogen Species (RNS) and Reactive Oxygen Species (ROS)[81]. Pro-inflammatory CKs induced cytotoxicity is thought to be related to the induction of an endoplasmic reticulum stress and apoptosis[82], whereas RNS and ROS induced damages are characterized by the fragmentation of basic cellular components such as the cytoplasmic membrane or the DNA by oxidation[83]. By being unspecific, the cytotoxicity of microglia affects as well others glial cells and neurons[84,85] leading to an accumulation of cellular debris and apoptotic bodies, consequently triggering an additional level of microglial phagocytosis to clear and initiate the downregulation of inflammation.

The last mandatory step for a proper restoration of homeostasis is the termination of the immune response to avoid escalating inflammatory stimulations and allow the repair of the damaged parts of the tissue[67]. Microglia inhibit peripheral cells recruitment and promote angiogenesis and tissue reorganization after inflammation through the release of anti-inflammatory mediators, such as IL-10[86] or IL-4[87] along with phagocytosis of inflammatory cellular and myelin debris, together with the remaining apoptotic cells that can be realized without re-induction of inflammation through the TREM2/DAP12 pathway[88]. In addition, microglial will support neuronal, glial and BBB health[89] through the release of neurotrophic factors, such as TGF-β[90] or IGF-1[91]. Finally, microglia enter in cellular death to adjust its population size back to baseline[92].

This simplistic overview does not encompasses the variations of immune regulation needed to face all possible stimulations but rather depicts the characteristic steps necessary in the general process of microglial immune challenge and displays the different functions used to fulfill that role.

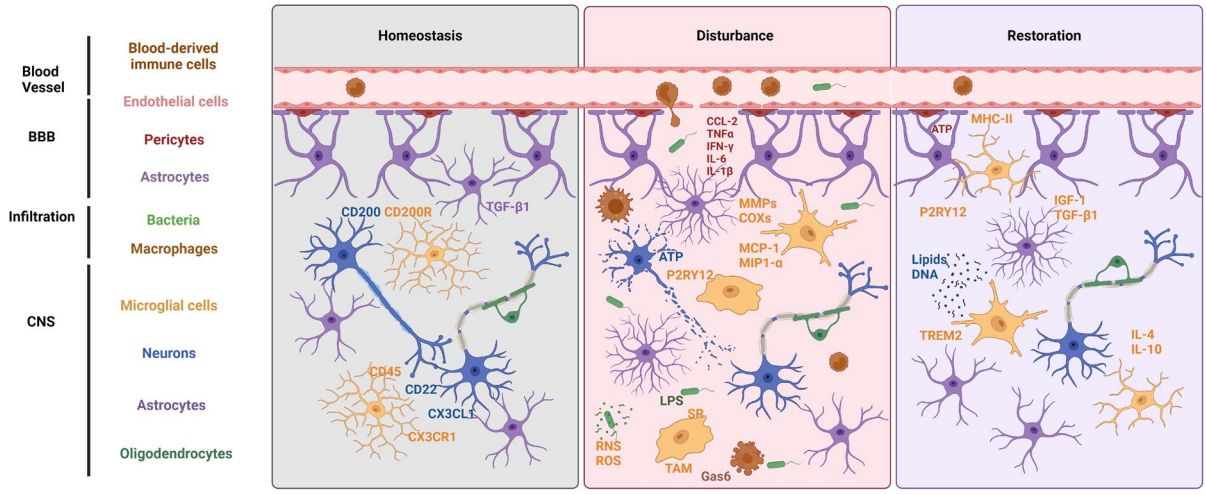

Figure 2. Immunocentric role of microglia in murine bacterial infection:

In a homeostatic brain environment, defined by a relative consistency of physiological reactions, microglia are moving their processes and through their sensome, monitor the overall well-being of the parenchyma. This microglial phenotype, referred as homeostatic and managed by immune checkpoints to avoid uncontrolled deleterious reactions of microglia is induced by neurons secretions of CX3CL1, CD200 and CD22[93] , together with astrocytic TGF-β1[94]. Following the sensing of a bacterial systemic immune perturbation, pericytes of the BBB start secreting CCL-2[95] to attract microglial cells and follow by secreting TNFα, IFN-ɣ, IL-1β and IL-6[96,97] that will be recognized as a first sign of homeostasis dysbalance by microglia and enhanced their proliferation[98]. This disturbance signaling can be further increased by both the release of ATP from dying neurons and, the cessation of homeostatic inducing secretions from the distress surrounding leading to a phenotypical adaptation of microglial cells[99]. This distress-induced phenotype will first lead to the secretion of BBB modulating agents such as COXs and MMPs, followed by the secretion of MCP-1 and MIP1α to recruit peripheral immune cells, cytotoxic compounds like RNS and ROS to annihilate the source of disturbance together with pro-inflammatory CKs to activate astrocytes. Microglial phagocytosis of apoptotic cells will be triggered by P2RY12, viable stressed neurons by Tyro3/Axl/Mer (TAM)[100] and bacterial pathogen *via* Scavenger receptors (SRs)[101]. After the annihilation of the source of disturbance, pericytes of the BBB promote the resolution of inflammation by secreting IL-33 and CX3CL1[102,103], driving microglial secretion of IL-4 and IL-10 in order to repair the tissue. Following ATP release from the disrupted BBB, microglial cells expressing P2RY12[104] migrate and establish physical contact with endothelial cells and basement membrane through MHC II[105] to repair the BBB and stabilize parenchymal microenvironment[106]. Phagocytosis of inflammatory residuals through the TREM2/DAP12 pathway will terminate the inflammation and restore the homeostasis.

Created with Biorender from[107,54]. CCL2: C-C motif chemokine ligand 2, CD200: Cluster of Differentiation 200, CD200R: CD200 Receptor, Gas6: Growth arrest specific 6, IFN-ɣ: Interferon gamma, IL-1β: Interleukin 1 beta, IL-4: Interleukin 4, IL-6: Interleukin 6, IL-10: Interleukin 10, LPS: lipopolysaccharides, MCP-1: Monocyte Chemoattractant Protein 1, MHC II: Major Histocompatility Complex II, MIP-1α: Macrophage Inflammatory Protein 1 alpha, P2RY12: Purinergic Receptor P2Y12, SR: Scavenger Receptor, TAM: Tyro3/Axl/Mer, TGF-β1: Transforming Growth Factor beta 1, TREM2: Triggering receptor expressed on myeloid cells 2, TNFα: Tumor Necrosis Factor alpha.

For decades, microglial was thought to act only in pathological settings with the immunological roles mentioned above. However, it is now known that microglial cells also fulfill a wide range of CNS-related functions from neurodevelopment to ageing.

3.2. Neurobiological role

3.2.1. From embryonic and post-natal development to adult brain

In the embryonic brain, as other glial cell types arise after NPCs have produced most neurons during the late embryogenesis, microglial cells are the only glial population during early gestation[108]. This bidirectional interaction between embryonic microglia and emerging NPCs leads to the maturation of both cell types and the establishment of the neuronal circuits[109]. As seen previously, microglial maturation during embryonic and post-natal life relies on NPCs and neuronal secretions (IL-34, CX3CL1, TGF-β1; Figure 1) but the process is reciprocal.

In embryonic brain development, microglial secretion of IL-1β, IL-6 and TNF-α will lead to the survival and maturation of NPCs[110]. In addition, microglia physically interact with NPCs to regulate the size of its population by phagocytosis of supernumerary viable progenitors. The physical contact between the two populations can also be directed towards dendritic spines, leading to the phagocytosis of exceeding synapses expressing C1q[111]. The participation of microglia in establishment of neuronal networks is particularly exemplified by the positioning of neocortical interneurons and the fine-tuning of dopaminergic neurons in the forebrain[112].

In addition to NPCs maturation and neuronal circuitry establishment, microglial cells also participate in the maturation of other glial cells. Microglial IL-1β and IL-6 secretion contributes to oligodendrocytes maturation, and, the phagocytosis of unnecessary oligodendrocyte precursors (OPCs) through CX3CR1 signaling, assuring a proper axon to oligodendrocyte ratio[113]. Even though microglial cells are not indispensable for the ensheatment of myelin, they are required for a proper structural integrity of myelin[114].

Finally, it is worth noticing that microglial cells also contribute to the establishment of the blood vessel architecture by secreting VEGF-α[115] and, through the CX3CL1/CX3CR1 pathway, regulate endothelial cells migration and vasculature formation[116]. Related to this finding, microglial cells are also involved in the maintenance of BBB integrity, sensing leakage through P2RY12[117] and sealing breaches *via* the expression of Claudin-5 and physical contacts with endothelial cells[106].

In the post-natal brain, microglial elimination of unnecessary elements still applies within developing circuits, from neurons to synapses, together with myelin debris and oligodendrocytes[118], in addition to radial fibers used by NPCs to migrate and rendered impractical and cumbersome afterwards[119]. Microglia will also continue to support gliogenesis of astrocytes through the release of IL-6 and

oligodendrocytes *via* TNFα, PDGF and neuropilin-1 (NRP-1). Finally, neuronal survival is under the influence of microglial IGF-1 and thrombospondin 1 and 2 (TSP-1,2)[120].

In the adult brain, microglia continue to monitor neurons' and glial cells' health and in the same manner *via* synaptic pruning, participate in synaptic refinement of sensory input processing throughout lifespan. They are also linked to learning and memory functions as well, *via* phagocytosis in the neurogenic regions of the brain, regulating adult neurogenesis[121]. Phagocytosis can be activated to remove apoptotic cells and cellular debris to avoid the induction of neurotoxic signaling[122]. Additionally, microglia interact with nodes of Ranvier of myelinated axons through potassium sensing, monitoring neuronal excitability and if needed, participating into remyelination[123].

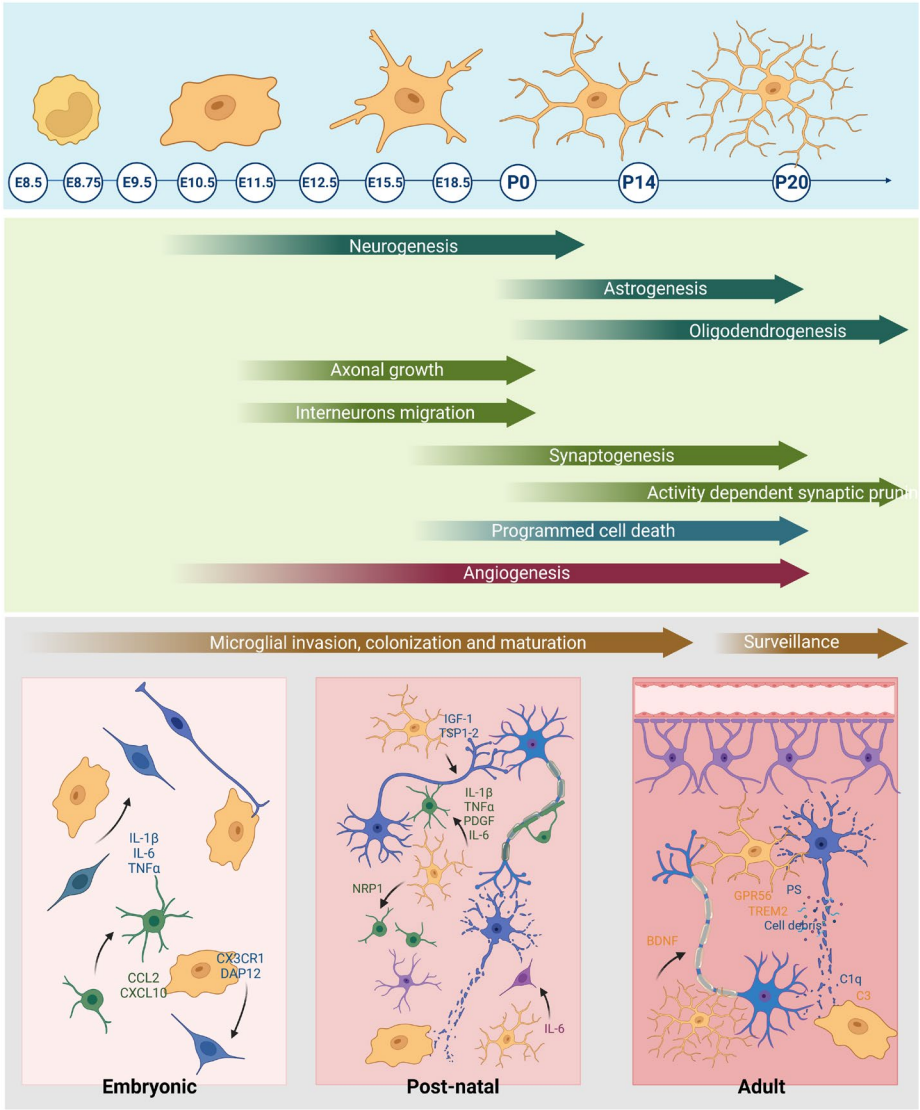

Figure 3. Neurobiological role of microglia in physiological mouse development and adulthood:

In the embryonic brain rudiment, amoeboid shaped microglia play essential roles in the emergence of neuronal circuits. Indeed, in the VZ/SVZ highly neurogenic niches are found a pool of different NPCs, namely the Pax6+ neural stem cells and the Tbr2+ intermediate progenitors[37] representing the potentiality of NPCs to differentiate into neuronal networks[124]. This balance between the two types of precursors is under the control of microglial secretions that are thought to be IL-1β, IL-6 and TNFα[110] in a CXCR4 dependent manner[124]. Furthermore, as the pool of Tbr2+ cells is destined to become neurons and are produced abundantly, microglial phagocytosis is crucial to eliminate the redundant ones that could impair the proper wiring of the brain[125]. In the wiring function *per se*, microglia are involved in the entrance and positioning of neocortical Lhx6+ interneurons into the pallium through signaling from CX3CR1 and DNAX-activating protein of 12 kDa (DAP12)[27,126]. Finally, microglia is implicated in oligodendrocytes and astrocytes maturation through the release of CCL2, CXCL10 and IL-6[127], respectively. In the post-natal brain, microglia is responsible for synaptic pruning of redundant dendritic spines, necessary for the proper formation of neuronal circuits through the complement receptor 3 (CR3) and the CX3CL1-CX3CR1 pathway[128,27]. Those functions are balanced by a neuronal inhibitory signal composed of SIRPα, detected by CD47 on microglia to avoid an excess in synaptic pruning[129]. It is also worth mentioning a process in which microglia could physically interact with presynaptic boutons and increase the neurotransmitter release by mechanical strength, leading to the stabilization of the synapse[130]. Both the pool and the maturation of OPCs is dependent on microglial phagocytosis through the CX3CR1 axis[113] and secretion of NRP1[131], IL-1β, IL-6, TNFα, PDGF[110] and IGF-1. The secretion of IGF-1 will also participate to the survival and health of emerging neurons, in addition of TSP-1-2[132]. Finally, maturation of astrocytes will be enhanced by microglial IL-6 secretion[127]. In the adult mouse brain, mature highly ramified microglia is monitoring neuronal circuits, removing dying neurons and cellular debris by phagocytosis, and participating to the BBB homeostasis. Microglia is also responsible for the proper functioning of synaptic plasticity involved in sensory input processing, learning and memory, mainly through the secretion of BDNF and through phagocytosis *via* TREM2 signaling pathway[133]. Microglial TREM2 is also implicated in the phagocytosis of apoptotic neurons in the adult brain, together with G protein coupled receptor 56 (GPR56)[134] and complement component receptor C3[135]. Finally, microglia promote synaptic remodeling *via* the phagocytosis of extracellular matrix around synapses[136].

Top panel: average morphology of evolving microglial along lifespan; Middle panel: CNS processes progression; Bottom panel: microglial CNS related roles. The color coding of the cell types can be found in Figure 2.

Created with Biorender, from[27,40,126]. BDNF: Brain Derived Neurotrophic Factor, C1q: Complement component 1q, C3: Complement component 3, CCL2: Chemokine (C-C motif) Ligand 2; CX3CR1: Fracktalin receptor; CXCL10: Chemokine interferon-ɣ inductible protein 10 kDa; DAP12: DNAX-activating protein of 12 kDa; GPR56: G protein-coupled receptor 56, IGF-1: Insulin Growth Factor 1; IL-1β: Interleukin 1 bêta; IL-6: Interleukin 6; NRP1: Neuropilin 1; OPC: Oligodendrocyte precursors cells; PDGF: Platelet Derived Growth Factor; PS: Phosphatidylserine, TNFα: Tumor Necrosis Factor alpha; TSP1-2: Thrombospondin 1 – 2.

3.2.2. The ageing brain

The healthy ageing brain is a more complex entity to unfold with both neurobiological and immunocentric related functions tangled up under the evolution of the entire cellular microenvironment, as well as the intrinsic changes within microglial cells.

On the one hand, the ageing brain environment is associated with an increased inflammatory status characterized by the accumulation of cellular and myelin debris[114] but also misfolded proteins[137]. Accompanied by an impaired BBB integrity, increased peripheral immune infiltration[138] and decreased lymphatic perfusion, together with an overall cellular senescence[139] or hyper-responsiveness[140].

On the other hand and as mentioned previously, microglia are very long-lived cells with a limited repopulation capacity and thus, are subjected to the deterioration of functions borne along the ageing process[141]. As a matter of fact, ageing microglia is often coined as "dystrophic", mostly referring to a change in morphological structure[142] but also linked to impaired migratory and phagocytic function and an overly excessive immune vigilance[141]. This state of aged microglia has been called "primed"[143] and is not thought to be more inflammatory *per se*, but displays responses to homeostasis disbalance that are strongly heightened and prolonged alongside an hampered resolution of inflammation[143]. The primed state of microglia has been related to an upregulation of sensing related receptors; like TLRs and NOD-like receptors (NLR)[144]; and pro-inflammatory secretions, like IL-1β and TNF-α. On the contrary, microglial homeostatic markers as P2RY12, TMEM119 and CX3CR1 are decreased[145] and the response to anti-inflammatory compounds is downregulated, leading to a deficiency in restoring homeostasis and resulting in a never-ending inflammatory status of the brain. In addition, as the ageing brain is linked to a significant decrease of microglial immune checkpoints (CD200, CX3CR1 and CD47)[143] together with TGF- β1 signaling, it is thought that the primed phenotype could arise from absence of overall homeostatic signaling stimulation[146].

In addition, the phagocytic function has been characterized as impaired in aged microglia when targeting myelin debris arising from neurodegenerative neurons, misfolded proteins such as Amyloid beta (Aβ), apolipoproteins, α-synuclein and apoptotic bodies[147]. The exact mechanisms are not known but the crucial CX3CL1/CX3CR1 and TREM2/DAP12 signaling pathways are decreased in the aged brain[148], it is also thought that the increase in phagocytosis inhibitor CD22[149] and the decrease in endogenous TGF-β1 signaling in the environment could be responsible for the impaired phagocytosis of apoptotic cells[150].

It worth mentioning that microglia senescent phenotype is thought to be found in the physiological ageing brain[151] thus aggravating the dysbalance in homeostatic regulation. Indeed, senescence is a normal process of cellular ageing induced by the shortening of telomeres[152] and characterized by the irreversible cell-cycle arrest by expression of cyclin-dependent kinase inhibitors Cdkn1a and Cdkn2a[153] leading microglial cells to adopt a very specific phenotype, named Senescent-Associated Secretory Phenotype (SASP)[154]. The SASP is still difficult to distinguish from the primed one, sharing common increased pro-inflammatory secretions, such as TNFα, IL-1β and IL-6[155] and until now, no SASP exclusive marker has been found.

With this in consideration, functions of microglia in the healthy ageing mouse brain could be summarized as a vain effort from exhausted microglia to re-establish an homeostatic local surrounding in a constantly triggered overall environment to secure as much as functional neuronal networks as possible, in order to slow the cognitive decline associated with the normal process of ageing.

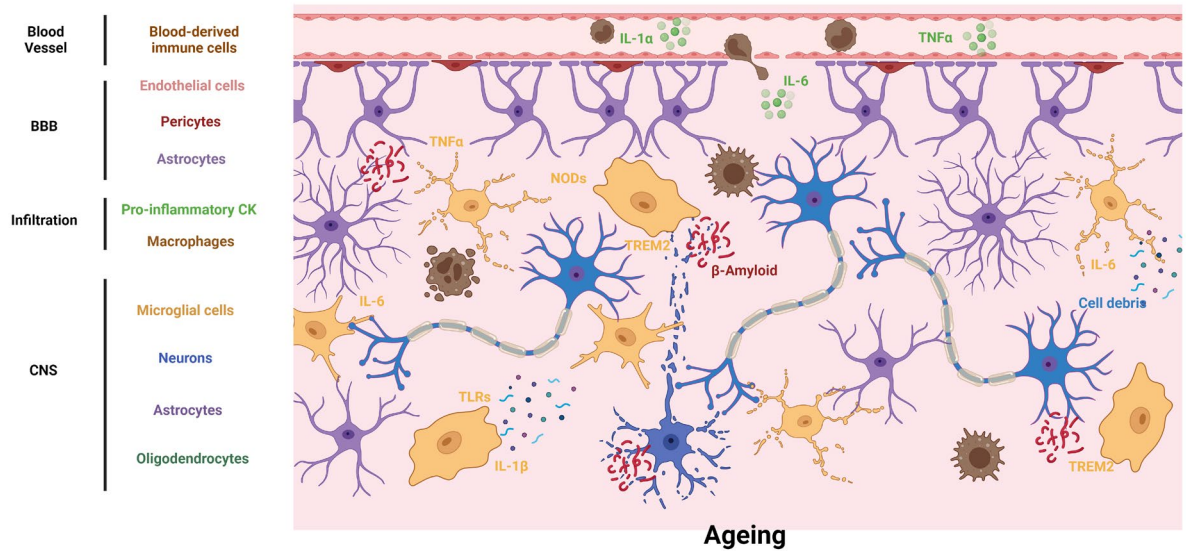

Figure 4. Neurobiological role of microglia in physiologically ageing in mouse brain:

In the healthy ageing mouse brain, the dystrophic microglia, characterized by reduced branching, increased soma size and cytoskeletal impairment[156], evolve in an inflammatory micro-environment surrounded by debris of all sorts, hyper responsivess and senescent glial cells, together with fragilized neurons. The disrupted BBB leads, in addition, to the accumulation of peripheral immune cells that can be already primed by the systemic inflammation observed in physiological ageing[157]. In a attempt to re-establish past brain homeostasis, microglia engage in phagocytosis through the remaining available receptors such as TREM2[158] to clear inflammatory waste as much as possible but fail due to exhaustion from age that can be observed by the accumulation of lipid droplets within the cells[159] or senescence,

characterized by a greater cytoplasmic accumulation of lupofuscin[160]. In the same manner, exhausted microglia fail on the one hand to produce neurotrophic factors, such as BDNF[144] and anti-inflammatory modulators like IL-10[161] to repair parenchymal damages and, on the other hand, cannot decrease its production of neurotoxic ones, like IL-6 and IL-1β, leading to a constant inflammatory status of the brain and a cognitive decline within the individual.

Created with Biorender. IL-1α : Interleukin 1 alpha; TLRs : Toll like receptors.

As we have seen, in addition to their indispensable role in protection of the CNS facing pathological insults, by participating into healthy neurogenesis, gliogenesis, wiring of neuronal networks and clearing of apoptotic and excessive elements, microglia are pivotal actors in brain development and maintenance in physiology[126,162].

It is challenging in such a stimulating environment to precisely isolate one function regulation in a given situation. The ascertainment of differential regulation of functions in opposite direction in aged microglia, with secretion being upregulated and phagocytosis downregulated, dismissed the common assumption that microglial behavior was an all-on/all-off process and highlighted that each function of microglia was finely tune individually to confer the most adapted response to a specific situation.

4. Microglial functions

In order to complete all their vital roles and as overviewed previously, microglial cells possess an abundance of effector functions modulated by CNS environmental cues.

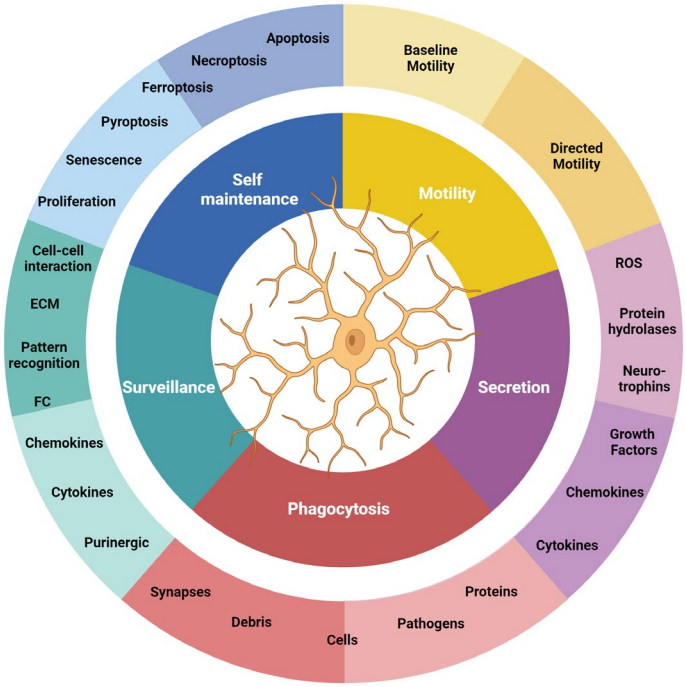

Figure 5. Microglial functions:

Microglial functions of surveillance, self-maintenance, motility, secretion and phagocytosis can be adapted in a various range of flavors to create the adapted response to the stimulations from the CNS environment. Inner ring: categories of functions microglia possess; outer ring: variants of those functions influenced by environmental cues.

Created with Biorender, from[163,164,78]. ECM: Extracellular Matrix, FC: Immunoglobulin FC receptors, ROS: Reactive Oxygen Species.

4.1. Surveillance

Microglial cells need to be in perpetual adaptation to the changing environment to survive and participate to the proper brain tissue organizational level, therefore they need to monitor external inputs and integrate the information content of the perceived signal to build an appropriate response[165]. All functional responses performed by microglia are thus induced following the sensing of an environmental change, making perception the most important one, and is initiated *via* the microglial sensome, encompassing an incredibly high number of membrane receptors (superior to a hundred in physiological conditions) allowing the recognition of extracellular matrix (ECM), amino acids, chemokines, CKs, purinergic molecules, pH divergences or even mechanical cues[63,164].

Biosynthesis of integral membrane bound receptors starts with the induction of the mRNA coding for the receptor protein under the influence of transcription factors (TFs) activated from intracellular pathways in reaction to an environmental change. From there, the mRNA is translated into a polypeptide within the endoplasmic reticulum (ER) to be correctly folded and submitted to post-transcriptional modifications (PTMs) prior to be encapsulated into secretory vesicles[166]. The receptor acquired last PTMs before being localized and inserted within the plasma membrane[167].

As it is a fastidious task to present all known microglial receptors, only few related to the responses developed below will be introduced here, including the purinergic receptor P2RY12, the CK receptor CSF1R, the chemokine receptor CX3CR1 and the PRR receptor TLR4.

Purinergic signaling is involved in both physiology and pathology of the brain by regulating cell proliferation and differentiation, inflammation and neuron-microglial cells cross-talk[168]. Metabotropic P2RY12 is a seven transmembrane domains G-protein-coupled purinergic receptor specifically expressed by microglia within the CNS and activated through paracrine or autocrine fixation of ATP or CD39 ectoenzyme processed ADP[169], ubiquitously secreted by all brain cell populations with variations of concentration in function of the environmental signal[170]. P2RY12 is considered a marker for physiological microglia and its activation leads to adaptation of microglial migration, phagocytosis and release of IL-6, IL-1β and TNF-α[171] through activation of PI3K, ERK1/2 and ROCK signaling cascades[78,172]. Expression of microglial P2RY12 vary between sexes, through development and ageing[173] and upon stimulation with different compounds, such as LPS or IL-4, linked to decreased and increased P2RY12 expression, respectively[174], even though the mechanism behind P2RY12 biosynthesis is not known, the expression of *P2ry12* mRNA is thought to be under the control of multiple TFs including CEBP/B, MEF2C and IRF8[175,176].

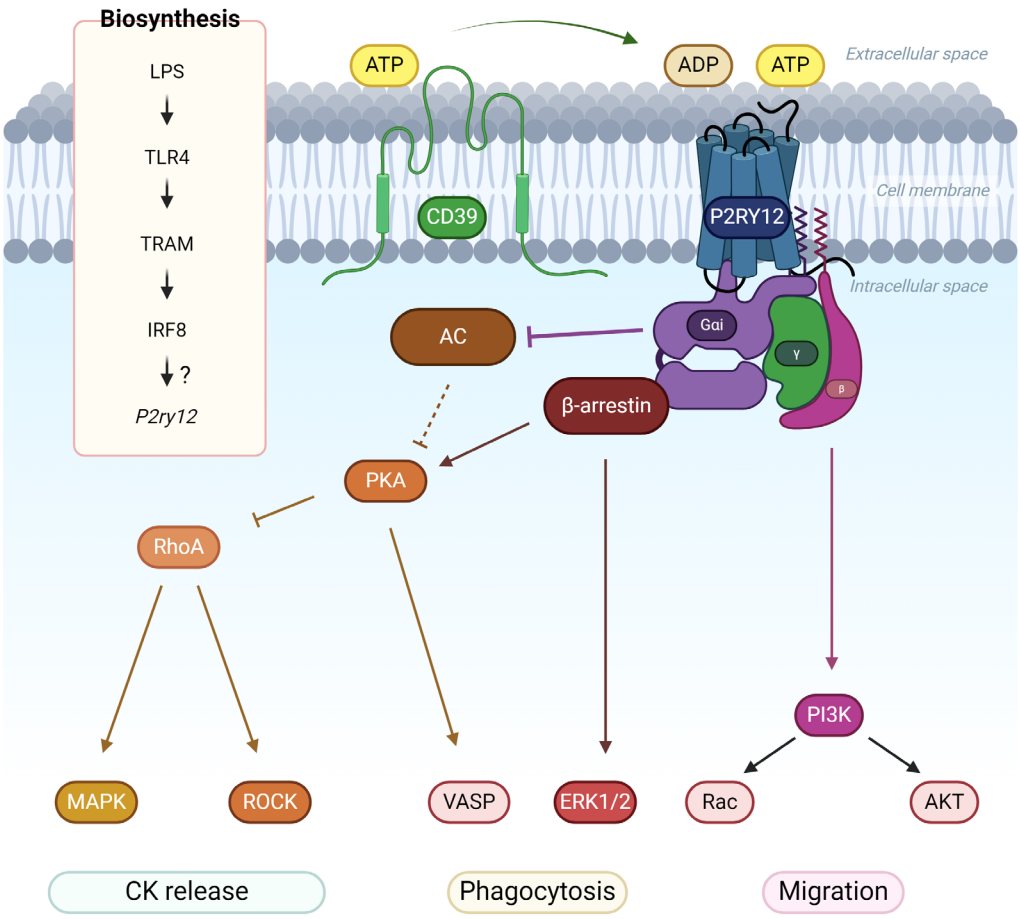

Figure 6. Proposed mechanism for P2RY12 activation and LPS-reduced biosynthesis:

Activation of P2RY12 can be induced by ATP or ADP, emerging from conversion of ADP from the CD39 receptor and leading to the inhibition of the adenylate cyclase thus decreasing the intracellular concentration of cyclic adenosine monophosphate (cAMP) indirectly inhibiting PKA. The absence of phosphorylation by PKA on RhoA leads to the activation of MAPK and ROCK pathways related to CK release[172]. Simultaneously, P2RY12 activation leads to the recruitment and activation of β-arrestin, able to activate PKA and leading to the activation of VASP, exhibiting a differential regulation of PKA that might be adapted to each individual situation[168]. In addition, β-arrestin is also activating the ERK1/2 pathway linked to microglial phagocytosis. Finally, activation of the beta sub-unit of the P2RY12 associated G-protein leads to the subsequent activation of PI3K pathway activating in turn Rac and AKT leading to microglial migration[177].

Biosynthesis proposal: LPS stimulation of TLR4 has been linked to microglial P2RY12 upregulation and *P2yr12* mRNA is known to be under the control of IRF8 TFs[175]. Both events can be linked by the TLR4 activation of TRAM, activating in turn IRFs, including IRF8[178], but the causality is way more complicated and must be linked to others TFs regulation, even though IRF8 has been shown to be both activator and inhibitor of transcription, it has been proved that activated IRF8 should lead to enhanced P2RY12 expression.

Created with Biorender from[168,172,179,180]. AC: Adenylate Cyclase, ADP: Adenosine Diphosphate, AKT: protein kinase B, ERK1/2: Extracellular signal-regulated kinases 1/2, MAPK: Mitogen-activated protein kinase 1, PI3K: Phosphoinositide 3-kinase, PKA: Protein kinase A, Rac: Rac GTPase, RhoA: Ras homolog family member A, ROCK: Rho-associated protein kinase, TRAM: Translocating chain-associating membrane protein, VASP: Vasodilator-stimulated phosphoprotein.

CSF1R is a key class III tyrosine kinase transmembrane receptor belonging to the CK superfamily of receptors and is essential for brain homeostasis, neurogenesis and neuronal survival[181]. In addition to endothelial cells, NPCs and some subpopulations of neurons, CSF1R is expressed by microglia and is crucial to induce and maintain its homeostatic identity, survival, proliferation and migration through its binding with neurons and astrocytes brain region specific[182] secretion of CSF1 or IL-34 leading to the activation of PI3K, JAK-STAT and ERK1/2 signaling axis[183,184]. Biosynthesis of CSF1R *via* transcriptional regulation of the *Csf1r* gene, encoded by the proto-oncogene *c-fms*[185] is under the control of various TFs, especially from the ETS family, in which can be found PU.1, well known for its major implication in microglial identity acquisition[186]. The transcriptional regulation of *Csf1r* has been well studied in macrophages and is highly complicated, emerging from a balance between activating and inhibiting TFs. For example, PU.1 activity can be enhanced by the presence of C/EBPβ TF that can be downregulated by Bach2 and Pax5 TFs and leading indirectly to downregulation of *Csf1r* expression and further biosynthesis[187,188]. Biologically, the microglial expression of CSF1R has been shown to be upregulated by stimulation with Aβ and in neuro-inflammatory diseases[189], in addition, it has been shown to be downregulated by LPS stimulation in macrophages[190] which also highlight the complexity of this receptor regulation since both ligands activate the TLR4[191].

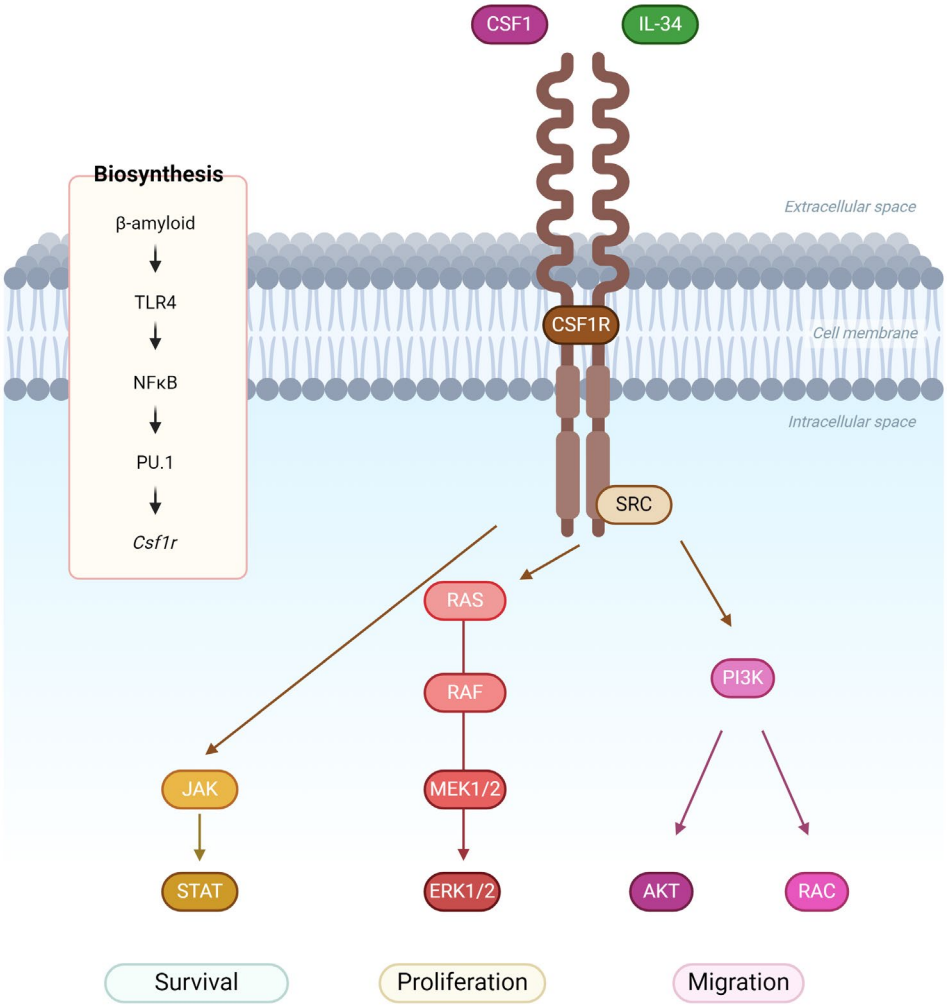

Figure 7. Proposed mechanism for CSF1R activation and β-amyloid induced biosynthesis:

Activation of the CSF1R receptor can be achieved through the binding of CSF1 or IL-34 and leads *via* SRC phosphorylation to activation of the PI3K pathway, further activating AKT and Rac, implicated in microglial migration. In addition, SRC will activate the ERK1/2 pathway associated with microglial proliferation. Finally, the JAK-STAT pathway, implicated in microglial survival and homeostatic identity will also be activated.

Biosynthesis proposal: Binding of β-amyloid on the TLR4 is known to induce an upregulation of the CSF1R receptor through the NFκB pathway. The transcriptional regulation of *Csf1r* is under the control of the PU.1 TF that can actually be induced by the NFκB pathway.

Created with Biorender from[191,181]. JAK: Janus kinase, MEK1/2: Mitogen-activated protein kinase kinase, RAF: Rapidely accelerated fibrosarcoma, RAS: Rat sarcoma virus, SRC: Proto-oncogene tyrosine kinase, STAT: Signal transducers and activators of transcription.

Finally, another important physiological microglia marker is the fractalkine receptor CX3CR1, belonging to the superfamily of seven transmembrane domain GPCRs chemokine receptors and is linked to MAPK and PI3K[192] signaling pathways induced by CX3CL1 constitutive secretion from neurons or occasional pathologically induced by astrocytes. It is worth mentioning that CX3CL1 exists in a soluble from on the one hand, acting as a pure chemoattractant for immune cells and inducing microglial proliferation, on the other hand, the membrane bound form, leading to physical interaction between neurons and microglia and associated with migration, survival and downregulation of inflammation[193]. The biosynthesis of CX3CR1 can be enhanced under the paracrine or autocrine stimulation with TGF-β[194] and TNF-α[195], or by hypoxic condition[196] through SMADs[94], NFκB[197] and supposedly HIF-1[198] signaling cascades and thought to be under the control of MEF2C and KLF6 TFs[176]. On the contrary, the expression of CX3CR1 can be reduced under the stimulation of LPS or with the physiological process of ageing, which, interestingly, is thought to be one of the reasons behind age related-overexpression of IL-1β since its downregulation is maintained through CX3CR1 activated PI3K pathway[148].

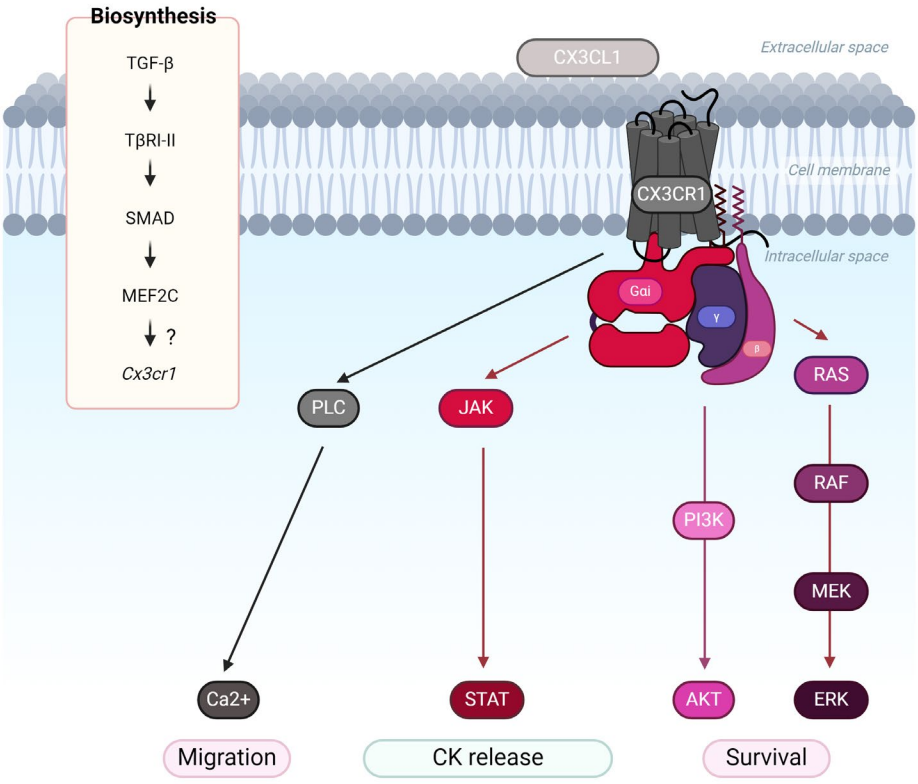

Figure 8. Proposed mechanism for CX3CR1 activation and TGF-β induced biosynthesis:

Activation of the CX3CR1 microglial receptor can be reached by the binding with soluble or membrane-bound CX3CL1 ligand and leading to the activation of ERK and AKT pathways known for microglial

survival, JAK-STAT inducing the secretion of anti-inflammatory CKs and PLC pathway, increasing Ca2+ concentration and leading to microglial migration.

Biosynthesis proposal: CX3CR1 is known to be enhanced by fixation of TGF-β on the TGF-β receptors I and II (TβRI-II) and the transcriptional regulation of *Cx3cr1* is known to be under the influence of the MEF2C TF. As SMADs are known to be activated by TGF-β and leading to the activation of MEF2C, it seems to be a correlation but it has also been proved that MEF2C activation was leading the transcriptional repression of *Cx3cr1* transcription, highlighting a missing component to this transcriptional regulation of CX3CR1 biosynthesis.

Created with Biorender, from[192,199,94]. MEF2C: Myocyte enhancer factor 2C, PLC: Phospholipase C, SMAD: Mothers against decapentaplegic.

In addition, TLR4, part of the PRR superfamily of receptors is a type I integral membrane glycoprotein highly expressed in microglia and astrocytes and crucial to mount an immune response when facing infectious challenge[164]. Microglial TLR4 and its main co-receptor CD14 are implicated in the recognition of the LPS component of Gram-negative bacteria strains and lead to both the phagocytosis of the bacterial compound and the secretion of pro-inflammatory chemokines and CKs such as IL-6, TNFα and IL-1β but also microglial pyroptosis[200] through the NFκB pathway. Biosynthesis of TLR4 is enhanced by stimulation with BBB pro-thrombin kringle-2[201], following hypoxic exposure[202] or under the stimulation with GM-CSF[203], through JNK[201], NFκB[204] and ERK1/2[203] signaling pathways, linked to c-Jun and PU.1 or HIF1 TFs[204].

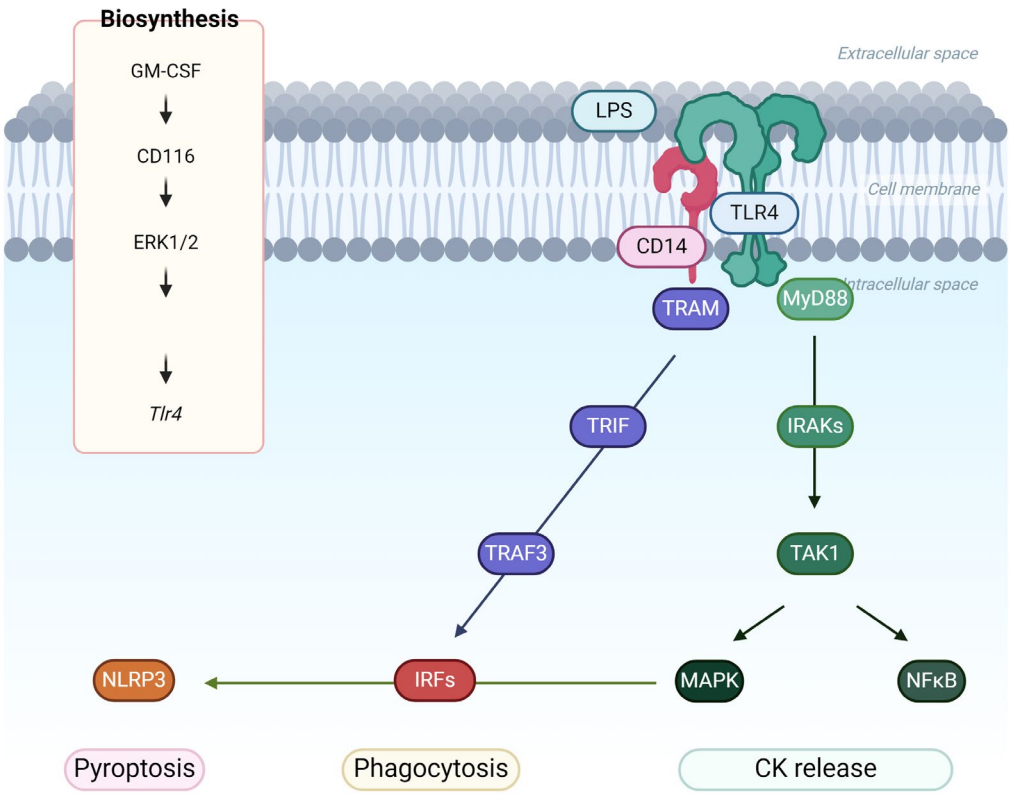

Figure 9. Proposed mechanism for TLR4 activation and GM-CSF induced biosynthesis:

Activation of the TLR4 can be made by fixation with LPS, ultimately leading to the activation of the MyD88-dependent pathway activating *via* TAK1 the MAPK and the NFκB pathways related to pro-inflammatory CKs release, but also the induction of NLRP3 and pro-IL-1β genes, leading to microglial pyroptosis. TLR4 activation *via* LPS also leads to the induction of the MyD88 independent pathways characterized by TRAM activation of IRFs and linked to endocytosis and phagocytosis of the TLR4.

Biosynthesis proposal: It is known that TLR4 is upregulated following the binding of GM-CSF on CD116 and that *Tlr4* expression is under the control of c-Jun TF. The two events can be linked by the known activation of c-Jun through the ERK1/2 pathway activated by GM-CSF.

Created with Biorender, from[205,206,207]. GM-CSF: Granulocyte-macrophage colony-stimulating factor, IRAK: IL-1R associated kinase, IRF: Interferon regulatory factor, NFκB: Nuclear factor kappa-light-chain-enhancer of activated B cells, TRAF3: TNF receptor associated factor 3, TRIF: TIR domain containing adaptor molecule 1.

As displayed here, it is important to note that microglial sensome constitution evolve under the influence of other receptors' activation and biosynthesis and, because of the considerable amount of receptors present on microglial membrane and the possible interactions and counter-activations between them (as the one from TLR4 and TREM2, for instance[208]), the impact on microglial perception

is obviously major but difficult to target and need further investigation. Thus, the microglial sensome change in various environmental conditions including sex, localization and age. Indeed, healthy ageing is characterized by an evolution of the microglial sensome in a specific manner, expression of receptors for phagocytosis (CD14, CD11b, CD68) stay unchanged, whereas purinergic receptors (P2RY12 and P2RY13) are decreasing, suggesting an adaptative strategy to avoid an overly inflammatory reaction to a large amount of ATP release by normal increase in cell death while keeping an intact clearance activity[63]. It is therefore needed to be aware of such sensome modifications leading to drastic changes in microglial behavior, as the one observed in ageing where the dysregulation of microglia leading to detrimental CNS responses could, in part, be led by misperception of the environmental cues.

Once the signals are received, microglia integrate and decode the informations gathered from the sensome about the state of the environment and initiate a set of pertinent responses to re-equilibrate the brain homeostasis.

4.2. Self-maintenance

As shown previously, physiological microglial cells population dynamics are independent of peripheral myeloid cell recruitment, under the control of a low turnover rate and self-renewal mechanisms and confering a long lifespan to individual microglial cells[209].

As microglia monitor a specific parenchymal area in a given localization and need to be rapidly mobilized in case of an alteration of homeostasis, the efficiency of their responses to any stimulus also rely on the density of the population[210]. An oversized microglial population can be responsible for an excessive reactivity facing a minor challenge, leading to deleterious effects on the CNS, whereas an undersized population leaving territories unsupervised can lead to the spreading of an injurious stimulus within the CNS[211].

Homeostatic density of microglia is achieved by a balance between proliferation and situation specific types of cell death, such as apoptosis, ferroptosis, necroptosis and pyroptosis, induced by stimulation of the microglial sensome[209,210].

In physiological conditions from neurodevelopment to adulthood, microglial proliferation is controlled by the CSF1R receptor, which can be activated by the two independent ligands CSF1 and IL-34[181,183]. Even though the entire signaling cascade has not been explored in microglial cells, it is known that both ligands binding with CSF1R leads to its dimerization and activates the PI3K/Akt and PKC signaling pathways, further activating the transcription factors STAT3, Jun and Fos[212] respectively, most likely

leading to the active transcription of proliferative and anti-apoptotic target genes, such as *C-Myc, CyclinD1, Bcl-2 and Bcl-xL*[213].

Microglia is also able to proliferate under stimulation from an homeostatic dysbalance, mostly through the same signaling PI3K/Akt and/or PKC pathways activation differentially induced by the binding of microglial TREM2 with Aβ[214], CCR2 with CCL2[215] or mIL6R with IL-6[216], amongst many others[210].

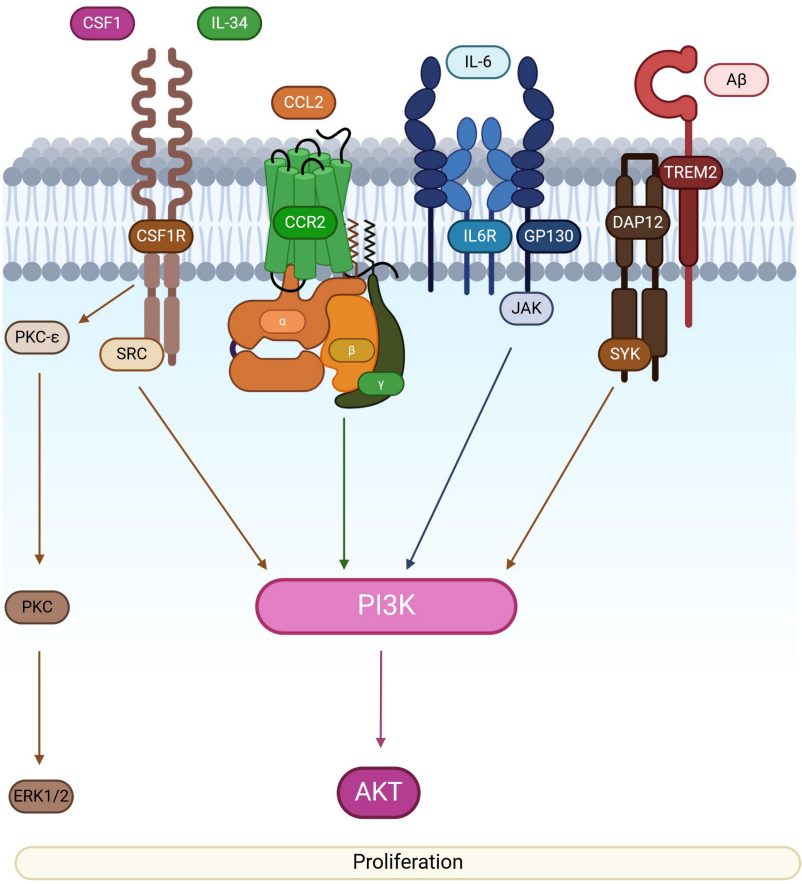

Figure 10. Illustration of possible signaling cascades underlying microglial proliferation:

The two major signaling pathways responsible for microglial proliferation are ERK1/2 and AKT, which can be activated by PKC and PI3K, respectively. In microglia, PI3K can be induced through different sets of kinases, such as JAK, SYK or SRC *via* stimulation with IL-6, Aβ or CSF1/IL-34. The ERK1/2 pathway activation can be achieved by the PKC *via* IL34/CSF1 binding.

Created with Biorender from[214,217,216]. GP130: Glycoprotein 130, SYK: Spleen tyrosine kinase, PKC-ε: Protein kinase C epsilon.

Following physiological proliferation and the increase of the population density, an equilibrium is reached by the apoptosis programmed cell death of superfluous microglial cells *via* the caspases cascade[218]. Apoptotic cell death is induced by the controlled dismantlement of intracellular components to avoid inflammation by a highly coordinated cascade of zymogens activation, leading to chromatin condensation, nuclear fragmentation and cytoplasmic membrane blebbing[219]. The apoptotic caspases activation pathway can be initiated *via* an intrinsic route dependent of mitochondria and relative to internal stress, or extrinsic one dependent of membrane receptors and related to external stress signaling[220].

On the one hand, the intrinsic caspase activation starts with the activation of pro-aptoptotic enzymes Bak and Bax, inactivating anti-apoptotic ones Bcl-2 and Bcl-xL and leading to the disruption of the mitochondrial outer membrane and release of cytochrome-c into the cytosol for constitution of the apoptosome that, in turn, activates the caspases 9, 3, 6 and 7, cleaving cellular components ultimately leading to cell death. On the other hand, the extrinsic caspase activation is initiated by ligand binding on surface receptors such as the TNF receptor family, leading to the activation of the caspases 8 and 10 further activating the caspases 3, 6 and 7 following the same outcomes as the intrinsic pathway[221]. The transcriptional regulation of pro- and anti-apoptotic genes have not been elucidated in microglia but has been explored in various types of cells and showed to be under the control of various TFs such as p53, NFκB, IRFs and STATs[222]. For instance, anti-apoptotic gene *Bcl-2* has been proved to be transcriptionally activated by NFκB binding *via* TNFα[223] and, in the same manner, the pro-apoptotic gene *Bak* has been shown to be activated by p53[224]. It would be interesting to know the transcriptional machinery orchestrating microglial apoptosis.

The underlying mechanism of homeostatic microglial apoptosis is unknown but thought to be related to the cell contact inhibition required from microglial optimum density within a dedicated space that could be induced by the binding of Fas to Faslg, both expressed by microglia[225] and able to activate apoptotic signaling pathway *via* the activation of the caspase 8.

However, following an injury-related proliferation, baseline microglial density can be attained by stimulation of the microglial sensome towards apoptosis, through activation of the caspases cascade induced by TLR4, for example[226]. Interestingly, necroptosis; which is a form of necrotic cell death led by a rupture of the cellular membrane and release of cellular components[227]; can also be induced by the TLR4 activation of RIPK3 and MLKL, leading to the permeabilization of the membrane[228]. Moreover, ferroptosis is a form of non-apoptotic programmed cell death characterized by mitochondrial shrinkage and dependent on iron and lipid metabolisms[229] can be triggered in microglia by increased iNOS intracellular levels known to be upregulated in pro-inflammatory conditions[230]. In addition,

microglia can be subjected to a last form of cell death accompanied with inflammation named pyroptosis, characterized by plasma membrane rupture and release of pro-inflammatory CKs (IL-1β, IL-18)[231] and triggered by PRRs signaling[227].

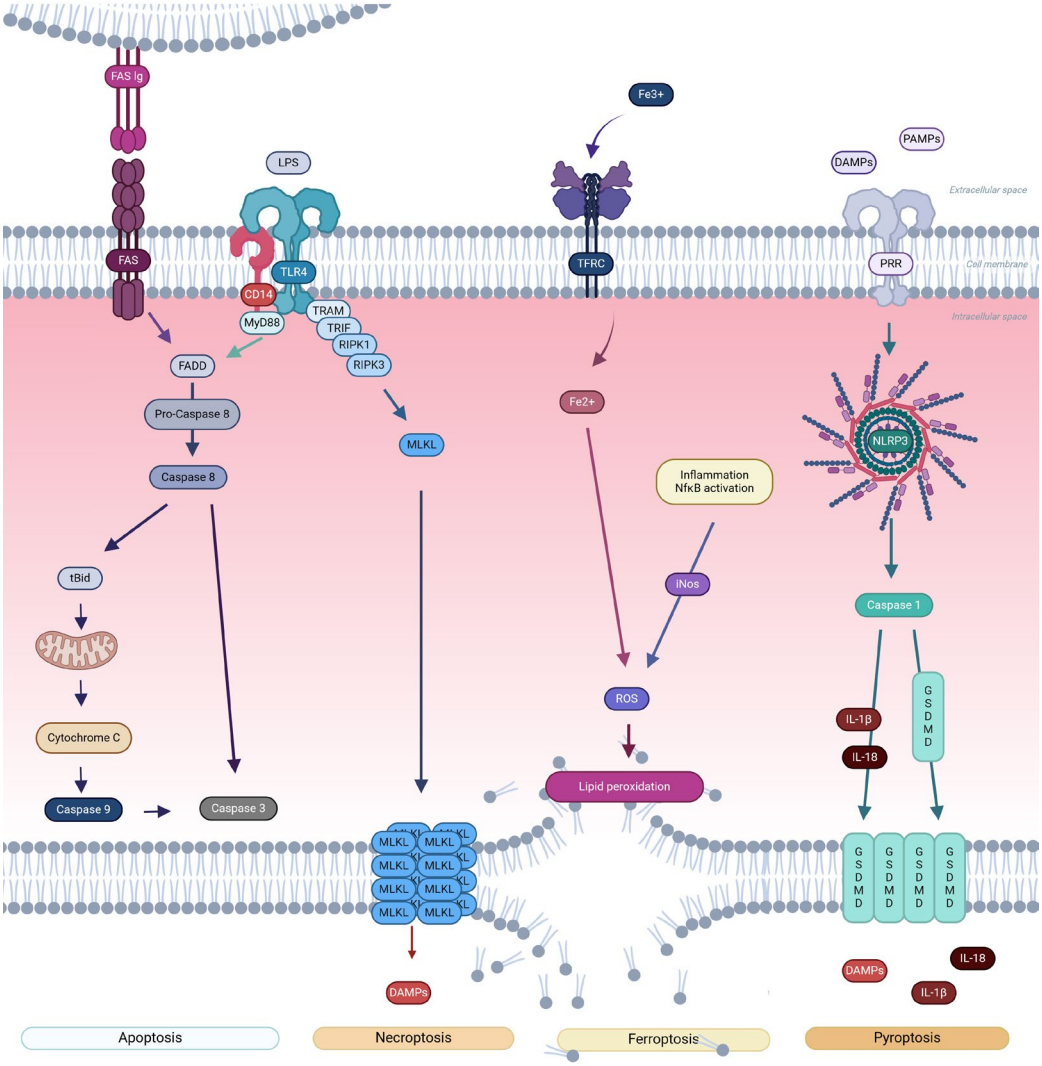

Figure 11. Illustration of possible signaling cascades underlying microglial cell death:

Different forms of cell death can be triggered in microglia, the tolerogenic apoptosis *via* Caspase 3 action, stimulated by the activation of the Fas and the TLR4 receptors; and the immunogenic necroptosis, ferroptosis and pyroptosis activated by different pro-inflammatory stimulations.

Created with Biorender from[232,233]. DAMP: Damage-associated molecular pattern, FADD: Fas-associated protein with death domain, GSDMD: Gasdermin D, iNOS: inductible nitric oxide synthase, MLKL: Mixed lineage kinase domain-like pseudokinase, NLRP3: NOD-like receptor family, pyrin domain containing 3, PAMP: Pathogen-associated molecular pattern, RIPK1/3: Receptor-interacting protein kinase 1/3.

The lack of experimental data on microglial turnover in health and diseases makes the exact molecular triggering signals, pathways and actors speculative but as similar mechanisms are well-known in cancer and immunity, transcriptomic reshuffles are obviously implicated.

4.3. Motility

As evoked previously, microglial cells are both highly motile and mobile with the capacity to follow chemotactic gradients on long paths, migrate locally or simply move their protrusions in the microenvironment[234]. In the physiological adult mouse brain, microglial surveillance is made possible by the constant isotropic extension, retraction and movement of the processes without change in the soma localization, in a process named "baseline motility"[235]. When in baseline motility mode, microglial processes browse their surroundings with a velocity from 2.5 to 4 µm/minute and can cover 60 µm of parenchyma around them. On the contrary, the "directed motility"[236] of microglia consists in the anisotropic and targeted extension of processes towards a chemotactic gradient with movement of the soma going up to 80 µm away. In microglia, these two forms of motility are mutually exclusive and are governed by complex changes in actin cytoskeleton remodeling correspondingly to the stimulation perceived through the sensome[234].

The cytoskeleton is a highly versatile structure implicated in a myriad of physiological cellular processes, such as endocytosis, intracellular transport, adaptation of cell morphology and motility, amongst others. Composed of a network of microfilaments of actin, tubulin based microtubules and cell dependent specific intermediate filaments, the cytoskeleton dynamically assembles and dis-assembles the components of each filament and modulates the interconnections between them to confer to the cell a high level of adaptability[237]. Since microglial inner cytoplasmic membrane is covered by a thick layer of actin and the cytoplasm is occupied with an abundant three dimensional actin network, the most studied part of microglial cytoskeleton reorganization is the one dependent on actin remodeling (AR)[235]. AR is guided by a perpetual cycle of polymerization/depolymerization between monomeric globular actin (G-actin) and filamentous actin (F-actin) that can further be branched together through the Arp2/3 complex to build distinctive functional structures. In microglia, such structures are coined as the lamellipodia[238], behind the leading edge of the membrane, the filopodia[239] constituting the foremost protrusions and, the uropod [240] at the rear of the cell. In motility, lamellipodia and filopodia lead the movement toward, whereas the uropod pulls the rest of the cell.

Briefly, microglial coronin-1 (CORO1A) with an high affinity for F-actin, recruits the Arp2/3 complex near the end of a filament and leads to the addition of cytoplasmic available G-actin to elongated it in an ATP dependent manner[241]. The crosslinking protein Ionizied calcium-binding adapter molecule 1 (Iba1) bounds F-actin together to form parallel actin bundles necessary for the shape elaboration of lamellipodia and filopodia[242]. The disassembly of F-actin towards G-actin to constantly reshape the actin cytoskeleton and allow the cell to move, is done by cofilin 1 (CFL1)[243].

The mechanistic processes behind both microglial baseline and directed motilities are still unknown, but thought to be under the control of environmental ATP release, microglial G protein-coupled purinergic receptor P2RY12 and the two-pore-domain halothane-inhibited K+ channel subfamily K member 13 (KCNK13 or THIK-1)[35].

In the case of baseline motility, relying only in slight movements of protrusions, the source of ATP, diffused and at a low concentration emerges from astrocytes and the stimulation of THIK-1 is required, while P2RY12 activation is not mandatory. Since Knock-out (KO) of P2RY12 does not annihilate baseline motility, another mechanism is known to exist but has not been discovered yet. CX3CR1, which signaling leads to change in AR[244], is thought to be a good candidate since its KO lead to a 30% reduction of microglial basal motility[245].

On the contrary, directed motility, consisting in the formation of motion directed protrusions, adhesion to the substrate at front and loss on the rear of the cell followed by rear retraction[237], arises principally through the lamellipodium, by cell front Arp2/3 polymerization and cell rear CFL1 actin depolymerization[246]. Microglial directed motility is induced by high local ATP concentration released by neuronal distress, bound on P2RY12 and potentialized by THIK-1 activation, even though the latter is, in that case, dispensable.

It is known that binding of ATP to microglial P2RY12 leads to changes in the polymerization of actin filaments, increase of microglial motility and expression of ECM interacting CD11b adhesion molecules[234] but the signaling pathways implicated have not been explored in microglial cells. Nevertheless, it is established that stimulation of P2RY12 leads to the activation of the PI3K signaling cascade, further activating Akt and small Rho GTPase Rac, creating a loop of positive reinforcement of actin polymerization through the activation of the Arp2/3 complex[168]. Interestingly, activation of the candidate CX3CR1 for baseline motility regulation also leads to the activation of PI3K signaling pathway.

Such a complex and dynamic mechanisms require *de novo* synthesis of G-actin, together with crosslinking proteins, and therefore, a mechanism indicating the cytoplasmic polymerization status to the nuclear genome. Myocardin-related transcription factor (MRTF), activated by the absence of G-

actin, translocates to the nucleus and activates in turn the serum response factor (SRF), a nuclear TF targeting the expression of cytoskeletal genes, such as *ACT*, *ARP2* or *ARP3.* In absence of actin polymerization or increase of actin depolymerization, free G-actin binds to MRTF and inhibits its translocation to the nucleus[247,248].

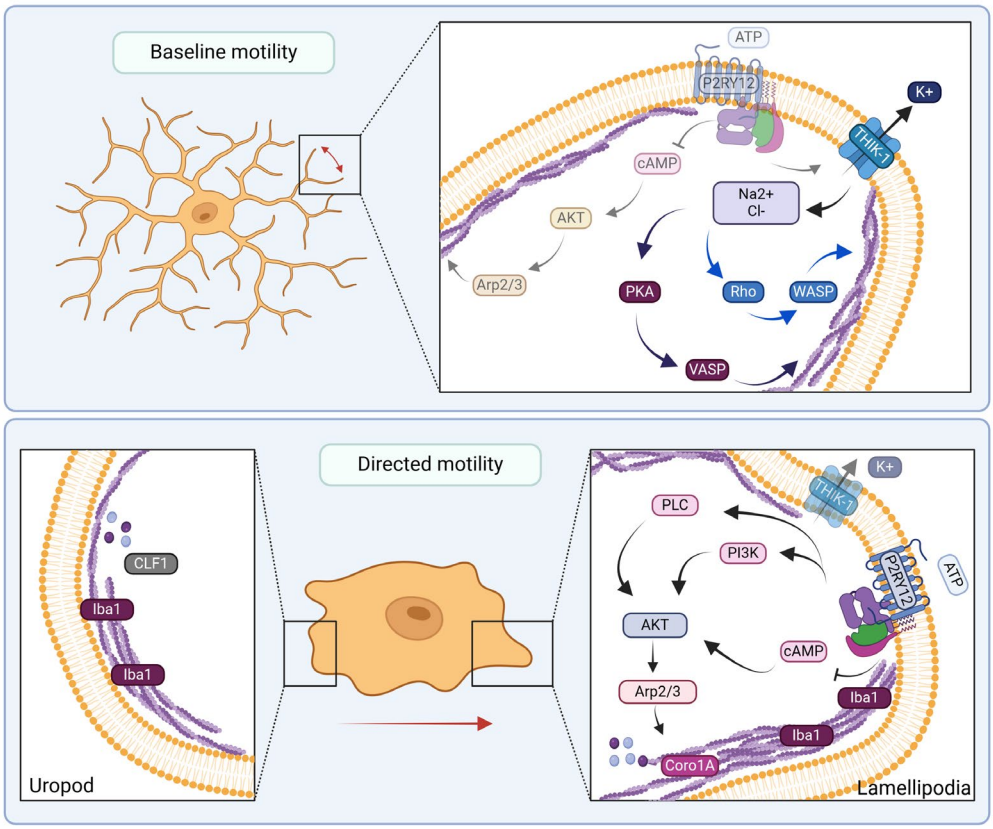

Figure 12. Molecular mechanisms behind microglial motility:

Two different modes of movement exist in microglia, on the top panel, the baseline motility (red arrows) modulated principally by the activation of THIK-1 that could, in theory, leads to changes in membrane potentialization and modulations of $Na2^{+}$ and Cl^{-} concentrations, capable of activating the VASP and WASP cytoskeleton remodeling proteins. On the bottom panel, the directed motility (red arrow indicating the direction of movement) which is thought to be induced by the P2RY12 activation modulating downstream AKT pathway and leading to the activation of the Arp2/3 complex at the lamellipodia and, probably *via* changes in G-actin concentrations at the uropod, the activation of the CLF1.

Created with Biorender from[249,250,251]. Arp2/3: Actin related protein 2/3 complex, CFL1: Cofilin, Coro1A: Coronin-1A, THIK-1: Two pore domain halothane-inhibited K^{+}, VASP: Vasodilator-stimulated phosphoprotein, WASP: Wiskott-Aldrich syndrome protein.

Further research is needed to unravel the complex machinery behind microglia motility but it is obviously orchestrated by fine tune molecular signaling pathways sensitive to local external gradients and thus, associated with gene expression regulation by TFs binding.

4.4. Secretion

Secretomics is one of the most important parameter of microglial function, allowing both effector capacities and communication with other cellular actors of the brain environment, but as large-scale proteomics studies of microglia are lacking, the entire secretome is still not complete.

However, as displayed previously, a lot of studies has been done over the years, gradually revealing an incredibly large panel of possible secretory products by microglial cell in physiological and pathological conditions[252,253,254]. Indeed, between 155[255] and 4938[256] different proteins have been identified in murine microglial cells supernatants and, amongst all of them, the most studied has been CKs; encompassing interleukins (IL-1 family, IL-6, IL-4, IL-13), chemokines (CX3CL1, MIPs, MCPs), growth factors (TGF-β, EGF, FGF), tumor necrosis factors (TNFα, -β), interferons (IFN-α, -β, -ɣ), colony-stimulating factors (G-CSF, M-CSF, GM-CSF), neurotrophins (BDNF, NGF, GDNF) and neuropoetins (LIF, CNTF, OM)[253]. Nonetheless, amino acids (L-glutamate), metabolites (prostaglandin E2, quinolinic acid), ROS and RNS (hydrogen peroxide, hydroxyl radical, peroxynitrite), enzymes (cathepsins, metalloproteinases), DAMPs (amyloid β) and phospholipids secretions (platelet activating factor) have also been linked to microglial physiology[257]. This non-exhaustive list of microglial secretory products already highlights the possible responses initiated by microglia to interact with its surroundings and is actually even more enhanced as a consequence of the pleotropic nature of those secretions and the possible combinations of them induced by different environmental settings[258].

CKs constitute a group of more than 300 soluble pleiotropic glycoproteins that can act synergistically or antagonistically to regulate innate and adaptive immune responses, inflammatory status of the tissue and modulate cell growth, differentiation and motility of diverse cell types[254]. Within the CNS, microglia produce various types of CKs in response to stimulation of their sensome to initiate an effector response or a communication with neurons, glial cells or peripheral immune cells[259]. Classically, the response induced in other cells by microglial CK secretion is made *via* the high affinity binding of the CK to its matching receptor leading to activation of downstream signaling pathways and TFs activation to modulate target genes expression, thus influencing the biological functioning of the targeted cell[253].

As it is arduous to review all microglial CK mechanisms and as it appears to be central to microglial communication in CNS physiology along lifespan, only the mechanism of action behind microglial secretion of IL-6, the most pleiotropic CKs in mammals[260] will be presented here.

Interleukins (ILs) were the first CKs ever studied and as their denomination suggests, they were firstly observed in the process of communication between leukocytes but were quickly found to be crucial to various range of other body cells functioning. Around 40 different ILs exist which can be pro-, anti-inflammatory or both, can act in paracrine or autocrine fashion and, are involved in cellular growth and differentiation, together with the modulation of the inflammatory status of the tissue[261].

IL-6 is a multifunctional CK displaying both pro- and anti- inflammatory effects, that can be partly explained by its receptor configuration assembly, arising from either the membrane bound mIL-6R, the soluble sIL-6R, characteristically inducing a cis- or trans-signaling cascade, respectively[262]. In addition, synergistic activation of both mIL-6R and sIL-6R activates a so called cluster signaling of IL-6. Both receptors, activated by IL-6 binding leads to the induction of the JAK/STAT and MAPK signaling pathways *via* β-subunit gp130, but the intensity between the two signaling pathways differs and leads to biological differences, the trans-signaling pathway inducing a pro-inflammatory response as compared to the cis-signaling pathway. The reason is thought to be related to the capacity of mIL-6R to be internalized upon binding, thus leading to a decrease in stimulation of the pathway compared to the one induced by sIL-6R, revealing another level of complexity in biological responses to CKs[263].

Within the CNS, IL-6 levels are constitutively low in physiological condition but play an important role in the establishment and maintenance of neuronal and synaptic homeostasis, as well as immune related roles when facing a CNS injury[264]. All glial cells and neurons can be receptive to IL-6 because of their ability to express IL-6 receptors and gp130 and, IL-6 itself can be produced by astrocytes, microglia and even neurons under rare circumstances[265].

Microglial cells secretion of IL-6 can be stimulated by TLR4 activation under LPS stimulation in pathogen infections[266], VEGF-R stimulation from NPCs VEGF secretion in neurodevelopment[267], and even by exogenous IL-6 binding on microglial IL-6 receptors in various conditions[268], amongst many others.

The case of the TLR4 induced IL-6 production is actually fascinating, exhibiting different degrees of regulatory feedbacks still unraveled totally today[269,270]. Briefly, fixation of LPS on the TLR4 leads to the activation of the NFκB TF, initiating the transcription of the *Il6* mRNA first into the endoplasmic reticulum followed by maturation in the Golgi apparatus. The nascent endogenous IL-6 peptide is then encapsulated and transported near the plasma membrane *via* endosome transport and, under the action of SNAREs proteins, released into the extracellular compartment[271] from which it will

autocrinally stimulates the mIL-6R, leading to the activation of the JAK/STAT pathway and leading the translation of *Il6* mRNA through STAT3. However, the signaling pathway initiated by LPS binding will also lead to the expression of SOCS3, inhibiting the *de novo* synthesis of IL-6 by interacting with the transcription factor STAT3, highlighting a very tangled positive and negative transcriptional feedback mechanism of IL-6 production[272].

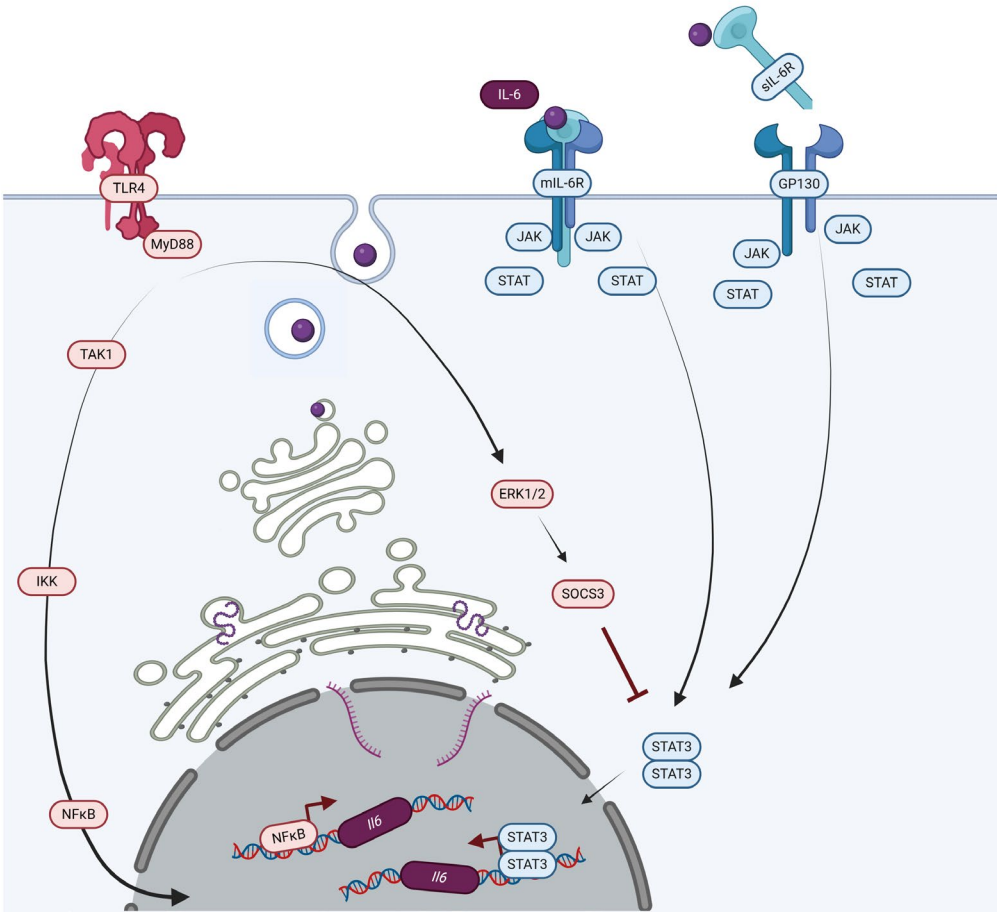

Figure 13. Molecular mechanisms behind IL-6 secretion in microglia:

IL-6 CK secretion in microglia is a good example for the complexity of the molecular mechanisms behind this function. Stimulation of the TLR4 with LPS leads to the activation of the NFκB TF which targets the *Il6* gene and leads to its transcription. The mRNA of *Il6* will then be translated into protein and secreted through exocytosis. However, IL-6 is capable of autocrinally stimulating the IL-6 receptors (soluble or membrane bound) known to be present on the surface of microglial cells, thus leading to the activation of the JAK/STAT signaling cascade and leading to the activation of the STAT3 TFs also targeting the *Il6* gene. In parallel, the activation of the TLR4 by LPS leads to the activation of the ERK1/2 pathway, leading to activation of SOCS3, able to inhibit STAT3.

Created with Biorender, from[273,274,275]. IKK: inhibitor of NFκB kinase, mIL-6R: membrane bound IL-6 receptor, sIL-6R: soluble IL-6 receptor, SOCS3: Suppressor of cytokine signaling 3.

It is obvious that the production of CKs by microglia requires a plethora of *de novo* proteins for signaling, trafficking, maturation and release of such compounds, that can only be realized from a highly dynamic transcriptional machinery further highlighted by the vast combination possible of CKs production at a given time[271,276].

4.5. Phagocytosis

Phagocytosis, the process by which cells engulf and degrade organisms or structures ranging from hundred of nanometers to tens of micrometers, is the first line of immune defense together with inflammation, but as highlighted previously, microglial phagocytosis, in addition to annihilate pathogens, also serves the purposes of neuronal networks wiring and maintenance along with overall clearing of potential cytotoxic debris and apoptotic cells, revealing a huge adaptability within the phagocytic process[78].

The general mechanism of phagocytosis starts with the binding of a stimulating ligand on a matching receptor presents on the surface of microglial membrane and inducing the internalization of the ligand into an early phagosome, maturing into a late phagosome merging with a lysosome to form a phagolysosome dissolving the stimulatory compound into small peptides.

Even though the exact molecular mechanisms of microglial phagocytic function have not been totally assessed until now, a large amount of data in both microglia and macrophages makes it in principle easy to draw a conclusion about the related functional regulation.

Following the sensing of a target to phagocyte through binding of ATP or CX3CL1 on P2R12 or CX3CR1, so called “find-me signal”, microglia chemotactically reach the target and *via* receptor-ligand interaction, make direct cell membrane contact to initiate the phagocytic process[277].

The repertoire of receptor-ligand leading to engulfment of the cargo is called “eat-me signal” and can be classified in two groups, the ones responsible for the engulfment of PAMPs, realized through TLRs and associated SRs such as the TLR4/CD14[278] and the ones involved in the process of apoptotic cells-associated cellular patterns (ACAMPs) related mostly to the recognition of phosphatidylserine by phosphatidyl receptors[279], but also able to trigger TREM2. It has to be noted that the definition of engulfment receptors and phagocytosis-initiation contributing receptors is still not clear and for the purpose of clarity, receptors presented here will be classified as engulfment receptors.

To avoid unintentional ingestion of healthy elements, “eat-me signals” are balanced by the opposite repertoire, expressed by healthy cells and named “don’t-eat-me signals” in which are found CD47 binding on microglial SIRPα[280], PS and lipids on CD300a or glycans on Siglec family of receptors[281].

As microglia are exposed to various type of cargo, it is not surprising to find a vast amount of different engulfment receptors, targeting live neurons, myelin debris, synapses, lipids or ECM[100,282,122]. In addition, secreted molecules like complement proteins or antibodies can opsonize targets and be recognized by microglial surface receptors to initiate phagocytosis, as it is the case for C1q opsonins on C3R microglial receptors[283].

This initiation step leads to the formation of a phagocytic synapse[284], a highly elaborated structure composed of a myriad of receptor clusters, dynamically formed by actin reorganization (elegantly reviewed by[285]) specifically congregating together intracellular kinases and small GTPases and excluding phosphatases to avoid hampering of the phosphorylating signal[286]. This spatial organization further induces, *via* phosphorylation of downstream effector molecules, both the formation of the phagocytic cup to physically engulf the cargo as well as the activation of intraphagocyte signaling pathways for further processing and parallel adapted extracellular responses[287].

Briefly, within the initiated phagocytic synapse, activation by ligand binding of TREM2 and co-activator DAP12, TLR4 and CD14 and C3R all lead to the activation of the kinase SYK, activating in turn CRKII, DOCK180 and ELMO then Rac towards the Arp2/3 complex actin remodeling[288]. In parallel, SYK can also activate Arp2/3 through the signaling cascade NCK/CDC42/WASP, further acting towards the cytoskeleton modulation required for the elongation of microglial processes forming and closing the phagocytic cup around the cargo[289]. In addition, SYK activates the PI3K signalling pathway leading to the accumulation of activated kinases and regulating the activation state of PKC, ERK1/2 and MAPK signaling cascade within the phagocytic cup[290].

Closure of the phagocytic cup form the phagosome, a membrane bound compartment isolating the structure to degrade within the phagocytic cell that mature following sequential fusions with early then late endosomes and finally lysosome in order to obtain the essential proteins and reach the optimal pH for successful degradation of the cargo[291].

The first step of phagosome maturation is constituted by its fusion with an early endosome forming the early phagosome characterized by a mild acidic pH of 6.1 and carrier of important proteins such as Ras-associated binding GTPases, proton pumping vacuolar ATPases (vATPases), as well as inactive hydrolases and proteases. In a nutshell, early endosome expressing the GTPase Rab5 activates Vsp34 leading to the activation of PI3K, further recruiting early endosomal antigen 1 (EEA1) guiding the

tethering between the early phagosome and the early endosome, then recruiting SNAREs proteins to strengthen the docking and leading to the membranes' fusion.

In a similar manner, the early phagosome next fuses with a late endosome through Rab7 and SNAREs proteins tethering system and acquires additional hydrolases, cathepsins and lysosome-associated proteins (LAMPs), to give rise to a late phagosome characterized by an increased number of vATPase enhancing the intra-phagosome pH to 5.5.

Finally, the late phagosome, bound to microtubules *via* Rab7, fuses with a lysosome containing up to 60 acid hydrolases and characterized by a pH of 4.5 allowing the activation of pH dependent glycosidases, DNAses, proteases and lipases within the phagolysosome to efficiently annihilate its content[292,78,287].

The transcriptional regulation of phagocytosis in general has not been study in depth but is already known to encompass the transcriptional control of membrane biosynthesis through transcription of *Ldlr*, *Pparg* and *Gpat* genes under the control of the TFs SREBP-1α and SREBP-2[293] and cytoskeleton remodeling through the expression of *Act*, *Arp2* and *Arp3* genes *via* the TF SRF[294,248]. In addition, the lysosomal modulation of *Lamp1*, *Hexb* and *ATP6V1H* genes through the TF TFEB[295] and the different components of each induced phagocytic pathways. For instance, complement molecules gene *C1qa* *via* TFs PPARɣ and RXRα or some engulfment receptors genes *Cd36*, *Mertk* and *Axl* with LXR/RXR TFs[296].

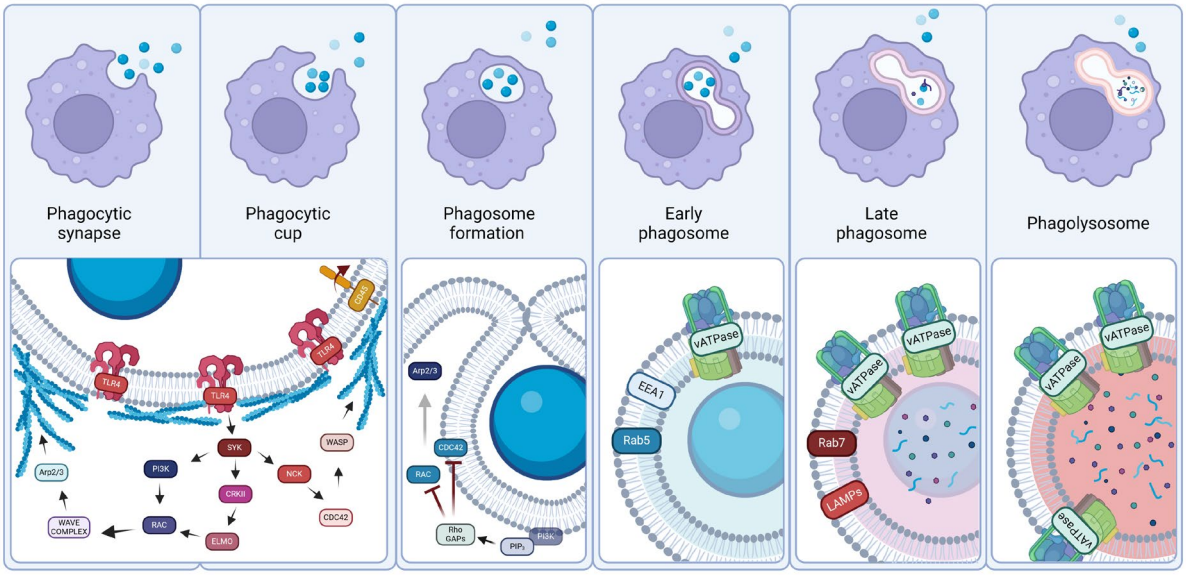

Figure 14. Molecular mechanisms orchestrating microglial TLR4 induced-phagocytic function:

Under stimulation of the TLR4, the actin remodeling complex Arp2/3 and WASP will be activated *via* the SYK kinase. The accumulation of phosphorylation will lead to the exclusion of the phosphatases, such as CD45, from the phagocytic synapse. The accumulation of the PIP_3 produced by the previous

activation of the PI3K signaling pathway will in turn activates Rho GTPases activating proteins (GAPs) inhibiting the Arp2/3 complex and allowing the closure of the phagocytic cup in the phagosome conformation. The phagosome will fusion with a serie of endosomes containing increased vATPases and inactivated proteases and hydrolases, leading to the degradation of the cargo.

Created with Biorender from[297],[298],[299]. CD45: Cluster of differentiation 45, CDC42: Cell division protein 42 homolog, CRKII: Crk adaptor protein II, EEA1: Early endosome antigen 1, ELMO: Engulfment and cell motility, NCK: Nck adaptor protein 1, PIP_3: Phosphatidylinositol (3,4,5)-trisphosphate, Rab5/7: Ras-related protein in brain 5/7, vATPase: vacuolar type ATPase.

Phagocytosis is obviously a very complicated process requiring a considerable amount of *de novo* proteins synthesis[300] for the mechanism in itself but, in addition, it is worth mentioning that the differential engulfment receptors leads to activation of other signaling cascades, thus leading to diverse responses accompanying microglial phagocytosis. For example, TREM2 activation leads to a non-inflammatory external response whereas TLR4 induced phagocytosis process is characterized by an inflammatory rush[301], increasing the potential features adopted by this function according to environmental cues[302] and revealing a highly selective transcriptional plasticity.

4.6. Potential antigen presentation

In addition, one of the most important function of innate immune cells is the presentation of antigens to lymphocytes in order to launch an adaptive immune response. Such a function requires the interaction between the T-Cell Receptor and MHC I/II bound with processed antigens from phagocytosis of foreign entities exposed on the surface of antigen-presenting cells[67,303].

The presence of the BBB composed of endothelial cells and astrocytes limiting the circulation of leukocytes and immune mediators within the CNS gave rise in the 1920s to the notion of “immune privilege” for the brain parenchyma, characterized by the absence of adaptive immune response and low expression level of MHC I and II molecules[304]. However, the discovery of CNS draining lymphatic vessels have led to the reassessment of this privileged status of the brain[305] and the reconsideration of the long asked question on microglial antigenic presentation capacities.

Initially, it was observed that under certain inflammatory conditions, microglial cells displayed an increased expression of MHC II proteins but antigen presentation remains weak or absent, making it

difficult to know for sure if microglia is able to present antigens on their surface to directly initiate an adaptive immune response[306]. One of the hypothesis states that the increase in MHC II expression is not sufficient to induce antigenic presentation since the expression of necessary co-stimulators CD80 and CD86 remains low[307]. Instead, it is thought that microglia could recruit and prime professional CNS antigenic presenting cells, as dendritic cells or infiltrating monocytes derived macrophages, to interact with CD4+ lymphocytes outside of the brain parenchyma[308]. Until now, there is no proof for direct antigen presentation by microglial MHC II to CD4+ T-cells *in vivo*, but this hypothesis is still considered (reviewed by[309]).

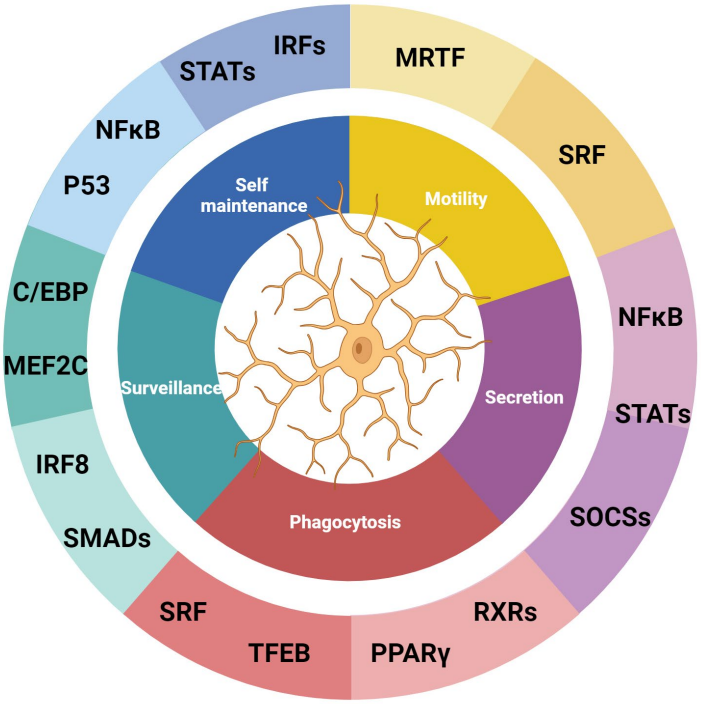

Figure 15. Microglial functional plasticity is linked to a multitude of TF regulation:

To summarize the previous part on microglial functional plasticity, this scheme presents a small fraction of the underlying TFs orchestrating microglial behavior, already highlighting the necessity of highly dynamic chromatin to adapt microglial cell to the environment.

Created with Biorender. C/EBP:CCAAT-enhancer-binding protein, IRF: Interferon regulatory factor, MEF2C: Myocyte-specific enhancer factor 2C, MRTF: Myocardin-related transcription factor, NFκB: Nuclear factor kappa-light-chain-enhancer of activated B cells, PPARγ: Peroxisome proliferator-activated receptor gamma, RXR: Retinoid X receptor, SMAD: Mothers against decapentaplegic, SOCS: Suppressor of CK signaling, SRF: Serum response factor, STAT: Signal transcducer and activator of transcription, TFEB: Transcription factor EB.

Considering the large amount of roles realized by microglial cells, the amount of possible combinations of function and the delicate and dynamic environment that the CNS is, it is incredibly clear that microglial cells are capable of displaying a high functional plasticity[310]. Even with the evident lack of knowledge concerning the underlying molecular mechanism, it appears obvious that multitude of TFs and downstream target genes are implicated in such functional plasticity, further demonstrated by the incredible heterogeneity within the microglial cell populations[311].

5. Microglial heterogeneity and classification

The heterogeneity regarding morphology, secretomic profiles[312] and surface markers[313] has been noticed for a long time but was further emphasized by an obvious functional heterogeneity of microglia facing different *in vitro* stimulations[314], *in vivo* in different brains regions[33] , between sexes[315] or in accordance with development, ageing and disease conditions[316]. The myriad of microglial phenotypes made challenging the attempts from the scientific community to define universal microglial behaviors and ultimately highlighted the need for a strong classification system with a standardized microglial nomenclature[317].

5.1. The M1/M2 paradigm

Facing the multitude of microglial phenotypes and functionalities, researchers have tried to create a classification of distinct models of microglial reactivity to unravel mechanisms of action in defined conditions of physiology and diseases. The M1-M2 classification was elaborated from macrophages polarization biology and based on cellular characteristics upon stimulation with a specific compound[318] itself inspired by the lymphocytes Th1 and Th2 concept[319]. Indeed, Th1 CK IFN-ɣ has been linked to the initiation of a specific phenotype in macrophages named the M1 and characterized by pro-inflammatory features, whereas the Th2 CK IL-4 has been linked to an anti-inflammatory phenotype in macrophages named the M2. Once the polarization is induced, morphological and functional features were measured to build the M1/M2 macrophage paradigm and, as described as the macrophages of the brain, the concept was ultimately extended to microglia[320].

Originally, the M1/M2 classification stated that microglial cell reactivity could be defined as either quiescent (M0), neurotoxic (M1) or neuroprotective (M2). But quickly different shades of M2 phenotypes appeared (M2a, M2b and M2c), to finally become a spectrum of activation between the

M1 and the M2 phenotype[321]. Even with this evolution in the classification, the dichotomic view of microglial polarization remained in the microglial research field and has only starting to be abandoned recently[322].

As stated by the M1/M2 paradigm, M0 phenotype was initially describing a quiescent microglial state, regarded as inactive, before being re-evaluated as surveying, in which microglia is characterized by an homeostatic signature and an elongated morphology with numerous ramified processes moving along the dedicated parenchymal space allocated to each microglial cell to react to any disturbance[323].

On one side of the spectrum, M1 phenotype could be obtained by exposing microglia to an acute inflammatory environment, mimicked *in vitro* by stimulation with LPS and/or IFN-ɣ[324]. This phenotype should be defined by a morphological change towards an amoeboid phenotype, characterized by an enlarged soma and a decrease in processes numbers and length[325]. It should be associated with a change in transcriptomics expression and secretome composition towards a release of pro-inflammatory CKs and chemokines (TNFα, IL-6, IL-1β…) and should lead to phagocytosis of pathogens. This phenotype is related to cytotoxicity of microglia and was linked with neurodegenerative diseases, such as Alzheimer's disease (AD)[326] or Parkinson's disease (PD)[327], both being characterized by an overly active microglia and a failure to resolute inflammation.

On the other side of the spectrum, the M2 phenotype could be observed after exposure of microglia to IL-4 and/or IL-13[324], and should exhibit a very small soma with long and thin processes[325], transcriptome and secretome composition towards the secretion of anti-inflammatory CKs[99], neurotrophic and angiogenic mediators (VEGF, TGFβ, BDNF…)[328] and should lead to phagocytosis of cellular debris and apoptotic cells. This phenotype is thought to be implicated in the development and progression of brain tumors in which microglial cells adopt a pro-tumor phenotype characterized by the production of the CKs cited above and failure to eliminate cancer cells[329].

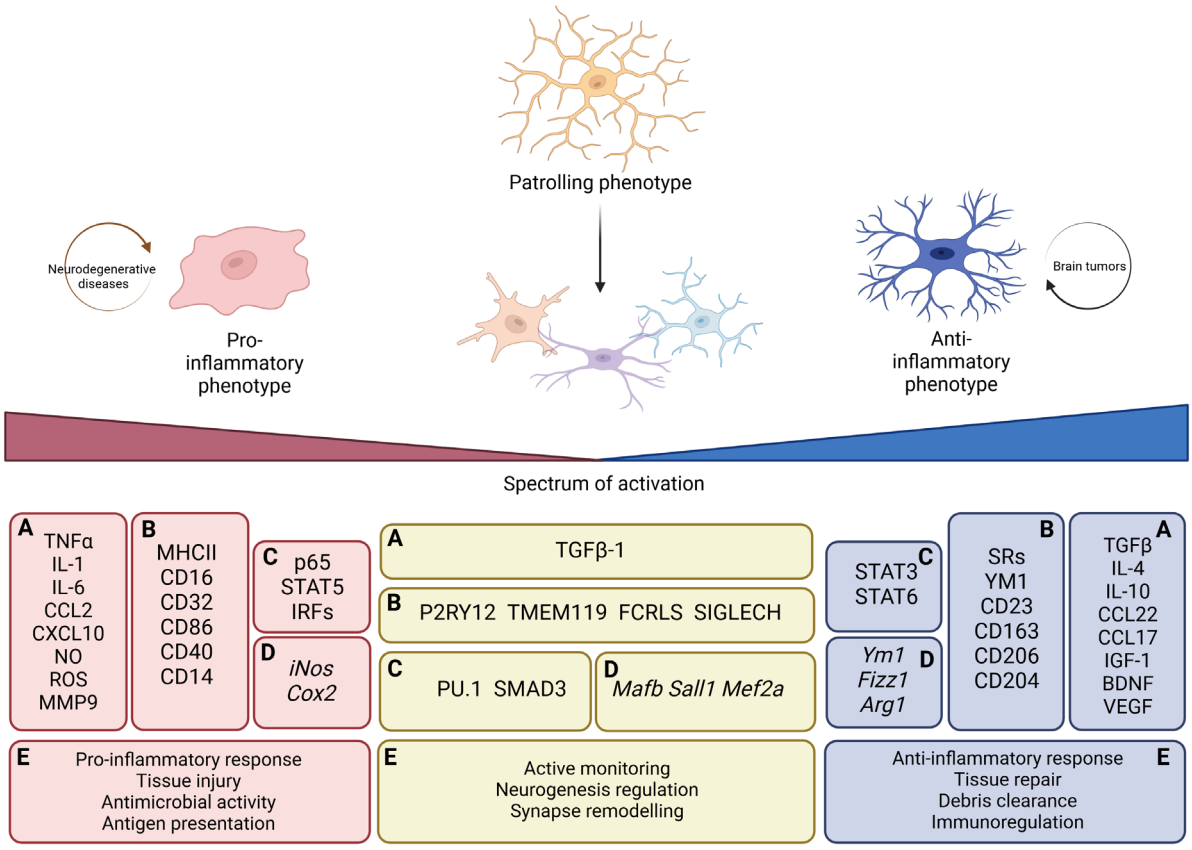

Figure 16. The microglial M1/M2 paradigm *in vitro*:

Schematic representation of the principal characteristics of the M1/M2 paradigm in microglial biology. Right panel: The M2 or anti-inflammatory end of microglial activation spectrum, middle panel: the M0 or homeostatic microglia, left panel: M1 or pro-inflammatory. (A) Secretome, (B) membrane markers, (C) transcription factors (D) and target genes, (E) Roles.

Created with Biorender, from[330,324,331]. CD: Cluster of differentiation, FCRLS: Fc receptor-like molecule, NO: Nitric Oxide, SIGLECH: Sialic-acid-binding immunoglobulin-like lectin H, TMEM119: Transmembrane protein 119, YM1: CHIL3, chitinase-like protein 3.

The fact that microglial functional plasticity is linked to signaling pathways modulation and TFs regulation suggests very complex and fine-tuned transcriptional dynamics that needed to be explored and included in the M1/M2 classification system.

At the era of transcriptomics, after identifying a core microglial transcriptional identity in comparison to other tissue macrophages[224] and other CNS myeloid cells; such as perivascular, choroid-plexus and meningeal macrophages together with engrafted monocytes and macrophages, such as *Tmem119*, *P2ry12* and *Hexb*[332,43,333], studies started to reveal that the combination of transcriptional signatures within any microglial population was gigantic.

Indeed, different transcriptomic-based clusters of microglial subsets have been explored and exhibit divergences regarding the species[334], the sex[335], the age[336], the physiological status of the individual[337] and the cellular localization within the CNS[338], but also regarding microbiome constitution and exposure to environmental changes[339]. Thus, the plasticity of microglia, exemplified by a high amount of subsets in relation to local and global environment, is observed not only on the morphological, proteomic or functional level but also on the transcriptional one, rendering the classification of microglia difficult.

Concerning the M1/M2 classification, comparison study between different transcriptomic datasets of induced M1/M2 microglia phenotypes independently generated revealed that only few genes were overlapping, highlighting the inadequacy of this classification system[340]. In addition, when the M1/M2 paradigm is applied to a specific physiological or pathological momentum, only few characteristics are matching between what is observed and the extreme polarizations present within the classification, both M1 and M2 markers being found within microglial subpopulations[341]. Finally, witnessing different context dependent molecular profiles of microglia does not imply a relationship to functionality, the only feature of microglia being important for development of therapies targeting microglia reprogramming in diverse diseases, thus needing a new innovative method of classification and comparison.

Establishing an adequate classification is a major requirement to find distinct microglial responses patterns and the underlying mechanisms orchestrating the functions and dysfunctions that can be further manipulated for therapeutic purposes.

To build such an efficient classification, researchers recently decided to unify the field of research to align experimental designs and be able to compare data and extract the more knowledge as possible. Using the same terminology and experimental rules could suppress at least the bias generated from the experimentally induced environmental cues of the precise microglial phenotype studied.

5.2. Redefining microglial identity

Even though it is now known that outstanding heterogeneity of microglial cell population makes it difficult to access successfully to the core mechanism orchestrating microglial behavior in a given context, the benefit of the outdated M1/M2 classification relies on the observable and measurable common traits to define microglial identity. Those traits should not be overlooked nor assumed to be holding truth of microglial functionality, but used as tools and included in the frame of any given study.

In their 2022 review titled "*Microglial states and nomenclature : A field at its crossroads*", Paolicelli et *al*. defined as critical the need to specify microglial states in function of the specific context they are evolving in, namely the species, the sex, the spatial location and the age of the individual. Then the level of observations that dictate microglial functions should be noted and multiplexed from phenomics, proteomics, transcriptomics, metabolomics and epigenetics in order to unravel the precise identity of the microglial population studied and thus, allowing predictions for future behaviors in the same frame or parallel mechanisms in another experimental frame[322].

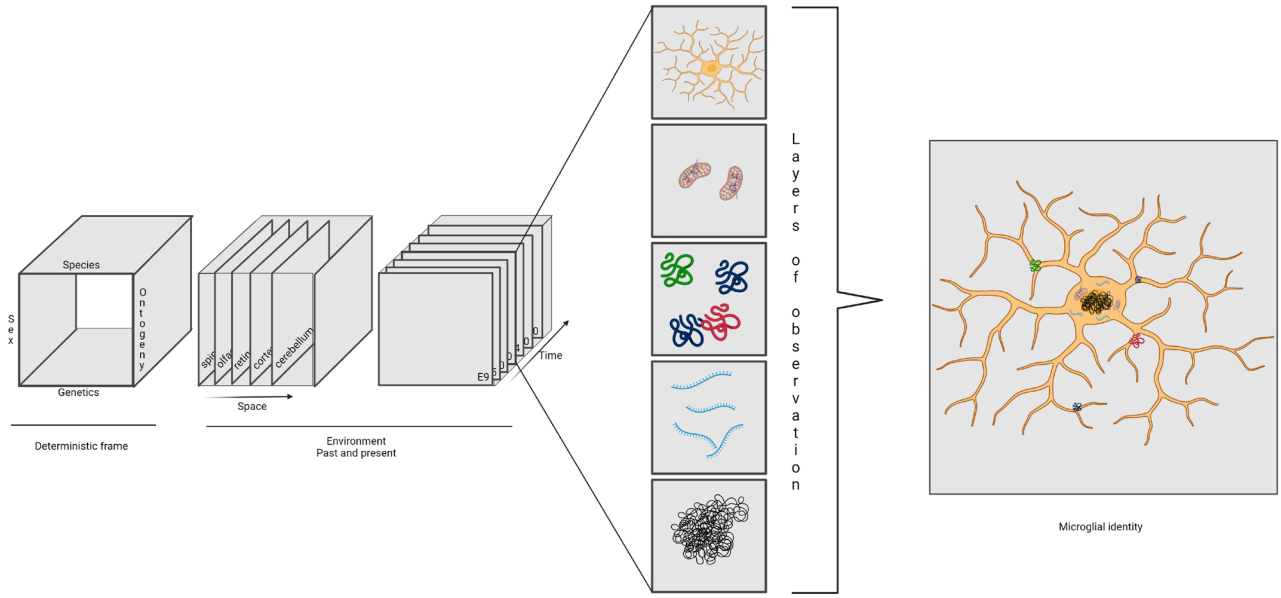

Figure 17. Beyond the microglial M1/M2 paradigm:

Microglial identity is now known to be much more complex than previously thought with the elaboration of the M1/M2 paradigm. It depends on multiple deterministic factors (species, sex and genetics of the individual, ontology of the macrophage population) but is also dependent on the localization in the CNS and the age of the individual/cell itself in an environmental sensitive fashion. Indeed, the space and time to study a microglial cell within a given individual encompass also past and present environmental cues such as communication with other cells, pathogens and drugs exposures, metabolites from nutrition and microbiota-derived bacterial fermentation products, air pollutants, amongst others. Then arise new layers of complexity in this scheme, brought by the choice of level to observe microglial cells, from morphology to epigenome. The informations gathered will only represent a part of the entire microglial identity. Only this mosaic can reflect microglial identity in a given context and help understand the exact functioning behind such identity. Middle panel, from top to bottom: phenomics, metabolomics, proteomics, transcriptomics and epigenomics[322,342]. Created with Biorender.

Considering the large amount of roles and functions of microglia in development and maintenance of brain homeostasis, together with its outstanding plasticity facing dynamic environmental signaling, it is not surprising to find correlations between microglial dysfunctions and brain diseases, in which microglia do not have a dichotomic beneficial/detrimental assignment as seen *via* the M1/M2 classification but a specific identity induced by the changing environment, since only few diseases-inducing mutations has been found in microglial cells directly (exemplified by TREM2 mutation in Nasu-Hakola neurodegenerative disease)[343,344].

6. Microglial dysfunctional reactivity and pathological conditions

After a century of research, the view of microglia as passive bystanders of the CNS dramatically evolved to the certainty that microglial behavior, even indirectly, was involved in virtually all pathological neurological conditions, including neurodevelopmental disorders, psychiatric conditions, traumatic and ischemic brain injuries, neuro-immunological diseases, brain tumors and neurodegenerative diseases, amongst others.

6.1. Neurodevelopmental disorders

Neuro-developmental disorders (NDD) are complex conditions defined by dysfunctional development of the nervous system and leading to the appearance of symptoms in the early childhood of the affected individual. NDDs encompass a variety of conditions such as schizophrenia (SZ), or Attention Deficit Hyperactivity Disorders (ADHD) but are mostly represented amongst public community by Autism Spectrum Disorder (ASD).

ASD is a condition arising in early childhood but having a major impact on the entire lifetime of the affected individuals and their caretakers. ASD is typically characterized by impairments in sensory, cognitive, emotional and behavioral regulation leading to social interactions difficulties and repetitive behaviors preventing the individual to have an efficient and productive insertion into society in the best case (high-functioning ASD) or even survive in the worst case (low-functioning ASD). The annual incidence of ASD worldwide was for a very long time estimated to be 1% but recent studies indicate a prevalence increase of 243%[345], and there is still no cure for ASD, the most used therapy being behavioral therapy, anti-depressant and anti-psychotic drugs to miminize the irritability characteristics of ASD[346].

The neuropathological features of ASDs are not clearly understood but known to emerge from abnormalities in the limbic structures, characterized by unusually small and densely packed neurons with reduced arborization and within the cerebellum with a lower amount of Purkinje cells and an increased amount of pro-apoptotic and oxidative stress markers. In addition, an overall aberrant organization in cortical structures accompagnied by an increased density of dendritic spines, which is compatible with a defect in neurodevelopmental patterning. Finally, a vast amount of studies have shown ASD to be associated with an general neuro-inflammatory phenomenon with increased density and reactivity of microglial cells[347].

Regarding the fundamental role of microglia in neuronal network establishment during neurodevelopment, it is not surprising that ASD symptoms were rapidely linked to microglial dysfunction as suggested by the simplified Maternal Immune Activation (MIA) theory, even though the causal relationship between ASD and microglia remains unclear.

In the MIA, a viral or bacterial induced inflammation during the first trimester of pregnancy leads to the activation of microglia influencing the proper development of the brain. Indeed, microglia from the MIA model will be numerous and will exhibit aberrant phagocytosis leading to an imbalance in NPCs, together with a deficit in apoptotic cells clearing, thus impairing normal neurogenesis. In addition to phagocytic deficit also hampering the proper pruning function, microglia from the MIA model display abnormal levels of neurotrophic factors leading to and altered neural circuitry[348].

It as been proved that the use of minocycline, an inhibitor of microglial activation with anti-inflammatory properties, in the MIA model, could lead to decrease activation of microglia and a reduction of the ASD symptoms, highlighting the therapeutic potential of targeting microglial cells in NDDs[349].

6.2. Neuroimmunological diseases

Immunological diseases of the CNS are a group of neurological disorders characterized by the inflammation and/or demyelination induced by the cellular immune responses towards CNS antigens, the most widely known being Multiple Sclerosis (MS).

MS is the most frequent autoimmune disease of the CNS and the most prevalent neurological disability with a prevalence of 120/100 000 individuals ranging from 20 to 40 years old. MS leads to severe physical symptoms such as difficulty with walking and balance, visual impairments, intestinal and urinary disorders and fatigue, but also cognitive dysfunction like learning and memory impairment.

Different forms of MS exist, characterized by the progression and remission phases of the disease but all are characterized by the appearance of demyelination lesions within the brain parenchyma, impacting the correct transmission of nerve impulses leading to the neuronal dysfunction[350]. The MS lesions are characterized by a core of inflammatory breakdown of myelin surrounded by reactive gliosis and accompagnied by an infiltration of peripheral immune cells (CD4+, CD8+ lymphocytes) allowed by the breakdown of the BBB[351]. The gold standard of care for MS is high dose of corticosteroids to reduce the inflammation and increase the time of remission but do not constitute a cure, thus leaving this neurodegenerative disease, a burden for young individuals and their caretakers[352].

Even though the differentiation of blood-derived monocytes makes it hard to distinguish macrophages from microglia, it has been shown that MS lesions could be constitue at 80% of microglial-like cells, and that a microglial reactivity could be noted from the earliest phases of the disease. On the one hand, microglia in MS have been characterized by secreting pro-inflammatory CKs and oxidative stress, thus leading to the destruction of the myelin sheath and the damage of axons. On the other hand, other studies have observed the opposite, and characterized some microglia in MS to be mostly leading to tissue repair and remyelination with specific secretion of neurotrophic factors and increased phagocytosis of myelin debris. Those contradictory observations are thought to be related to the phase of the disease from which the microglia have been isolated and corresponding microglial phenotypes related to the acute phase, the recovering phase and states in between. The major view on microglia in MS progression remains the detrimental one with a pro-inflammatory phenotype. The hypothesis of microglial cells constituting a deleterious phenotype in MS could be related to a chronic pro-inflammatory stimulation of microglia leading them to adopt a rigid primed phenotype, making reactivity modulation an interesting therapeutic avenue for all types of MS[353].

6.3. Neurodegenerative diseases

Neuro-degenerative diseases (NDs) are an heterogenous group of neurological disorders characterized by the progressive loss of neurons in the nervous system inducing impairment in cognitive and/or motor functions within the affected individual, the most known ND being AD[354].

AD is a progressive ND mostly occurring in people older than 60 years old and, by being the cause of 60 to 80% of the dementia cases, is responsible for an extreme dependence of the affected individuals suffering from memory loss and cognitive decline but also depression, impaired communication, disorientation and overall behavioral changes. With the overall ageing of the population worldwide, AD represents an important burden for caretakers and society that is thought to worsen in the

upcoming years. The physiopathology of AD is characterized by the accumulation of aggregated proteins, namely Aβ plaques and tau neurofibrillary tangles (NFTs), inducing neurotoxicity and leading to chronic detrimental oxidation and neuro-inflammation. The progressive destruction of neurons leads to neurotransmitters imbalance, that the AD gold standard therapeutic strategy try to restore but there is still no cure to AD[355,356].

Microglia have been shown to be activated in AD brains, moreover in the enriched Aβ plaques areas and a specific transcriptomic signature was found in microglia associated with Aβ clearance in AD, called the Disease-Associated Microglia subgroup (DAM) confirming the capacity of microglia to adapt to the AD microenvironment. The effect of the DAM subgroup on the spreading of Aβ and Tau proteins are still under debate, controversial results showing both positive and negative effects that could be linked to the disease state. Nevertheless, microglial activation in AD has been linked to a progressive increase in neuro-inflammation with production of pro-inflammatory CKs and an impaired phagocytosis.

As the therapeutic strategy of lowering the Aβ level has been shown unsatisfactory in clinical trials, one of the best option to date consists in targeting microglia to decrease the neurotoxic neuro-inflammation and increase its phagocytic capacity[357].

6.4. Brain tumors

Brain tumors encompass multiple entities, characterized by an uncontrolled and anarchic proliferation of tumor cells within the brain. Brain tumors can originate in the brain and thus be primary; or arise from periphery metastasis and be secondary. Primary brain tumors are organized into grades according to the World Health Organization (WHO) classification and based on the histology of the cell of origin and its molecular characteristics. One of the most common and aggressive brain tumor is the glioblastoma (GB)[358].

GB is a CNS WHO grade 4 malignant brain tumor affecting mostly individual over 40 years with a median prevalence of 4/100 000 persons/year; and characterized by a very low survival rate of 35% one year after diagnosis. The quality of life of the affected individuals rapidly declines with the invasion of the tumor mass and the destruction of the neuronal networks highlighted by headaches, seizures, cognitive decline and personality changes. Gold standard of care for GB has not been improved considerably since 2005 and still consists in the combinaison of surgical resection, radiotherapy and

chemotherapy with the alkylating agent temozolomide. GB remains to this date an incurable cancer[359,360].

The aggressiveness of GB can be explained by the high ability of invasion of GB cells into nearby tissues, together with the tumor promoting microenvironment that can account for up to 40% of microglia-like cells. Indeed, GB pathology is characterized by the breakdown of the BBB and the recruitment of blood-derived monocytes differentiating into microglial-like cells called Glioma Associated Macrophages (GAMs) that are hardly distinguishable from microglia, making it difficult to understand the different immune roles play by both cell types. Nevertheless, GAMs are now known to be mostly reprogrammed by neoplastic cells to secrete anti-inflammatory and immunosuppressive CKs, neurotrophic and angiogenic factors along with ECM remodeling enzymes, making the environment supportive of the GB development[361]. Even though it is highly challenging, reprogramming of pro-tumor microglia towards an aggressive pro-inflammatory phenotype represent a promising therapeutic avenue.

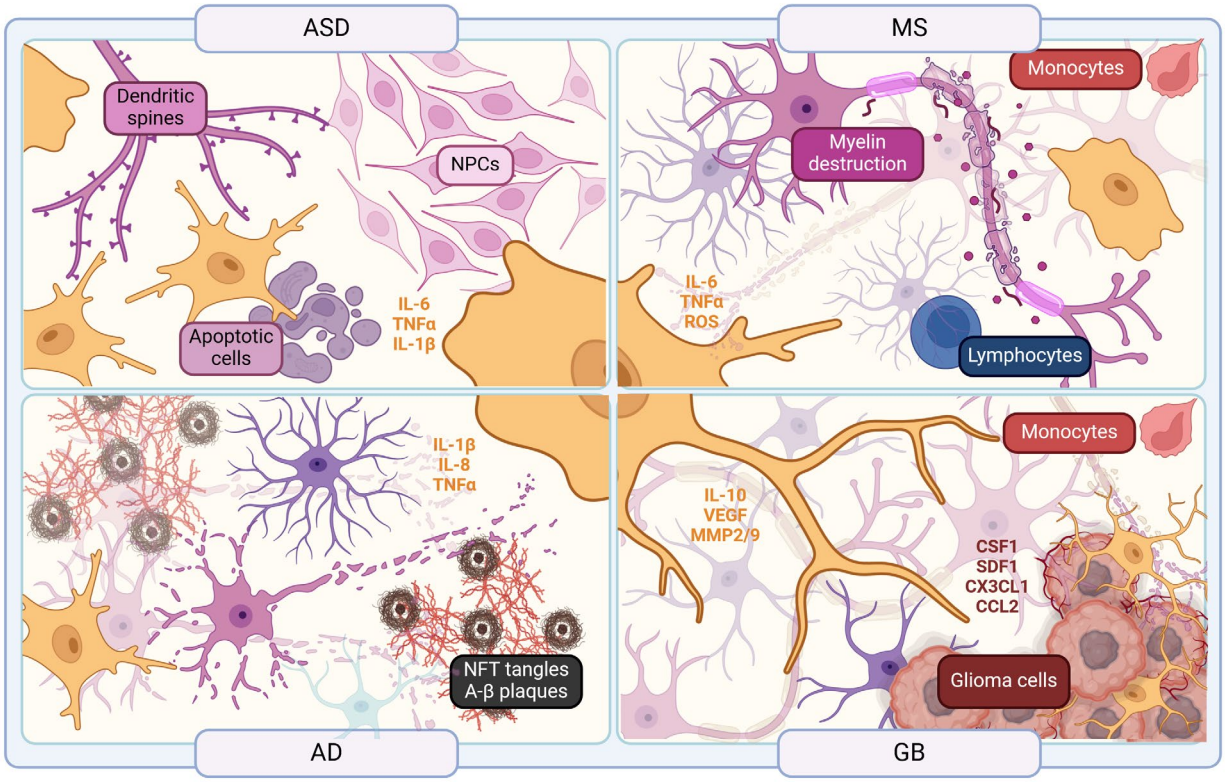

Figure 18. Microglial contribution to neurological disorders:

Microglial cells are known to be implicated in all neurological diseases, including ASD (top left), MS (top right), AD (bottom left) and GB (bottom right). Only few examples of the microglial contribution to the evolution of the already advanced pathology are presented, focusing on the secretion of CKs and the

phagocytosis. Indeed, in ASD, a defect in phagocytosis of NPCs, apoptotic cells and dendritic spines has been observed, together with an increased secretion of pro-inflammatory IL-6, TNFα and IL-1β. In MS, microglia are known to increase the secretion of IL-6, TNFα and ROS contributing to the burst of pro-inflammation that, together with peripheral immune cells, lead to the destruction and increased phagocytosis of myelin. In GB, cancer cells secretion of CCL2 leads to the recruitment of blood-derived monocytes contributing to the pool of GAMs. In addition, GB cells, by producing CSF1, SDF-1 and CX3CL1 lead to the reprogrammation of microglia and GAMs towards a supporting tumor phenotype characterized by the production of ECM remodelling MMP2 and MMP9, pro-angiogenic VEGF and the anti-apoptotic IL-10, together with a decrease of phagocytosis of the GB cells. Finally, in AD, heavy and progressive accumulation of misfolded Aβ and Tau proteins leads to the chronic activation of microglia towards a pro-inflammatory phenotype characterized by the secretion of IL-1β, IL-8 and TNFα and an exhaustion of microglial phagocytosis becoming less efficient and leading to neurotoxic injuries and initiating vicious circles of neuro-inflammation.

Created with Biorender from[362,363,364,365]. SDF1 : Stromal derived factor 1.

As seen, by adapting to the pathological microenvironement, microglia participate in the emergence or worsening of the disease evolution, its outstanding plasticity highlighted by distinctive functional identities becoming detrimental. Understanding the origin of microglial reactivity could pave the way to therapeutic avenues targeting nearly all neurological diseases.

Decades of research on the underlying mechanisms responsible for the transciptional changes of microglia induced by the environment, already highlighted by the numerous TFs implicated in each function of microglia, logically led to an epigenetic origin of microglial plasticity.

7. Epigenetics of microglial identity

Epigenetics, term coined by Conrad Waddington in 1942, is the study of the modifications of gene expression without changes in the DNA sequence and encompasses three major mechanisms : DNA modifications, histones modifications and non coding RNAs[366].

Even though the field of epigenetics of microglia is still new and majority of mechanisms still have to be discovered, the basic core establishment of microglial identity and its evolution in a stimulus dependent manner are started to be elucidated, while the mechanism of microglial immune memory only starts to emerge. This knowledge has mainly been observed through the lens of histone modifications and non coding RNAs, while the DNA methylation implication in microglial identity stays

to this date, very obscure. The non coding RNAs will only be mentioned in Figure 19 and not be discussed further.

7.1. Transcriptional regulatory elements and chromatin accessibility

As seen all along the introduction, microglia can exhibit distinctive transcriptomics profiles characterized by the expression of genes sets, specifically triggered in response to the environment. Those changes in gene expression are regulated by TFs binding to specific transcriptional regulatory elements and recruitment of the transcription machinery to the chromatin, to lead to mRNA synthesis. Amongst those regulatory elements can be found promoters, mostly proximal to the Transcripion Start Site (TSS) and promoting the assembly of the RNA Polymerase II (RNA Pol II) transcription complex. On the other hand, enhancers, regulatory elements more distal to the TSS, are able to play different roles from RNA pol II recruitement and proximal pausing or transcription elongation[367].

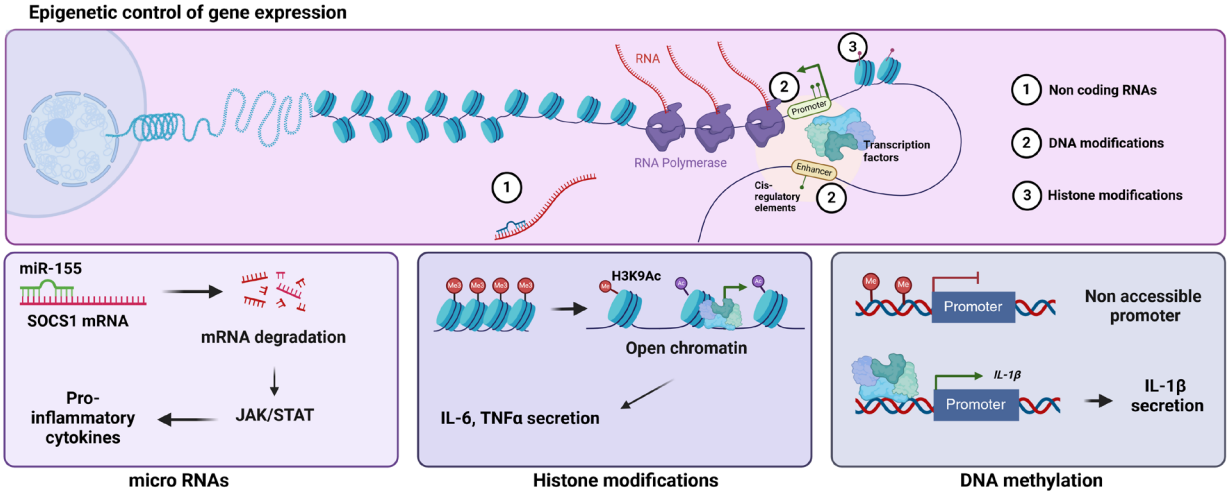

Figure 19. Major epigenetic mechanisms implicated in gene expression modulation:

The major epigenetic mechanisms in gene expression regulation are miR, histone modifications and DNA methylation. miR are small non coding RNAs with a sequence capable of hybridizing to their target mRNA leading to translational suppression. Histone modifications are chemical modifications present on the tails of histone molecules affecting their affinity with the DNA and thus, changing the chromatin accessibility. 5mC DNA methylation are chemical modifications of the cytosine base of the DNA leading to changes in affinity between DNA sequences and TFs. In microglia, miR-155 is known to target the SOCS1 mRNA leading to the expression of pro-inflammatory CKs through the modulation of the JAK/STAT pathway, while the acetylation of the lysine 9 of the H3 histone (H3K9ac) leads to the active

transcription of pro-inflammatory CKs. Finally, the decrease in DNA methylation of the IL-1β promoter leads to its increased transcription. Created with Biorender from[368,369,370].

Promoters are mandatory elements for the initiation of the transcription and are mostly sites for Signal-Dependent TFs (SDTFs) and broadly expressed TFs binding, making them inadequate for the establishment of cell identity related gene expression programs. Enhancers, on the other hand, constitute most of the binding sites for Lineage-Determining TFs (LDTFs) but also SDTFs thus representing ideal sites for internal signals integration[371].

Modulation of the gene expression is a result of the chromatin accessibility of those transcriptional regulatory elements by the transcription machinery and associated specific TFs, and is realized by epigenetic modifications, especially histone modifications that can be used to define the state of the chromatin composing the regulatory element and predict its effect on downstream gene expression. The histone code is yet not fully elucidated but the major marks and their effects has been classified as leading to active, primed, latent, poised or repressed for enhancer while promoters are mainly characterized as active, repressed or poised[372].

7.2. Establishment of microglial core transcription program

As mentioned above, the transcriptional programs responsible for cell identity are established by the acquisition of an enhancer landscape formatting the set of genes accessible for expression. Because of their EMP origin, microglia share the core enhancer landscape of macrophages and characterized by the activity of the pioneer LDTF PU.1. PU.1, coded by the *Spi1* gene in mouse, is a master regulatory TF of the hematopeitic compartement belonging to the Erythroblast Transcription Specific (ETS) family, controlling the expression of hundred of genes implicated in cell growth, adhesion, TFs and signaling mediators. PU.1 is considered a pioneer TF from its ability to generate nucleosome-free chromatin regions by interacting with nucleosomes and recruiting the SWItch/Sucrose Non-Fermentable (SWI/SNF) family of chromatin remodeling complexes leading to a redistribution of the partners TFs and their stable binding to regulatory elements[373]. The collaborators of PU.1 responsible for the establishment of macrophage core identity are CCAAT/enhancer binding protein delta (C/EBPΔ) and Activator protein 1 (AP-1) LDTFs, all interacting with the SWI/SNF complex, recruiting dozen of other TFs and leading to histone modifications of enhancer constituting chromatin at tens of thousands of

locations through the genome. Those modifications of enhancer accessibility from LDTFs create a macrophage core repertoire of primed enhancers, enriched with the H3K4me1, H3K4me2 or H3K4me3 histone modifications and allowing the further binding of others TFs for the obtention of active enhancers in response to environmental adaptation materialized as internal active signaling pathways[371]. This primary epigenetic landscape defines the basic macrophage functions such as CSF1R dependent differentiation and survival, efficient phagocytosis and the ability to rapidely respond to inflammatory triggers[374].

In order to achieve the microglial specific enhancer repertoire, others LDTFs are required on top of the core macrophage signature and induced by the CNS environement during development. Indeed, the LDTFs IRF8, heterodimeric partner of PU.1; SALL1 and RUNX1, induced by the brain produced TGF-β, are required to interact in the early stages on microglial development on the previously established enhancer landscape to define the precise microglial identity.

The lack of those collaborative LDTFs results in an improprer colonization of the brain parenchyma, an inadequate amount of microglia, a default in morphology, a lack of maturity and/or absence of physiological properties of microglia[186]. Later in development, the secretion of GM-CSF, in addition to TGF-β, leads to the binding of the MafB TF, followed in adulthood by MEF2a and MEF2c, known to decrease during ageing. Deficit in those last LDTFs in later stage of microglial maturation leads to defective microglial self-renewal, reduced expression of homeostatic markers and increased pro-inflammatory sensitivity.

During the development, the dynamics of LDTFs binding and chromatin remodeling complexes recruitment will modulate the chromatin state of the enhancer landscape, leading to differential levels of active transcription histone marks (H3K27ac and H3K9ac), primed (H3K4me1) and poised (H3K27me3, H3K4me1)[375]. Lots of mechanistic data are lacking but what is known is that the dynamics of histones modifications in microglia are modulated by the SWI/SNF complex, the polycomb group, recruitment of HDACs and finally in more depth, that the binding of SALL1 leads to the recruitment of histone deacetylase complex[376,377].

This combination is completed by all the repressed enhancers (H3K9me) by lack of corresponding TFs to constitute the core microglial physiological identity. However, as it has been shown, microglia constitute a very heterogenous population with a various range of transcriptomic signatures in function of the environment that can be explained by the modulation of this microglial core by the binding of the multitude of SDTFs, as the ones evoked in the microglial function part of this introduction.

7.3. Stimulation dependent microglial modulation

Under changes in the microenvironement sensed by the microglial sensome and translated into activation/inhibition of different signaling pathways, SDTFs will be able to reach their binding sites if their chromatin state, defined by the LDTFs, allows it to modulate the expression of specific transcriptomic programs amongst the microglial core identity.

A myriad of such SDTFs is known in microglia, a glimpse of them already presented in the functions part of this introduction. The more famous being the NFκB family of TFs, responsible for apoptosis and inflammatory regulation, and known to be induced in response to CKs, stress or TLRs activation, and targeting genes such as *Tnf*, *c-fos*, *Il-1β*, *Il-6* or *Mmp* [378,371]. The exact mechanisms of gene expression by NFκB in microglia are not known but could, as seen in macrophages, be related to the recruitment the H3K9m2 demethylase Aof1[379]. Even though the SDTF induced chromatin accessibility in microglia remains unclear, it is known to be linked to the recruitment of histone modifications enzymes such as histone acetyl transferases (p300) and deacetylase (HDAC1/2), and histone methyltransferase (EZH2, Polycomb repressive complex 2) and demethylases (JMJD3)[380].

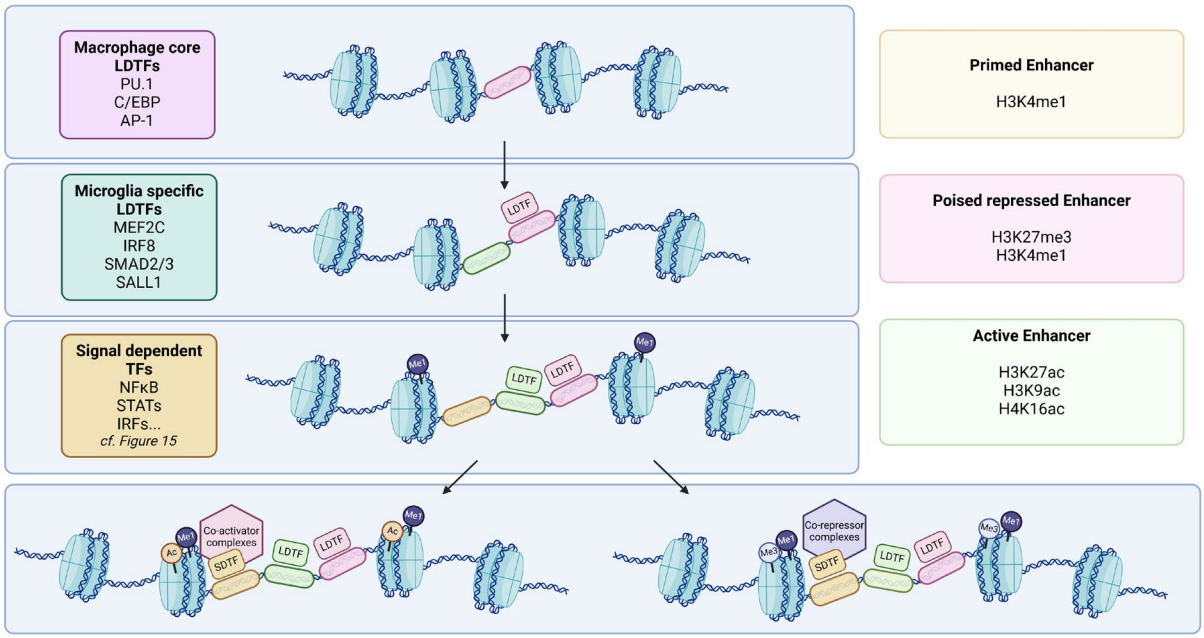

Figure 20. Establishment and modulation of microglial transcriptional programs:

The establishment of microglia identity, defined by the expression of gene sets, is determined by the landscape of chromatin accessibility, especially at enhancer regulatory elements. Microglial core program comes from macrophage lineage and characterized by the nucleosome displacement generated by pioneer TFs such as PU.1 and allowing the binding of others LDTFs, like C/EBP or AP-1.

Because of the specific environment that the brain represents, microglial cells will develop specialized enhancer repertoire by the binding of others LDTFs such as MEF2C or SALL1. Finally, under the changes in microenvironmental cues, separate SDTFs will lead to the expression of gene sets to allow the best adaptation of microglia to the dynamic environment.

The enhancers can be primed by methylation of the lysine 4 of the histone protein 3 (H3K4me1) leading to a facilitated accessibility to the chromatin for TFs. They can also be poised/repressed by the combination of H3K4me1 and H3K4me3, leading to an open chromatin but difficult to access for TFs. Finally, enhancers can be active with acetylation of the lysines 9 or 27 of the histone 3 (H3K9ac, H3K27ac) or the acetylation of the lysine 16 of the histone 4 (H4K16ac) and leading to accessible chromatin and an active transcription of the downstream genes. Created with Biorender from[371,377].

The vast amount of different environment induced TFs and the huge combinaison of post-transcriptional modifications of histone tails support the notion that the phenotypical heterogeneity observed amongst the microglial community arise from adaptation of the chromatin to the never-ending changing microenvironment.

7.4. Microglial immune memory

Observation that microglia specific responses were established by an epigenetically controlled enhancer repertoire and that the latter was plastic in reaction to the signals arising from the environment to primed responses in order to be rapidely adapted, led to the concept of immune memory of the long-lived microglial cells. Indeed, it has been shown that the response of microglial cells could be different when the inducing stimulation had already been encountered in the past, one or more times. Those phenomenom, called microglial training and tolerance have been characterized by an enhanced and a diminished response to the same stimulation, respectively. For instance, mice injected peripherally with LPS twice will exhibit an increased secretion of IL-1β, TNF, IL-6 and IFN-ɣ by microglial cells, while the same treatment but four times will lead to decreased secretion of those CKs by microglial cells[381].

Those phenomenom have not been explained yet but are known to be orchestrated by epigenetic mechanisms. Another study on LPS primed microglia showed a reduction of H3K4me3 marks *on Il-1ß* and *Tnf* promoters after an LPS conditioning, to prevent from an excessive inflammatory reaction[382]. Recently, it was shown that LPS-primed microglia were exhibiting higher level of H3K27ac and

H3K4me1 and 3 after stimulation with manganese, highlighting the possible interaction between the stimulus leading to a particular identity of microglial cells in a given context[383].

Interestingly, microglial memory has been linked to DNA methylation *in vivo*, where handling of neonatal rats programs the differential expression of the IL-10 CK in microglial cells and by modulating the DNA methylation statuts of the *Il-10* gene, leads to a better response to drug addiction in adulthood[384].

Given the long-lasting life of microglial cells and the amount of TFs implicated in its identity, understanding the mechanisms behind the conditioning of its response by exploring DNA methylation seems necessary.

7.5. DNA methylation associated with microglial reactivity

DNA methylation (5mC) is the most studied DNA modification and correspond to the transfer of a methyl group from the S-adenosyl-L-methionine (SAM) to the 5-carbon position of a cytosine base of the DNA, catalyzed by DNA methyltransferases (DNMTs) enzymes[385]. Three catalytically active DNMTs are known, DNMT1, referred as the maintenance DNMT because of its high affinity for hemimethylated double-stranded DNA and the so-called *de novo* DNMT3A and DNMT3B. In addition, DNMT3-like protein (DNMT3L) belongs to the family of DNMT but is devoid of methyltransferase activity with low affinity for DNA, instead, DNMT3L increases the affinity of DNMT3A and DNMT3B for methyl donor SAM[386].

The demethylation of the cytosine base can be done passively, by the absence of DNMT1 enzyme and thus, the loss of the methylation group; or actively, by the action of the Ten-eleven translocase (TETs) family enzymes, catalizing the metabolization of the 5mC into 5-hydroxymethylcytosine, 5-formylcytosine and 5-carbocytosine prior to its catalization into cytosine by the Thymine DNA glycosylase (TDG)[387].

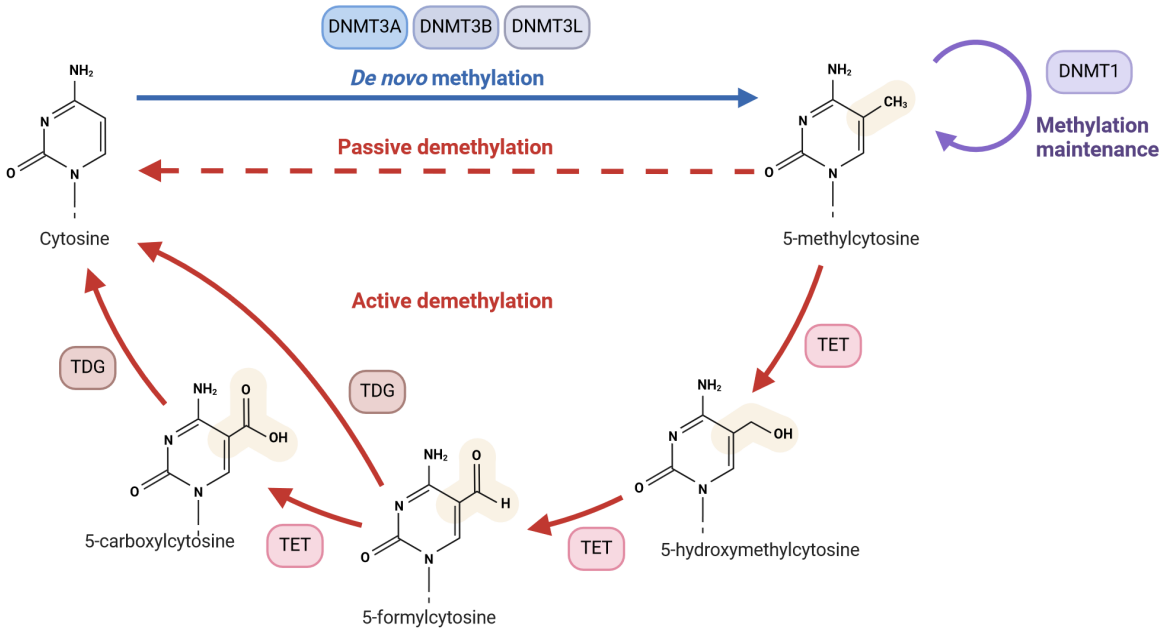

Figure 21. DNA methylation and demethylation mechanisms:

DNA methylation, 5mC, corresponds to the chemical addition of a methyl group on the cytosine base of an unmethylated strand of DNA *via* the action of the DNMT3A/B and the co-activity of DNMT3L. The established 5mC pattern on the DNA strand is maintained through cellular generation *via* the action of DNMT1. In absence of DNMT1, the DNA strand will be copied without any writing of 5mC pattern and be lost from one generation to the next. This phenomenom is called passive demethylation. Demethylation can also be achieved actively through the action of the TETs methylcytosine dioxygenases, leading to succession of chemical modifications of the cytosine base to be suppressed by the TDG and base excision repair system. The 5mC intermediates are thought to be related to gene expression modulation but are lesser explored than 5mC.

Created with Biorender from[388]. DNMT: DNA methyltransferase, TDG: Thymine-DNA glycosylase, TET: Ten-eleven translocation.

The 5mC modification can happen at any C-G dinucleotide along the genome but has mostly been explored in the context of the promoter and been linked to the transcription inhibition, by directly hampering the binding of TFs or indirectly by affecting the chromatin remodeling machinery[389]. Only a very recent study has explored the role of DNA methylation in enhancers and has shown that only 3% were sensitive to DNA methylation by controlling the binding intensity of TFs[390].

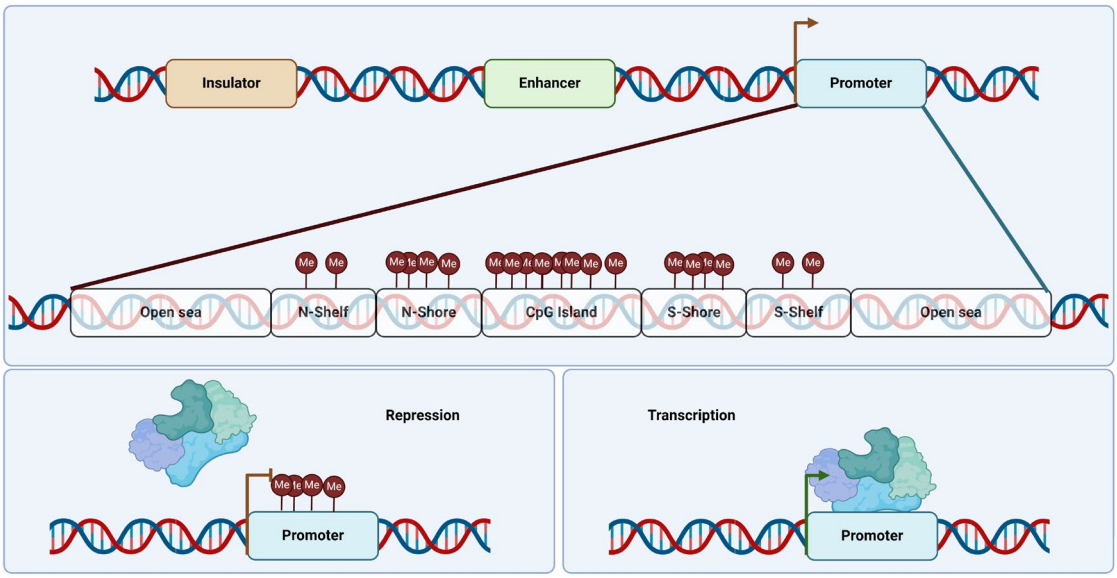

Figure 22. CpG organization and gene expression:

DNA methylation modifications are mostly studied in the context of CpG islands, highlighting an organization of the ratio of C-G dinucleotides in different parts of the genome. A CpG island represents a region greater than 500 base pairs with a G-C content superior to 55%. Shores are regions located at 0 to 2 kb away from the CpG island and shelves at 2 to 4 kb, the ratio of C-G dinucleotides decreasing with the distance from the CpG island. CpG islands are mostly explored in promoters, since 60% of all CpG islands are located in promoters. A gene promoter highly methylated has been linked to a transcriptional repression due to the binding incapacity of TFs and transcription machinery or to the recruitment of chromatin compaction systems. Created with Biorender from[391,392].

In the context of the brain, the global DNA methylation level is known to be decreasing with age and associated with NDs, but the precise cell populations and genes affected are not known[393]. Globally, it was also shown aberrant DNA methylation patterns in PD and ALS patients, even though no further exploration has been made[394,395]. Finally, it was also shown that a global hypomethylation was found in glia and neurons of AD patient hippocampus, while a global hypermethylation was noted in cognition-associated brain areas[396].

Concerning microglia, the very few studies made on the subject tend to align with the global hypomethylation in ageing hypothesis. Indeed, two independent studies have shown that the microglial expression of IL-1β, characteristically increased in ageing, was striclky dependent on the methylation status of the Il-1β promoter[368,397].

7.6. DNA methylation based microglial reprogramming

As it was shown, microglia uncontrolled reactivity has been linked to brain pathologies, and this reactivity is now known to be under the control of epigenetic mechanisms. Consequently, one of the major therapeutic avenues for a broad range of neurological disorders is to reprogram microglial cells towards a beneficial phenotype.

Little is known about DNA methylation implicated in microglial cell reactivity, but one of the most important recent therapeutic approach for AD is the inhibition of Beta-site APP cleaving enzyme 1 (BACE1) in microglia to hamper its neuro-inflammatory phenotype and impair the generation of neurotoxic Aβ. This could be realized by DNA methylation modulation since the expression of *Bace1* gene is regulated by the DNA methylation statuts of two sites located in its 5'UTR regions in microglia[398].

Exploring genome wide DNA methylation profiles of reactive microglial cells could unravel the intimate establishment of microglial identity in face of environmental challenges and pave the way for novel therapeutic approaches targeting the reprogramming of microglia towards a more anti-tumoral phenotype in brain tumors or more supporting phenotype in NDs.

Part II. Aims of the thesis

Microglial cells, the resident immune cells of the brain parenchyma and specialist of the CNS environment, exert important roles for the proper establishment and maintenance of the brain functioning. Microglia are able to perform those roles through adaptability of their core functions *via* constant communication with all cellular actors of the environment and leading to a phenomenal behavioral plasticity. As such, functional microglial dysregulation has been linked to nearly all neurological disorders, rendering them an interesting therapeutic target under the condition of understanding the core mechanisms behind such functional plasticity and, therefore, be able to manipulate it.

Microglial behavior is under the control of complex and tangled molecular mechanisms constantly evolving alongside the heterogenous CNS microenvironment and this intimate communication between the extracellular compartment and the genome is linked to epigenetic mechanisms. Whereas histone modifications and non-coding RNAs are under extensive exploration, DNA modifications, such as DNA methylation, are not. As those modifications impact gene expression in a dynamic but stable manner, they could represent a fast and efficient way for the cell to adapt part of his genome to a specific situation without totally affecting the cell core identity.

We thus hypothesized that microglial adaptation or reactivity to environmental changes could be in part, held by DNA methylation patterns reorganization. As no big dataset of microglial methylation patterns has been generated yet, we decided to take advantage of the newly release Mouse Methylation Arrays from Illumina, allowing the interrogation of 285 000 different CpGs along the mouse genome.

The first aim of the thesis was to induce microglial reprogramming through stimulation with well-known compounds leading to activation of membrane receptors, signaling pathways and TFS, potentially inducing chromatin remodeling. Measures of distinct features were made to insure the accomplishment of differential identities in microglial cells and to characterize as much as possible each one of them.

Following the induction of microglial plasticity mechanisms, the second aim was to explore DNA methylation patterns associated with each microglial identity and try to unravel the potential causality between the genome methylation and gene expression in differential microglial identity.

Part III. Materials and methods

1. Ethical statement

The animal experiments carried out in this study have been approved by the Animal Experimentation Ethics Committee (AEEC) of the University of Luxembourg and the relevant government agencies. In addition, all procedures necessary have been performed regarding the 2010/63/EU European Union Directive.

The CD-1 mice pups used in the study were provided by the Animal Facility of the University of Luxembourg in Esch-sur-Alzette (27 Rue Henri Koch, 4354 Esch-sur-Alzette, Luxembourg). A total of 266 CD-1 pups ranging from one to three days old was used in the present study.

2. Primary microglial culture

Mixed glial cell cultures were obtained from the dissection of newborns CD-1 mice brains. The meninges were removed and the brains were mechanically dissociated in cold Phoshate Buffered Saline (PBS) solution. For the second part of the study, the dissociated brains were pooled together, whereas for the third part requiring a genotyping of the mice, each brain was resuspended individually.

The cells were resuspended in a media composed of Dulbecco's Modified Eagle Medium (DMEM) supplemented with 10% Fetal Bovine Serum (FBS) and 1% Penicilin-Streptomycin (P/S); hereafter named DMEM Full; and let to grow for two weeks at 37°C in a 5% CO_2 humidified incubator. Microglial cells were isolated from the glial culture by using a Magnetic Activated Cell Separation (MACS) system with CD11b antibodies, according to manufacturer's instructions (Miltenyi Biotec). Microglial cells where then resuspend in a culture medium composed of DMEM full and mixed glial cell culture conditioned media (50/50; v/v) prior to treatment.

3. Genotyping for sex of primary culture

Tail fragment (0.5 cm) of each newborn included in the last part of the study was suspended in 200 µL of Direct PCR Tail lysis buffer (Viagen) and 4 µL of proteinase K was added (Invitrogen). The suspension

was incubated at 55°C for at least 5 hours. After addition of 350 µL of isopropanol, the solution was vortexed and centrifuged at 13000 rpm for 10 minutes at 4°C. The pellet was then washed in 350 µL of 70% Ethanol (EtOH), centrifuged at 13000 rpm for 10 minutes at 4°C and resuspended in 350 µL of RNAse free water (H_2O). Polymerase Chain Reaction (PCR) assay was performed using the gDNA extracted from the tail and primers targeting *Uba1* and *Ube1y1* genes localized on the X and Y chromosomes, respectively. The PCR reaction containing 12.5 µL of KAPA2G Fast HotStart DNA Polymerase (5U/ µL; Sigma-Aldrich), 1 µL of forward and revserse *Ube* primer, 9.5 µL of H_2O and 1 µL of gDNA was submitted to a denaturation step at 94°C for 2 minutes, 35 cycles with 94°C for 30 seconds, 57°C for 30 seconds and 72°C for 30 seconds, followed by an elongation step at 72°C for 5 minutes. PCR products were analyzed using a agarose electrophoresis on a 2% agarose gel containing SYBR Safe (Invitrogen) and analyzed under Ultra Violet (UV) illumination.

Table 1. Primer sequence for genotyping PCR.

Target gene	Primer forward sequence	Primer reverse sequence
Ube	TGG-TCT-GGA-CCC-AAA-CGC-TGT-CCA-CA	GGC-AGC-AGC-CAT-CAC-ATA-ATC-CAG-ATG

4. Cell lines culture

Murine microglial cell BV2 was kindly donated by Dr. Tony Heurtaux (University of Luxembourg), and murine glioma cell line GL-261 was purchased from DSMZ (Cat. ACC 802).

Both cell lines were maintained in DMEM containing Ultraglutamine (Lonza) and Sodium Pyruvate (Gibco), supplemented with 10% FBS (Gibco) and 1% P/S (Lonza). Cells were kept at 37°C in a humidified atmosphere of 5% CO_2.

For generation of GBM-Conditioned medium (CM-GL261), 1 x 10^6 GL-261 cells were seeded in a total volume of 8 mL culture medium in a T75 flask for 48 hours. The GBM-CM was then collected and filtered with a sterile 0,45 µm filter prior to microglia treatment.

Microglial cells were treated 24 hours after seeding. For GBM-CM treatment, the total volume of medium was replaced with fresh harvested GBM-CM. The following compounds: LPS (Sigma, Cat. L2143), IFNɣ (Gibco, Cat. PMC4033) or IL-4 (Gibco, Cat. PMC0046) were diluted at 100 ng/mL in 1X PBS,

added to the culture medium at a final concentration of 10 ng/mL and cells were incubated for 1, 6, 12, 24 or 48 hours at 37°C in a humidified atmosphere of 5% CO_2

5. Proliferation assay

Microglial cells were seeded at 1 x 10^4 cells per well in 96-well cell culture plates (Cat. 650101, Greiner) in 200 µL of DMEM Full and were allowed to attach for 24 hours before treatment with LPS, IFNɣ, IL-4 and CM-GL261 as described above. Plates were inserted into the IncuCyte® S3 live-cell analysis system (Sartorius) for real-time imaging of four Regions of Interest (ROI) per well under 10X magnification. Phase contrast images were taken every 2 hours for a total of 96 hours. Image data were analyzed using the IncuCyte® software version 2020B and proliferation was plotted as change in the percentage confluency of surface area. All experiment were realized three time independently and containing technical triplicates. Raw pictures were exported from the ClarioStar system and processed with FIJI image software. Processed confluency data were exported from the Incucyte software. Both set of data were normalized to untreated microglia's results, followed by statistical analysis using GraphPad Prism software (9.0.0 (121)). Data are represented as mean +/- standard error of the mean, containing at least three biological replicates per condition. Significant differences in confluency between untreated and treated microglia were determined using a Paired t test, and reported as adjusted P-values with * $p < 0.05$, ** $p < 0.001$, *** $p < 0.0001$.

6. Viability assay

Cell viability after treatment was assessed at 1, 6, 12, 24 or 48 hours using the CellTiter Glo® 2.0 assay (Promega, Cat. G9242) according to manufacturer's instructions. In brief, 1 x 10^4 microglial cells were plated in each well of a white opaque 96 wells plate (Thermo Scientific, Cat. 165306) in 100 µL of media prior to appropriate treatment. Then, 100 µL of CellTiterGlo 2.0 reagent were added in each well and cells were incubated for 10 minutes at room temperature. The read-out was done using a Clariostar microplate reader (BMG Labtech). Luminescence raw data were exported from the MARS software (BMG Labtech), corrected for media induced background luminescence and normalized to untreated microglia's results, followed by statistical analysis using GraphPad Prism software (9.0.0 (121)). Data are represented as mean +/- standard error of the mean, containing at least three biological replicates per condition.

Significant differences in viability between untreated and treated microglia were determined using Row stat then two tailed Paired t test, and reported as adjusted P-values with * $p < 0.05$, ** $p < 0.001$, *** $p < 0.0001$.

7. Phagocytosis assay

Phagocytosis was assessed by using pH sensitive fluorescent latex beads and a ClarioStar plate reader. In brief, 1 x 10^4 microglial cells were plated in each well of a transparent 96 wells plate (Cat. 650101, Greiner) in 100 µL of FluoroBrite DMEM supplemented with 10 % of FBS 24 hours prior to appropriate treatment. After treatment, the pHrodo Red E.Coli Bioparticles (Invitrogen, Cat. P35361) were diluted in PBS at a concentration of 1 mg/mL and 10 µL were dispensed in each well; a negative control containing microglial cells without beads was include in the plate. The plate was inserted into the ClarioStar plate reader and the fluorescence 560/585 nm was read every 30 minutes for 8 hours.
Fluorescence raw data were exported from the MARS software (BMG Labtech), corrected for media induced background fluorescence and normalized to untreated microglia's results, followed by statistical analysis using GraphPad Prism software (9.0.0 (121)). Data are represented as mean +/- standard error of the mean, containing three biological replicates per condition realized in technical triplicates. Significant differences in percentage of phagocytosis between treatments of microglia were determined using a two ways ANOVA, with correction for multiple comparisons (Tukey) and reported as adjusted P-values with * $p < 0.05$, ** $p < 0.001$, *** $p < 0.0001$.

8. Immunofluorescent staining and imaging

Microglial cells were plated at the density of 5 x 10^4 in each well of a 24 well plate (Greiner) on Poly-L-lysine (Sigma) coated glass coverslips (VWR, Cat. 6310713). After appropriate treatment, cells were fixed for 10 minutes with a 4% Paraformaldehyde (PFA) solution, permeabilized for 10 minutes (0,4% Triton X-100, 0,1% Bovine Serum Albumin (BSA) in 1X PBS), blocked for 45 minutes with a 3% BSA solution in 1X PBS and incubated overnight at 4°C with primary antibodies targeting Iba1 and F4/80 (see Table 2 for details). Followed by two hours incubation with secondary antibodies solution (3% BSA in 1X PBS) Coverslips were retrieved from each well and mounted on SuperFrost® glass slide (VWR) with Fluoromount-G DAPI (DAPI: 4',6-diamidino-2-phenylindole ; Invitrogen Cat. 00495952).

Coverslides were imaged by using a Zeiss LSM 780 confocal microscope with a 20X air and 40X oil objectives, and pictures were taken and scaled using with Zen Blue software (Zeiss).

Table 2. Antibodies used for IF staining.

Antibody	Host	Supplier	Dilution
Anti-mouse iba1	Rabbit	BioCare Medical	1/500
Anti-mouse F4/80	Rat	BioRad	1/500
Alexa Fluor 647-Anti-Rabbit	Donkey	Jackson ImmunoResearch	1/500
Alexa Fluor 488-Anti-Rat	Goat	Jackson ImmunoResearch	1/500

9. Cytokine arrays

Supernatants from 1 x 10^6 plated glioma or microglial cells were harvested following treatments and submitted to Abcam Cytokine Arrays for secretome analysis (Abcam; Cat. ab193659). The list of all targets is present in Annexe 1. Arrays were blocked for 30 minutes prior to an overnight incubation at 4°C with 2 mL of supernatant, followed by an overnight incubation with biotin-conjugated anti-CK antibodies, and a 2 hours incubation with HRP-conjugated Streptavidin prior to chemiluminescence detection using Image Quant LAS4000 (GE Healthcare). Images were imported into FIJI ImageJ software to measure signal intensity of each CK spot. Background intensity was substracked from each raw data, all arrays were normalized and intensity of the media itself was substracked. Processed data were further analyzed with GraphPad Prism software (9.0.0 (121)) and are represented as mean +/- standard error of the mean, containing at least two biological replicates per condition (in technical duplicates). Significant differences in expression levels between times of exposure to treatments were determined using two-way ANOVA with correction for multiple comparisons (Tukey) and reported as adjusted P-values with * $p < 0.05$, ** $p < 0.001$, *** $p < 0.0001$.

10. RNA isolation, Reverse-transcription and qPCR

Pellets were constituted from microglial cells plated at a density of 1 x 10^6 in a T25 flask for the BV2 study and between 5 x 10^4 and 1 x 10^5 in 6-well plates for primary microglial cells, from which total RNA was extracted using Qiagen Rneasy Mini Kit (Qiagen, reference 74104). The RNA was reverse transcribed using the iScript cDNA Synthesis Kit (Bio-Rad, reference 1708891) according to

manufacturer's instructions; a total amount of 1 µg of RNA for BV2 cells, 500 ng of RNA for primary bulk microglial cells and 200 ng of RNA for male and female microglial cells were used. qPCR was carried out using Fast SYBR Green Master Mix (Thermo Fisher Scientific, reference 4385612), primer mix (5 µM final), RNAse free water and the Quant Studio-5 (Thermo Fisher Scientific) with an annealing temperature of 60°C.

Raw Ct-values were extracted from the Quant Studio Design & Analysis software (v 1.5.1; Thermo Fisher Scientific) and used to calculate the relative gene expression by using the ΔΔCt method, normalized to the house-keeping gene *Rpl27*.

Data were further analyzed with GraphPad Prism software (9.0.0 (121)) and are represented as mean +/- standard error of the mean, containing at least three biological replicates per condition (in technical triplicates).

Significant differences in expression levels between times of exposure to treatments were determined using one-way ANOVA with correction for multiple comparisons (Tukey) and reported as adjusted P-values with * $p < 0.05$, ** $p < 0.001$, *** $p < 0.0001$.

All primers were designed using PerlPrimer software and purchased from Eurogentec, sequences details can be found in Table 3.

Table 3. Sequences of primers for RTqPCR.

Target gene	Primer forward sequence	Primer reverse sequence
Tnf	CCT-ATG-TCT-CAG-CCT-CTT-CTC	CAT-TTG-GGA-ACT-TCT-CAT-CCC-T
IL-1ß	GTT-CTT-TGA-AGT-TGA-CGG-ACC-C	CCT-GTC-TTC-CTG-GGA-AAC-AAC
Cxcl10	CTC-TCG-CAA-GGA-CGG-TC	TGC-GAG-CCT-ATC-CTG-CCC
Ccl9	TTT-CAC-ATG-GGC-TTT-CAA-GAC-TC	TCT-TGC-TGA-TAA-AGA-TGA-TGC-CC
Hexb	GTA-CAA-GAA-CCA-GTA-GCC-GT	CAT-TGA-TGG-TGA-AAG-TCC-CGA
Arg1	AGA-CAG-CAG-AGG-AGG-TGA-AGA-G	CGA-AGC-AAG-CCA-AGG-TTA-AAG-C
Ym1	CCG-TCA-GAT-ATT-CAT-TCA-GTC-AG	TTA-CGC-ATT-TCC-TTC-ACC-AG
Fizz1	ATG-AAG-ACT-ACA-ACT-TGT-TCC-C	AGG-GAT-AGT-TAG-CTG-GAT-TGG
Cx3cr1	GCC-GGA-AGC-CCA-AGA-GCA-T	CAC-AAA-GAG-CAG-GTC-GCT-CAA
Rpl27	CGG-AAG-TGT-CCT-TCT-TTC-CT	CCA-TCA-TCA-ATG-TTC-TTC-ACG-A

11. DNA isolation

Genomic DNA from cells pellets was extracted using the DNeasy Blood & Tissue Kit (Qiagen). DNA was eluted in 100 µl of Nuclease-free water and concentrations were measured using the Qubit 4.0

fluorometer (Thermo Fisher Scientific) together with the Qubit dsDNA BR Assay kit (Thermo Fisher Scientific) following manufacturer's instructions.

12. MethylMouse Methylation arrays

Methylation arrays with Infinium® MethylMouse were processed according to manufacturer's instructions. Briefly, 250 ng of gDNA were bisulfite-converted using the Zymo EZ DNA Methylation kit (Zymo Research, Cat. D5001) followed by a whole genome amplification, DNA fragmentation, hybridization on MethylMouse beadchips, single nucleotide extension and finally staining of the arrays. The arrays were then scanned using Illumina iScan system and quality control of the overall experiment was done using the Genome Studio software with the Methylation module v1.8 (Illumina).

13. DNA Methylation data analysis

Concerning the BV2 model: the raw IDAT files with the annotation sheet were transferred to the LIH Bioinformatics platform (LIH, Luxembourg) and analyzed by Dr. Reka Toth. The Illumina Mouse Methylation array data was processed using RnBeads 2.16.0. Fourty-six probes were removed due to low quality using RnBeads' greedycut algorithm. The methylation levels were normalized using the bmiq algorithm. Probes (n=14277) located on the sex chromosomes were removed. The differential methylation analysis was performed using the limma package based on the M-values. False-discovery rate was used to adjust for multiple testing. The CpG sites were annotated using the ChIPseeker package, using TxDb.Mmusculus.UCSC.mm10.knownGene as reference. Promoter regions were defined as -3kb - +0.5 kb from the transcription start site (TSS). Functional regions were assigned based on ChromHMM tracks from the forebrain of the mouse, age P0. Enrichment of the differentially methylated sites were calculated using a fisher exact test with all sites as a background with functions from the annotatr R package. P values < 0.05 were indicated as significant. Enrichment of the DMLs overlapping with promoters were calculated using the clusterProfiler, msigdbr and ReactomePA packages and visualized with the help of the enrichplot package. The promoter overlap was assessed by using the "mm10_genes_promoters" track from the annotatr package.

Concerning the primary microglial cells model: the raw IDAT files and complementary SDF files were imported into GenomeStudio software and processed with the Methylation Module v1.9.0. The intensity of probes fluorescence was normalized using internal control probes and the backgroung was substracked. The description of the probes array content was done using the Infinium Mouse Methylation Beadchip v1.0 A2 Array manifest file (.bpm). The differential methylation analysis was

performed with IlluminaCustom algorithm and the false discover rate was computed. The probes located on the X and Y chromosomes were removed. The probes were further annotated with the MouseMethylation-12v1-0_A1_annotation_Mus_Musculus (.csv) file.

14. RNA sequencing and analysis

Total RNA extracts from BV2 cell pellets were transferred to the LuxGen sequencing platform (LNS, Luxembourg) and the sequencing was performed using the Illumina technology® (NovaSeq, SP Flow Cell), paired-end 75 bp strand specific aiming at library size of approx. 19 million fragments per samples at the LuxGen platform.

Raw fastq files were quality checked using a combination of fastqc, fastqscreen and RSeQC tools followed by a preliminary analysis composed of read trimming, mapping and counting using Cutadapt, STAR 2.7.9a and the Mouse genome (GRCm39 – Mus_musculus.GRCm39.104.gtf). All of these steps are integrated into a local *snakemake* environment.

Differential Gene Expression analysis was conducted using R statistical software version 4.2.3 and DESeq2 version 1.38.3 using the resulting gene count tables.

Part IV. Results

1. LPS and IFN-ɣ induced BV2 reactivity is associated with significantly differentially methylated sites

In order to investigate whether or not DNA methylation patterns could play a role in the modulation of microglial identity, it was necessary to define different phenotypes that could represent specific identities, possibly acquired by microglial cells amongst their spectrum of activation. To induce such a reprogramming, we choose to treat the BV2 microglial cell line with compounds known and characterized within the macrophage and microglial field of research. First, the LPS and the IFN-ɣ, known to induce a microglial reprogramming related to inflammation, ressembling a bacterial and viral infection, respectively[310]. Second, to tackle the anti-inflammatory related phenotype, we decided to use IL-4, reproducing the tissue repair programming induced after a trauma[399]. Finally, to try to investigate the less known microglial identity in brain tumors, we decided to produce media conditioned by the GL261 mouse glioma cell line (Annexe 8), mimicking the effects of glioma secretions on microglial cells. The concentrations of products and the times of treatment used for the study were defined by a pilot study (Annexes 5, 6 and 7) and were settep-up on 10 ng/mL final concentration and a 48 hours time of media conditioning by GL261 cells. The cells were treated for 6, 12, 24 and 48 hours.

1.1. BV2 viability and proliferation are not impacted by LPS, IFN-ɣ, IL-4 or CM-GL261

To ensure that treatments were not affecting the viability and the proliferation of the BV2 cells, a Cell Titer Glo assay and an Incucyte® monitoring were performed (Figures 23 and 24). On Figure 23, we observed a slight reduction of viability at 24 hours of treatment compared to the control untreated cells, especially for IFN-ɣ (Figure 23B), but the viability never reaches less than 80% of viability. Figure 23C, shows a significant decrease of viability at 24 hours (~6%) for IL-4 treated cells. Otherwise, no significant changes are observed between untreated and treated BV2 for the timepoints between six and 48 hours.

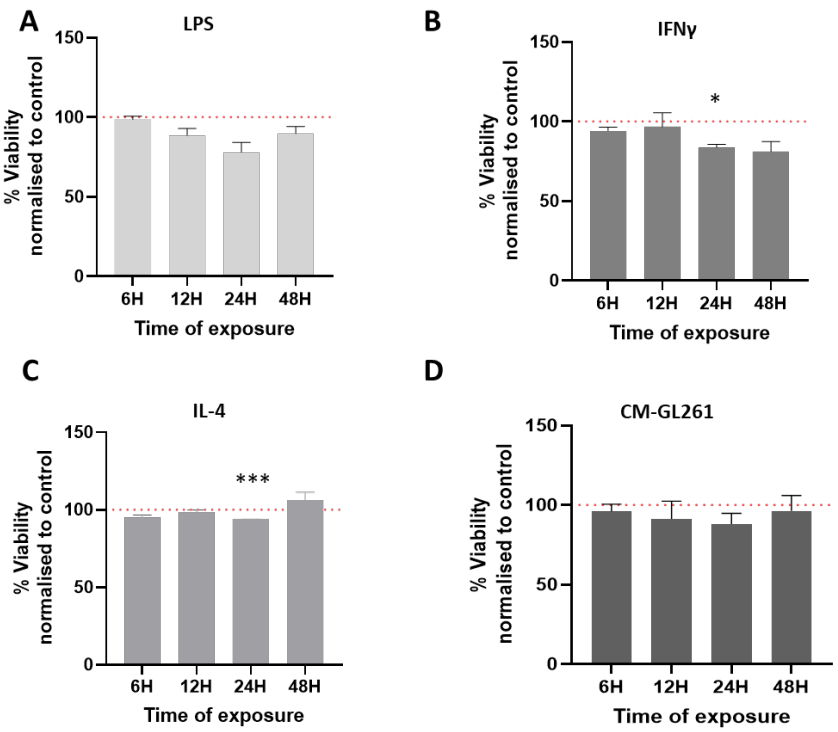

Figure 23. Viability of BV2 is not impacted by treatments with LPS, IFN-ɣ, IL-4 and CM-GL261:

Effect of 10 ng/mL of LPS (A), IFN-ɣ(B), IL-4 (C) or CM-GL261 (D) exposure on the viability of BV2 cells treated for 6, 12, 24 and 48 hours. The cell viability of treated cells was assessed relatively to the control, untreated cells (red line). Statistical analysis constituting of an Ordinary One-Way ANOVA with Multiple comparisons (Tukey's) was performed using GraphPadPrism 9. Asterisks represent significant differences (* $p<0.05$; *** $p<0.001$). Data are representative of three independent experiments, each of which done at least in technical triplicates and are represented as mean ± Standard Error of the Mean (SEM).

Concerning the proliferation, as shown in Figure24 (left panel), the cell confluence measured by the Incucyte® system indicates unsignificant and modest changes between control untreated and treated BV2 cells. We can note a trend in pro-inflammatory treated cells to exhibit an unsignificant increase in proliferation at six hours timepoint for LPS with 11% increase in confluence compared to control (Figure 24A) and from six to 18 hours timepoints for IFN-ɣ with 14% increase (Figure 24C).

As we could observe on the Incucyte® system that BV2 cells were morphologically changing (Annexe 10) during the treatment time, we decided to add a manual counting of cells to ensure that the confluence measurement was not biased by the changes of the BV2 soma size (Figure 24, right panel). To avoid observer bias, the counting was realized by a third party. Even if no significant difference between control and treatment were noted, we could nevertheless observe that the amount of cells

was not always associated with the confluence. As observed in figure 24B, the cell number is higher in LPS condition compared to control at the earliest and latest time points (12% and 8 % higher at 0 and 72 hours, respectively). Similarly to the confluence measurement at 36 hours, the cell number is lower by 11% in the LPS-treated cells compared to the control (Figure 24B). For the IFN-ɣ condition, Figure 24D shows that the number of treated cells are always lower compared to the control and the highest decrease in cells is reached at 36 hours with 24 % lower than the control, that does not match the result observed in the confluence measurement for the same condition (Figure 24C). Concerning the IL-4 condition, the amount of cells is highly associated to the confluence measurement with an higher number of cells in the 36 and 72 hours timepoints compared to control, with an increase of 11% and 4% cells, respectively (Figure 24F versus Figure 24E). Finally, as seen in Figure 24, H, the amount of cells is higher at 36 and 72 hours compared to the control, with a maximum increase of 16% at 72 hours, thus being associated to the measure of the confluence (Figure 24G).

In summary, we can conclude that the concentration of treatments used in our study are not impacting significantly the BV2 viability and proliferation within a time frame ranging from 0 to 72 hours.

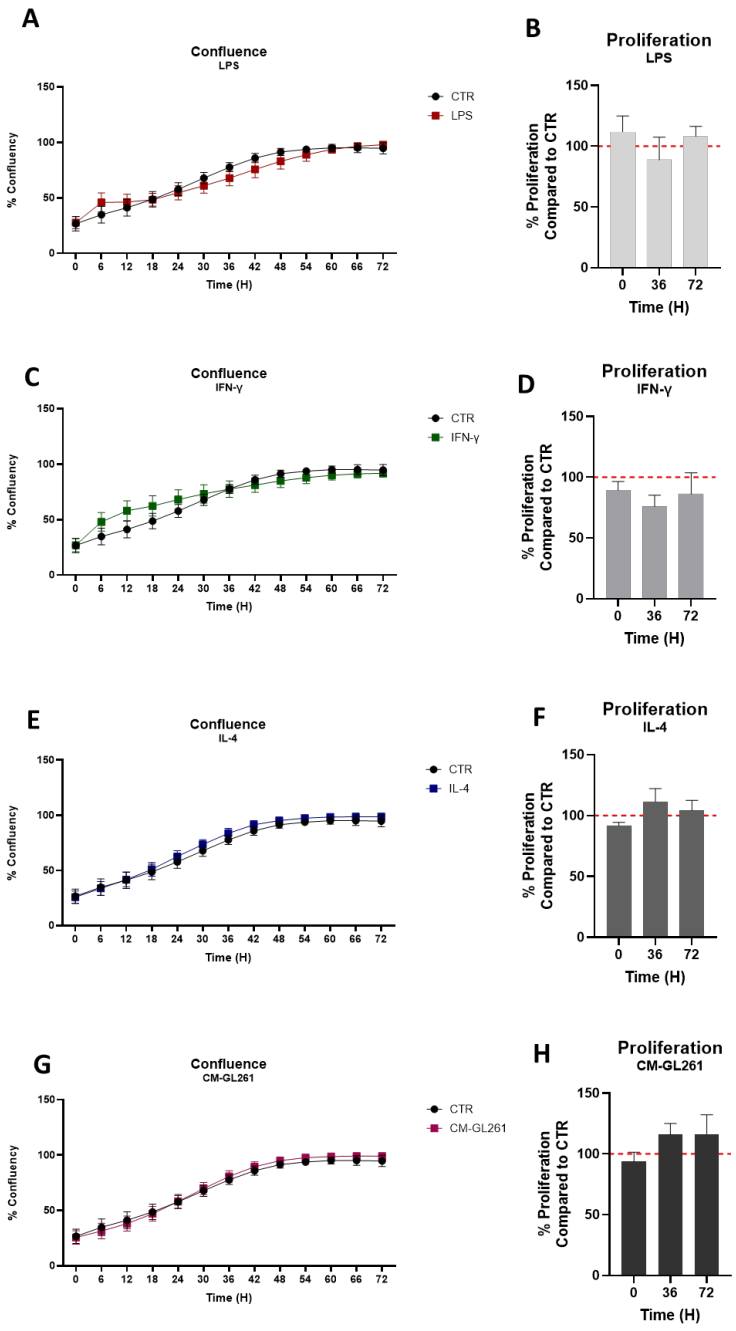

Figure 24. Confluence of BV2 cells is not impacted by treatments with LPS, IFN-γ, IL-4 or CM-GL261:

Effect of 10 ng/mL of LPS (A,B), IFN-γ(C,D), IL-4 (E,F) or CM-GL261 (G,H) exposure on the confluence (left panel) and proliferation (right panel) of BV2 cells treated for 72 hours. The cellular confluence of treated cells was monitored and analyzed by the Incucyte® system. Proliferation was assessed by counting of the cells from the pictures generated by the Incucyte® system and compared to the control (CTR, red line, untreated cells). Statistical analysis was performed using GraphPadPrism 9 applying a two-way ANOVA with correction for multiple comparisons (Sìdàk). Data are representative of three independent experiments, each of which done in technical triplicates and are represented as mean ± SEM.

Following the notification that treatments were not affecting in a significant way the BV2 cells viability and proliferation, we could start assessing the question of microglial phenotypical reprogramming, starting with the exploration of BV2 morphologies.

1.2. Morphological changes of BV2 cells are suggesting a reactive activation upon treatments.

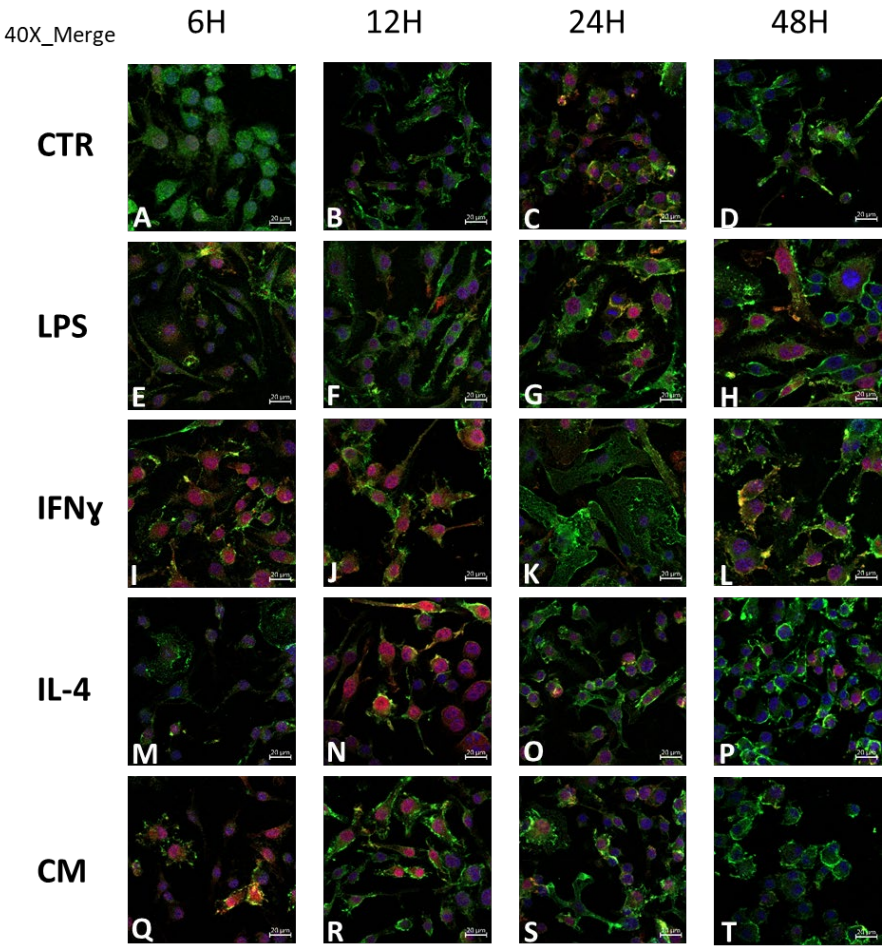

Figure 25. Morphological changes are induced in BV2 upon treatments with LPS, IFN-ɣ, IL-4 or CM-GL261:

Morphological assessment of BV2 cells treated with 10 ng/mL of LPS (E-H), IFN-ɣ(I-L), IL-4 (M-P) or CM-GL261 (Q-T) for 6, 12, 24 and 48 hours; compared to untreated cells (A-D). Confocal images (40X objective) showing the co-labelling of Iba1 (red) and F4/80 (green) in cultured BV2. DAPI is shown in blue; scale bar: 20 µm.

Microglial morphologies have been extensively characterized and linked to reactivity to a various range of stimulations in literature, both *in vivo* (reviewed by[400]) and *in vitro*[401,402] and it is now acknowledged that changes in microglial morphology constitute a sign of reactivity. To know if the treatments were inducing a phenotypical change in BV2 cells, a morphological assessment using immunofluorescent (IF) staining of microglial specific cytosolic marker Iba1[403] and macrophage specific cell surface glycoprotein F4/80[80] was performed, 4'6-diamidino-2-phenylindole (DAPI) staining was used to highlight the nucleus.

On Figure 25 (Annexe 13 for 20X pictures), we observed a change of BV2 morphology after six hours of treatment. Compared to the untreated cells (CTR, Figure 25A), most BV2 treated with LPS for six hours exhibit a modest increase in the soma size, an increase in processes number and length with no thickness change (E). Similarly, Figure 25 shows that compared to control, IFN-ɣ treated cells exhibit an enlargement of the soma and an increase in processes number but these last are less elongated and thicker (I) than the ones observed in the LPS condition (E). On the contrary, we noticed that, compared to the control, the IL-4 treated cells (M) are characterized by a decrease in the soma size and a decrease and elongation of the processes. Finally, Figure 25 shows that most of the cells treated with CM-GL261 (Q) display a decrease in soma size, less processes but similar to the control (A) in length and thickness and shorter that the ones treated with IL-4 (M).

After 12 hours of treatment, we observed a stronger change in BV2 morphology. After 12 hours of LPS (F), we still witness the enlargement of the soma of the cells; the number of processes is similar to control (B) but increased in length and thickness (F). The BV2 treated with IFN-ɣ display a morphology similar to control in terms of soma size, processes number and thickness but exhibit a slight increase in length (J). We can also note that BV2 treated with IL-4 exhibit a decrease in soma size, a decrease in processes number and thickness, together with an increase in the latest length (N). Finally, for CM-GL261 treated BV2 we observed a morphology similar to the control with only few cells exhibiting either few elongated processes or an increase in soma size (R).

Figure 25 also shows that, after 24 hours of treatment, the morphological changes of treated BV2 cells are undeniable. Compared to control (C) and in the continuity of what is observed at 12 hours, LPS-treated BV2 exhibit an increase of soma together with an increase of longer and thicker processes (G). In comparison to both control and LPS-treated cells, IFN-ɣ-treated BV2 are displaying a characteristic amoeboid morphology with exceeding large soma and no branche (K). Most of the cells treated with

IL-4 (O) exhibit a soma smaller than the control, less processes but longer and thinner. Finally, we observed different phenotypes within the cells treated with CM-GL261, ranging from amoeboid to round cells, with long thin processes to no protusion at all (S).

Lastly, we noticed that the observed phenotypes tend to regress after 48 hours of treatment when compared to their 24 hours counterpart. Nevertheless, compared to the control (D), the LPS-treated are still exhibiting a larger soma and a lesser amount of shorter and thicker processes (H), very similar on all parameters to the IFN-ɣ-treated cells (L). On the opposite and compared to control (D), IL-4 treated cells display a decreased soma with a similar amount of processes, however being shorter and thinner (P). Finally, we observed that the CM-GL261 treated cells exhibit a very homogenous phenotype characterized by a soma decrease in size and very few thick and minuscule processes (T).

To summarize, Figure 25 (and Annexe 13) shows that characteristic morphological changes are gradually induced over time in all treatment conditions, especially after 24 hours and more manifest in the pro-inflammatory conditions. Indeed, LPS and IFN-ɣ are inducing a significant increase of BV2 soma size accompanied with a decrease and thickening of processes length. On the contrary, anti-inflammatory (IL-4) treatment leads to an extension and thinning of BV2 processes and reduction of the soma size when compared to untreated BV2. Those results are in alignment with the literature classifying microglial morphologies suggesting a polarization of BV2 cells towards pro- and anti-inflammatory[325] phenotypes *in vitro*, respectively. In the CM-GL261 condition, mixed phenotypes are observables with elongated cells coupled with amoeboid ones, making it difficult to summarize a homogenous induced microglial phenotype. The observation that the cell shapes are changing suggests a phenomenon of cellular reactivity to the treatments in our experimental design.

To observe if that effect could be measurable at the functional level, we next assessed the phagocytosis of treated BV2 cells by using pH sensitive fluorescent *Escherichia coli* particles (Figure 26).

1.3. No significant changes in phagocytosis upon treatment are observed in BV2 cells

Phagocytosis, as one of the major function of microglial cells, represents a key parameter for functional change assessment. To evaluate phagocytosis, pH sensitive fluorescent particles of *Escherichia coli* were placed in the medium of BV2 cells treated or not with LPS, IFN-ɣ, IL-4 or CM-GL261. Upon phagocytosis, the particles, activated by the pH of the phagolysosome, emit red fluorescence

measured by a plate reader system, so the intensity of the fluorescence correlates with the amount of beads phagocyted by BV2 cells.

The huge variability between biological replicates and translated in very high Standard Error of the Mean (SEM) and absence of significance on Figure 26 makes it hard to conclude on the phagocytic behavior of BV2 treated cells.

Nevertheless, we observed several phases illustrated in Figure 26:

Phase A is characterized by a slight decrease in phagocytosis for all treatment conditions compared to the untreated control cells, indicating that all conditions exhibit a phagocytosis capacity lower than the control.

Phase B is characterized by an intense decrease followed by an intense increase of phagocytosis in all conditions with phagocytotic activity still being lower as compared to the control.

Phase C shows different trends according to the treatment condition with LPS condition exhibiting a huge increase followed by a decrease in phagocytosis, above the control values; CM-GL261 condition showing a slight increase followed by a decrease below the control values; finally a decrease followed by an increase of phagocytosis below the control values were observed for IL-4 and IFN-ɣ conditions.

Phase D shows a slight and gradual increase for all conditions, the phagocytosis from the LPS treatment being above the control whereas the IFN-ɣ, IL-4 and CM-GL261 being below.

Phase E shows a more complex pattern, with an increase above the control phagocytosis for all treatment conditions, a decrease below the control values, except for the LPS treatment and an increase below the control values for all treatment conditions but the LPS one.

Phase F exhibits a stable increase for all treatment conditions, LPS values being above the control, IFN-ɣ and IL-4 closely below and CM-GL261 strongly below the control values.

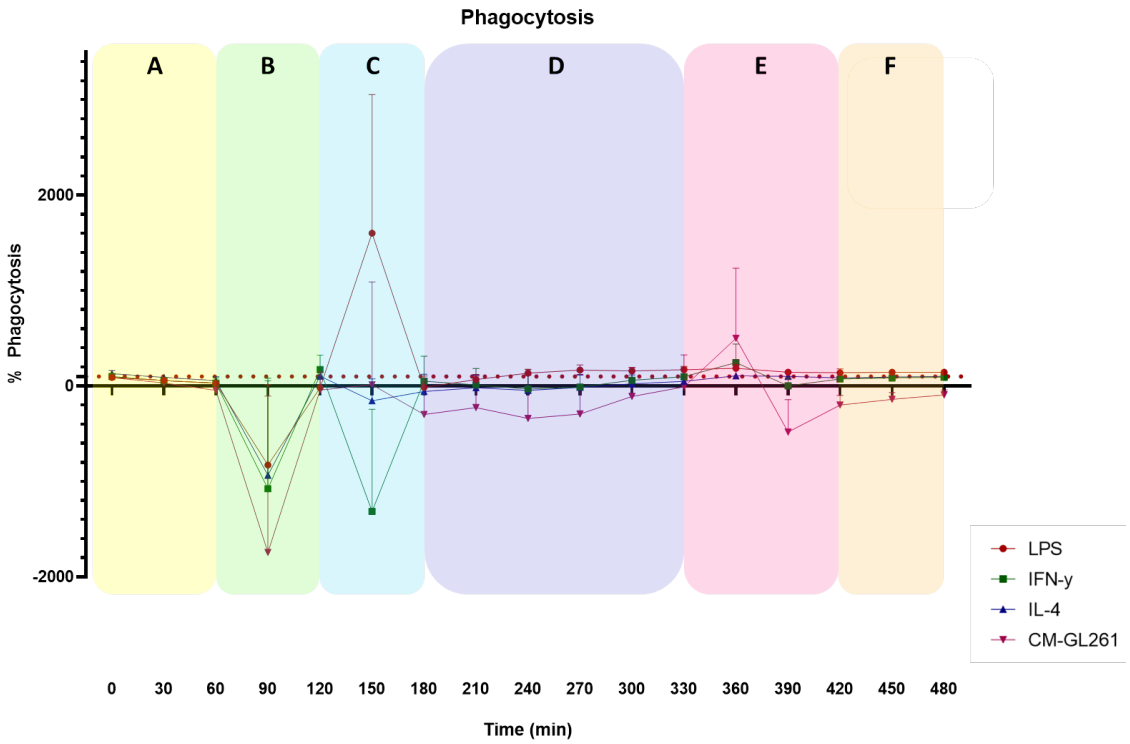

Figure 26. Phagocytic function of BV2 is not significantly impacted by treatments with LPS, IFN-ɣ, IL-4 or CM-GL261:

Effect of 10 ng/mL of LPS (red), IFN-ɣ (green), IL-4 (blue) or CM-GL261 (purple) exposure on the phagocytic function of BV2 cells by use of pH dependent fluorescent beads monitored in the Clariostar® system for eight hours. Phagocytosis of treated cells was assessed relatively to the control, untreated cells (red dotted line, 100%). Statistical analysis was performed using GraphPadPrism 9, applying a two-way ANOVA corrected for multiple comparisons (Tukey). Data are representative of three independent experiments, each of which done at least in technical triplicates and are represented as mean ± Standard Error of the Mean (SEM).

Despite the high SEM, we can still attest that the trend of decreased phagocytosis in the CM-GL261 treated cells seems to be accurate since the SEM are less prominent and in accordance with literature[404], suggesting that functional reprogramming might have been reached.

In the same manner, we observed a trend of increase in phagocytic activity after 150 minutes of treatment with LPS (Figure 26C), which is also in accordance with literature[405]. Concerning the IL-4 treatment, it is supposedly inducing increase in phagocytosis in primary microglia[406], questioning the strength of our IL-4 treatment or the responsiveness of the BV2 cell line to it. Finally, concerning the IFN-ɣ treatment, we observed a slight tendency towards a decrease in phagocytosis which has been

observed in primary microglia and supposed in BV2 cells by the IFN-ɣ induced downregulation phagocytosis implicated genes[407].

We can not conclude that a functional reprogramming has been reached by the design of our experiment. Nevertheless, to further characterize the BV2 populations we obtained by treating the cells, we decided to explore the secretome using Cytokine arrays, targeting 96 different CK.

1.4. BV2 cells exhibit differential secretomic changes upon treatments.

As seen in the introduction, the secretory function of microglial cells is a crucial part of microglial reaction to a particular environment and one of the major group of secreted products is composed of CKs, thus, assessing the secretion of CKs represents an effective way of establishing the level of reactivity of the BV2 cells in our study.

In order to measure the CKs, commercially available ELISA based membrane assays directed against 96 well known CKs (Annexes 1 and 22) were performed on the culture supernatant of BV2 treated or not for six to 48 hours with LPS, IFN-ɣ, IL-4 or CM-GL261. Those membranes are covered with capture antibodies recognizing CK and revealed by detecting biotinylated antibodies further activated by HorseRadish Peroxidase (HRP) conjugated streptavidin producing chemiluminescence. The intensity of the luminescence is thus positively associated to the amount of CKs present in the supernatant.

Figure 27 exhibits a panel of six well known CKs in microglial biology, IL-4, an anti-inflammatory CK (A); IL-6 (B), IFN-ɣ (C) and TNFα (E), pro-inflammatory CKs; MMP2 (D) a metalloproteinase and G-CSF, a growth factor (F). The X-axis represents the timepoints of treatment, and Y-axis the mean pixel intensity measured on the blot picture. This Figure allows the comparisons of the CK secretion intensity at each timepoint between different conditions but also in each individual condition between timepoints.

Even though the graphs presented in Figure 27 exhibit high SEM and no statistical significance, we observed some similarities and divergences in the patterns of CKs secretion between treatments and control along timepoints.

For instance, the IFN-ɣ treated BV2 and the control group seem to follow the same patterns of IL-4 (A), IL-6 (B), TNF-α (E) and G-CSF (F) secretions along time points. The LPS and CM-GL261 seem similar in secretion patterns of IL-4 (A), IFN-ɣ (C) and MMP2 (D) but interestingly, patterns of secretion of IL-6 (B) for LPS and CM-GL261 treated BV2 are opposite, rising interrogations on the different CK secretion

regulation by different treatments. Some patterns of secretion along timepoints are otherwise unique, we observed for instance that, compared to all the other conditions (control included), the BV2 treated with IL-4 exhibit distinctive patterns of secretion for IL-4 (A), IL-6 (B), IFN-ɣ (C) and G-CSF (F). Another interesting pattern of secretion is the one concerning the TNFα (E), where BV2 treated with CM-GL261 is the only one following a distinctive trend along timepoints compared to the control, LPS, IFN-ɣ, and IL-4.

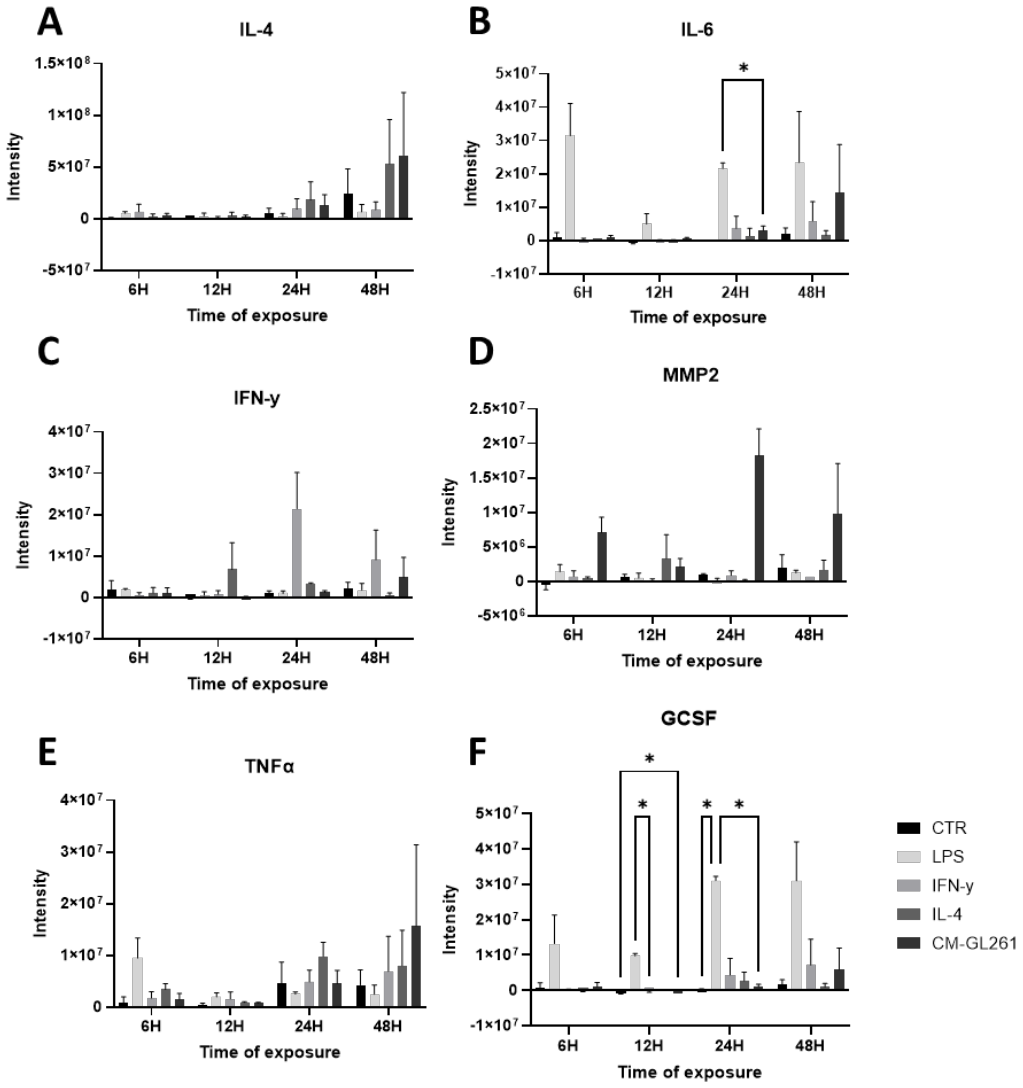

Figure 27. Changes in secretome are induced in BV2 cells upon treatment with LPS, but not with IFN-ɣ, IL-4 or CM-GL261:

Effect of 10 ng/mL of LPS, IFN-ɣ, IL-4 or CM-GL261 exposure on the CK secretion of BV2 cells treated for 6, 12, 24 and 48 hours, compared to untreated cells (CTR). Selected CK from the 96 targets present on the arrays are (A) IL-4, (B) IL-6, (C) IFN-ɣ, (D) MMP2, (E) TNFα and (F) G-CSF. Measure of pixel intensity on the arrays were made using FIJI ImageJ software, normalized to the background pixel

intensity and to the pixel intensity generated by the DMEM media itself. Statistical analysis was performed using GraphPadPrism 9 and applying two-way ANOVA with a correction for multiple comparisons (Tukey). Asterisks represent significant differences (* $p<0.05$). Data are representative of two independent experiments, each of which done in technical duplicates and are represented as mean ± Standard Error of the Mean (SEM).

Despite the absence of significance for CKs results, we observed a trend between the profiles of secretion for each treatment condition and each individual treatment is associated with the secretion of at least one CK compared to the other treatments and to the control. Indeed, we can state that the BV2 treated 24 hours with LPS are exhibiting the highest intensity of IL-4 and G-CSF secretion compared to all other conditions of treatment and time, including control untreated BV2 (Figure 27A and F, respectively). Otherwise, the BV2 treated with IFN-ɣ for 48 hours are characterized by the highest secretion of IL-6 and IFN-ɣ (B and C, respectively) compared to all conditions of time and treatments. In addition, the BV2 treated with IL-4 for 24 hours display the highest secretion of TNFα (E) and, finally the BV2 treated with CM-GL261 for 48 hours shows the highest secretion of MMP2 (D) compared to all condition of treatment and timepoints. We can then conclude that our treatment leads to differential secretomic profiles in BV2 cells suggesting that microglial reactivity has been reached after 24 or 48 hours of treatments.

After observing that BV2 cells adopt phenotypical changes upon our treatments, we choose to investigate the transcriptomics behind BV2 reactivity to the treatments by assessing mRNA expression of characteristics microglial signature genes.

1.5. Transcriptomic analysis shows significantly differential expression upon treatments

Microglial transcriptomics has also been widely investigated in various conditions to assess the genes underlying microglial reactivity towards specific phenotypes, amongst them *Cxcl10, Tnf* and *Il1ß; Arg1, Ym1* and *Fizz1* genes associated with pro- and anti-inflammatory properties, respectively[408]. We decided to measure the quantity of mRNA in BV2 treated or not with LPS, IFN-ɣ, IL-4 or CM-GL261 from six to 48 hours by performing RT-qPCR. We assessed the expression of those mRNAs in comparison to the housekeeping gene *Rpl27*. The results, normalized to the control group mRNA counterparts are presented in Figure 28. The left panel of the Figure 28 shows the mRNA expression for the pro-

inflammatory associated genes *Tnf* (A), *Il-1β* (B) and *Cxcl10* (C) whereas the right panel shows the mRNA expression for the anti-inflammatory associated genes *Arg1* (D), *Ym1* (E) and *Fizz1* (F). In all figures, X-axis refers to each of the treatment conditions with each color representing a timepoint; the Y-axis representing the mRNA expression of each gene relative to the control untreated counterpart.

Figure 28A shows the result for the expression of *Tnf* mRNA in each treatment condition relatively to the untreated control BV2. We observed that the *Tnf* mRNA expression values of all treatments conditions at all timepoints are above the control but level of significance was only reached for LPS treatment after six and 12 hours and for IFN-ɣ after six hours. We also observed that, except for the CM-GL261 condition, all are following a trend of gradually decrease over time.

Indeed, LPS treatment is inducing, amongst all treatments, the strongest response at six hours with a 103-fold increase compared to the respective control. The LPS-induced expression of *Tnf* mRNA decreases along timepoints, with a decrease of 72-fold between 6 and 12 hours. Lesser than the LPS treatment with a difference of 75-fold change, IFN-ɣ is nevertheless inducing a strong increase of 28-fold change in *Tnf* mRNA expression in BV2 cells at six hours timepoint compared to the control. This induction of *Tnf* mRNA is gradually decreasing along timepoints. We observed that pro-inflammatory conditions led to a statistically significant induction of the *Tnf* mRNA expression in BV2 cells, while the glioma mimicking (CM-GL261) and the anti-inflammatory treatment are not inducing changes compared to control.

Figure 28B shows the expression of the *IL-1β* mRNA in the different treatment conditions relative to the untreated control BV2. We observed that all treatments led to the insignificant induction of the *IL-1β* mRNA expression at all timepoints, except for the LPS at six and 12 hours. For instance, the LPS condition exhibit a strong increase of 330-fold change at six hours compared to the control followed an increase to reach 383 at 12 hours and a decrease afterwards. We observed that, compare to the control, LPS treatment led to a statistically significant induction of *IL-1β* mRNA expression in BV2 cells, all the other treatments, including the pro-inflammatory IFN-ɣ did not induce significant changes compared to the control.

Figure 28C shows the expression of the *Cxcl10* mRNA in the different treatment conditions relative to the control untreated BV2. All treatments lead to a insignificant induction of the *Cxcl10* mRNA expression at all timepoints, except for LPS and IFN-ɣ conditions that were characterized by a dramatic increase of *Cxcl10* mRNA expression after six hours with positive fold changes of 3744 and 2170 at six hours, respectively. We conclude that the pro-inflammatory treatments lead to a significant induction

of *Cxcl10* mRNA expression after six hours, while anti-inflammatory associated treatments are not inducing any change compared to control.

Figure 28D shows the expression of the anti-inflammatory associated *Arg1* mRNA in the different treatment conditions relative to the control untreated BV2. We observed that the LPS and IFN-ɣ treatment conditions are not inducing any significant changes in the *Arg1* mRNA expression, while IL-4 and CM-GL261 treatments leads to significant increase at all timepoints. Within the IL-4 condition, the significant induction of the *Arg1* mRNA expression at 48 hours is the strongest of all in our settings with a positive fold change of six, which, in comparison to the previous pro-inflammatory mRNAs induction, seems rather modest. Concerning the CM-GL261 condition, we observed an increase of two positive fold change at 12 hours, being the peak of *Arg1* mRNA expression in this condition. We can conclude that, compare to the control, the anti-inflammatory treatment IL-4 and the glioma mimicking CM-GL261 treatment leads to significant induction of *Arg1* mRNA expression, while the pro-inflammatory treatments do not.

Figure 28E shows the expression of the anti-inflammatory associated *Ym1* mRNA in the different treatment conditions relative to the control untreated BV2. We observed that only IL-4 treatment leads to a significant induction of the *Ym1* mRNA expression from 12 to 48 hours, the peak of induction being reached at 12 hours with a positive fold change of five. We can conclude that only the anti-inflammatory treatment IL-4 has an influence on the expression of *Ym1* mRNA in BV2 cells.

Lastly, Figure 28F shows the expression of the anti-inflammatory associated *Fizz1* mRNA in the different treatment conditions relative to the control untreated BV2. We observed that all treatments lead to the insignificant induction of the *Fizz1* mRNA expression at all timepoints, except for the IL-4 condition at six hours and the CM-GL261 at 12 hours. For the IL-4 condition, Figure 28 shows that the expression of *Fizz1* mRNA is strongly induced at six hours with a positive fold change of three, while for the CM-GL261 condition shows a strong increase up to three at 12 hours.

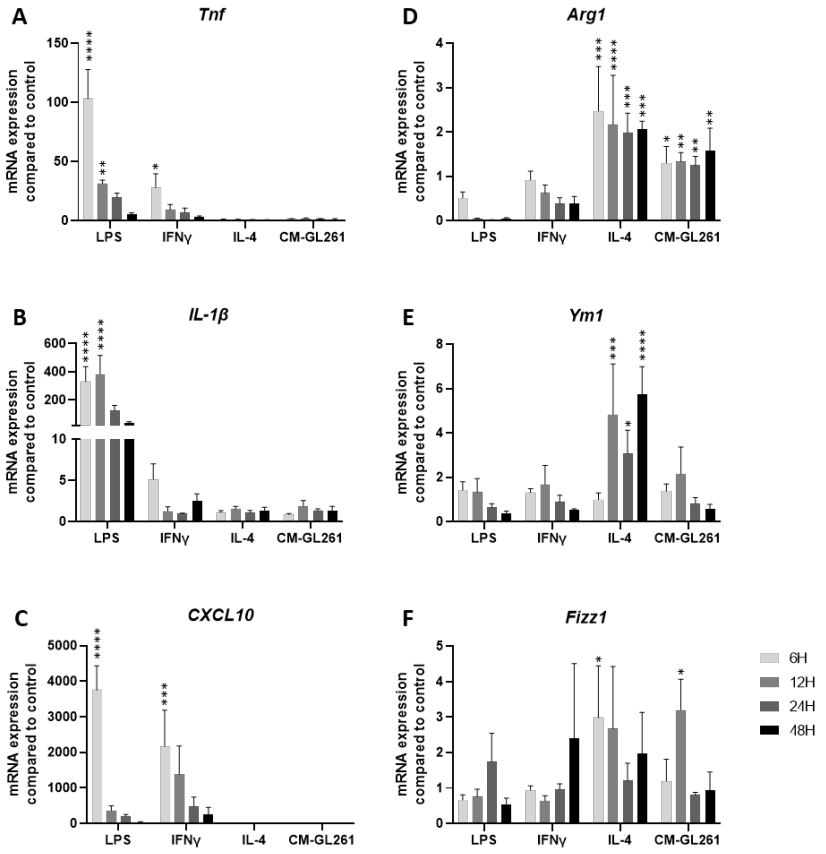

Figure 28. Stimulation treatments lead to differential expression of mRNAs in BV2 cells:

Effect of 10 ng/mL of LPS, IFN-ɣ, IL-4 or CM-GL261 exposure on mRNA expression of BV2 cells treated for 6, 12, 24 and 48 hours, normalized to untreated cells. Selected mRNA targets are characteristics of a pro-inflammatory (top panel) and anti-inflammatory (bottom panel) reactivity. Namely (A) *Tnf*, (B) *IL-1β*, (C) *Cxcl10*, (D) *Arg1*, (E) *Ym1* and (F) *Fizz1*. *Rpl27* was used as a housekeeping gene for normalization of gene expression. Values were normalized to the control untreated BV2 values. Statistical analysis was performed using GraphPadPrism 9 and applying two-way ANOVA with a correction for multiple comparisons between control and treatments (Dunnett) and in between treatments (Tukey). Data are representative of three independent experiments, each of which done in technical triplicates and are represented as mean ± Standard Error of the Mean (SEM).

On the overall Figure 28, we observe the significant induction of a pro-inflammatory associated signature by pro-inflammatory treatments and, in a lower range the significant induction of the anti-inflammatory signature by anti-inflammatory and glioma mimicking treatment. We can conclude that the treatments used in the study are inducing significant transcriptomic changes in the BV2 microglial cells, characterized by the expression of *Tnf*, *Il1ϐ* and *Cxcl10* for the LPS; *Tnf and Cxcl10* for the IFN-ɣ;

Arg1, *Fizz1* and *Ym1* for the IL-4 and *Arg1* and *Fizz1* for the CM-GL261. We can confidently attest acquisition of different microglial identity with our experimental setting.

From those results and according to Paolicelli et al. guidelines, we can state that we are studying different types of induced phenotypes in BV2 microglial cells characterized by the following features :

Table 4. BV2 features induced by treatments

Versus CTR	LPS	IFN-γ	IL-4	CM-GL261
Morphology	Bushy	Amoeboid	Elongated	Mixed
Phagocytosis *Trends*	Increased	Similar	Similar	Decreased
Secretome *Trends*	IL-4 and G-CSF	IL-6 and IFN-γ	TNFα	MMP2
Transcriptome	*Tnf, Il1β* and *Cxcl10*	*Tnf* and *Cxcl10*	*Arg1, Fizz1* and *Ym1*	*Arg1* and *Fizz1*

Taken together, we can conclude that BV2 cells are reacting to each of our treatment *via* a reprogramming affecting at least morphology and transcriptome, and we can hypothetize that this reprogramming is emerging from a change in chromatin compaction and structure. Following this assumption, DNA isolated from BV2 cells treated or not with LPS, IFNɣ, IL-4 and CM-GL261 was bisulfite converted and submitted to Illumina MethylMouse arrays to unravel potential changes in DNA methylation patterns in accordance with the shift in cellular identity described above.

1.6. Significant changes in DNA methylation patterns are induced by LPS and IFN-ɣ treatments after 12 hours and by all treatments after 48 hours in BV2 cells

The mouse methylation arrays from Illumina are composed of 12 individual beadchips where the DNA samples are deposited to hybridize with oligonucleotide probes capturing more than 285000 CpG sites (targeting C-G dinucleotide), localized inside or in close proximity to promoters and regulatory elements within the mouse genome[409]. Each oligonucleotide probe is coupled with a fluorescent dye indicating a fully methylated CpG sites with green and totally unmethylated one with red; and is

duplicated multiple times on the beadchip, allowing the calculation of a mean methylation intensity (β-value) for each CpG site.

After each β-value were measured at each CpG site for each BV2 samples and transformed in M-value, we made comparisons of each treatment methylation patterns compared to the respective timepoint controls.

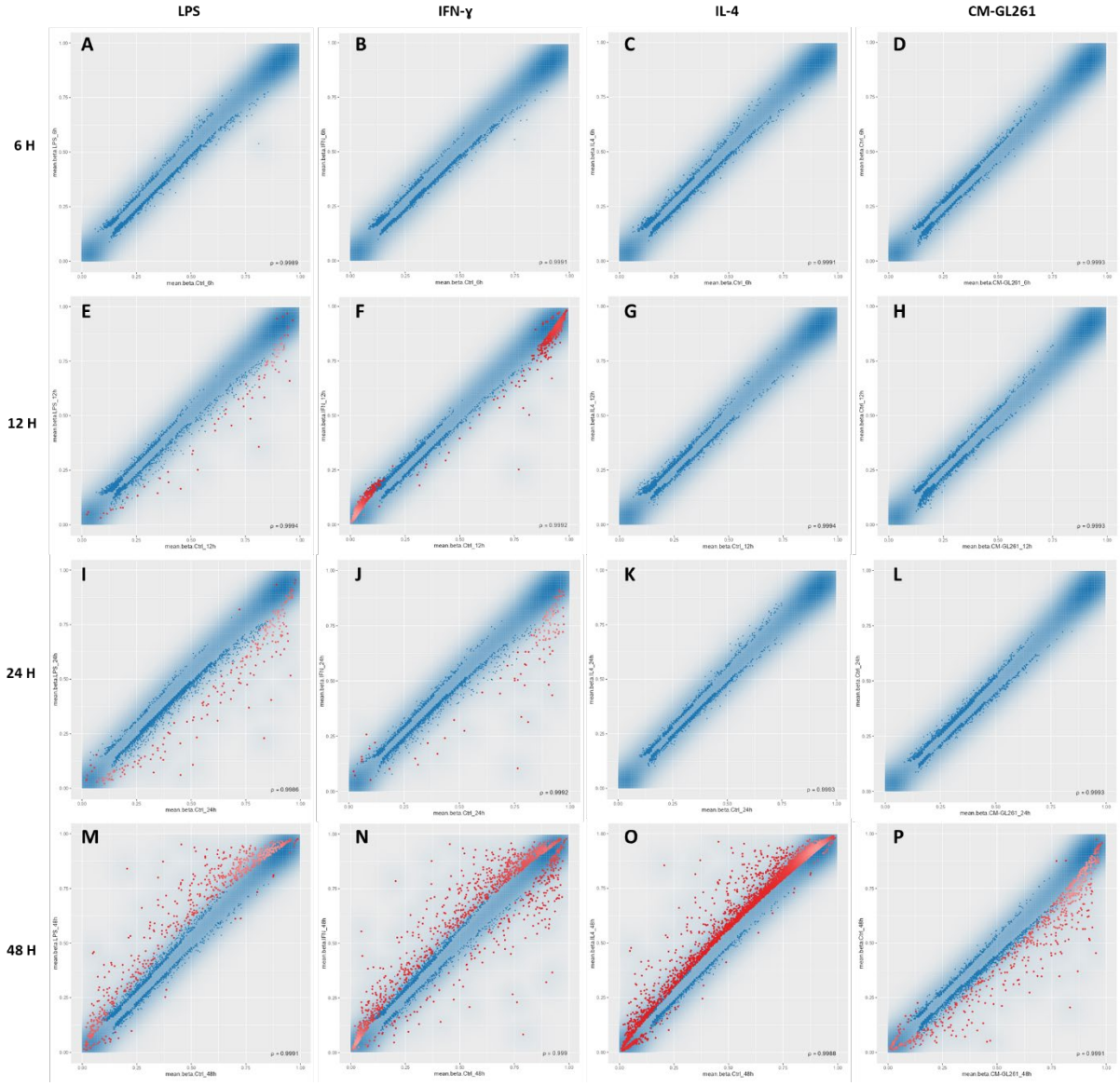

Figure 29. Differentially Methylation is induced by LPS and IFN-γ treatments at 12 hours and enhanced after 24 hours:

Effect of 10 ng/mL of LPS, IFN-γ, IL-4 or CM-GL261 exposure on DNA methylation patterns of BV2 cells treated for 6, 12, 24 or 48 hours, compared to the untreated control BV2 cells. Scatter plots of the differentially methylated sites in BV2 treated with LPS (A, E, I, M), IFN-γ (B, F, J, N), IL-4 (C, G, K, O)

or CM-GL261 (D, H, L, P) at six (A to D), 12 (E to H), 24 (I to L) and 48 hours (M to P) compared to the untreated BV2. The experiment was made on technical triplicate. Raw data from MethylMouse array were processed by Dr. Reka Toth, using RnBeads 2.16.0, differential methylation was performed using the limma package based on the M-values and the False discovery rate was used to adjust for multiple testing. Blue dots represent a Differentially Methylated CpG site, red dots highlight statistical significance.

Figure 29 displays the scatter plots for Differentially Methylated CpG Sites (DMS) in each treatment condition compared to the control, represented by the mean methylation level (M-value, transformation of the β-value) ranging from 0 indicating an unmethylation to 1, a full methylation. For LPS, IFN-ɣ and IL-4 conditions, each plot shows the mean M-value of the control group on the X-axis and the mean M-value of the treatment group on the Y-axis. Concerning the CM-GL261 condition, the mean M-values of the control group appear on the Y-axis, whereas the CM-GL261 detected mean M-values appear on the X-axis. Each dot represents a DMS between treatment and control conditions, statistically significant when colored in red (FDR adjusted pValue < 0,05).

On Figure 29, we see that there are no significant difference at the DNA methylation level between untreated and treated BV2 at the six hours timepoint, regardless of the treatment (A, LPS; B, IFN-ɣ; C, IL-4; and D, CM-GL261). We see that significant differences start to appear between the control and LPS (E) and IFN-ɣ (F) after 12 hours of treatment; while no differences are induced upon IL-4 (G) and CM-GL261 (H) treatment. Similarly, at the 24 hours timepoint, significant differences in methylation patterns are observed in the LPS (I) and IFN-ɣ (J) treated BV2 compared to untreated BV2; while no significant difference can be seen in the IL-4 (K) and CM-GL261 (L) treated BV2. Finally, we see on Figure 29 that all treatment conditions lead to significant DMS at 48 hours compared to the control, the most striking condition being the IL-4 (0) (LPS, M; IFN-ɣ, N and CM-GL261, P).

The conditions exhibiting a significant DMS between treatment and control were explored individually in more depth, starting with the differences in DNA methylation patterns in BV2 induced by pro-inflammatory treatment IFN-ɣ after 12 and 24 hours, compared to the respective control untreated BV2.

1.7. BV2 cells treated with IFN-ɣ show DNA hypomethylation gradually increasing over time

Figure 30 displays different features of the comparisons of the DMS between BV2 treated with IFN-ɣ for 12 and 24 hours and the respective untreated control.

First of all, a Principal Component Analysis (PCA) was made on all the processed samples (all treatments, all timepoints) for DNA methylation profiles on all filtered CpG sites to pinpoint the variability components and identify the level of variation between each sample. Principal Components (PC) represent combination of variables to facilitate the comparison between the samples, PC1 and PC2 are combinations explaining the most variation (40 % variance in total; Annexe 31) between the samples (mostly treatments, position on the array and array number; Annexe 32). Each PCA plot displays the eigenvalues of the PC1 on the X-axis and the eigenvalues of the PC2 on the Y-axis, representing the amount of variance carried in each PC for each individual sample.

To facilitate the comparisons of distance between samples on the plots, only the presented comparisons were highlighted on each plot. For instance, Figure 30A, displays the PCA results of only IFN-ɣ (green dots) and untreated (orange dots) BV2 samples (technical triplicates) at the 12 hours timepoint. What we can observe on Figure 30A, is a segregation between the IFN-ɣ treated samples and the untreated samples without a superposition of replicates, meaning that despite a variability amongst the replicates, a 12 hours treatment with IFN-ɣ (means PC1: 1.6, PC2 : 2.6) leads to variability in DNA methylation compared to the control (means PC1: - 1.0, PC2 : - 0.7). We can draw the same conclusion from the Figure 30B, displaying the PCA results of IFN-ɣ (green triangles) and untreated (orange triangles) BV2 samples (technical triplicates) at the 24 hours timepoint. Indeed, we also observe a segregation between the IFN-ɣ treated samples (means PC1: - 0.9, PC2 : - 0.5) and the untreated samples (means PC1: - 5.8, PC2 : - 3.1) without a superposition of replicates.

Secondly presented in Figure 30, volcano plots (B and E) displaying on the X-axis the mean difference between the methylation level (M-value) of the DMS from the control condition and the M-value of those DMS from the IFN-ɣ, both at the 12 hours (B) and 24 hours (E) timepoints. The Y-axis displays the corrected P-value (less than 10% probability to make a false discovery) for each DMS M-value, the horizontal line corresponding to the FDR threshold. Each dot represents a DMS, with statistical significance when colored in green or red, with direction towards hypo- and hypermethylation, respectively.

We observe in Figure 30B, that 33 DMS exhibit a significantly positive difference between control and IFN-ɣ condition with a mean methylation difference threshold ranging from 0.1 and 0.6. The threshold being set as +/- 0.1, 1185 DMS with a significant negative difference above the threshold and 550 DMS with a significant positive difference below the threshold were excluded. Nevertheless, we can observe with confidence that 33 CpGs sites are hypomethylated in the IFN-ɣ treated BV2 compared to the untreated BV2 at the 12 hours timepoint. In Figure 30E, we see that 79 and three DMS are exhibiting significant positive and negative differences between the control and the IFN-ɣ condition, respectively with a mean methylation difference threshold ranging from – 0.2 and 0.5. It is worth noting that five DMS with a significant negative difference above the threshold and 23 DMS with a significant positive difference below the threshold were excluded. We observed that the 12 hours exposure to IFN-ɣ leads to a high number of small amplitude DNA methylation changes while the 24 hours exposure results in a low amount of big amplitude DNA methylation changes in BV2 cells. We can also note that the significantly high amplitude DNA methylation changes in both time points of exposure are leading towards hypomethylation.

Finally, on Figure 30C and F, the significant DMS are displayed in the rows of a heatmap with each column representing the clustering of the mean M-values of each site according to treatment (Tt) and timepoint (Tp). The mean M-value is symbolized as color ranging from a deep blue representing unmethylated site with a mean M-value of 0, to a dark red representing fully methylated site with a mean M-value of one.

We see on Figure 30C, that the 33 DMS are more methylated in the control group than in the IFN-ɣ group at 12 hours timepoint. We can also see that the control group at 12 hours displays some variability on the methylation level of those DMS, whereas the IFN-ɣ group at 12 hours are clustered together, exhibiting homogeneity in methylation levels for those DMS. Finally, it is worth noting that while there is no distinct methylation signature for those conditions, a cluster appears for those DMS regrouping the IFN-ɣ conditions at the timepoints 12, 24 and 48 hours with a gradual decrease in β-values along timepoints. Interestingly, the six hours timepoint of the IFN-ɣ condition, while not being clustered with the other timepoints, is the direct neighbor of the 12 hours IFN-ɣ timepoint. All those observations suggest gradual and homogenous DNA methylation modifications for those probes in response to IFN-ɣ treatment in BV2 cells, in a time exposure dependent manner.

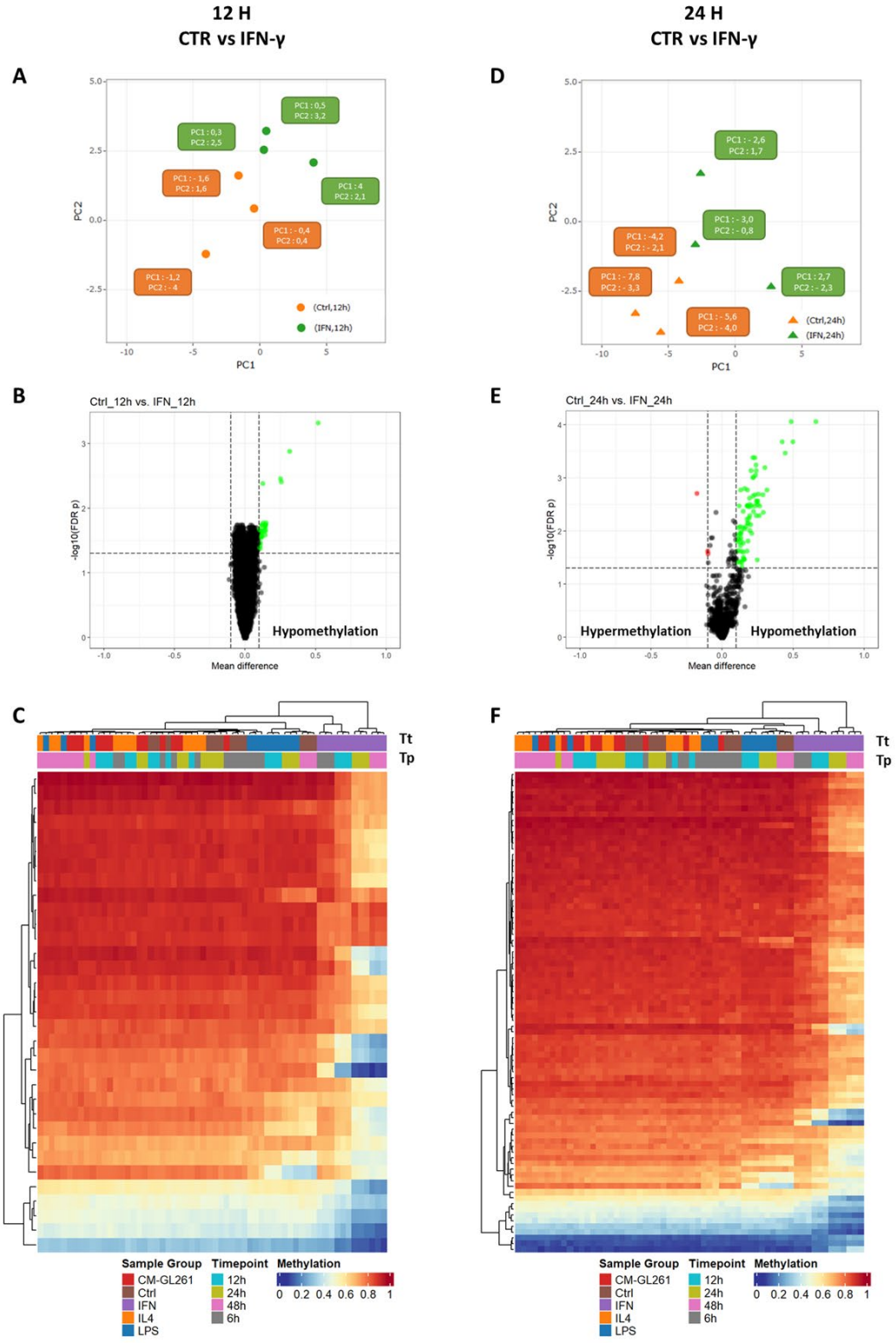

Figure 30. BV2 cells treated with IFN-ɣ exhibit significantly differentially hypomethylated sites:

Effect of 10 ng/mL of IFN-ɣ exposure on DNA methylation patterns of BV2 cells treated for 12 hours, compared to the untreated control BV2 cells. The experiment was made on a technical triplicate. Raw data from MethylMouse array were processed by Dr. Reka Toth, using RnBeads 2.16.0, differential methylation was performed using the limma package based on the M-values and the False Discovery

Rate was used to adjust for multiple testing. Left panel: 12 hours exposure to IFN-ɣ. Right panel: 24 hours exposure to IFN-ɣ. (A, D) PCA plots of DNA methylation profiles based on all CpG sites (after filtering; see Materials and Methods); IFN-ɣ: green and control: orange; Time of exposure to IFN-ɣ: 12 hours: dots; 24 hours: triangles. (B, E) Volcano plots displaying mean DNA methylation differences between IFN-ɣ and control untreated BV2 at all filtered CpG sites. The vertical lines represent the 0.1 mean M-values difference boundary while the horizontal line represent the statistical significance treshold ($P < 0.05$). The significant DMS appeared in green and red, hypo- and hypermethylated in IFN-ɣ condition compared to control, respectively. (C, F) Hierarchical clustering was performed and represented as a heatmap showing the mean methylation levels of the DMS between the IFN-ɣ and the control. Columns represent the samples relative to treatment (Tt) and timepoint (Tp), while the rows represent the DMS. The methylation levels are illustrated as colors ranging from deep blue (M-Value = 0, unmethylated) to deep red (M-Value = 1, fully methylated).

We see on Figure 30F, that those results are similar after a 24 hours exposure. Indeed, the significant DMS are more methylated in the control group than in the IFN-ɣ group at 24 hours timepoint. In addition, it is worth noting that the cluster formed of the IFN-ɣ condition at 12, 24 and 48 hours in Figure 30C is not appearing here for those DMS. Nonetheless, the 24 and 48 hours timepoints are clustered together and the six and 12 hours timepoints are clustered next, showing a homogeneity in the response of BV2 cell DNA methylation to the IFN-ɣ treatment along time. In addition, 28 DMS are common between the 12 and 24 hours IFN-ɣ conditions (Annexe 33; only five DMS are specific of the 12 hours timepoint), confirming the homogenous response relative to DNA methylation patterns reorganization in response to IFN-ɣ exposure in BV2 cells.

Taken together, Figure 30 shows that BV2 exposed to 12 and 24 hours of IFN-ɣ exhibit significant gradual changes in DNA methylation patterns mostly towards hypomethylation.

1.8. DNA methylation changes induced by IFN-ɣ are localized in transcriptional regulatory elements predicted to be associated with active chromatin state

To bring biological meaning to the phenomenon of methylation induced differences by the IFN-ɣ treatment in BV2 cells, we use computational analysis of the data to localize the DMS within the genome allowing identification of regulatory elements that might have been modified by DNA methylation. For instance, Figure 31A, shows the genomic annotation associated to the DMS in the IFN-ɣ condition compared to the control at the 12 and 24 hours timepoints. The X-axis displays the

percentage of each genomic feature associated with the DMS. Promoter is defined as – 3 kb to + 0,5 kb from the Transcription Start Site (TSS).

We observe in Figure 31A, that the hypomethylated DMS induced in the IFN-ɣ condition at the 12 hours timepoint are mostly located in promoters in less or equal to 1 kb of the TSS (~37,5%). In addition, DMS are found in distal intergenic regions (~15%) and in first intron (~15%). In comparison, the hypomethylated DMS induced by a 24 hours treatment with IFN-ɣ are equally localized in promoters and distal intergenic regions (~25% each) together with the first intron and other introns (~20% each). Here, the results show that the hypomethylation induced by IFN-ɣ compared to the control can be located in different areas of the genome but targeting a high amount of gene promoters suggesting differential gene architecture regulation in response to IFN-ɣ. In addition, the time of exposure to IFN-ɣ seems to change the DNA methylation patterns along the genome with an increase in the DMS within the intergenic regions and a decrease in the promoter regions, again suggesting an evolution of the DNA methylation landscape of BV2 cells in response to the treatment.

Additionally, to assess at best the implications of DNA methylation on gene expression, we included the chromHMM method to identify the chromatin states associated with the localization of the DMS. This method consists of the integration of ChIP-seq data from eight histone modifications (H3K27ac, H3K27me3, H3K4me3, H3K4me2, H3K4me1, H3K9me3, H3K9ac and H3K36me3) that, in combination, describe 15 chromatin states used to predict regulatory elements within the genome. Figure 31B, displays the prediction of the DMS induced in the IFN-ɣ condition compared to the control at 12 and 24 hours timepoints. The X-axis displays the direction of the methylated DMS (hypomethylated in IFN-ɣ (Hypo) or hypermethylated in IFN-ɣ (Hyper)) and the Y-axis displays the type of chromatin state predicted according to the chromHMM method. The fold-change of the IFN-ɣ DMS compared to control is indicated by a dot within a color range (deep blue and far red for the most important changes), the log of the P-value is represented by the size of the dot and the significance is highlighted by a dark outer ring. Even though we observe no significant prediction within the DMS induced by the IFN-ɣ compared to the control at the 12 hours timepoint, the highlighted predicted chromatin states at this timepoint become significant at the 24 hours timepoint. Those states are Permissive Transcription (Tr-P), a state of chromatin being not closed nor opened but accessible to TFs; Promoter Active (Pr-A), a state indicating promoters of transcriptionally active genes and Weak Enhancer (En-W), a state of chromatin with less active marks but no repressive marks. Those predicted chromatin states are mostly associated with transcription activation or at least, not transcriptional repression. The DMS induced by IFN-ɣ are gradually located in those states along time of exposure, suggesting a specific mechanism of transcriptional regulation by DNA methylation modifications.

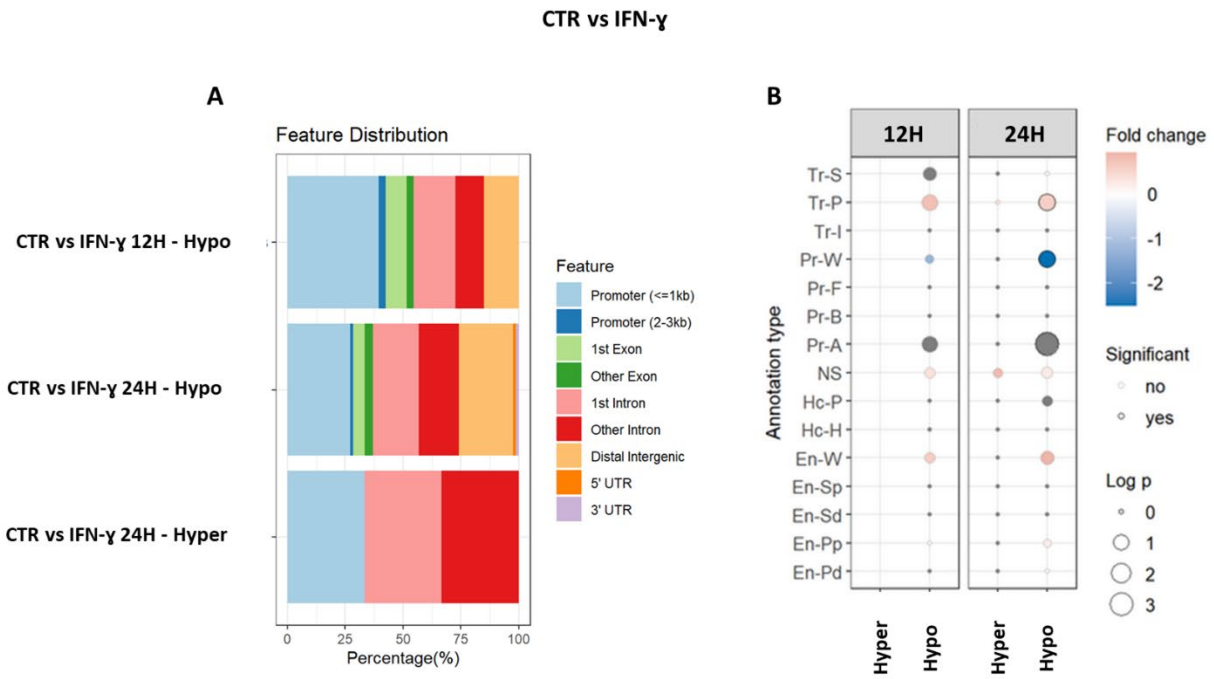

Figure 31. IFN-ɣ induced hypomethylated DMS are mostly located in gene promoters with a chromatin state predicted to be transcriptionally active:

Effect of 10 ng/mL of IFN-ɣ exposure on DNA methylation patterns of BV2 cells treated for 12 and 24 hours, compared to the control untreated treated BV2 cells. The experiment was made on a technical triplicate. Raw data from MethylMouse array were processed by Dr. Reka Toth, using RnBeads 2.16.0, differential methylation was performed using the limma package based on the M-values and the False discovery rate was used to adjust for multiple testing. Functional regions were assigned based on ChromHMM tracks from the forebrain of the mouse, age P0. (A) Representation of the genomic features distribution of the DMS in the IFN-ɣ condition compared to the control (Hypo = Hypomethylated; Hyper = Hypermethylated in IFN-ɣ). Promoter regions were defined as -3kb +/- 0.5 kb from the transcription start site. (B) Representation of the predicted chromatin states associated with the DMS induced by IFN-ɣ treatment compared to control in BV2 cells. The fold change of the IFN-ɣ induced DMS compared to control is indicated by a dot within a color range (deep blue and far red for the most important changes), the log of the P-value is represented by the size of the dot and the significance (Pvalue < 0.05) is highlighted by a dark outer ring. Tr-S: Transcription Strong; Tr-P: Transcription Permissive; Tr-I: Transcription Initiation; Pr-W: Promoter Weak; Pr-F: Promoter Flanking Region; Pr-B: Promoter Bivalent; Pr-A: Promoter Active; NS: No Significant Signal; Hc-P: Heterochromatin Polycomb-associated; Hc-H: Heterochromatin H3K9me3-associated; En-W: Enhancer Weak; En-Sp: Enhancer Strong TSS-proximal; En-Sd: Enhancer Strong TSS-distal; En-Pp: Enhancer Poised TSS-proximal; En-Pd: Enhancer Poised TSS-distal.

Concerning the hypermethylated DMS induced by the IFN-ɣ treatment after a 24 hours exposure, we see that they are equally located in promoters, first intron and other introns (~33% each, A) and that no significant prediction of chromatin state could be found.

In conclusion, Figure 31 shows that the hypomethylation induced by the IFN-ɣ treatment in BV2 cells occurs in a time dependent manner all along the genome with a high proportion in gene promoters, in chromatin states predicted to be associated with active transcription. Those results point out that DNA methylation patterns in transcriptional regulatory elements occurs in response to IFN-ɣ treatment and insinuate a role in gene expression regulation.

1.9. Differentially methylated genes in IFN-ɣ treatment condition are linked to interferon signaling pathways

Finally, to explore whether those IFN-ɣ induced DMS could have an impact on the cellular functioning of the BV2, we conducted a gene set enrichment analysis on the significant DMS located only in the promoters, named differentially methylated genes (DMGs). No results were found for the 12 hours timepoint. Nevertheless, Figure 32 shows the results for the 24 hours timepoint, targeting the reactome (A, for hypermethylated DMGs in IFN-ɣ compared to the control) and the molecular signature database (B, left panel for hypomethylated DMGs, right panel for hypermethylated DMGs).

Concerning the reactome, no enrichment was found for the hypomethylated DMG and one was found for the hypermethylated ones. Indeed, in A, one of the DMG, *Cd81*, hypermethylated in the IFN-ɣ treatment condition is associated with the regulation of the complement cascade, mostly related to promotion of inflammation.

Concerning the molecular signature, both the hypo- and hypermethylated DMS gave significant results. In B, left panel, we also observe that the hypomethylated DMGs in the IFN-ɣ condition are associated with the IFN alpha and gamma's responses. In B, right panel, we observe that the DMGs hypermethylated in IFN-ɣ seems to be linked to the STAT5 inflammatory pathway or the P53, both connected to inflammatory mechanisms in microglia.

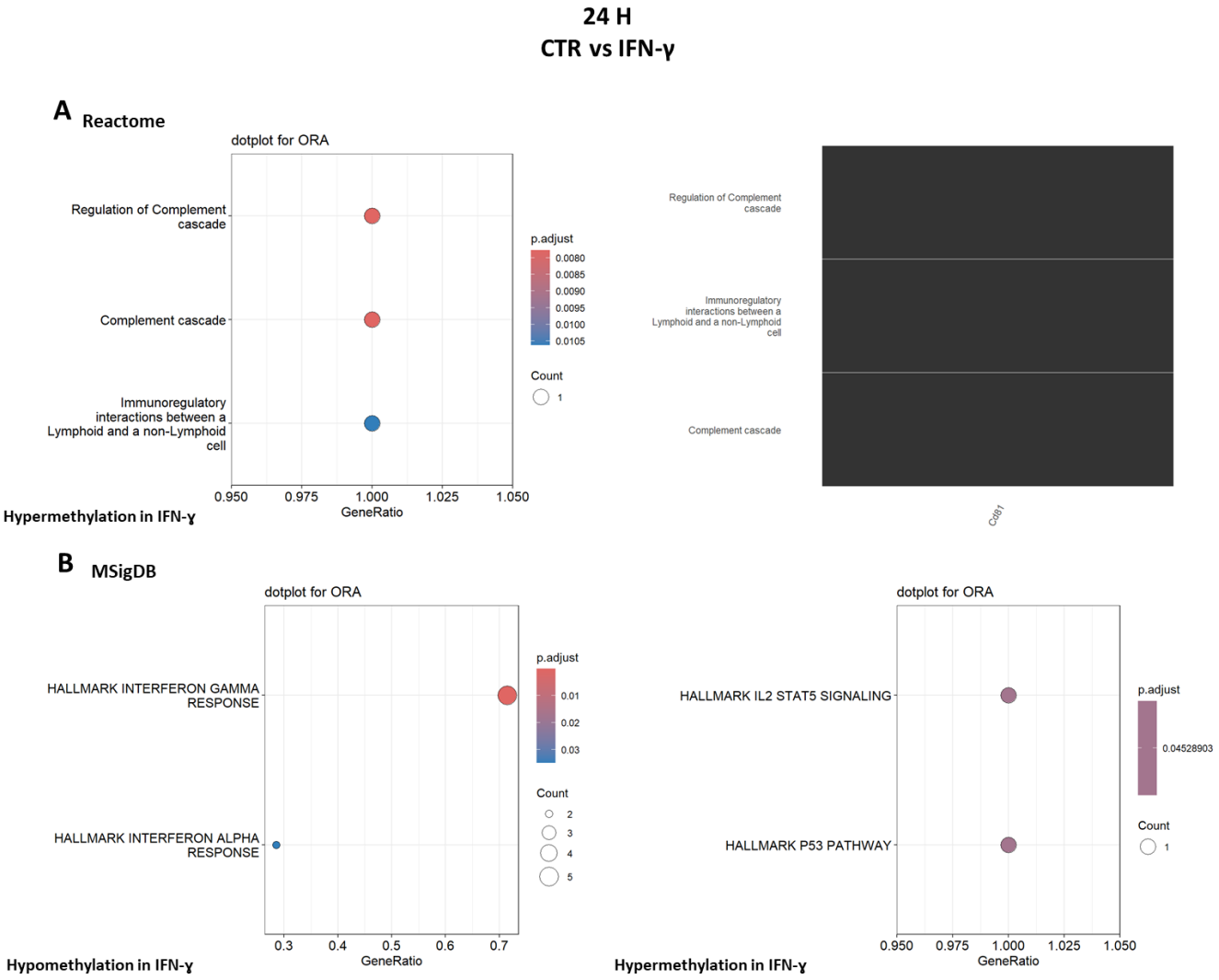

Figure 32. IFN-γ induced promoter hypomethylation is linked to interferon response:

Effect of 10 ng/mL of IFN-γ exposure on DNA methylation patterns of BV2 cells treated for 24 hours, compared to the control untreated BV2 cells. The experiment was made on a technical triplicate. Raw data from MethylMouse arrays were processed by Dr. Reka Toth, using RnBeads 2.16.0, differential methylation was performed using the limma package based on the M-values and the False discovery Rate was used to adjust for multiple testing. Enrichments of the DMS were calculated using a Fisher exact test with all sites as a background with function from the annotatr R package. P-values < 0.05 were indicated as significant. Enrichments of the differentially methylated locis overlapping with promoters were calculated using the clusterProfiler, msigdbr and ReactomePA packages and visualized with the help of the enrichplot package. The dot plot shows the reactome (A) and the molecular signature according to the MSigDB database (B) associated enrichment for the DMS induced in the IFN-γ condition compared to the control after 24 hours. The size of the dots stands for gene counts and the colors from blue (low) to red (high) represent the adjusted P-value.

Those results indicate that the DMGs observed between IFN-ɣ treated and untreated BV2 are all related to inflammation. More precisely, the DMS hypomethylated in promoters of the genes within the IFN-ɣ treatment condition are linked to a response to interferons stimulation and pro-inflammation regulation, suggesting that indeed, DNA methylation could be implicated in the regulation of biological function in IFN-ɣ induced BV2 reactivity.

1.10. Genes differentially expressed in BV2 exposed to 24 hours treatment with IFN-ɣ are associated with DNA hypomethylation

The possible link between the biological functions associated with the DMS rise the question whether the mRNA expression of the DMGs is changed. RNA sequencing experiments were made to observe the top differentially expressed genes (DEGs) in the different treatment conditions to know if they were common to the DMGs.

Figure 33A, displays the 20 top significant DEGs between the IFN-ɣ treated and untreated BV2 at the 24 hours timepoint. On each box plot, the X-axis displays the treatment condition, while the Y-axis shows the normalized counts (log transformed) of the reads overlapping the genomic region corresponding to a specific gene annotated on top of each plot. Each sample is represented by a symbol, blue and red for the untreated (CTR) and IFN-ɣ conditions, respectively. The dots represented the samples from BV2 passage 17, triangles from passage 21 and squares from passage 23.

We observe in Figure 33A, that all twenty top DEGs are upregulated in the IFN-ɣ condition compared to the control.

Amongst them, we can see seven DEGs modestly upregulated IFN-ɣ, *C1qb*, *Cmpk2*, *Aif1*, *Evl*, *Ifit1bl1*, *Ifi3b* and *Ifi47* with an increase normalized log counts ranging from 1 to 2,5 compared to control. Then four DEGs ranging from four to five counts increase, we can observe *Ifit44*, *Gm1965*, *Calhm6* and *Baft2*. Finally, nine highly upregulated in IFN-ɣ condition, ranging from seven to ten increased counts, we find *Gm4951*, *Lyc6a* and *Lyc1*, *Tgtp1*, *Serpina3g* and *Serpina3f*, *Gbp2* and *Gbp4* and *Cxcl9*.

Within those IFN-ɣ upregulated DEGs, we notice *Baft2*, a TF associated with microglial identity master TFs AP-1 and IRF8. Unsurprisingly, we also see eight genes that are IFN-regulated ones and known to be associated with pro-inflammatory reactivity in microglia (*Gm4951*, *Gbp2* and *Gbp4*, *Ifi44* and *Ifi47*, *Ifit1bl1* and *Ifi3b* and *Tgtp1*). Also, and even though, they belong to different biological categories, eight genes upregulated in IFN-ɣ condition are found to be associated with pro-inflammatory phenotype of microglia. The *Aif1* gene coding for the well-known cytoskeleton-associated microglial

marker Iba1 and the actin interacting gene *Evl*, the immunomodulatory ion channel *Calhm6* and kinase *Cmpk2*, the pro-inflammatory chemokine *Cxcl9* and the serine peptidase inhibitors *Serpina3f* and *Serpina3g* and finally, the complement cascade associated *C1qb*. Surprisingly, two DEGs, *Ly6a* and *Ly6c1,* are related to the monocytic lineage. At last, *Gm1965*, a long intergenic non coding RNA has not been related to microglia nor immunity.

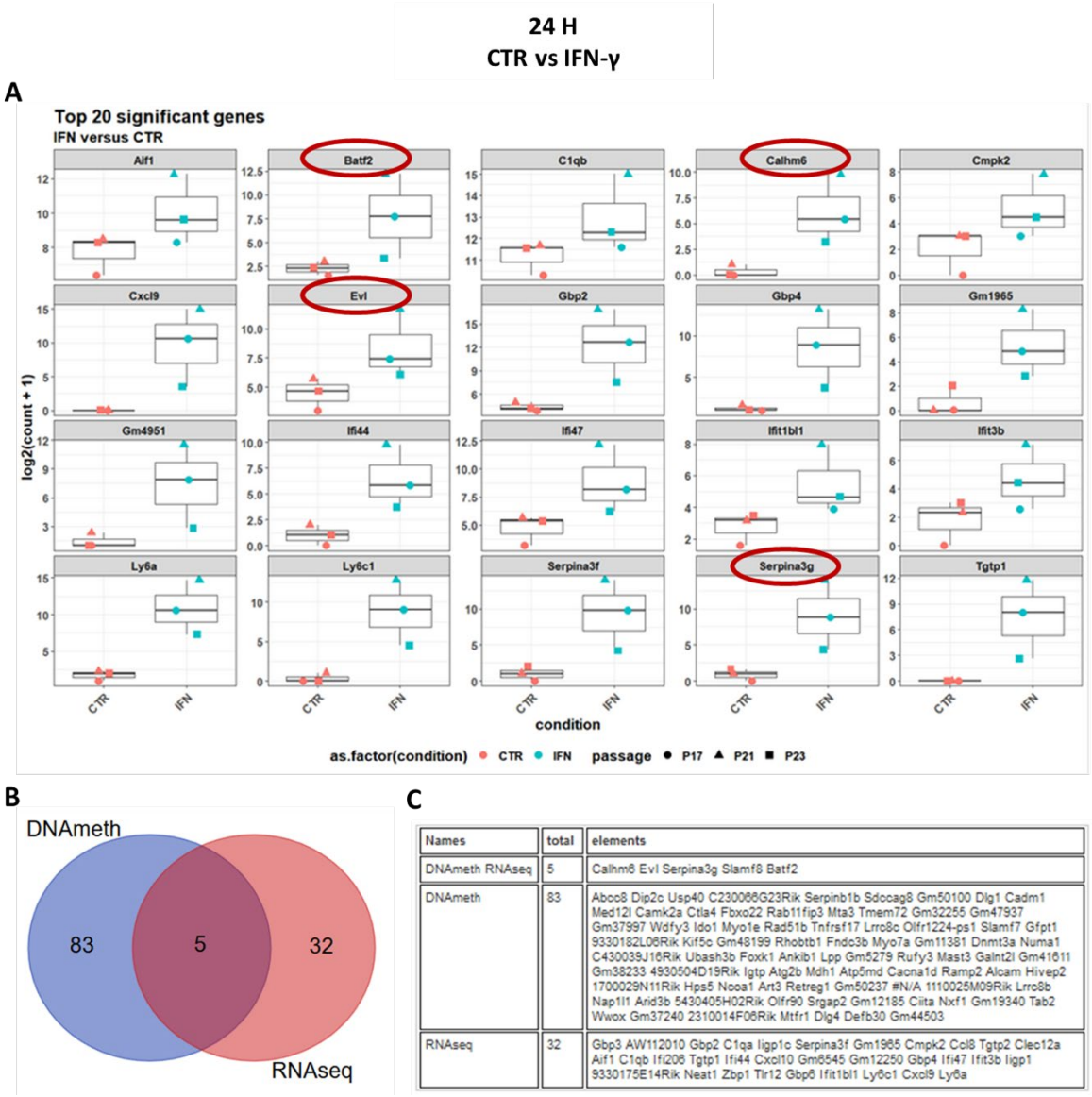

Names	total	elements
DNAmeth RNAseq	5	Calhm6 Evl Serpina3g Slamf8 Batf2
DNAmeth	83	Abcc8 Dip2c Usp40 C230066G23Rik Serpinb1b Sdocag8 Gm50100 Dlg1 Cadm1 Med12l Camk2a Ctla4 Fbxo22 Rab11fip3 Mta3 Tmem72 Gm32255 Gm47937 Gm37997 Wdfy3 Ido1 Myo1e Rad51b Tnfrsf17 Lrrc8c Olfr1224-ps1 Slamf7 Gfpt1 9330182L06Rik Kif5c Gm48199 Rhobtb1 Fndc3b Myo7a Gm11381 Dnmt3a Numa1 C430039J16Rik Ubash3b Foxk1 Ankib1 Lpp Gm5279 Rufy3 Mast3 Galnt2l Gm41611 Gm38233 4930504D19Rik Igtp Atg2b Mdh1 Atp5md Caona1d Ramp2 Alcam Hivep2 1700029N11Rik Hps5 Ncoa1 Art3 Retreg1 Gm50237 #N/A 1110025M09Rik Lrrc8b Nap1l1 Arid3b 5430405H02Rik Olfr90 Srgap2 Gm12185 Ciita Nxf1 Gm19340 Tab2 Wwox Gm37240 2310014F06Rik Mtfr1 Dlg4 Defb30 Gm44503
RNAseq	32	Gbp3 AW112010 Gbp2 C1qa Iigp1c Serpina3f Gm1965 Cmpk2 Ccl8 Tgtp2 Clec12a Aif1 C1qb Ifi206 Tgtp1 Ifi44 Cxcl10 Gm6545 Gm12250 Gbp4 Ifi47 Ifit3b Iigp1 9330175E14Rik Neat1 Zbp1 Tlr12 Gbp6 Ifit1bl1 Ly6c1 Cxcl9 Ly6a

Figure 33. IFN-ɣ induced gene expression is associated with changes in DNA methylation:

Effect of 10 ng/mL of IFN-ɣ exposure on RNA expression (A) and DNA methylation patterns (B, C) of BV2 cells treated for 24 hours, compared to control untreated BV2 cells. (A) RNA sequencing experiment was made on BV2 cells untreated or treated for 24 hours with IFN-ɣ by the LuxGen sequencing platform. The experiment was made on a biological triplicate. Raw data were analyzed using the DESeq2 pipeline. The box plot represents the top 20 DEGs between the IFN-ɣ condition and the control at the 24 hours timepoint. (B, C) Processed differential methylation data from BV2 cells treated or not for 24 hours with IFN-ɣ focusing on the significant differentially methylated sites (FDR adjusted

P-value < 0.05) and processed RNAseq data encompassing all the significant DEGs (FDR adjusted P-value < 0.05) were uploaded into a Venn Bioinformatics application tool (Ghent University).

To try to find a link between gene expression and DNA methylation in IFN-ɣ treated BV2, all the significant DEGs and DMSs were compared and the results, presented in Figure 33B and C, shows that five genes in our study are differentially methylated and differentially expressed. Among those, *Calhm6*, *Evl*, *Serpina3g* and *Baft2* are a part of the twenty more differentially expressed (Figure 33A).

It is worth noting that the amount of significant DMGs is higher than the amount of significant DEGs, highlighting the gap between DNA methylation and gene expression.

Nevertheless, we conclude that a 24 hours exposure to IFN-ɣ leads to the differential methylation and expression of common genes in BV2 cells. To unravel the possible mechanisms between DNA methylation and gene expression of those four genes, methylation data were uploaded into the UCSC genome browser and databases concerning regulatory elements, chromatin accessibility and states were interrogated.

On Figure 34, the UCSC genome browser view for the *Serpina3g* gene is shown, indicating that not a lot of data are available concerning this gene. Indeed, we find that the chromatin state according to the ChromHMM is non significant, and the association between regulatory elements are not known. Nevertheless, we can still note that according to the ATACseq data, the chromatin seems to be in a closed state all along the gene and also, that no CpG island is present. Finally, only an enhancer and a promoter are known to regulate the expression of *Serpina3g*, in the latter, we found localized the probe significantly differentially hypomethylated in the IFN-ɣ condition (cg31053542).

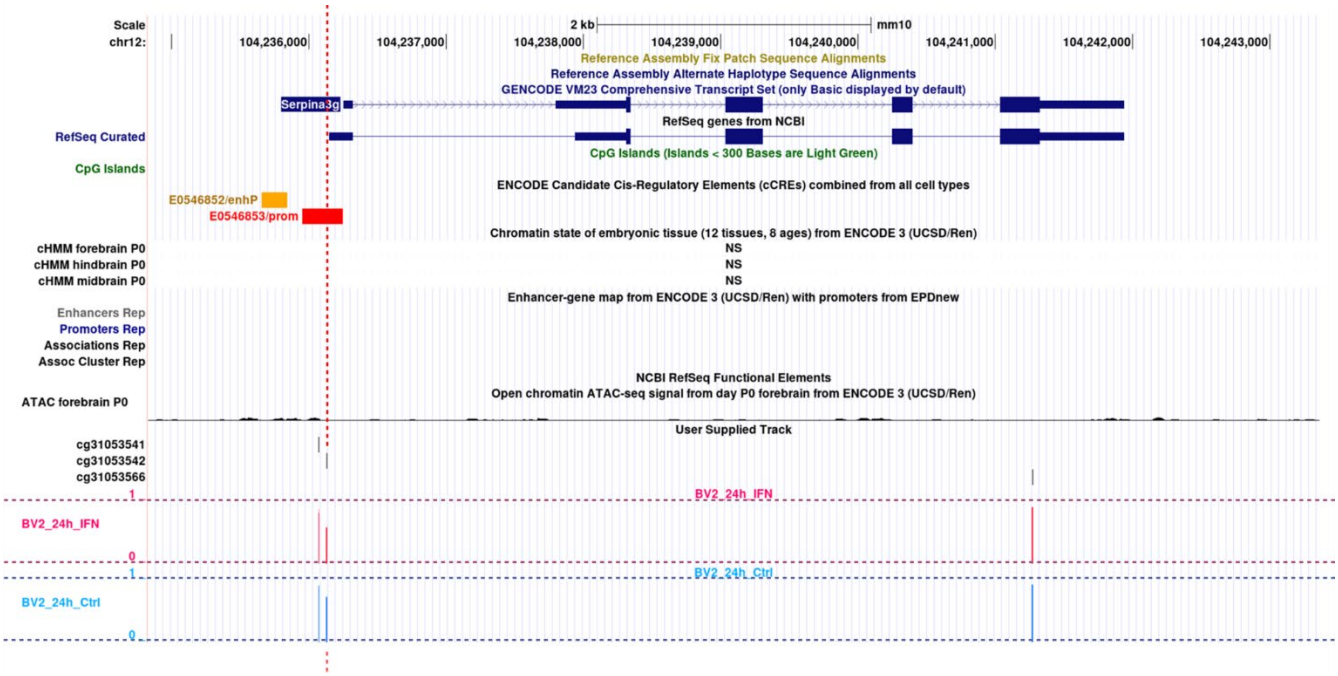

Figure 34. IFN-γ induced upregulation of *Serpina3g* is associated with significant hypomethylation of its promoter:

UCSC Genome Browser view of the *Serpina3g* gene from mouse GRCm38/mm10 genome, including tracks (from top to bottom) for RefSeq gene from NCBI (Annotation release 108.20200622); CpG islands; ENCODE cis-regulatory elements, chromatin states predicted according to the ChIP-seq databases on forebrain, hindbrain and midbrain of P0 mouse pups; enhancers and promoters functional associations, ATAC-seq database on forebrain of P0 mouse pups and Illumina Mouse Methyl probes localization. The last tracks correspond to the sum of the methylation level of the three replicates at each probe site for each condition. The horizontal lines represent the level of methylation from 0 to 1; Light blue: control. Pink: IFN-γ. The vertical red line represents the significantly differentially methylated site in the *Serpina3g* gene.

Without all the data concerning the chromatin states and the interactions between regulatory elements orchestrating the regulation of *Serpina3g* expression, it is difficult to conclude on the implication of DNA methylation. However, as we observe an upregulation of *Serpina3g* expression (Figure 33A) and a hypomethylation of its promoter (Figure 34), we can strongly hypothetize that IFN-γ induced expression of *Serpina3g* in BV2 cells is associated with an underlying control by DNA methylation modulation.

The same profile and the same conclusions can be drawn for *Baft2* gene (Annexe 34).

On Figure 35, the UCSC genome browser view for the *Calhm6* gene is showing that more data are available concerning this gene. Indeed, the probe exhibiting the significant methylation changes in the IFN-ɣ condition is characterized by a strong hypomethylation compared to control. In addition, we can see that this probe aligns with a promoter with a chromatin state predicted to be weak, indicating that the chromatin at this location displays less active histone marks but no repressive ones.

In that regard, it is also interesting that the ATACseq tracks shows no peaks at this location, confirming the closed state of the chromatin. Finally, we find that the probe is not located in a CpG island and that the other probes are not significantly different between control and IFN-ɣ condition, questioning the real impact of a single site DNA methylation modulation on *Calhm6* expression.

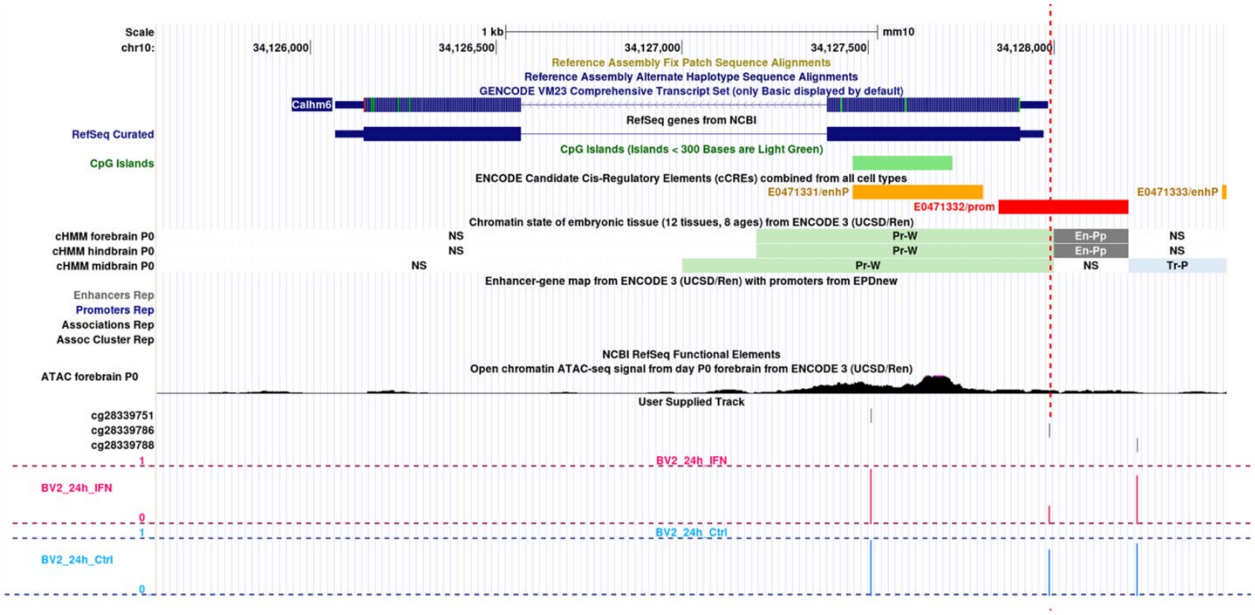

Figure 35. Upregulation of *Calhm6* expression is associated with hypomethylation in its promoter with a chromatin state predicted to be weak:

UCSC Genome Browser view of the *Calhm6* gene from mouse GRCm38/mm10 genome, including tracks (from top to bottom) for RefSeq gene from NCBI (Annotation release 108.20200622); CpG islands; ENCODE cis-regulatory elements, chromatin states predicted according to the ChIP-seq databases on forebrain, hindbrain and midbrain of P0 mouse pups; enhancers and promoters functional associations, ATAC-seq database on forebrain of P0 mouse pups and Illumina Mouse Methyl probes localization. The last tracks correspond to the sum of the methylation level of the three replicates at each probe site for each condition. The horizontal lines represent the level of methylation from 0 to 1; Light blue: control. Pink: IFN-ɣ. The vertical red line represents the significantly differentially methylated site in the *Calhm6* gene.

Even though Figure 34 displays more data concerning the *Calhm6* gene architecture and even if those data were arising from a matching BV2 dataset, it would be difficult to draw a straightforward conclusion about the effect of DNA methylation on *Calhm6* expression. Nevertheless, as we see an upregulation of *Calhm6* expression (Figure 33A) and a significant hypomethylation of its promoter (Figure 35), it is still plausible to hypothesize that a single CpG site DNA methylation change could lead to gene expression modulation under the influence of a 24 hours IFN-ɣ treatment.

A similar profile, with a significant IFN-ɣ induced hypomethylation of CpG site located in a promoter with a chromatin state predicted to be transcription permissive can be observed for *Evl* gene (Annexe 35).

In conclusion, we observe that BV2 microglial cells treated with IFN-ɣ for 24 hours, exhibiting differential transcriptomic and morphological phenotypes, display significant changes in DNA methylation patterns related to the biological processes of IFN responses, suggesting a role of DNA methylation modifications in microglial reactivity to IFNs. In addition, we observe that the hypomethylation of transcriptional regulatory elements are linked to upregulation of those genes under the IFN-ɣ treatment. Despite the lack of causal mechanisms between the two events, those results strongly suggest a mechanistical role of DNA methylation in gene expression regulation.

Further research is needed concerning the overall chromatin accessibility, the histones modifications and the interactions between proximal and distal regulatory elements present on those genes to understand the real biological meaning of DNA methylation in response to IFN-ɣ treatment of BV2 cells.

1.11. BV2 cells treated with LPS display gradual hypomethylation increasing with time of exposure

Figure 36 displays different features of the comparisons of the DMS between BV2 treated with LPS for 12 and 24 hours and the respective untreated control.

First of all, Figure 36A, displays the PCA results of LPS (purple dots) and untreated (orange dots) BV2 samples (technical triplicates) at the 12 hours timepoint. What we can observe on Figure 36A, is a segregation between the LPS treated samples and the untreated samples without a superposition of replicates, meaning that despite a variability amongst the replicates, a 12 hours treatment with LPS

(means PC1: 2.9, PC2: - 0.3) leads to variability in DNA methylation compared to the control (means PC1: - 1.0, PC2: - 0.7). We can draw the same conclusion from Figure 36B, displaying the PCA results of LPS (purple triangles) and untreated (orange triangles) BV2 samples (technical triplicates) at the 24 hours timepoint. Indeed, we also observe a segregation between the LPS treated samples (means PC1: 2.9, PC2 : - 0.3) and the untreated samples (means PC1: - 5.8, PC2: - 3.1) without a superposition of replicates.

Secondly presented in Figure 36, volcano plots (B and E) displaying on the X-axis the mean difference between the M-value of the DMS from the control condition and the M-value of those DMS from the LPS, both at the 12 hours (B) and 24 hours (E) timepoints. The Y-axis displays the corrected P-value (less than 10% probability to make a false discovery) for each DMS M-value, the horizontal line corresponding to the FDR threshold. Each dot represents a DMS, with statistical significance when colored in green or red, with direction towards hypo- and hypermethylation, respectively.

We observe in Figure 36B, that 52 DMS exhibit a significant positive difference between the control and the LPS condition with a mean methylation difference threshold ranging from 0.1 and 0.6. The threshold being set as +/- 0.1, 5 DMS with a significant negative difference above the threshold and 17 DMS with a significant positive difference below the threshold were excluded. Nevertheless, we can observe with confidence that 52 CpGs sites are hypomethylated in the LPS treated BV2 compared to the untreated BV2 at the 12 hours timepoint. In Figure 36E, we can see that 139 DMS are exhibiting a significant positive difference between the control and the LPS condition, with a mean methylation difference threshold ranging from 0.1 and 0.6. It is worth noting that nine DMS with a significant negative difference above the threshold and 55 DMS with a significant positive difference below the threshold were excluded.

While the IFN-ɣ condition was characterized by a high number of small amplitude DNA methylation changes at 12 hours and a low number of high amplitude DNA methylation changes, the LPS condition exhibits a ratio between low and high amplitude DNA methylation changes that remain the same, but the amount of DMS increases along time of exposure.

Similarly to the IFN-ɣ condition, we can also note that the significant high amplitude DNA methylation changes in both time of exposure are leading towards hypomethylation.

Finally, on Figure 36C and F, the significant DMS are displayed in the rows of a heatmap with each column representing the clustering of the mean M-values of each site according to treatment (Tt) and timepoint (Tp). The mean M-value is represented as color ranging from a deep blue representing unmethylated site with a mean M-value of 0, to a dark red representing fully methylated site with a mean M-value of 1.

On Figure 36C, 52 DMS are more methylated in the control group than in the LPS group at 12 hours timepoint. We also observe that the control group at 12 hours displays some variability on the methylation level of those DMS whereas the LPS group at 12 hours are clustered together, exhibiting homogeneity in methylation levels for those DMS. Finally, it is worth noting that, while there is no distinct methylation signature for those conditions, a cluster appears for those DMS regrouping the LPS conditions at the timepoints 12 and 24 hours with a gradual decrease in β-values along timepoints. Interestingly, the six hours timepoint of the LPS condition, while not being clustered with the other timepoints, is the direct neighbor of the 12 hours LPS timepoint. All those observations suggest gradual and homogenous DNA methylation modifications for those probes in response to LPS treatment in BV2 cells, in a time exposure dependent manner.

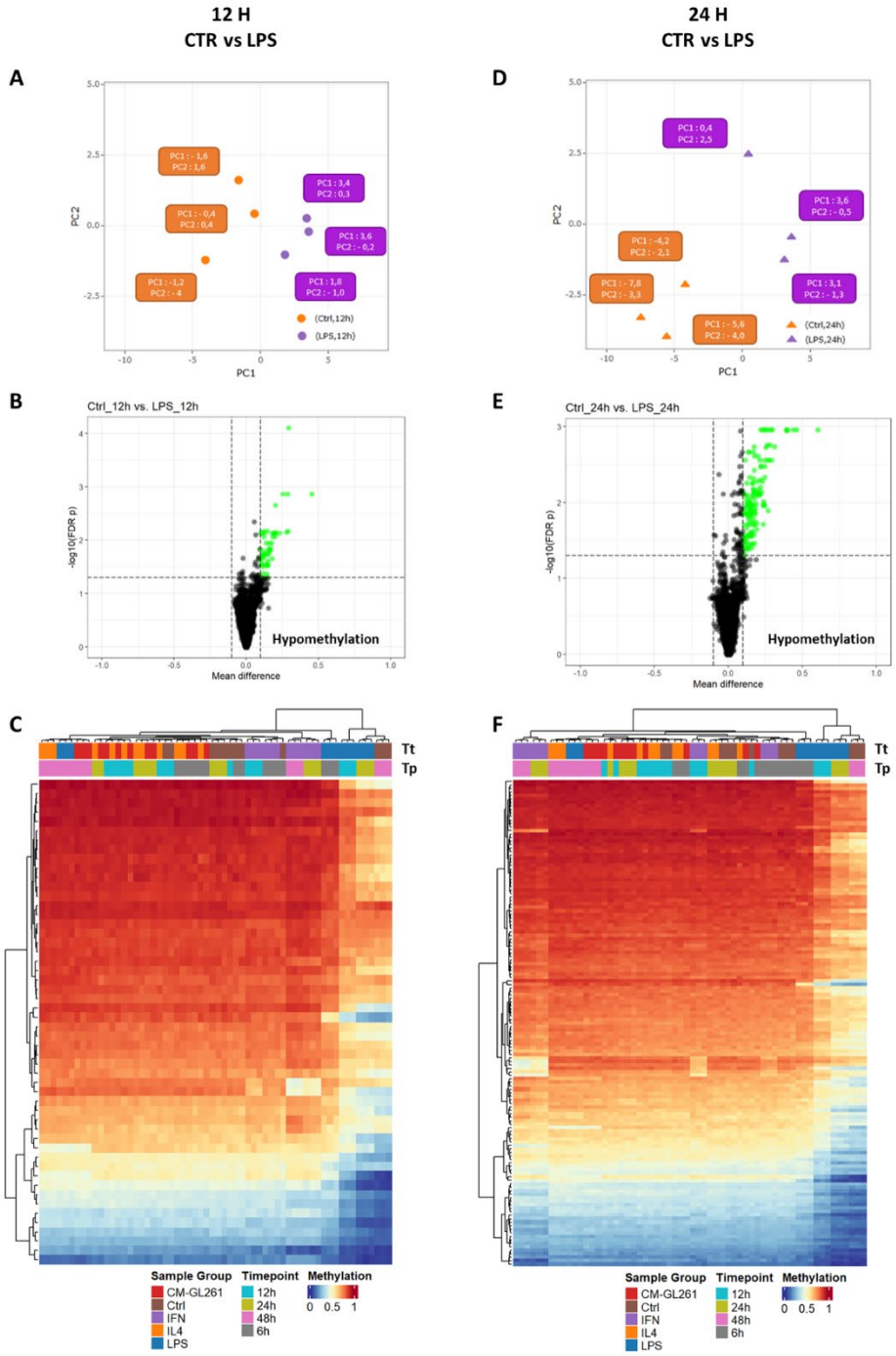

Figure 36. BV2 cells exposed to LPS display significant hypomethylated sites:

Effect of 10 ng/mL of LPS exposure on DNA methylation patterns of BV2 cells treated for 12 and 24 hours, compared to the untreated control BV2 cells. The experiment was made on a technical triplicate. Raw data from MethylMouse array were processed by Dr. Reka Toth, using RnBeads 2.16.0, differential methylation was performed using the limma package based on the M-values and the False Discovery Rate was used to adjust for multiple testing. Left panel: 12 hours exposure to LPS. Right panel: 24 hours exposure to LPS. (A, D) PCA plots of DNA methylation profiles based on all CpG sites (after filtering; see Materials and Methods); LPS: purple and control: orange; Time of exposure to LPS: 12 hours: dots; 24 hours: triangles. (B, E) Volcano plots displaying mean DNA methylation differences between IFN-ɣ

and control untreated BV2 at all filtered CpG sites. The vertical lines represent the 0.1 mean M-values difference boundary while the horizontal line represent the statistical significance boundary ($P < 0.05$). The significant DMS appear in green and red, hypo- and hypermethylated in LPS condition compared to control, respectively. (C, F) Hierarchical clustering was performed and represented as a heatmap showing the mean methylation levels of the DMS between the LPS and the control. Columns represent the samples relative to treatment (Tt) and timepoint (Tp), while the rows represent the DMS. The methylation levels are illustrated as colors ranging from deep blue (M-Value = 0, unmethylated) to deep red (M-Value = 1, fully methylated).

Figure 36F displays similar results after a 24 hours exposure. Indeed, once again the significant DMS are more methylated in the control group than in the LPS group at 24 hours timepoint. In addition, the cluster formed of the LPS condition at 12 and 24 hours in Figure 36C also appears for those DMS, while the six hours timepoint clusters next to it, showing again a similarity in the response of BV2 cell DNA methylation to the LPS treatment over time.

In addition, 46 DMS are common between the 12 and 24 hours LPS conditions (Annexe 36; only five DMS are specific of the 12 hours timepoint), confirming the homogenous response in terms of DNA methylation patterns reorganization in response to LPS exposure in BV2 cells.

Taken together, Figure 36 shows that BV2 exposed to 12 and 24 hours of LPS exhibits significant gradual changes in DNA methylation patterns mostly towards hypomethylation.

1.12. DNA hypomethylation induced by LPS is localized in transcriptional regulatory elements predicted to be associated with active chromatin state

To explore the biological meaning of methylation that is differently induced by LPS treatment in BV2 cells, we use computational analysis of the data to localize the DMS within the genome to identify regulatory elements that might have been modified by DNA methylation. For instance, Figure 37A shows the genomic annotation associated to the DMS in LPS condition compared to control at 12 and 24 hours timepoints. The X-axis displays the percentage of each genomic feature associated with the DMS. Promoter is defined as – 3 kb to + 0.5 kb from the TSS.

Figure 37A shows that the hypomethylated DMS induced in LPS condition at the 12 hours timepoint are mostly located within introns others than the first one (~30%). In addition, DMS are found to a lower degree in distal intergenic regions (~20%) and in first intron (~1%). After a 24 hours exposure to

LPS, the hypomethylated DMS induced are still mainly located in other introns (~30%) but we observe an increase in DMS located in promoters (~20%) and in distal intergenic regions (~25%).

Here, the results show that the hypomethylation induced by LPS compared to the control can be located in different areas of the genome. Compared to the IFN-ɣ that was leading to changes mostly in gene promoters, the LPS exposure seems to induce most of its DNA methylation changes in introns, suggesting differential gene architecture regulation in response to different treatments.

In addition, the time of exposure to LPS seems to change the DNA methylation patterns along the genome with an increase in the DMS within the promoters and a decrease in the distal intergenic regions, again suggesting an evolution of the DNA methylation landscape of BV2 cells in response to the LPS treatment.

Additionally, to assess at best the implication of DNA methylation on gene expression, we included the chromHMM method to identify the chromatin states associated with the localization of the DMS. Figure 37B displays the prediction of the chromatin states related to the DMS induced in the LPS condition compared to the control at the 12 and 24 hours timepoints. The X-axis displays the direction of the methylated DMS (hypomethylated in LPS (Hypo)) and the Y-axis displays the type of chromatin stated predicted according to the chromHMM method. The fold change of the LPS DMS compared to control is indicated by a dot within a color range (deep blue and far red for the most important changes), the log of the P-value is represented by the size of the dot and the significance is highlighted by a dark outer ring.

Significant predictions have been found within the DMS induced by the LPS compared to the control at the 12 hours timepoint. Those states are Permissive Transcription (Tr-P), a state of chromatin being neither closed nor opened but accessible to TFs; Promoter Active (Pr-A), a state indicating promoters of transcriptionally active genes and Promoter Weak (Pr-W), a state of chromatin with less active marks but no repressive marks. Interestingly, after 24 hours of treatment with LPS, similar predictions were obtained with even higher fold changes and significance. In addition, also the state Enhancer Weak (En-W) became significant, suggesting gradual DNA methylation changes of the same regulatory elements and chromatin states over time of treatment with LPS.

We find that those predicted chromatin states are mostly associated with transcription activation or at least, not with transcriptional repression and that the DMS induced by LPS are gradually located in those states along time of exposure, suggesting a specific mechanism of transcriptional regulation by DNA methylation modifications.

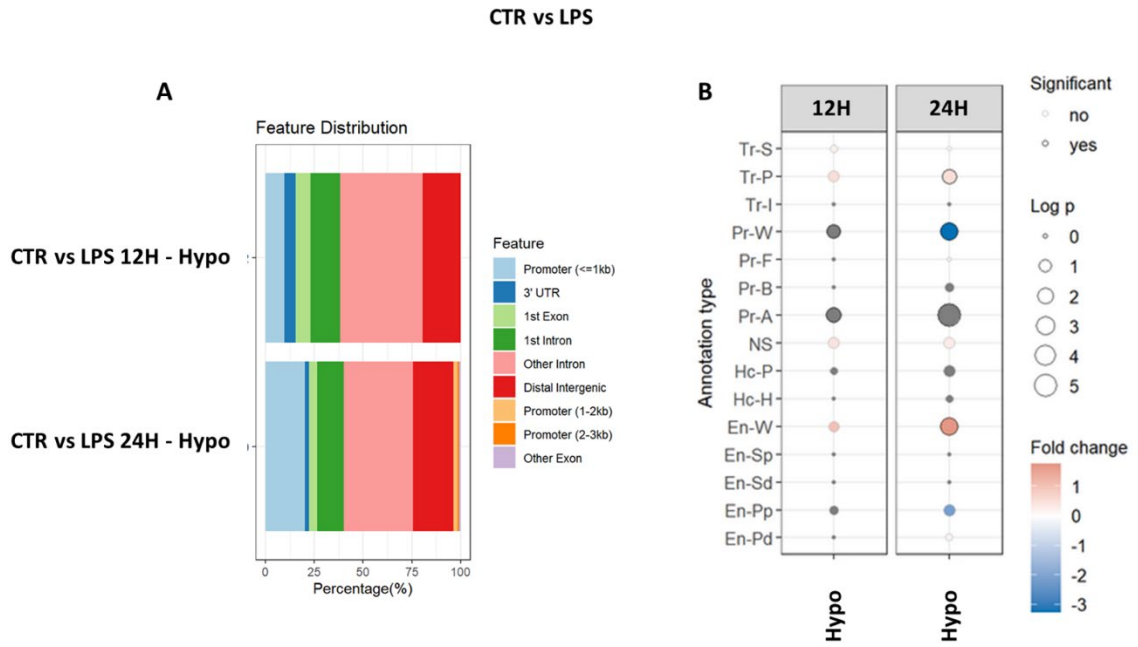

Figure 37. Significant hypomethylation induced by LPS treatment is found in promoters with a chromatin state predicted to be active:

Effect of 10 ng/mL of LPS exposure on DNA methylation patterns of BV2 cells treated for 12 and 24 hours, compared to the control untreated treated BV2 cells. The experiment was made on a technical triplicate. Raw data from MethylMouse array were processed by Dr. Reka Toth, using RnBeads 2.16.0, differential methylation was performed using the limma package based on the M-values and the False discovery rate was used to adjust for multiple testing. Functional regions were assigned based on ChromHMM tracks from the forebrain of the mouse, age P0. (A) Representation of the genomic features distribution of the DMS in the LPS condition compared to the control (Hypo = Hypomethylated in LPS). Promoter regions were defined as -3kb +/- 0.5 kb from the transcription start site. (B) Representation of the predicted chromatin states associated with the DMS induced by LPS treatment compared to control in BV2 cells. The fold change of the LPS induced DMS compared to control is indicated by a dot within a color range (deep blue and far red for the most important changes), the log of the P-value is represented by the size of the dot and the significance (P-value < 0.05) is highlighted by a dark outer ring. Tr-S: Transcription Strong; Tr-P: Transcription Permissive; Tr-I: Transcription Initiation; Pr-W: Promoter Weak; Pr-F: Promoter Flanking Region; Pr-B: Promoter Bivalent; Pr-A: Promoter Active; NS: No Significant Signal; Hc-P: Heterochromatin Polycomb-associated; Hc-H: Heterochromatin H3K9me3-associated; En-W: Enhancer Weak; En-Sp: Enhancer Strong TSS-proximal; En-Sd: Enhancer Strong TSS-distal; En-Pp: Enhancer Poised TSS-proximal; En-Pd: Enhancer Poised TSS-distal.

In conclusion, Figure 37 shows that the hypomethylation induced by the LPS treatment in BV2 cells occurs in a time dependent manner all along the genome with a low proportion in gene promoters however exhibiting chromatin states predicted to be associated with active transcription. Those results point out that DNA methylation patterns in transcriptional regulatory elements occurs in response to LPS treatment and insinuate a role in gene expression regulation.

1.13. Differentially methylated genes in LPS treatment condition are linked to the NFκB-mediated TNF signaling pathway.

Finally, to explore whether those LPS induced DMS could have an impact on the cellular functioning of the BV2, we conducted a gene set enrichment analysis on the significant DMS located only in the promoters, and corresponding to DMGs. Figure 38A, targeting the reactome, demonstrates that for the 12 hours timepoint, one hypomethylated DMG, *Tnfaip3*, is linked to the TNF signaling pathway.

Figure 38C shows that this pathway is strengthened after 24 hours of LPS exposure with three associated DMGs (*Tnfaip3*, *Tab2* and *Traf1*) and interestingly, one other DMG, *Tnip1*, is associated to *Tnfaip3* regulation (Annexe 37) , revealing a gradual and homogenous DNA methylation response to the LPS treatment in BV2 cells. In addition, the TNF signaling associated with pro-inflammation, is known to be activated in response to LPS in microglia.

The other gene ontology showed by Figure 38C, is the chemokine response with association to *Cxcl2* and *Cxcl11*, coding for pro-inflammatory chemokines known to be secreted by LPS exposed microglia. Those results suggest an impact of DNA hypomethylation modification under the influence of LPS treatment associated with the switch in signaling pathways occurring in microglial reactivity phenomenom.

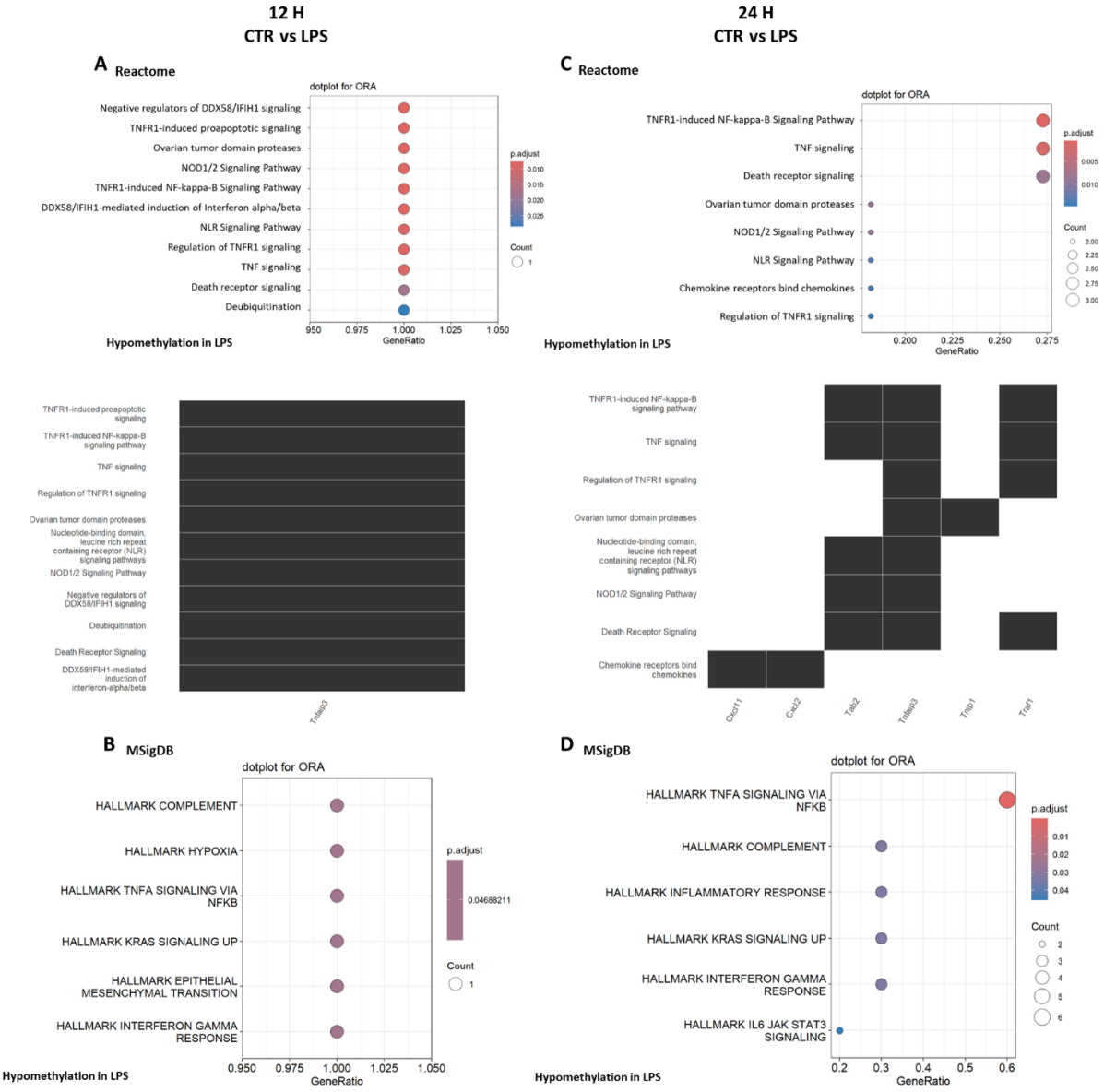

Figure 38. Differentially methylated genes induced by LPS treatment are linked to TNFα signaling *via* NFκB:

Effect of 10 ng/mL of LPS exposure on DNA methylation patterns of BV2 cells treated for 12 and 24 hours, compared to the control untreated BV2 cells. The experiment was made on a technical triplicate. Raw data from MethylMouse array were processed by Dr. Reka Toth, using RnBeads 2.16.0, differential methylation was performed using the limma package based on the M-values and the False discovery Rate was used to adjust for multiple testing. Enrichment of the DMS were calculated using a Fisher exact test with all sites as a background and function from the annotatr R package. P-values < 0.05 were indicated as significant. Enrichment of the differentially methylated locis overlapping with promoters were calculated using the clusterProfiler, msigdbr and ReactomePA packages and visualized with the help of the enrichplot package. The dot plot shows the reactome (A and C) and the molecular signature according to the MSigDB database (B and D) associated enrichment for the DMS induced in the LPS condition compared to the control after 12 hours (left panel) and 24 hours (right panel). The

size of the dots stands for gene counts and the colors from blue (low) to red (high) represent the adjusted P-value.

Concerning the molecular signature, Figure 38B and D show that the LPS induced hypomethylated DMGs are again associated to the TNF pathway, linking TNFα responses to NFκB signaling, a well known pathway in microglia reactivity. We also find that this response is amplified with increased time of exposure, suggesting the gradual activation of biological cascades in response to LPS in BV2 cells.

Those results mean that the DMGs observed between LPS treated and untreated BV2 are all related to inflammation. More precisely, the DMS hypomethylated in gene promoters within the LPS treatment condition are linked to the TNF response and pro-inflammation regulation *via* NFκB, known to be involved in microglia induced LPS reactivity and suggesting that DNA methylation could be implicated in the underlying mechanisms.

1.14. Genes differentially expressed in BV2 exposed to a 24 hours treatment with LPS are associated with DNA hypomethylation

The possible link between the biological functions associated with the DMS rise the question whether the mRNA expression of the gene differentially methylated is changed. RNA sequencing experiments were made to observe the top DEGs in the different treatment conditions to know if they were common to the DMGs.

Figure 39A, displays the 20 top significant DEGs between the LPS treated and untreated BV2 at the 24 hours timepoint. On each box plot, the X-axis displays the treatment condition, while the Y-axis shows the normalized counts (log transformed) of the read overlapping the genomic region corresponding to a specific gene annotated on top of each plot. Each sample is represented by a symbol, red and blue for the untreated (CTR) and LPS conditions, respectively. The dots represented the samples from BV2 passage 17, triangles from passage 21 and squares from passage 23.

We observe in Figure 39A, that all twenty top DEGs are upregulated in the LPS condition compared to the control.

Amongst them, we find eight DEGs modestly upregulated LPS, *Ppfibp2*, *Pilrb2*, *Gpr84*, *CCl7*, *Cmpk2*, *Gm13571, Ifit1b1* and *Hp* with an increase normalized log counts ranging from two to five compared

to control. Then nine DEGs ranging from five to eight counts increase, we can observe *Clec4e*, *Gm19026*, *Ifit3b, Il6, Marco*, *Slc39a4, Traf1, Fpr2* and *H2M2*. Finally, three highly upregulated in LPS condition, ranging from 8 to 13 increased counts, we find *Saa3*, *Lcn2* and *Ccl5*.

Within those LPS upregulated DEGs, we observe eleven genes belonging to different biological categories but that are known to be associated with pro-inflammatory reactivity in microglia. Indeed, we find the *Ccl5 and Ccl7* genes coding for pro-inflammatory chemokines and the *Il6* coding for the pro-inflammatory CK IL-6. In addition, there are the immunomodulatory kinase *Cmpk2*, the cytoskeleton associated *Marco* and the receptors coding *Clec4e* and *Gpr84*. And finally, the INF regulated genes *Ifi1b1* and *Ifit3b*, the TNF associated *Traf1* and the lipoprotein associated *Saa3*.

Very interestingly, two DEGs, *Frp2* and *Hp,* are related to the resolution of inflammation in microglial cells, suggesting a potential negative feedback mechanisms to balance the LPS induced inflammatory reactivity.

In addition, some of the DEGs upregulated in response to the LPS exposure have not been related to microglia but to the control of immunity in other cells, such as *H2M2* related to the HMC class II molecules, transporter protein coding *Slc394a* and immunoglobulin-like associated receptor coding *Pilrb2*. Finally, *Pplibp2*, *Gm13571* and *Gm19026* have not been related to microglia nor immunity.

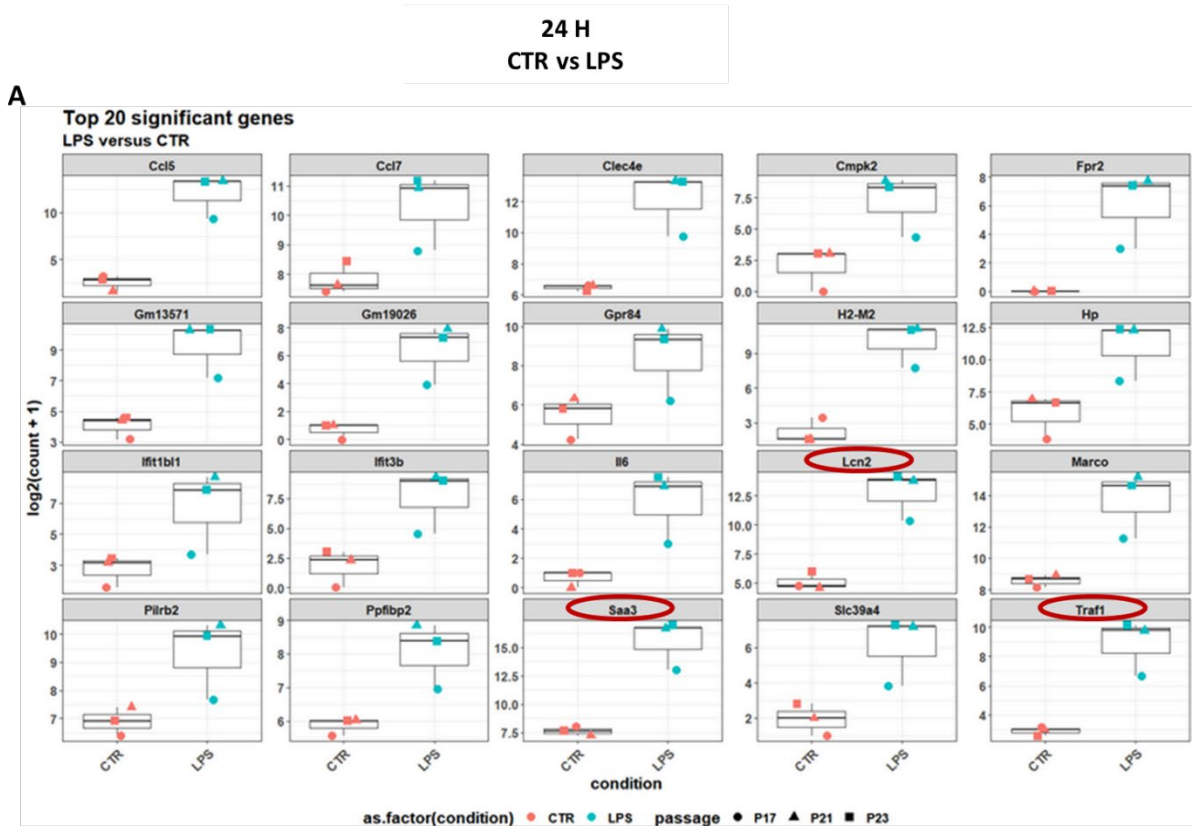

B

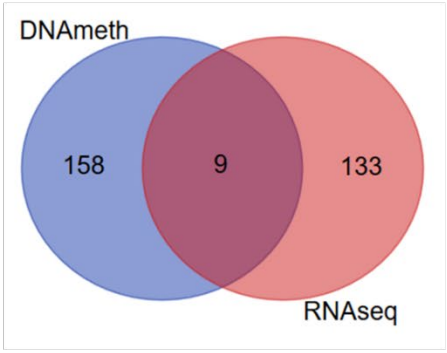

C

Names	total	elements
DNAmeth RNAseq	9	Konf1 Rab11fip1 Lcn2 Tnip1 Il20rb Saa3 Cxcl2 Traf1 Gm32089
DNAmeth	158	Nus1 Limk2 Gm15964 Hmg20a Foxp1 Nars2 Gm22087 Gm38304 Gm47922 Gm37852 Sema4a Cfb Mir7688 Pdia4 Zfyve26 Adamts10 Gm24803 Atg2b Hcar2 Nfia Speoc1 Ank2 Kat6a Tns1 Abr Cdc14a Art3 Retreg1 Cd2ap Tmem44 Gm29243 Diaph3 Lrp1 Sowahc Prkch Mirt2 Dtx2 Gm25888 Sox4 Ncoa4 Adamts14 Arid5b Sdocag8 Rfx8 Tent4b Onecut1 Gm45253 Mtap Supt3 Nrp2 Naip1 Hpn Eml2 Adarb1 Gm41148 Pde4b Gm14051 Itpr1 Rnf145 Ston2 Itpk1 Zdhhc6 Gm43724 Dnal4 Sbno2 Gng12 Tanc1 Ifitm1 Gas7 Pknox1 Clec16a Mdm2 Gm37336 Trappc9 Tab2 Ucp3 Wdr48 Wdr11 Bcat2 Myo10 5430437J10Rik Bcl2l1 Gm34276 Rims3 9330182L06Rik Fam214a Neurod1 Wasf2 Zeb2 Fndc3b Stim2 Cd9 Sh3bp4 Gm16675 4930402H24Rik Gm11200 Gm29266 Cfap77 Crybb1 Adamtsl4 D630003M21Rik Slc25a18 Myl4 Gm37872 Pou4f1 Scarb1 Cox6c Eif1a Tekt3 5430405H02Rik Junos Gm11973 Wwox Ltbp2 9530052E02Rik Trcg1 Nphp1 Dennd2a Arhgdib Rad51b Gm12596 Smad7 Pcid2 Rab10 Myom1 Tnfaip3 Rxra Dock10 Ikbkb 4930543E12Rik C430039J16Rik St6gal1 Inpp5f Cd300c2 Slc10a6 Extl3 Serpina3g Rnf157 Gm2349 Mthfd1l Mefv Atp10a Tnfrsf9 Fbxl13 Pparg Bend4 #N/A Slc37a1 Sema4d 1700066B17Rik Tg Rnf10 Fam49a Mob3b Vash1 Gm36913 Atxn1 Spi1
RNAseq	133	Tarm1 Mx2 Id3 Ms4a6c Ets2 Osbpl3 Icosl Igsf6 6530402F18Rik Maff Aoah Irf9 Cd302 Lilrb4b Slc7a11 Marco Cybb Ifit3 Ifi44 Pou2f2 Pilrb1 Ccl9 Slc15a3 Rsad2 Ndrg1 H2-K2 Oas1a Plpp1 Slc39a4 4930438A08Rik Cleo4n Slfn5 Ifit1bl1 Filip1l Gm13571 Gm20658 Slpi Tlr2 Ptges Nfkb1 Tnfrsf8 Ccl7 Cyria Ppfibp2 Ccl4 Ccl5 Gm19026 Ddit3 Rnf149 Gm41724 Zfp933 Lrrc25 Acod1 Hp Sgms2 Oas1b Apol9a Mcoln2 Gpr84 Nlrp3 Serpine1 Gbp2 Fpr2 Arhgap22 Bcl2a1d Treml4 Pilrb2 Milr1 Clec4e Siglece Pla2g2d Nfkb2 Vnn3 Adgb Zfp811 Irf7 Irak3 Calcrl Zc3h12a Cyb5a Il6 Ell2 Oas1g Hdc Pilra Ifit3b H2-M2 Il1b Marcksl1 Cd300e Ifit1 Gm49774 Oas2 Bbln Isg15 Slc49a3 Creg2 Gbp3 Trpc4 AW112010 Ppp1r3b Tnip3 Il1a Slc8a12 Cflar Msr1 Cmpk2 Lpcat2 Rtn2 Ebi3 Apol9b Fyb Adgre1 Gm16712 Rtp4 Pde8b Wfdc17 Aqp3 Ntng2 Nfkbiz Nupr1 Cxcl10 Psmd10 Cfap251 Acsl5 Slc11a2 Ifit1bl2 Gm20559 Ly6i Gm49254 Slc28a4 Loxl2 Slfn4

Figure 39. LPS induced gene expression is linked to DNA methylation reorganization:

Effect of 10 ng/mL of LPS exposure on RNA expression (A) and DNA methylation patterns (B, C) of BV2 cells treated for 24 hours, compared to control untreated BV2 cells. (A) RNA sequencing experiment was made on BV2 cells untreated or treated for 24 hours with IFN-ɣ by the LuxGen sequencing platform. The experiment was made on a biological triplicate. Raw data were analyzed using the DESeq2 pipeline. The box plot represents the top 20 DEGs between the LPS condition and the control at the 24 hours timepoint. (B, C) Processed differential methylation data from BV2 cells treated or not for 24 hours with LPS focusing on the significant differentially methylated sites (FDR adjusted P-value < 0.05) and

processed RNAseq data encompassing all the significant DEGs (FDR adjusted P-value < 0.05) were uploaded into a Venn Bioinformatics application tool (Ghent University).

To try to find a link between gene expression and DNA methylation in LPS treated BV2, all the significant DEGs and DMSs were compared and the results, presented in Figure 39B and C, shows that nine genes in our study are differentially methylated and differentially expressed. Along those, *Lcn2*, *Saa3* and *Traf1* are a part of the twenty more differentially expressed (Figure 39A).

We can conclude from Figure 39 that a 24 hours exposure to LPS leads to the differential methylation and expression of common genes in BV2 cells. To unravel the possible mechanisms between DNA methylation and gene expression of those three genes, methylation data were uploaded into the UCSC genome browser and databases concerning regulatory elements, chromatin accessibility and states were interrogated.

On Figure 40, UCSC genome browser view for the *Traf1* gene shows that the probe exhibiting the significant methylation changes in the LPS condition (cg38274290) is characterized by a strong hypomethylation compared to control. In addition, we find that this probe aligns with a promoter with a chromatin state predicted to be associated to permissive transcription, meaning that the chromatin at this location is quiescent, displaying low level of histone marks and a closed conformation. It actually aligns with the ATACseq tracks showing no peak at this location, confirming the inactive state of the chromatin. Finally, we notice that the probe is not located in a CpG island and that the other probes are not significantly different between control and LPS condition, questionning the real impact of a single site DNA methylation modulation on *Traf1* expression.

The same profile is exhibited by on the *Lcn2* gene and the same conclusions can be drawn from it (Annexe 38).

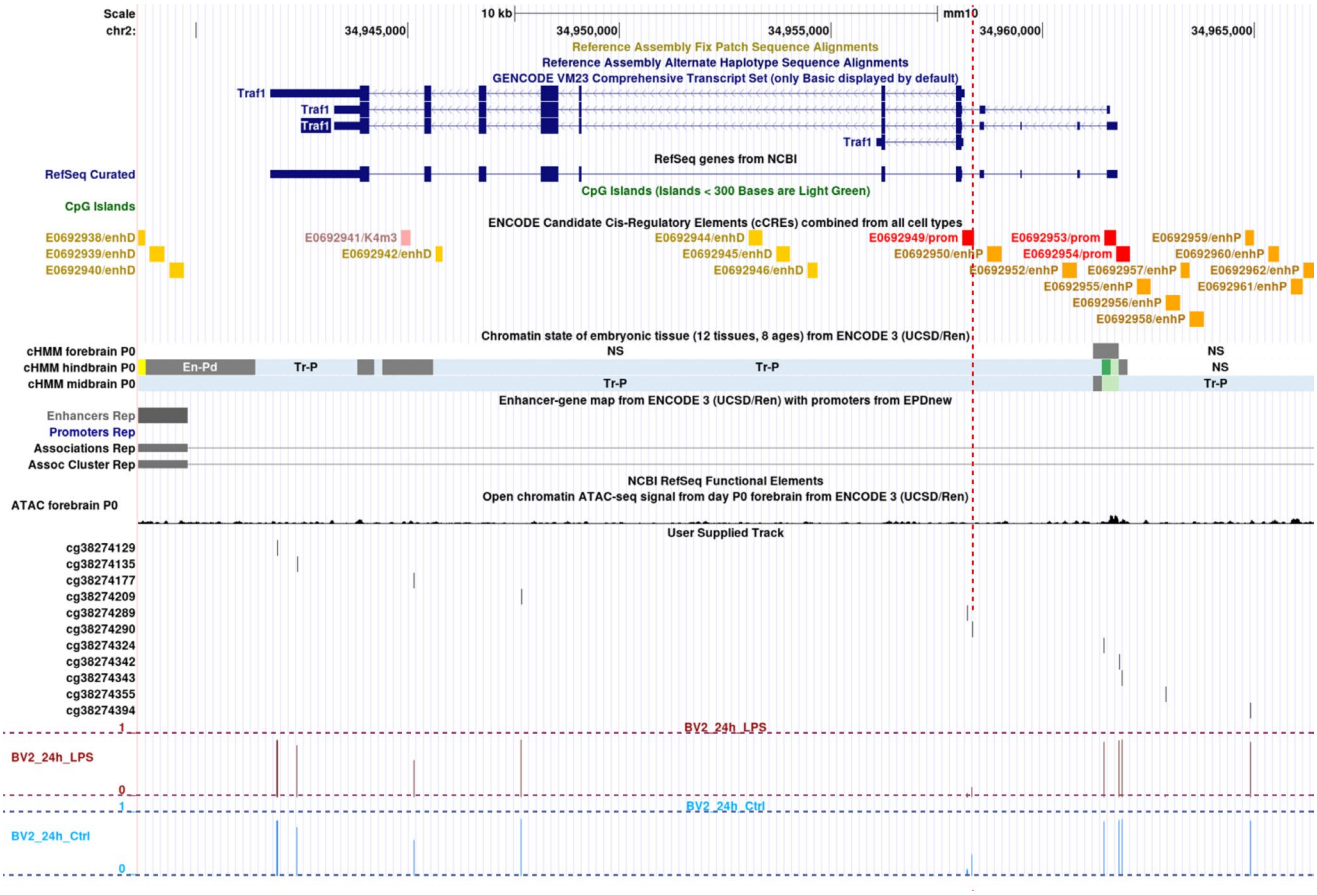

Figure 40. LPS induced *Traf1* expression is associated with DNA methylation changes in chromatin region predicted to be permissive:

UCSC Genome Browser view of the *Traf1* gene from mouse GRCm38/mm10 genome, including tracks (from top to bottom) for RefSeq gene from NCBI (Annotation release 108.20200622); CpG islands; ENCODE cis-regulatory elements, chromatin states predicted according to the ChIP-seq databases on forebrain, hindbrain and midbrain of P0 mouse pups; enhancers and promoters functional associations, ATAC-seq database on forebrain of P0 mouse pups and Illumina Mouse Methyl probes localization. The last tracks correspond to the sum of the methylation level of the three replicates at each probe site for each condition. The horizontal lines represent the level of methylation from 0 to 1; Light blue: control. Red: LPS. The vertical red line represents the significantly differentially methylated site in the *Traf1* gene.

On Figure 41, the UCSC genome browser view for the *Saa3* gene shows that the significant methylation changes in the LPS condition (cg44539754) is characterized by a strong hypomethylation compared to control. Interestingly, it appears that this probe does not align with any regulatory element but localize in a chromatin state predicted to be associated to permissive transcription. It also aligns with the ATACseq tracks showing no peak at this location, confirming the inactive state of the chromatin. Finally,

we observe that the probe is not located in a CpG island and that the other probes are not significantly different between control and LPS condition. Those interesting results may lead to the discussion about whether DNA methylation in a region devoid of any regulatory element could affect the expression of a gene. However, it makes it difficult to understand the impact of DNA methylation on the expression of *Saa3*.

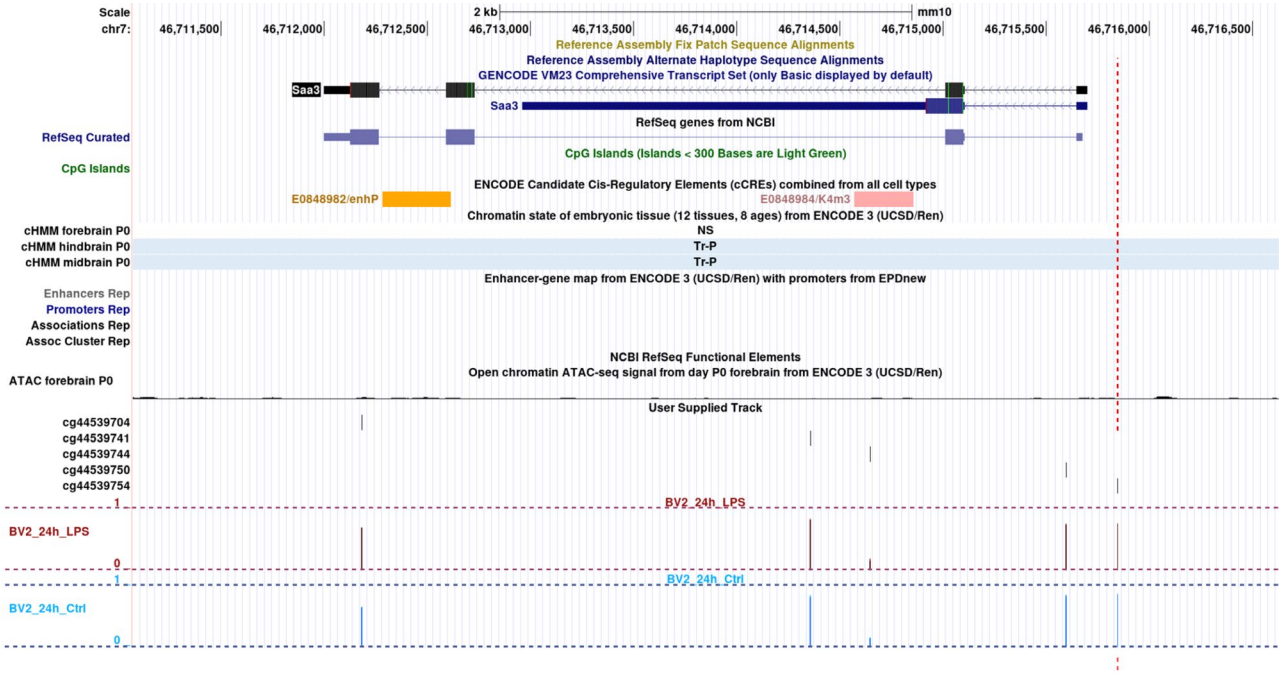

Figure 41. LPS induced *Saa3* expression is associated with DNA methylation changes in chromatin region with unknown chromatin statut:

UCSC Genome Browser view of the *Saa3* gene from mouse GRCm38/mm10 genome, including tracks (from top to bottom) for RefSeq gene from NCBI (Annotation release 108.20200622); CpG islands; ENCODE cis-regulatory elements, chromatin states predicted according to the ChIP-seq databases on forebrain, hindbrain and midbrain of P0 mouse pups; enhancers and promoters functional associations, ATAC-seq database on forebrain of P0 mouse pups and Illumina Mouse Methyl probes localization. The last tracks correspond to the sum of the methylation level of the three replicates at each probe site for each condition. The horizontal lines represent the level of methylation from 0 to 1; Light blue: control. Red: LPS. The vertical red line represent the significantly differentially methylated site in the *Saa3* gene.

In conclusion, BV2 microglial cells treated with LPS for 24 hours exhibit differential transcriptomic and morphological phenotypes, together with significant changes in DNA methylation patterns related to the biological processes of IFN responses. Those findings suggest a role of DNA methylation modification in microglial reactivity to IFNs. In addition, we notice that the hypomethylation of

transcriptional regulatory elements are linked to upregulation of those genes under the IFN-ɣ treatment. Despite the lack of causal mechanisms between the two events, those results strongly suggests a mechanistical role of DNA methylation in gene expression regulation.

Further research are needed concerning the overall chromatin accessibility, the histones modifications and the interactions between proximal and distal regulatory elements present on those genes to understand the real biological meaning of DNA methylation in response to LPS treatment of BV2 cells.

1.15. The significantly differentially methylated regions observed at 48 hours in all treatment conditions seem to arise from the culture condition rather than each individual treatment

Figure 42 displays different features of the comparisons of the DMS between BV2 treated with IFN-ɣ for 48 hours and the control.

First, Figure 42A shows a volcano plot displaying the mean difference between the control DMS M-values and the IFN-ɣ DMS M-values at the 48 hours timepoint, we observe around 38 DMS with a significant positive difference (ranging from 0.2 to 0.7; 218 DMS under the 0.2 threshold) between the control and the IFN-ɣ condition.

On the other hand, 90 DMS exhibit a significant negative difference (ranging – 0.2 to – 0.6; 1129 DMS under above the – 0.2 treshold) between the control and the IFN-ɣ condition. This indicate that 38 CpGs sites are significantly hypomethylated and 90 are hypermethylated in the IFN-ɣ treated BV2 compared to the untreated BV2 at the 48 hours timepoint. We observe that the IFN-ɣ treatment condition at 48 hours timepoint is different in the amount of DMS but also the trend to hypermethylation that was not previously seen in our setting.

Second, on the Figure 42 heatmap (B), the DMS mean M-values are displayed, according to treatment (Tt) and timepoint (Tp). Concerning the comparison between the IFN-ɣ treatment and the control, we see different clusters of DMS, clusters 1 and 4 being characterized by hypomethylation compared to the control, whereas clusters 2, 3 and 5 display a hypermethylation in IFN-ɣ compared to the control. Cluster 4 exhibits a strong hypomethylation in IFN-ɣ and a medium hypermethylation in the control, whereas cluster 1 shows a middle hypomethylation in IFN-ɣ and a strong hypermethylation in the control. Clusters 2 and 3 show similar trends of strong hypermethylation in the IFN-ɣ and a mild

hypomethylation in the control, while the cluster 5 exhibit a medium hypomethylation in the IFN-ɣ condition and a strong hypomethylation in the control. The DNA methylation changes in those clusters indicate a remodeling of the epigenetic landscape of multiples families of genes that may represent transcriptional programs, suggesting a BV2 reprogramming in response to the IFN-ɣ treatment.

We further notice on Figure 42B, that IFN-ɣ treatment at the timepoint 48 hours replicates are clustered together, showing a homogenous response to the treatment as previously seen in Figure 30; but the control replicates at 48 hours are clustered together, which was not the case in the previous Figures, suggesting a homogenization of response after 48 hours in culture.

Finally, it is worth noting that the cluster formed of the IFN-ɣ condition at 24 and 48 hours in Figure 30 (C and F) is still present in this set of DMS and the 12 hours timepoint is clustered next, confirming a homogeneity in the response of BV2 cell DNA methylation to the IFN-ɣ treatment along time.

Lastly, Figure 42C, shows the genomic annotation associated to the DMS in the IFN-ɣ condition compared to the control. We observe that both the hypomethylated and hypermethylated DMS induced by IFN-ɣ treatment for 48 hours are mostly (~30%) located in promoters in less or equal to 1 kb of the TSS, within the first intron (~10%) or within the other intron (~25%). However, it is important to note that the percentage of each location are always slightly higher for the hypomethylated DMS.

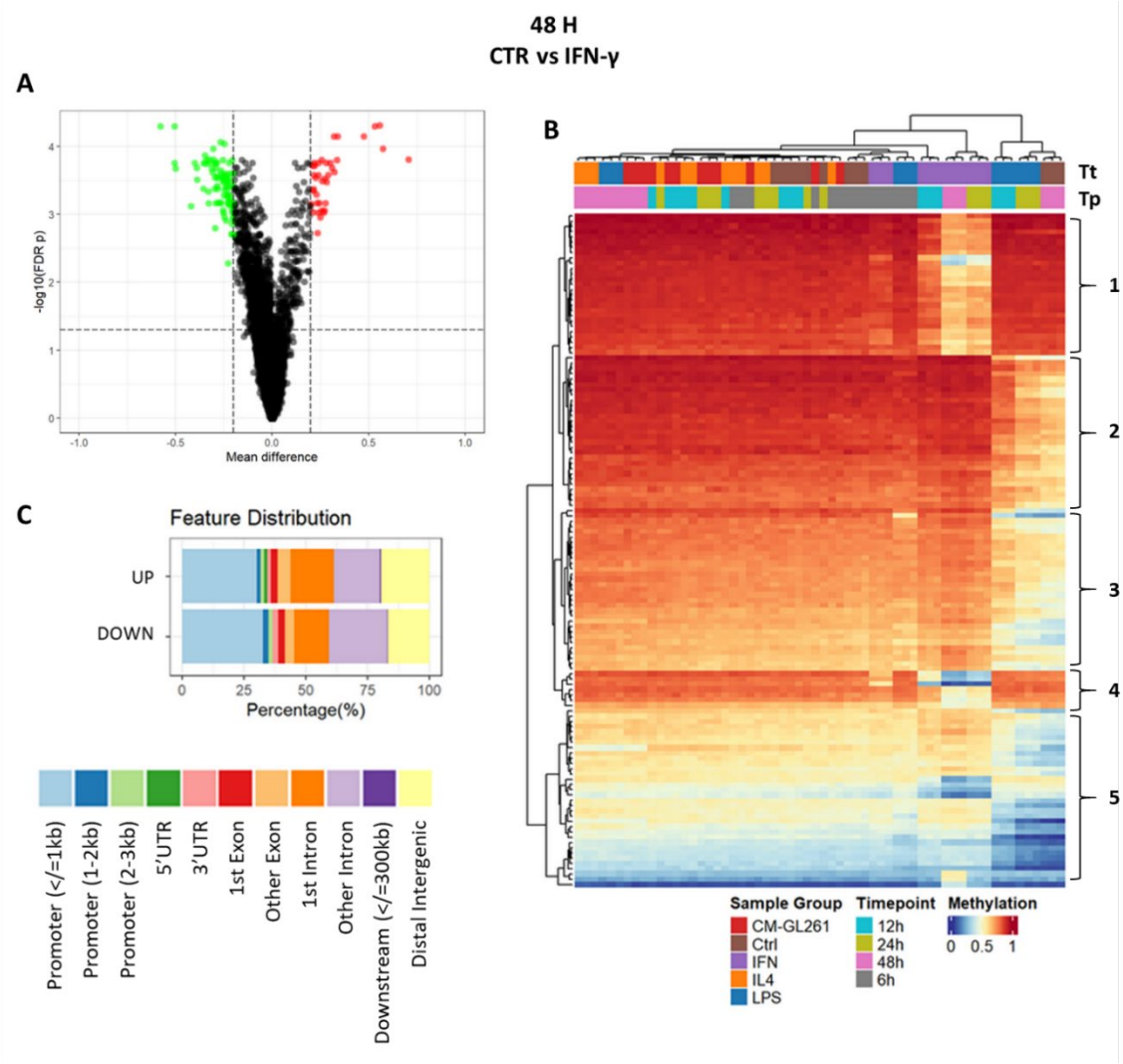

Figure 42. IFN-ɣ treatment leads to hypo- and hypermethylation of promoters in BV2 after 48 hours:

Effect of 10 ng/mL of IFN-ɣ exposure on DNA methylation patterns of BV2 cells treated for 48 hours, compared to the untreated control BV2 cells. The experiment was made using a technical triplicate. Raw data from MethylMouse array were processed by Dr. Reka Toth, using RnBeads 2.16.0, differential methylation was performed using the limma package based on the M-values and the False discovery rate was used to adjust for multiple testing. (A) Volcano plot displaying mean DNA methylation differences between IFN-ɣ and control untreated BV2 at all filtered CpG sites. The vertical lines represent the 0.2 mean M-values difference boundary while the horizontal line represent the statistical significance boundary (P-value < 0.05). The significant DMS appeared in red and green, hypomethylated and hypermethylated in IFN-ɣ condition compared to control, respectively. (B) Hierarchical clustering was performed and represented as a heatmap showing the mean methylation levels of the DMS between the IFN-ɣ and the control. Columns represent the samples relative to treatment (Tt) and timepoint (Tp), while the rows represent the DMS. The methylation levels are illustrated as colors ranging from deep blue (M-Value = 0, unmethylated) to deep red (M-Value = 1, fully methylated). (C) Representation of the genomic features distribution of the DMS in the IFN-ɣ condition

compared to control (Down = decrease M-Value compared to control; Up = increase M-Value compared to control; Hypomethylated and Hypermethylated in IFN-ɣ, respectively). Promoter regions were defined as -3kb +/- 0.5 kb from the transcription start site.

We conclude that significant changes in DNA methylation induced by IFN-ɣ after 12 and 24 hours of treatment are enhanced upon a treatment of 48 hours, increasing hypo- and hypermethylation of different clusters in gene promoters and first introns of BV2 cells suggesting a gene expression regulation in response to IFN-ɣ treatment.

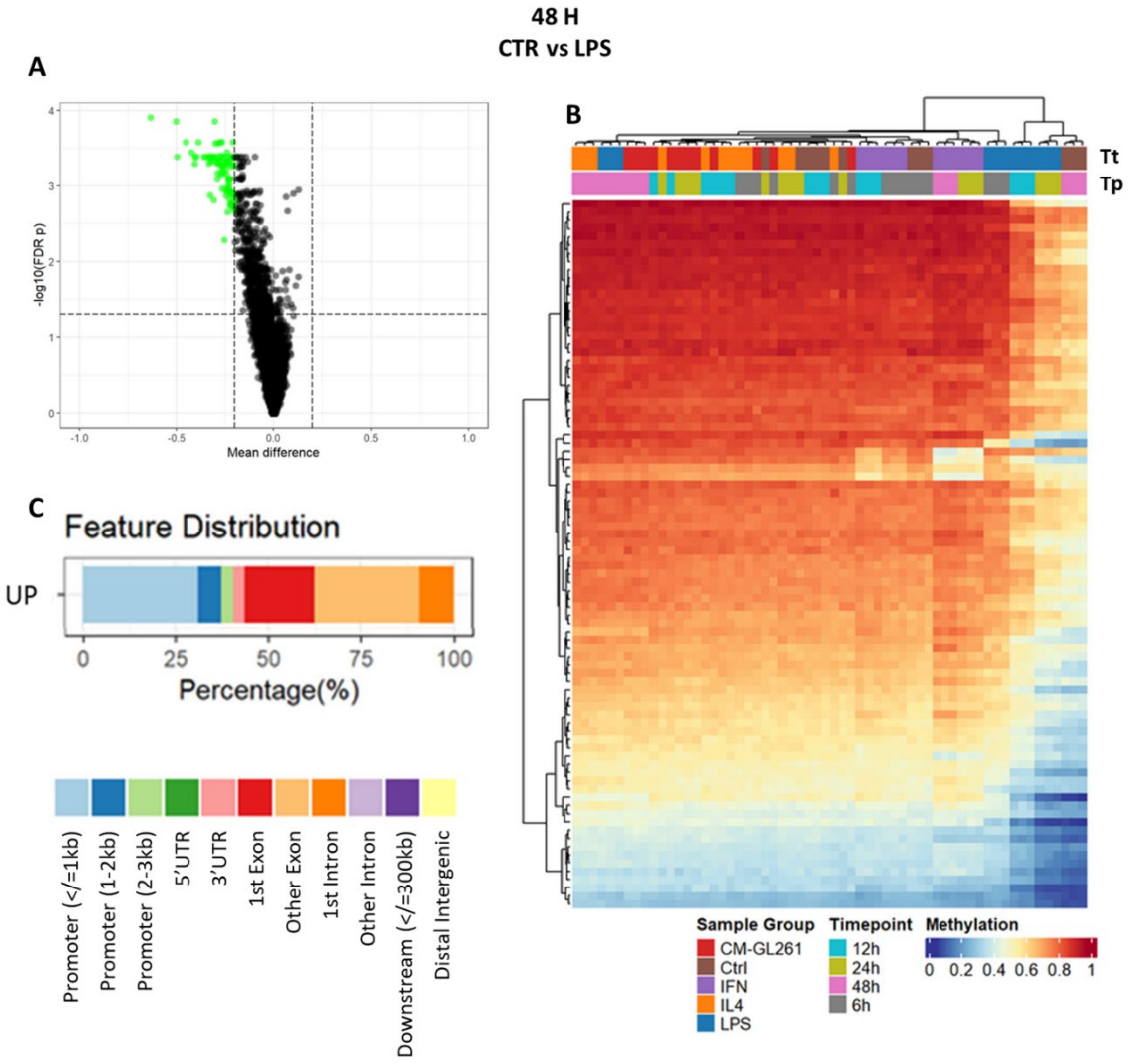

Figure 43. LPS treatment leads to significant promoter and exon hypermethylation in BV2 after 48 hours:

Effect of 10 ng/mL of LPS exposure on DNA methylation patterns of BV2 cells treated for 48 hours, compared to the untreated control BV2 cells. The experiment was made using a technical triplicate. Raw data from MethylMouse array were processed by Dr. Reka Toth, using RnBeads 2.16.0, differential methylation was performed using the limma package based on the M-values and the False discovery rate was used to adjust for multiple testing. (A) Volcano plot displaying mean DNA methylation differences between LPS and control untreated BV2 at all filtered CpG sites. The vertical lines represent the 0.2 mean M-values difference boundary while the horizontal line represent the statistical significance boundary (P-value < 0.05). The significant DMS appeared in red and green, hypomethylated and hypermethylated in LPS condition compared to control, respectively. (B) Hierarchical clustering was performed and represented as a heatmap showing the mean methylation levels of the DMS between the LPS and the control. Columns represent the samples relative to treatment (Tt) and timepoint (Tp), while the rows represent the DMS. The methylation levels are illustrated as colors ranging from deep blue (M-Value = 0, unmethylated) to deep red (M-Value = 1, fully methylated). (C) Representation of the genomic features distribution of the DMS in the LPS condition compared to control (Down = decrease M-Value compared to control; Up = increase M-Value compared to control; Hypomethylated and Hypermethylated in LPS, respectively). Promoter regions were defined as -3kb +/- 0.5 kb from the TSS.

Figure 43 displays different features of the comparisons of the DMS between BV2 treated with LPS for 48 hours and the control.

First, Figure 43A, shows a volcano plot displaying the mean difference between the control DMS M-values and the LPS DMS M-values at the 48 hours timepoint, we can observe 86 DMS with a significant negative difference (ranging from – 0.2 to – 0.7; 511 DMS above the threshold of – 0.2 and 33 DMS with a positive difference below the 0.2 treshold) between the control and the LPS condition.

This indicate that those 86 CpGs sites are hypermethylated in the LPS treated BV2 compared to the untreated BV2 at the 48 hours timepoint. This result is in opposition to the previous results seen in the LPS condition at 12 and 24 hours, exhibiting gradual hypomethylation compared to control.

On the Figure 43 heatmap (B), the DMS mean M-values are displayed, according to treatment (Tt) and timepoint (Tp). We can see no distinctive DMS clusters beside that all CpG sites are less methylated in the control group than in the LPS group at 48 hours timepoint.

However, we see on Figure 43B, that LPS treatment at the timepoint 48 hours replicates are clustered together, showing a homogenous response to the treatment as previously seen in Figure 36; but the control replicates at 48 hours are clustered together, which was not the case in the previous Figures, suggesting a homogenization of response after 48 hours in culture.

In addition, it is important to notice that the pattern seen in Figure 36 and characterized by a cluster of LPS at the timepoints 12 and 24 hours closely to the 6 hours timepoint is still observed in Figure 43 for those DMS, but extremely different compared to the 48 hours timepoint by being clustered with the control at 48 hours.

In addition, we observe a cluster at the 48 hours timepoint composed of the IL-4, LPS and CM-GL261 treatment conditions, indicating that for those DMS at 48 hours, the pro-inflammatory treatment LPS, the anti-inflammatory treatment and the glioma-mimicking (CM-GL261) treatment are exhibiting similar DNA methylation patterns characterized by hypermethylation.

Finally, Figure 43C, shows the genomic annotation associated to the DMS in the LPS condition compared to the control and we find that the hypermethylated DMS induced by LPS treatment for 48 hours are mostly (~30%) located in promoters in less or equal to 1 kb of the TSS, within the first exon (~20%) or in the other exons (~25%).

This distribution also exhibits differences compared to the previous timepoints of the LPS treatment condition mostly characterized by hypomethylated DMS in promoters and introns (Figure 37).

We conclude that the significant changes in DNA methylation induces by the LPS after 48 hours of treatments are different from the ones induced by the same treatment for 12 and 24 hours.

Indeed, in opposition to the increase of gene promoters and introns hypomethylation noticed at 12 and 24 hours timepoint, treatment for 48 hours leads to the hypermethylation of promoters and exons. This observation and the fact that the LPS condition at 48 hours treatment is clustered far away for the cluster of LPS treatment at the other time condition and from the control, suggest that a deep DNA modification reprogramming is induced between 24 and 48 hours of treatment with the LPS. This reprogramming exhibits differences between the untreated cells but also in comparison to the previous treatment timepoints.

We also note that overall, the pattern of methylation that was similar between the pro-inflammatory treatments IFN-ɣ and LPS along timepoints 12 and 24 hours and characterized by a hypomethylation in promoters and introns of genes, diverges at 48 hours timepoint. Indeed, the IFN-ɣ response at 48 hours still displays some similarities with the previous timepoints with hypomethylation of DMS within gene promoters and introns, but differs in a way that some hypermethylation are also noted on gene promoters and introns. On the contrary, the LPS condition at the 48 hours timepoint is in opposition to their 12 and 24 hours counterparts with a hypermethylation of gene promoters and introns.

We conclude that a change in DNA methylation patterns is induced by LPS and IFN-ɣ between six and 12 hours of treatment compared to the control. We also conclude that this change is amplified

between 12 and 24 hours of treatment compared to the control untreated BV2. Finally, the change induced by the treatment seems to be directed towards another direction between 24 and 48 hours of treatment for BV2 cells. Those conclusions suggest that another factor than the treatment could affect the DNA methylation or that the treatment operate a switch in DNA methylation after 48 hours.

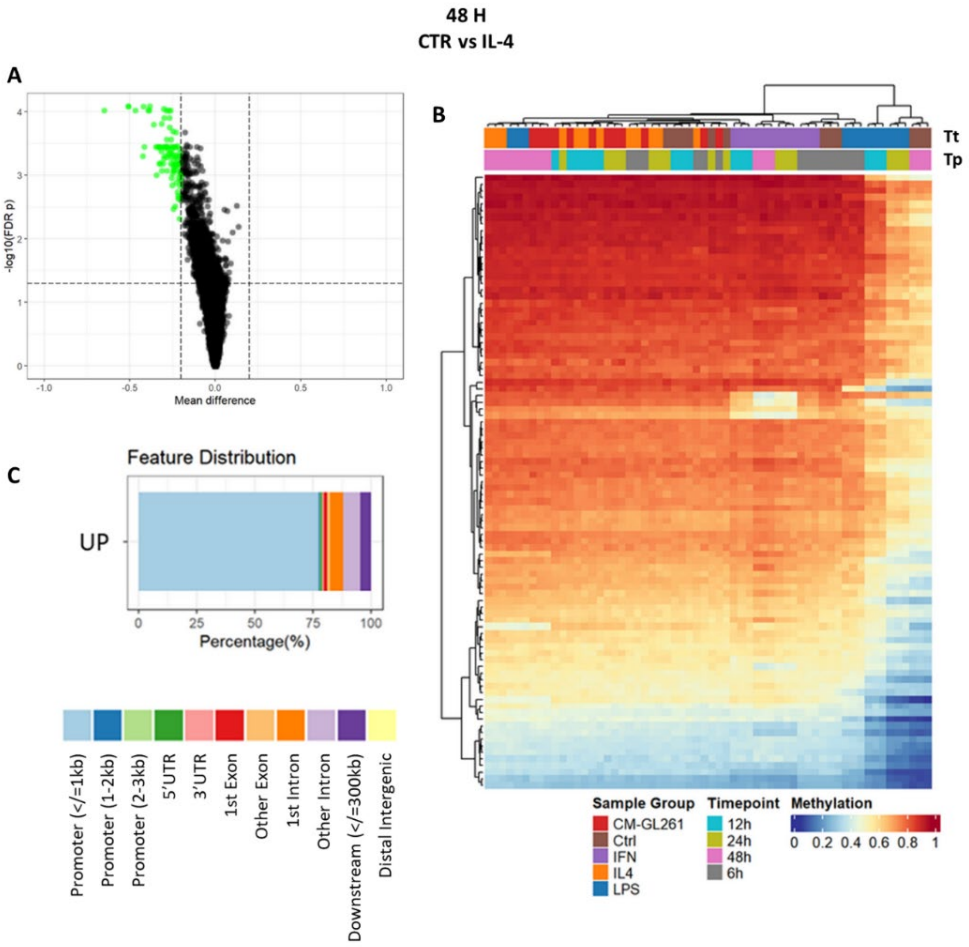

Figure 44. IL-4 treatment leads to promoter hypermethylation in BV2 after 48 hours:

Effect of 10 ng/mL of IL-4 exposure on DNA methylation patterns of BV2 cells treated for 48 hours, compared to the untreated control BV2 cells. The experiment was made on a technical triplicate. Raw data from MethylMouse array were processed by Dr. Reka Toth, using RnBeads 2.16.0, differential methylation was performed using the limma package based on the M-values and the False discovery rate was used to adjust for multiple testing. (A) Volcano plot displaying mean DNA methylation differences between IL-4 and control untreated BV2 at all filtered CpG sites. The vertical lines represent the 0.2 mean M-values difference boundary while the horizontal line represent the statistical significance boundary (P-value < 0.05). The significant DMS appeared in green, hypermethylated in IL-4 condition compared to control. (B) Hierarchical clustering was performed and represented as a heatmap showing the mean methylation levels of the DMS between the IL-4 and the control. Columns represent the

samples relative to treatment (Tt) and timepoint (Tp), while the rows represent the DMS. The methylation levels are illustrated as colors ranging from deep blue (M-Value = 0, unmethylated) to deep red (M-Value = 1, fully methylated). (C) Representation of the genomic features distribution of the DMS in the IL-4 condition compared to control (Up = increase M-Value compared to control; Hypermethylated in IL-4). Promoter regions were defined as -3kb +/- 0,5 kb from the TSS.

Figure 44 displays different features of the comparisons of the DMS between BV2 treated with IL-4 for 48 hours and the control.

First, Figure 44A, shows a volcano plot displaying the mean difference between the control DMS M-values and the IL-4 DMS M-values at the 48 hours timepoint, we observe 93 DMS with a significant negative difference (ranging from – 0.2 to – 0.6; 6587 DMS above the threshold of – 0.2 and 340 DMS with a positive difference below the 0,2 treshold) between the control and the IL-4 condition.

This indicates that those 93 CpGs sites are hypermethylated in the IL-4 treated BV2 compared to the untreated ones after 48 hours of exposure. Compared to the results exhibited previously, the IL-4 treatment did not leads to any significant DNA methylation differences compared to control at any time point (Figure 29) before this one but this tendency to hypermethylation is also seen in the LPS condition at 48 hours (Figure 43).

On the Figure 44 heatmap (B), the DMS mean M-values are displayed, according to treatment (Tt) and timepoint (Tp). We see no distinctive DMS clusters beside that all CpG sites are less methylated in the control group than in the IL-4 group at 48 hours timepoint, at the point of IL-4 and control condition being at the both ends of the Figure 44.

We nevertheless see that the cluster of IL-4, LPS and CM-GL261 observed in Figure 43 is still represented in Figure 44 with this different set of DMS, suggesting again a homogenous response of the BV2 at 48 hours. Because those treatments are so different, one being pro-inflammatory, one being anti-inflammatory and the last being glioma mimicking (CM-GL261), it raises question about the intensity of the treatment used. However, because the LPS treatment was inducing DMS at earliest time points, it suggests that the variability of DMS arise from the timepoint itself.

Finally, Figure 44C, shows the genomic annotation associated to the DMS in the IL-4 condition compared to the control and we find that the hypermethylated DMS induced by IL-4 treatment for 48 hours are in vast majority (~80%) located in promoters in less or equal to 1 kb of the TSS, within the first intron (~5%) or in the other introns (~5%).

Compared to the other conditions at 48 hours, we note that the proportion of gene promoters hypermethylation is considerable which is surprising since no significant DNA methylation changes were observed at the previous timepoints. Those results suggest that the IL-4 treatment could need more time to induce DNA methylation changes in BV2 cells or that the 48 hours timepoint is in cause of such significant variability.

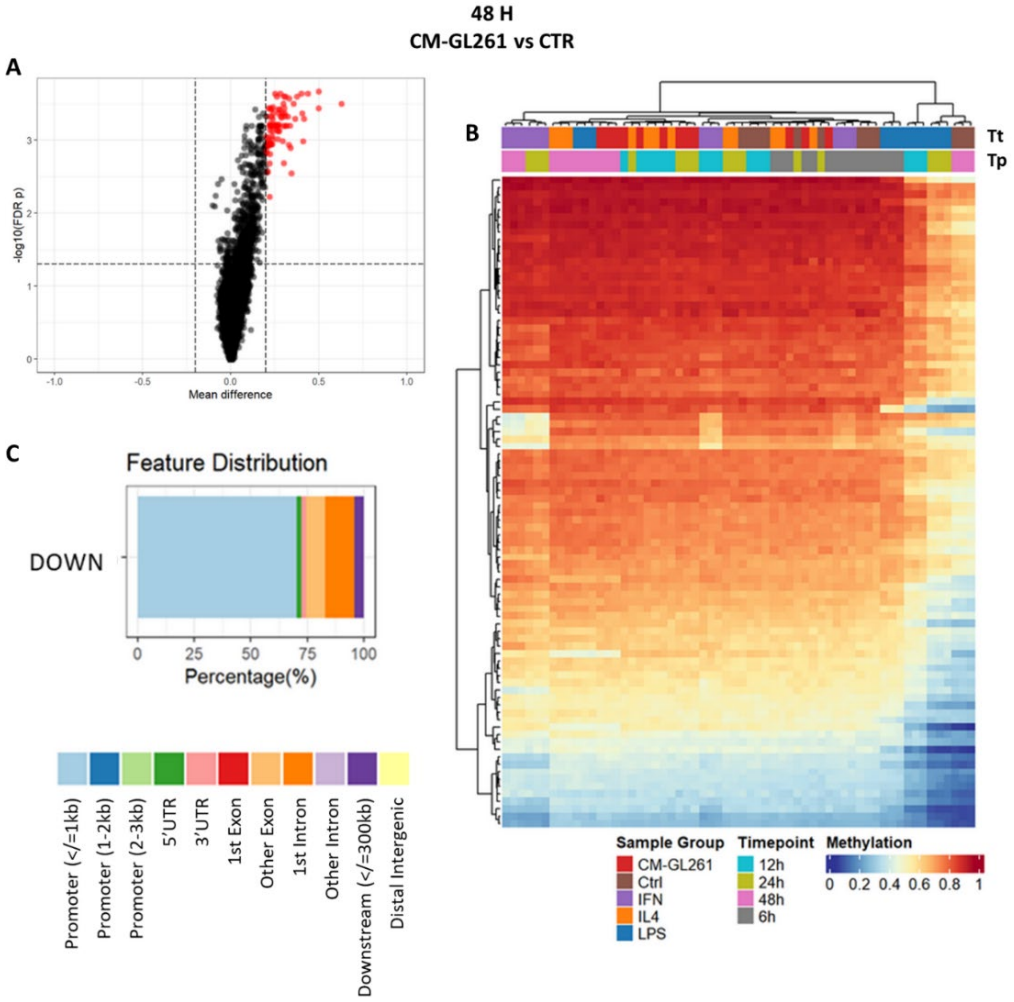

Figure 45. CM-GL261 treatment leads to promoter hypermethylation in BV2 cells after 48 hours:

Effect of CM-GL261 exposure on DNA methylation patterns of BV2 cells treated for 48 hours, compared to the untreated control BV2 cells. The experiment was made using a technical triplicate. Raw data from MethylMouse array were processed by Dr. Reka Toth, using RnBeads 2.16.0, differential methylation was performed using the limma package based on the M-values and the False discovery rate was used to adjust for multiple testing. (A) Volcano plot displaying mean DNA methylation differences between the control untreated and the CM-GL261 treated BV2 cells at all filtered CpG sites. The vertical lines represent the 0.2 mean M-values difference boundary while the horizontal line represent the statistical

significance boundary (P-value < 0.05). The significant DMS appeared in red, hypermethylated in CM-GL261 condition compared to control. (B) Hierarchical clustering was performed and represented as a heatmap showing the mean methylation levels of the DMS between the CM-GL261 and the control. Columns represent the samples relative to treatment (Tt) and timepoint (Tp), while the rows represent the DMS. The methylation levels are illustrated as colors ranging from deep blue (M-Value = 0, unmethylated) to deep red (M-Value = 1, fully methylated). (C) Representation of the genomic features distribution of the DMS in the control compared to the CM-GL261 condition (Down = decrease M-Value in control compared to CM-GL261; Hypermethylated in CM-GL261). Promoter regions were defined as -3kb +/- 0.5 kb from the TSS.

Figure 45 displays different features of the comparisons of the DMS between untreated and BV2 with CM-GL261 for 48 hours.

First, Figure 45A, shows a volcano plot displaying the mean difference between the CM-GL261 DMS M-values and the control DMS M-values at the 48 hours timepoint, we can observe 88 DMS with a significant positive difference (ranging from 0.2 to 0.6; 495 DMS below the threshold of 0.2 and 48 DMS with a negative difference above the 0.2 treshold) between the CM-GL261 and the control condition.

This indicates that those 88 CpGs sites are hypermethylated in the CM-GL261 treated BV2 compared to the untreated BV2 at the 48 hours timepoint. Compared to the results exhibited previously, the CM-GL261 treatment did not leads to any significant DNA methylation difference compared to control at any time point (Figure 29) before this one but this tendency to hypermethylation is also seen in the LPS (Figure 43) and the IL-4 (Figure 44) conditions at 48 hours.

On the Figure 45 heatmap (B), the DMS mean M-values are displayed, according to treatment (Tt) and timepoint (Tp). There is no distinctive DMS cluster beside that all CpG sites are less methylated in the control group than in the CM-GL261 group at 48 hours timepoint.

We nevertheless notice that the cluster of IL-4, LPS and CM-GL261 observed in Figures 43 and 44 is still represented in Figure 45 with that different set of DMS, suggesting again a homogenous response of the BV2 at 48 hours or that those hypermethylated DMS are all the same across treatments compared to the control. However, the question about the influence of the 48 hours timepoint regardless of the treatment, remains.

Finally, Figure 45C shows the genomic annotation associated to the DMS in the control condition compared to the CM-GL261 and we find that the hypermethylated DMS induced by CM-GL261 treatment for 48 hours are in vast majority (~70%) located in promoters in less or equal to 1 kb of the TSS, within the first intron (~20%) or in the other exons (~5%).

Compared to the other conditions at 48 hours, we observe that the proportion of gene promoters hypermethylation is similar to the one observed in IL-4 treatment at 48 hours (Figure 44).

This result, as the one for IL-4, is somehow surprising since no significant DNA methylation changes were observed at the previous timepoints, suggesting that the IL-4 and CM-GL261 treatment would need more time to induce DNA methylation changes in BV2 cells or that the 48 hours timepoint is in cause of such significant variability.

In conclusion, the overall pattern of methylation is similar between the pro-inflammatory treatments along timepoints 12 and 24 hours, characterized by a hypomethylation in gene promoters and introns. Those patterns diverge at 48 hours timepoint by being mostly characterized by hypermethylation of gene promoters, a pattern emerging in the IL-4 and CM-GL261 conditions at 48 hours timepoint. Because of those observations and the clustering of the LPS, IL-4 and CM-GL261 DNA methylation patterns at 48 hours, we could hypothesize that the timepoint itself is inducing the significant changes and not the treatment.

Figure 46 displays the PCA plots highlighting all the samples treated for 48 hours (A) and each treated samples plotted with the untreated samples (orange squares): IFN-ɣ (B, green), CM-GL261 (C, blue), IL-4 (D, red) and LPS (E, purple). We observe on Figure 46A that the technical control replicates are exhibiting the highest variability, whereas in each treatment, the technical replicates seem to be closer, especially for the IL-4 treatment for which the samples are superposed. We also note that the IFN-ɣ (B; mean PC1 : 4.2; mean PC2 : - 0.3), the CM-GL261 (C; mean PC1 : 4.6; mean PC2 : - 0.8) and the LPS (E; mean PC1 : 4.8; mean PC2 : - 0.8) are cluster together whereas the IL-4 (D; mean PC1 : 8.3; mean PC2 : - 0.9) condition is more variable than both the cluster of treatment and the control (mean PC1 : - 0.7; mean PC2 : -1.3).

We conclude that, at the 48 hours timepoint, regarding the entire methylation profile of each sample, the most important variability in methylation profiles arises within the untreated control group. The most divergent methylation profiles seem to appear between the control and the IL-4 conditions. The methylation profiles of the CM-GL261, LPS and IFN-ɣ conditions seem highly similar but differ from the control.

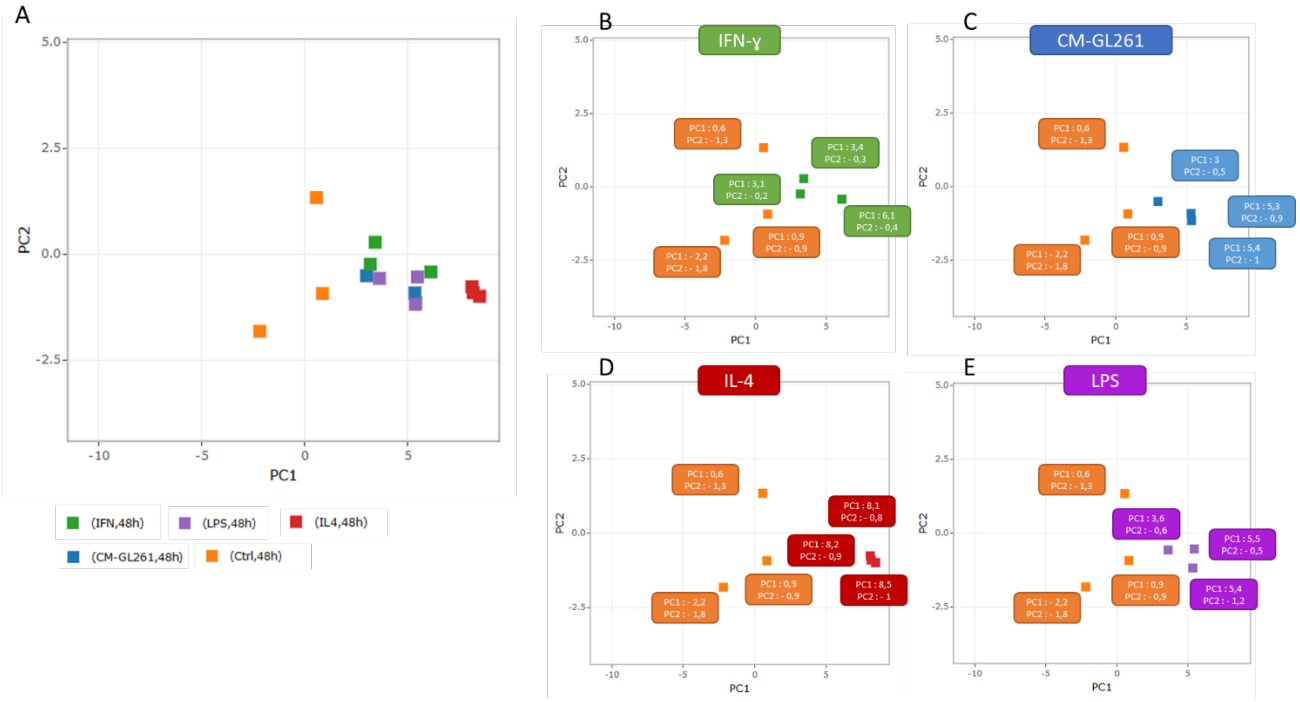

Figure 46. DNA methylation profiles of 48 hours treatment-exposed BV2 are highly similar:

Effect of 10 ng/mL of LPS, IFN-ɣ, IL-4 or CM-GL261 exposure on DNA methylation patterns of BV2 cells treated for 48 hours, compared to the untreated control BV2 cells. The experiment was made using a technical triplicate. Raw data from MethylMouse array were processed by Dr. Reka Toth, using RnBeads 2.16.0. (A) Principal Component Analysis (PCA) plot of DNA methylation profiles based on all CpG sites (after filtering; see Materials and Methods). (B) IFN-ɣ: green squares; (C) CM-GL261: blue squares; (D) IL-4: red squares; (E) LPS: purple squares and, control: orange squares.

We can conclude that the similarities between CM-GL261, IL-4 and LPS treatments observed on the previous Figures at 48 hours seem to be restricted to the set of hypermethylated probes highlighted in those different heatmaps (Figures 43 to 45).

Figure 47 shows the Venn diagrams of all significant DMS of each treatment when compared to the control (A) and all the hypermethylated DMS (B).

The most striking observation highlighted in Figure 47 is that 49 % of the total DMS are present amongst all the treatment conditions (A), representing 81% of the total DMS of the CM-GL261 condition, 55% for the IFN-ɣ, 76% for the IL-4 and 82% for the LPS condition.

This result shows that more than half of the DMS appears to be induced regardless of the treatment. We discover on B that the 71 DMS shared by all treatments are all hypermethylated ones, meaning that in addition to be differentially methylated in every treatments, those CpGs sites are modulated in the same direction.

Finally, we notice that IFN-ɣ, with the most DMS, is also the only condition exhibiting hypomethylated DMS, suggesting that the treatment is inducing a stronger DNA methylation pattern reprogramming compared to the other conditions; robust enough to be observed regardless of the background hypermethylation potentially induced by the culture after 48 hours.

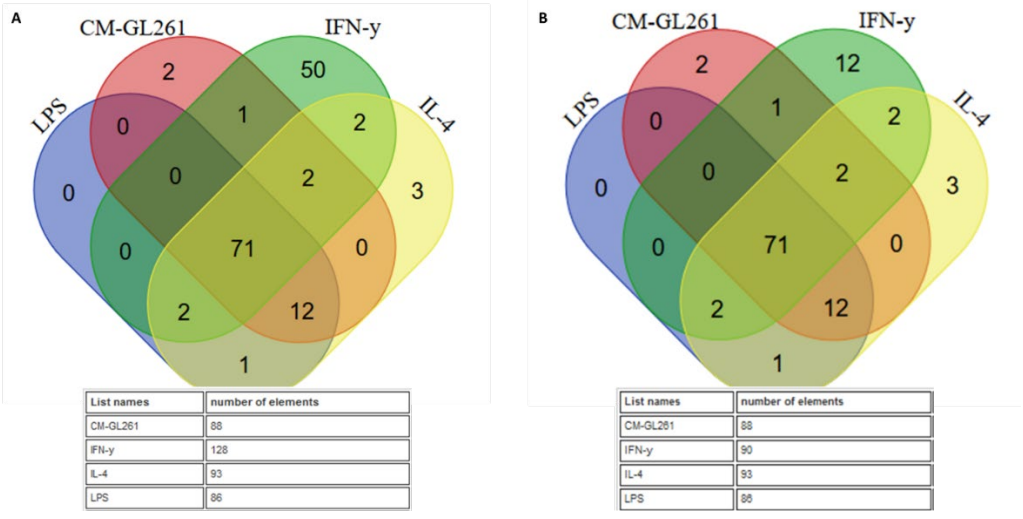

List names	number of elements
CM-GL261	88
IFN-y	128
IL-4	93
LPS	86

List names	number of elements
CM-GL261	88
IFN-y	90
IL-4	93
LPS	86

Figure 47. Most DMS induced at 48 hours are common and hypermethylated in all treatment conditions:

Effect of 10 ng/mL of LPS, IFN-ɣ, IL-4 or CM-GL261 exposure on DNA methylation patterns of BV2 cells treated for 48 hours, compared to the untreated control BV2 cells. Venn diagrams of the overlapping differentially methylated sites (A) and the hypermethylated sites (B) in BV2 treated with LPS (blue), IFN-ɣ (green), IL-4 (yellow) or CM-GL261 (red) after 48 hours compared to the untreated BV2. The experiment was made on a technical triplicate. Raw data from MethylMouse array were processed by Dr. Reka Toth, using RnBeads 2.16.0, differential methylation was performed using the limma package based on the M-values and the False discovery rate was used to adjust for multiple testing.

We conclude that all treatments are leading to the hypermethylation of similar 71 DMS at 48 hours of treatment suggesting that this DNA methylation change in BV2 cells is associated with the timepoint itself regardless of the treatment condition. Gene ontology analysis did not found any significant differences amongst all genes associated to those 71 DMS. However, when the gene ontology analysis was done on the genes containing DMS in their promoters (only 14), the most significant GO term was "Inflammatory response" linked to the *Sbno2*, *Cxcl2*, *Tnip1* and *Il20rb* genes. Even though the amount of genes studied is low and the biological relevance questionable, the fact that those four genes are all associated with the transcritomics of microglia from inflammatory pathology makes this result interesting.

Otherwise, because of the presence of significantly hypomethylated probes in the IFN-ɣ condition, we can hypothesize that the IFN-ɣ treatment is the only one in our setting inducing a response robust enough to be observed beside the one induced at 48 hours.

In conclusion, we showed that BV2 microglial cell line model displays significant phenotypical changes specific to towards LPS, IFN-ɣ, IL-4 and CM-GL261 stimulation at six hours of exposure. Those phenotypes were characterized by distinct morphological features, CK secretion and mRNA expression. We also showed that BV2 cells treated for 12 and 24 hours with LPS and IFN-ɣ displayed significant treatment-specific DNA methylation changes in genes presenting altered mRNA expression. Some of those differentially methylated and expressed genes were associated with signaling pathways and biological functions relevant for microglial identity. Those results suggest an association between DNA methylation, gene expression and microglial identity. Nevertheless, further investigations are needed to unravel both the biological meaning of DNA methylation in transcriptional regulatory elements and the exact chromatin state of those implicated genes, governed by other epigenetic mechanisms.

2. Reactive primary CD-1 microglial cells exhibit significant DMS after an hour of stimulus exposure

After concluding on the previous study, we aimed to overcome the bias led by the immortalization process on the epigenetic landscape of microglia by using primary microglial cells isolated from CD-1 mouse pup brains as a model. The microglia were isolated with a MACS system using CD11b antibodies.

We hypothesized that the primary microglial cells would be more sensitive to stimulation and decided to adjust the time of treatment to one and six hours only. The same experimental design previously used, was applied.

2.1. LPS, IFN-ɣ, IL-4 and CM-GL261 treatments do not affect primary microglial viability and proliferation

As for the BV2 study, we needed to ensure that treatments were not affecting the viability and the proliferation of the primary microglial cells. To do that, a Cell Titer Glo assay and an Incucyte monitoring were performed (Figures 48 and 49).

Figure 48 exhibits the percentage of viability of the primary microglial cells treated with LPS, IFN-ɣ, IL-4 or CM-GL261, normalized to the control untreated cells. The X-axis shows the treatment conditions, while the Y-axis displays the percentage of viability compared to the control untreated cells set as 100%. We observe a non-significant but important increase of viability after one hour of treatment (A), regardless the nature of the treatment, compared to the control untreated cells. Figure 48B shows that after six hours of treatment, the viability of primary microglial cells in all treatment conditions is non-significantly decreased in comparison to the one hour timepoint.

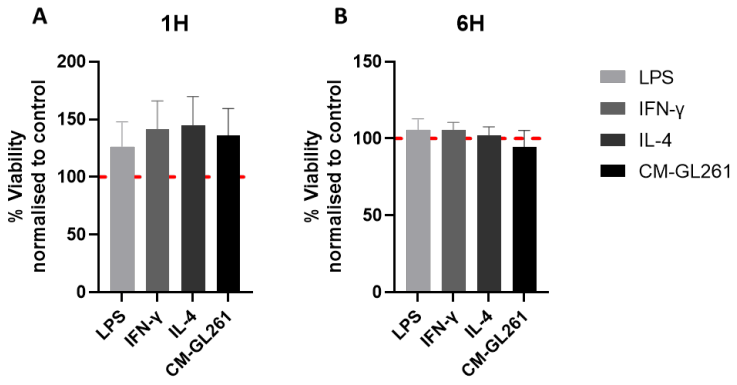

Figure 48. Viability of primary microglial cells is not significantly affected by the treatments:

Effect of 10 ng/mL of LPS, IFN-ɣ, IL-4 or CM-GL261 exposure on the viability of BV2 cells treated for one hour (left panel) and six hours (right panel). The cell viability of treated cells was assessed relatively to the control, untreated cells (red line). Statistical analysis constituting of an Ordinary One-Way ANOVA with Multiple comparisons (Tukey's) was performed using GraphPadPrism 9. Data are representative of three independent experiments, each of which done in technical triplicates and are represented as mean ± Standard Error of the Mean (SEM).

In conclusion, Figure 48 shows no significant difference between the viability of primary microglial cells treated or not with LPS, IFN-ɣ, IL-4 and CM-GL261 for one and six hours; allowing us to conclude that our treatments are not impacting primary microglial cells viability.

Figure 49 shows the confluence obtained from the Incucyte® system of primary microglial cells treated with LPS, IFN-ɣ, IL-4 or CM-GL261 for 24 hours and normalized to the values obtained from untreated control cells. Figure 49A displays the time in hours (X-axis), while the Y-axis presents the percentage of confluency normalized to the control, in respect for each time point. We find that no significant change in confluence are induced in microglia by any of the treatments compared to the untreated control microglia.

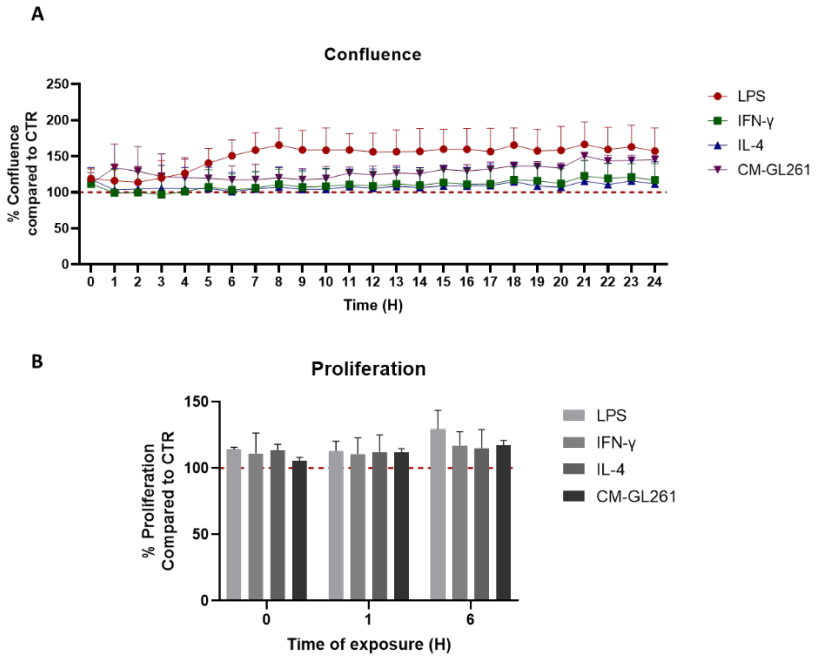

Figure 49. Confluence and proliferation rate of primary microglial cells are not impacted by the treatments:

Effect of 10 ng/mL of LPS, IFN-ɣ, IL-4 or CM-GL261 exposure on the confluence (A) and proliferation (B) of primary microglial cells treated for 24 hours. The cellular confluence of treated cells was monitored and analyzed by the Incucyte® system. Data were normalized to the control untreated cell (CTR, red dotted line). Proliferation was assessed by counting of the cells from the pictures generated by the Incucyte® system and compared to the control (CTR, red dotted line, untreated cells). Statistical analysis was performed using GraphPadPrism 9 applying a two-way ANOVA with correction for multiple comparisons (Tukey's). Data are representative of three independent experiments, each of which done in technical triplicates and are represented as mean ± SEM.

Figure 49B shows the manual counting of cell numbers in pictures generated by the Incucyte® system to validate that the measurements of confluency is not biased by the increase of cell soma size upon treatment. Graph B displays the timepoints in hours on the X-axis and the percentage of cell numbers (named proliferation) compared to the control.

We observed no significant changes in cell numbers upon treatments compared to the untreated control microglia. We nevertheless noticed that the measure of the confluence by measuring the area of the cell *versus* the number of the cells might not be relevant, the number of IFN-ɣ treated microglia being similar to the IL-4 and CM-GL261 ones while the confluence data show that the IFN-ɣ treated microglia confluence is below the IL-4 and CM-GL261 ones. This could mean that for morphologically sensitive cells like microglia, the measure of confluence could not be representative of the proliferation rate.

We then conclude that the 10 ng/mL LPS, IFN-ɣ, IL-4 or CM-GL261 treatments does not significantly affect the viability and proliferation of primary microglial cells when used from one to 24 hours.

To observe if the treatments were inducing phenotypical changes in primary microglia, an IF staining was performed.

2.2. LPS, IFN-ɣ, IL-4 and CM-GL261 lead to morphological changes in primary microglial cells after 6 hours

Figure 50 displays the pictures taken from the IF staining of the primary microglia cells treated or not with LPS, IFN-ɣ, IL-4 and CM-GL261 for 1, 6 and 24 hours. The staining targets Iba1 (in red) and F4/80 (in green) and was counterstained with DAPI to highlight the nucleus (in blue).

Figure 50 (and Annexe 36 for 20X pictures) shows that morphological changes are induced over time in all treatment conditions, especially after six hours and more manifest in the pro-inflammatory LPS condition, inducing a noticeable increase of microglia soma size accompanied with a decrease and thickening of processes length.

On the contrary to what was observed in BV2 cells and even though the phenotype still is elongated, anti-inflammatory (IL-4) treatment leads to a thickening of the processes with slight increase of the soma size compared to primary untreated microglia.

Those results are still in line with the literature classifying microglial morphologies suggesting a polarization of microglial cells towards pro- and anti-inflammatory[325] phenotypes *in vitro*, respectively. In the CM-GL261 condition, mixed phenotypes are observables with elongated cells coupled with amoeboid ones, making it difficult to summarize a homogenous induced microglial phenotype. The observation that the cell shapes are changing suggests a phenomenon of cellular reactivity to the treatments in our experimental design and we can notify that the morphological change appear more striking and sooner compared to the BV2 microglial cell line.

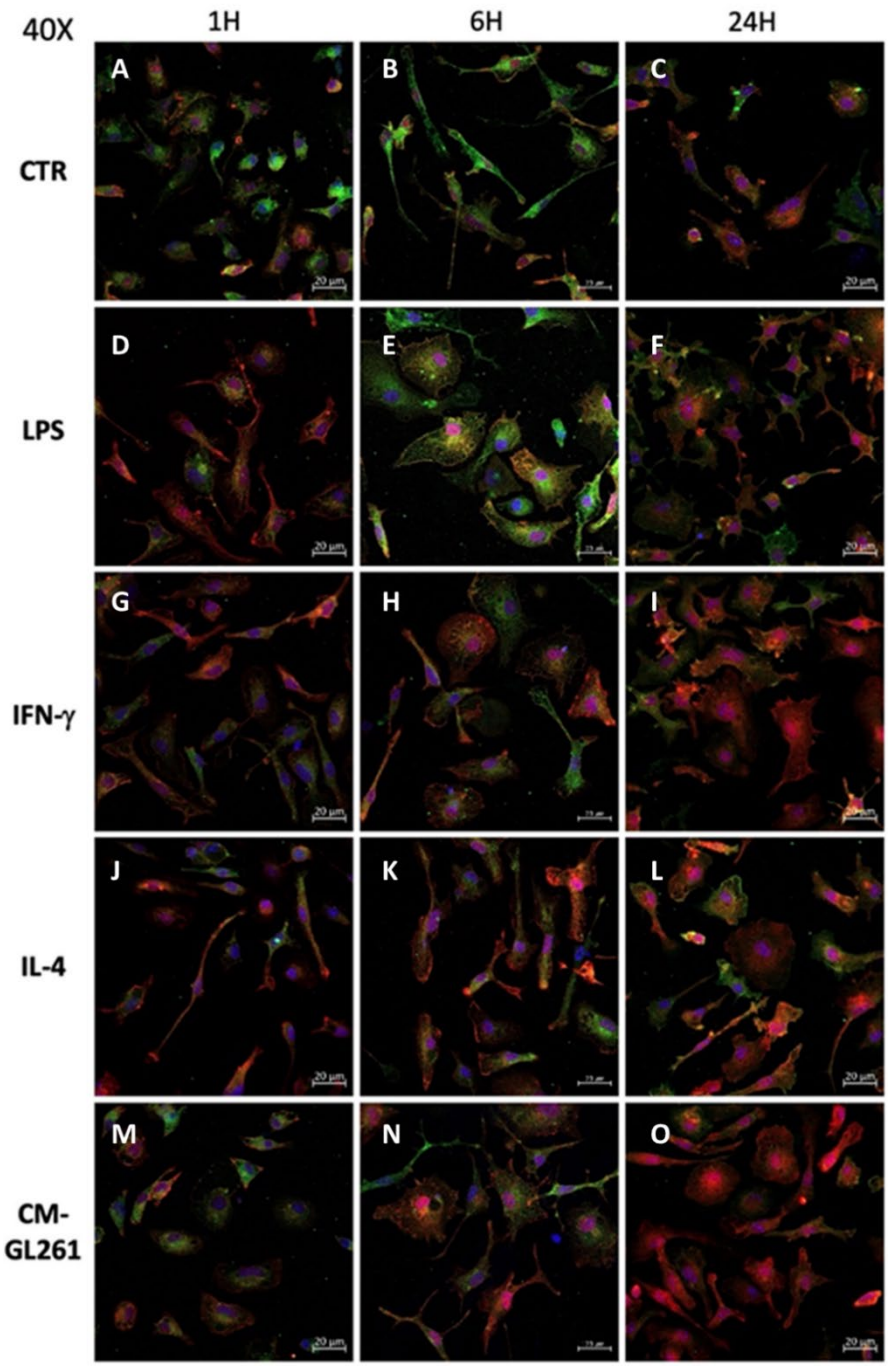

Figure 50. Morphological changes are induced in primary microglial cells by all treatments:

Effect of 10 ng/mL of LPS, IFN-ɣ, IL-4 or CM-GL261 for 1, 6 and 24 hours on primary microglial cells morphology. Confocal images (40X objective) showing the co-labelling of Iba1 (red) and F4/80 (green) in cultured primary microglia. DAPI is shown in blue; scale bar: 20 µm. Untreated control cells (CTR; A, B and C); LPS condition (D, E and F); IFN-ɣ condition (G, H and I), IL-4 (J, K and L) and CM-GL261 condition (M, N and O). One hour of treatment (A, D, G, J and M); six hours of treatment (B, E, H, K and N) and 24 hours (C, F, I, L and O).

To know if the reactivity suggested by IF staining was also observed at the transcriptomics level, RT-qPCR targeting known microglial reactivity-associated genes were realized.

2.3. LPS is inducing *Tnf* expression in primary microglial cells after an hour of treatment

Similarly to what was explored in the BV2 section, mRNA expression of characteristics microglial reactivity genes was assessed, including *Cxcl10, Ccl9* and *Tnf; Arg1* and *Fizz1* associated with pro- and anti-inflammatory reactivities, respectively. We decided to measure the quantity of mRNA in primary microglia treated or not with LPS, IFN-ɣ, IL-4 or CM-GL261 for one or six hours by performing RT-qPCR. We assessed the expression of those mRNA in comparison to the housekeeping gene *Rpl27*. The results, normalized to the control group mRNA counterparts are presented in Figure 51. The top panel of Figure 51 shows the mRNA expression for the one hour treatment conditions, while the bottom panel displays the results for the six hours treatment conditions. The displayed mRNAs are *Arg1*(A, F), *Fizz1* (B, G), *Cxcl10* (C, H), *Ccl9* (D, I) and *Tnf* (E, J). All the presented graphs X-axis refer to each one of the treatment with each color representing a timepoint; the Y-axis representing the mRNA expression of each gene relative to the control untreated counterpart.

Figure 51 shows that, except for the *Fizz1* mRNA, significant differences are induced by the treatments at the transcriptomic levels.

Indeed, concerning the anti-inflammatory associated genes, Figure 51A shows that after an hour, all conditions of treatment lead to an increase in *Arg1* mRNA expression in comparison to the control untreated microglia, while no significant difference are observed after six hours.

Concerning the pro-inflammatory associated genes, we can see in Figure 51H, that the LPS treatment leads to an increase in mRNA expression of *Cxcl10* at six hours with a 390 positive fold change. The LPS treatment also leads to the significant induction of *Ccl9* mRNA expression after an hour (D). Finally, LPS treatment also leads to an increase in *Tnf* mRNA expression after one and six hours (E and J), the strongest being after one hour with a positive 425-fold change compared to the control.

The trends of mRNA expression shows that the microglial reactivity to the pro-inflammatory treatments seems slightly stronger than the anti-inflammatory and glioma-mimicking ones, similarly to what was observed for the BV2 cell lines and suggesting that either those stimulations are too weak to induce an observable reprogramming or that the microglial cells are more prone to respond to pro-inflammatory insults.

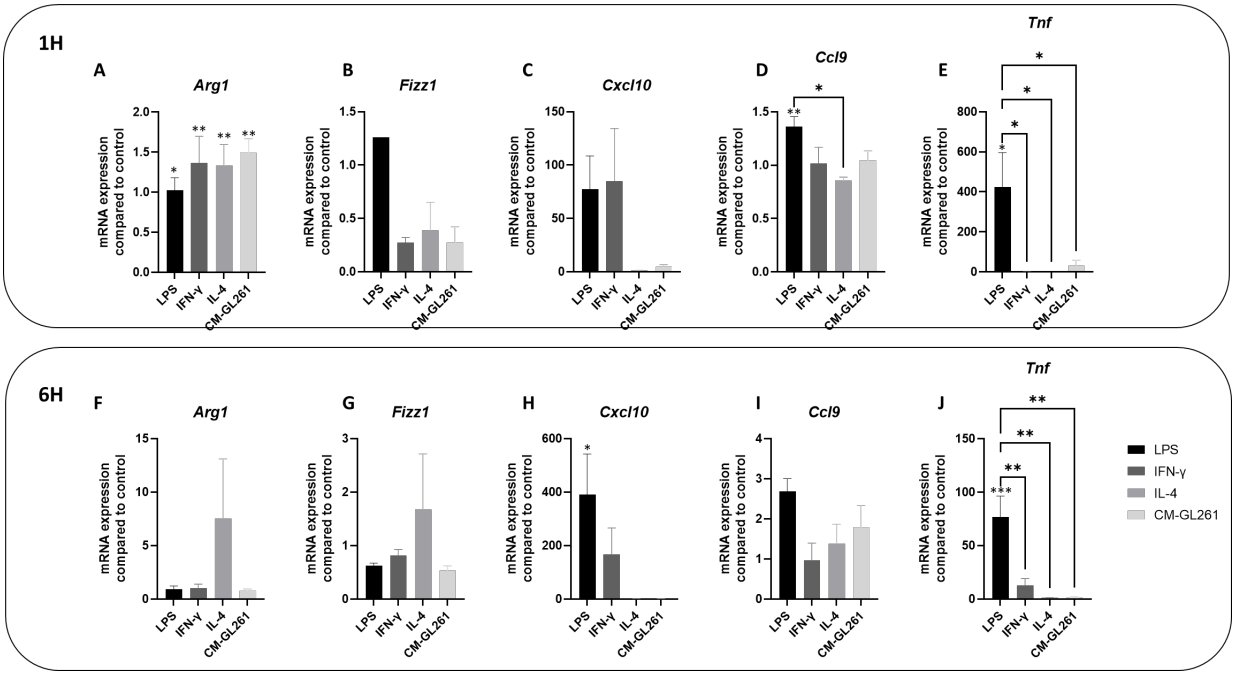

Figure 51. LPS treatment is the strongest inducer of transcriptional changes in primary microglial cells of all treatment conditions:

Effect of 10 ng/mL of LPS, IFN-ɣ, IL-4 or CM-GL261 exposure on mRNA expression of primary microglial cells treated for one (A to E) or six hours (F to J), normalized to untreated cells. Selected mRNA targets are characteristics of a pro-inflammatory (*Cxcl10*, *Tnf* and *Ccl9*) and anti-inflammatory (*Arg1* and *Fizz1*) reactivity. *Rpl27* was used as a housekeeping gene for normalization of gene expression. Statistical analysis was performed using GraphPadPrism 9 and applying one-way ANOVA with a correction for multiple comparisons between control and treatment (Dunnett) and inbetween treatments (Tukey). Except for *Fizz1* at one hour, data are representative of three independent experiments, each of which done in technical triplicates and are represented as mean ± Standard Error of the Mean (SEM). *Indicating a P-value < 0,05; ** indicate a P-value < 0,01; *** indicate a P-value < 0,001.

We conclude that all the trends in treatment-related mRNA expression changes as well as LPS treatment that is inducing the most significant transcriptomic changes in primary microglial cells, suggesting that a state of reprogramming might have been achieved.

After noticing a change in the mRNA expression in primary microglial cells, DNA methylation analyses were realized.

2.4. Methylation profiles of reactive microglial cells exhibit differences according to time of exposure and treatment condition

As with the BV2 study, the mouse methylation arrays from Illumina were used on the DNA extracted from primary microglial cells treated or not with LPS, IFN-ɣ, IL-4 and CM-GL261. The analysis was realized using GenomeStudio software measuring the methylation level (β-value) at each CpG site for each microglial sample, and comparing each treatment methylation pattern with the respective timepoint controls.

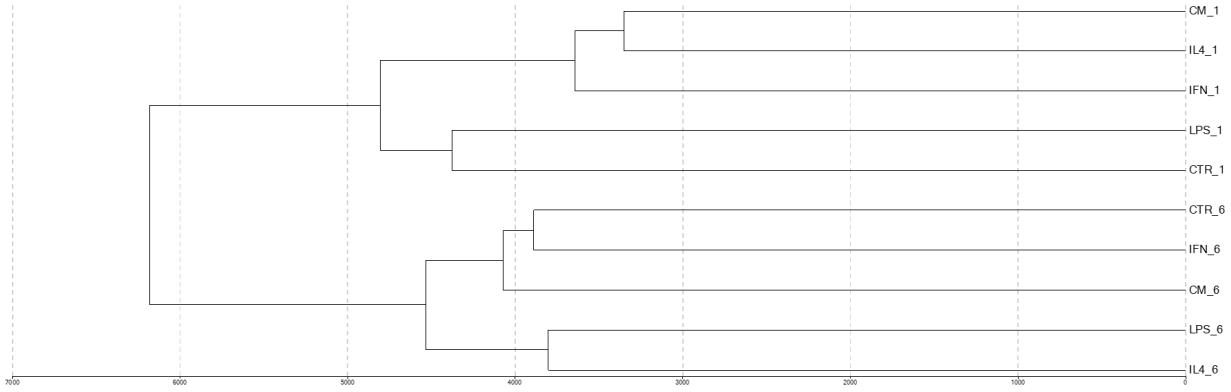

Figure 52. DNA methylation profiles of treated microglial cells cluster according to the time of treatment:

Effect of 10 ng/mL of LPS, IL-4, IFN-ɣ or CM-GL261 treatment for one or six hours on primary microglial cells DNA methylation patterns. Raw data from MethylMouse arrays were exported into Illumina GenomeStudio software, annotated using Illumina MouseMethylation 12v1 Annotation_Mus_musculus file; and normalized using IlluminCustom method. The probes located in the X and Y chromosomes were filtered and all the probes left were used in a hierarchical clustering using the Manhattan method. Results from three independent experiments.

Figure 52 shows the result of a hierarchical clustering based on all the detected probes, and we notice that the samples cluster related to the time of treatment, suggesting that the methylation profiles of the samples might be more strongly influenced by the culture condition as by treatment conditions.

2.5. Significant DMS are induced by all treatment conditions already after an hour of exposure

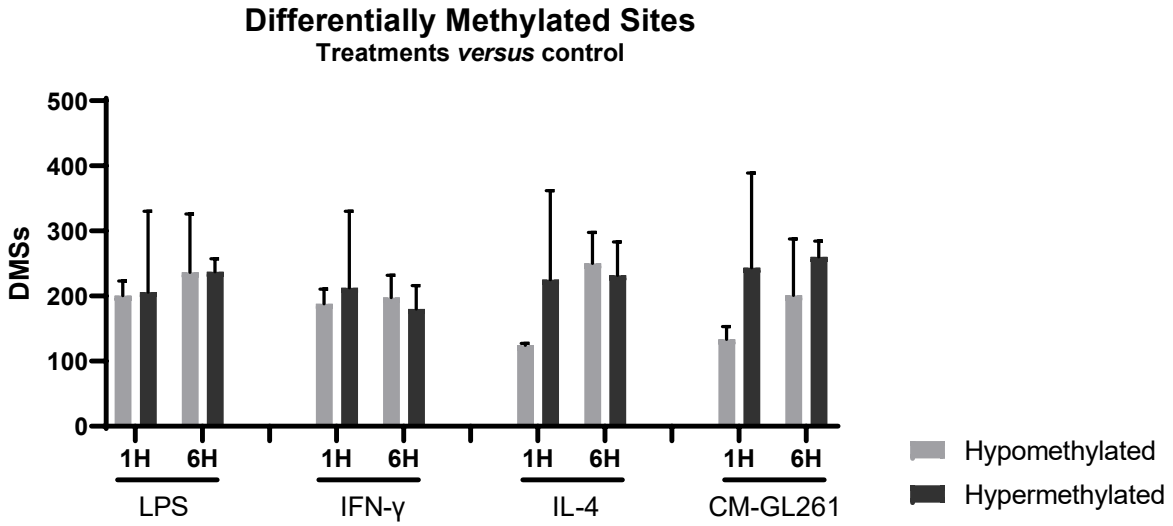

Figure 53. Significant DMS are induced by all treatments in primary microglial cells:

Effect of 10 ng/mL of LPS, IL-4, IFN-ɣ or CM-GL261 treatment for one or six hours on primary microglial cells DNA methylation patterns. Raw data from MethylMouse arrays were exported into Illumina GenomeStudio software, annotated using Illumina MouseMethylation 12v1 Annotation_Mus_musculus file; and normalized using IlluminCustom method before being compared to the control untreated primary microglial cells in order to obtain a score of methylation (DiffScore). The probes located in the X and Y chromosomes were filtered and only the significant DMS were counted and visualized using GraphPad Prism®. Significance was calculated according to the DiffScore, </= 13 or >/= -13 for a P-value < 0.05, FDR adjusted. Results from three independent experiments.

Figure 53 displays the overall significant hypo- and hypermethylated DMS induced by all treatment conditions compared to the control at the one and six hours timepoints.

We find significant DMS in all treatments and timepoint conditions, characterized by a similar range of DMS in each condition, together with equivalent ratio of hypo- and hypermethylated DMS, regardless of the treatment and the timepoint. We can take note that an hour exposure with IL-4 and CM-GL261 treatments are leading to less hypomethylation than the other conditions. In addition, except for the IFN-ɣ condition, all the treatment conditions lead to more DMS after six hour than after one hour of treatment. Finally, it is worth noting that the hypermethylated DMS exhibit a higher variation between biological replicates, suggesting that the hypomethylated ones could be more biologically meaningfull for the microglia to respond to the treatment exposure.

Because the significant DMS induced in primary microglial cells after one and six hours of LPS, IFN-ɣ, IL-4 and CM-GL261 exposure does not exhibit clear-cut differences, we decided to explore in more depth the localization of the probes differentially methylated in each condition.

2.6. Primary microglia exposed to LPS treatment for one or six hours exhibit significant DNA methylation changes, mostly in intergenic regions

In Figure 54, the localizations of the DMS between the LPS condition and the untreated control primary microglial cells at the one and six hours timepoints are presented, according to the distance between the probe (C-G dinucleotide) and the TSS of the gene.

In this Figure, the term “TSS-200” refers to a C-G probe located between 0 and 200 base pairs upstream the TSS, “TSS-1500” inbetween 200 and 1500 base pairs and “bodies” refers to a probe located between the ATG and the stop codon while “intergenics” means that the probe is found in between coding regions, not associated with any genomic features.

Most of the DMS induced by LPS regardless of the timepoint are located in the intergenic regions with similar ratios of hypo- and hypermethylated DMS at the different genetic locations, regardless of the time of exposure. Concerning differences induced by the time of exposure to LPS, no difference were observed, except for the gene bodies in which we noticed a slight increase in the amount of DMS from one to six hours of treatment (from 128 to 184 DMS). Concerning the promoter region, encompassing the TSS-200 and the TSS-1500, we do not notice huge variations but an increase in hypermethylation of the TSS-200 located probes from one to six hours (from three to eight DMS).

Those results are suggesting a reorganization of the DNA methylation patterns in reaction to LPS exposure in primary microglial cells, which would be similar between one and six hours of exposure.

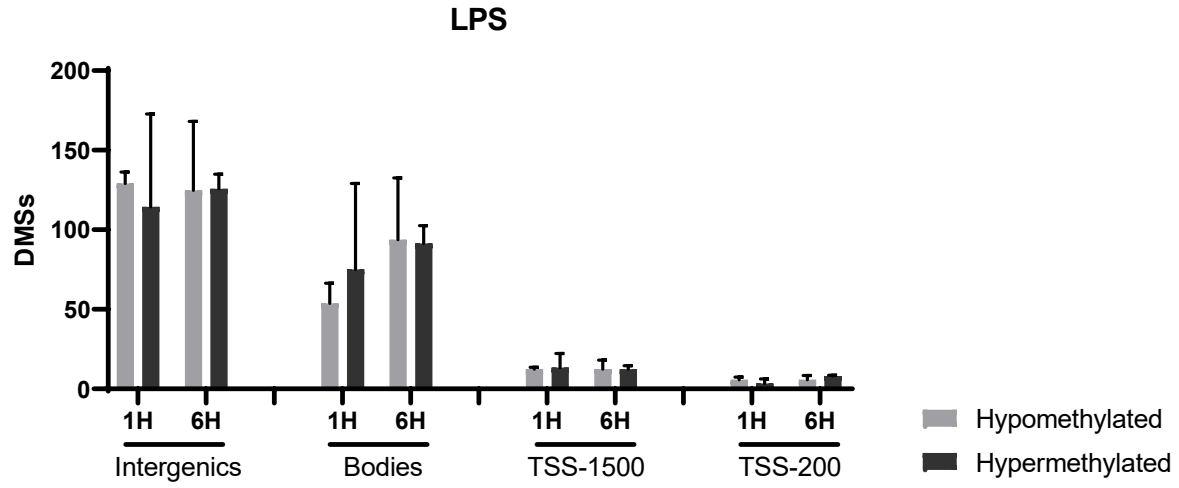

Figure 54. Most of the significant DMS induced by LPS treatment are located in intergenic regions:

Effect of 10 ng/mL of LPS treatment for one or six hours on primary microglial cells DNA methylation patterns. Raw data from MethylMouse arrays were exported into Illumina GenomeStudio software, annotated using Illumina MouseMethylation 12v1 Annotation_Mus_musculus file; and normalized using IlluminCustom method before being compared to the control untreated primary microglial cells in order to obtain a score of methylation (DiffScore). The probes located in the X and Y chromosomes were filtered. The significant DMS were plotted using GraphPad Prism®. Significance was calculated according to the DiffScore, </= 13 or >/= -13 for a P-Value < 0.05, FDR adjusted. Significant DMS in LPS condition compared to the control: localization according to genetic annotation. TSS200 = 0 to 200 kb upstream the TSS; TSS1500 = 200 to 1500 kb upstream the TSS; Bodies = between the ATG and the stop codon; Intergenics = with no annotated genomic features. Results from three independent experiments.

Figure 55A and B show the significant DMS in the LPS condition compared to the control at one and six hours timepoints, respectively. The heatmaps display in rows the mean β-value at each site, ranging from 0 (green) unmethylated to 1 (red) fully methylated. The columns display the treatment conditions.

In 55A, we see that, for this set of DMS, the direction of methylation is very similar between control and treatments mostly towards hypomethylation compared to the control. We notice slight differences in the methylation profiles of each treatment condition, suggesting the induction of DNA methylation reorganization specific to each treatment after one hour in primary microglial cells. In Figure 55B, more distinct DNA methylation profiles between the treatments are observed, with LPS

and IL-4 displaying similarly hypo- and hypermethylated probes while IFN-ɣ and the CM-GL261 resemble more the control methylation pattern.

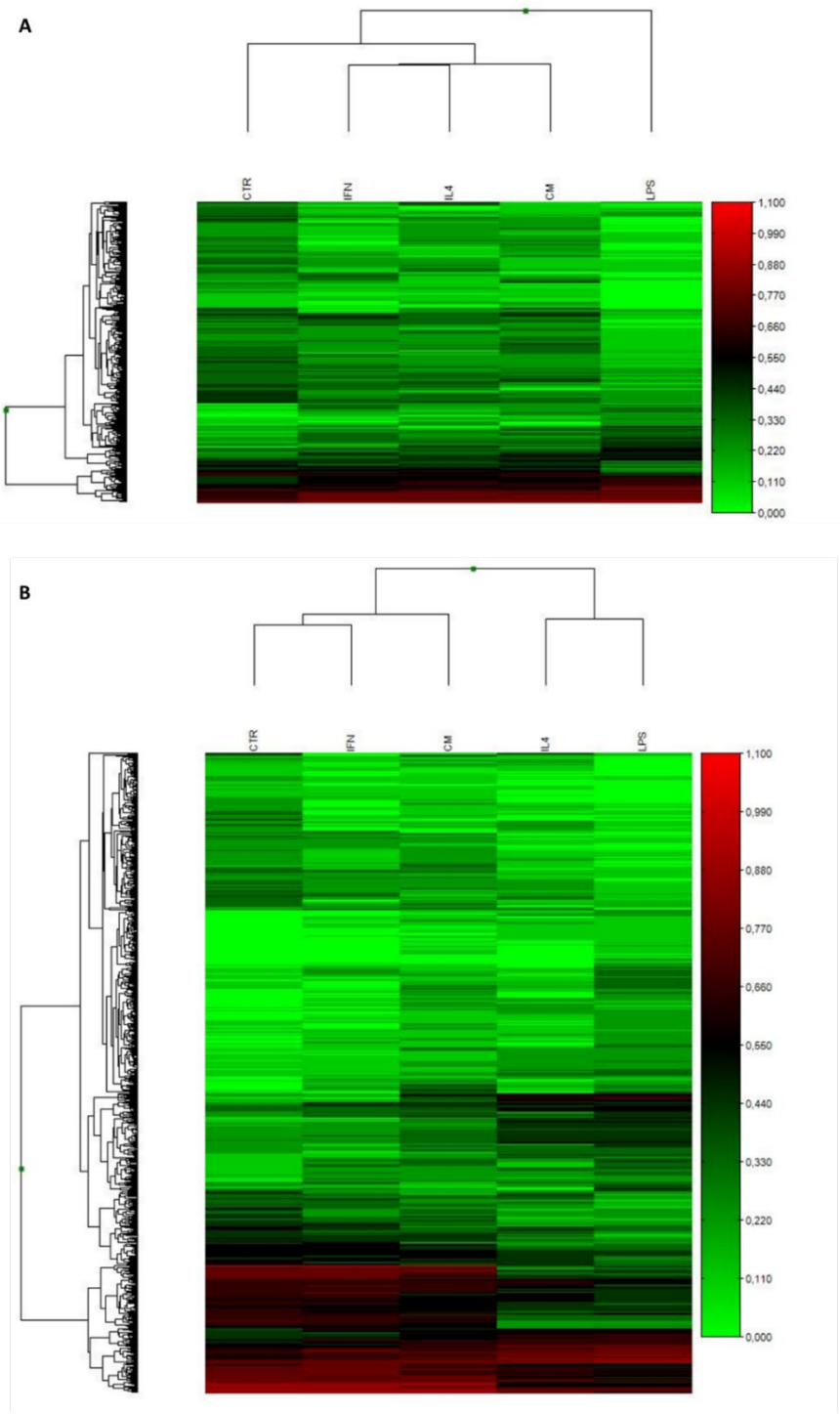

Figure 55. Significant DMS in LPS treatment display specific patterns for each treatment after six hours:

Effect of 10 ng/mL of LPS, IFN-ɣ, IL-4 and CM-GL261 on the DNA methylation patterns of primary microglial cells. Heatmap displaying the mean methylation values (β-Value) of the significant DMS in LPS condition compared to the control, in each treatment condition after one hour (A) and six hours (B). Realized on GenomeStudio. The β-values are displayed according to a color ranging from light green (0, unmethylated) to deep red (1, fully methylated). Results from three independent experiments.

We conclude that primary microglia exposed to LPS treatment exhibit significant DMS in all genomic features with the majority being located in intergenic regions. Those significant DMS display a DNA methylation signature that tends to be higly specific after an hour of treatment but seems to resemble to the one displayed by IL-4 after six hours of exposure.

2.7. Primary microglia exposed to IFN-ɣ treatment display significant DNA methylation changes, mostly located in intergenic regions

Figure 56 presents the genetic annotation of the DMS between the IFN-ɣ condition and the untreated control primary microglial cells at the one and six hours timepoints.

Similarly to the LPS condition, most of the DMS induced by IFN-ɣ regardless of the timepoint are located in the intergenic regions and the ratio of hypo- and hypermethylated DMS are similar at the different genetic locations. No relevant difference were observed regarding the time of exposure to IFN-ɣ, which is reflected by a high amount of highly similar DMS at one and six hours. Concerning the promoter region, encompassing the TSS-200 and the TSS-1500, we do not observe clear cut variation but an increase in hypermethylation of the TSS-200 located probes from one to six hours (from nine to 13 DMS).

Those results are suggesting a reorganization of the DNA methylation patterns in reaction to IFN-ɣ exposure in primary microglial cells that would be similar between one and six hours of exposure.

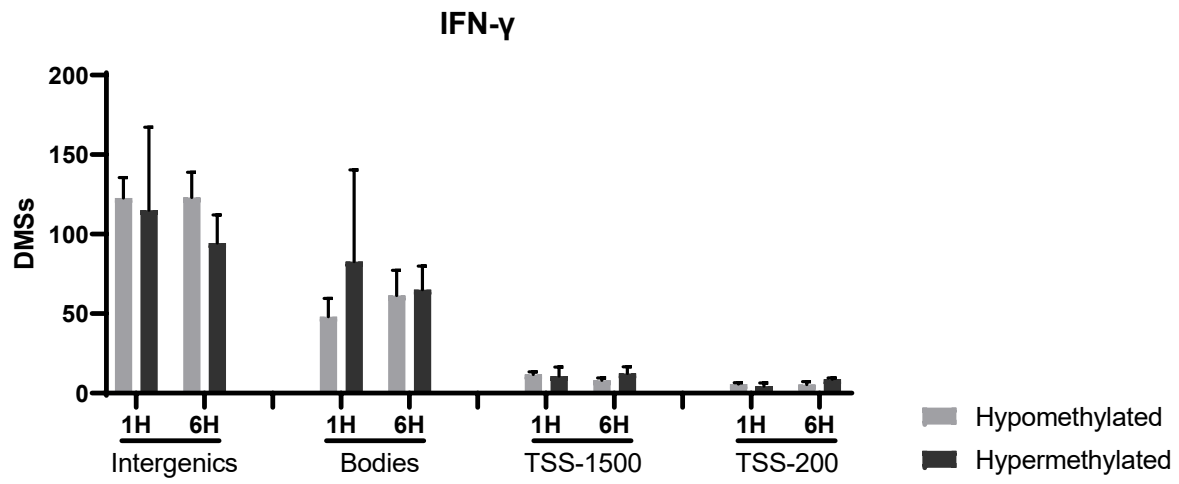

Figure 56. Most of the significant DMS induced by IFN-ɣ treatment are located in intergenic regions:

Effect of 10 ng/mL of IFN-ɣ treatment for one or six hours on primary microglial cells DNA methylation patterns. Raw data from MethylMouse arrays were exported into Illumina GenomeStudio software, annotated using Illumina MouseMethylation 12v1 Annotation_Mus_musculus file; and normalized using IlluminCustom method before being compared to the control untreated primary microglial cells in order to obtain a score of methylation (DiffScore). The probes located in the X and Y chromosomes were filtered. The significant DMS were plotted using GraphPad Prism®. Significance was calculated according to the DiffScore, </= 13 or >/= -13 for a P-value < 0.05, FDR adjusted. Significant DMS in IFN-ɣ condition compared to the control: localization according to genetic annotation. TSS200 = 0 to 200 kb upstream the TSS; TSS1500 = 200 to 1500 kb upstream the TSS; Bodies = between the ATG and the stop codon; Intergenics = with no annotated genomic features. Results from three independent experiments.

Figure 57A and B show the significant DMS in the IFN-ɣ condition compared to the control at one and six hours timepoints, respectively. The heatmaps display in rows the mean β-value at each site, ranging from 0 (green) unmethylated to 1 (red) fully methylated. The column displays the treatment conditions.

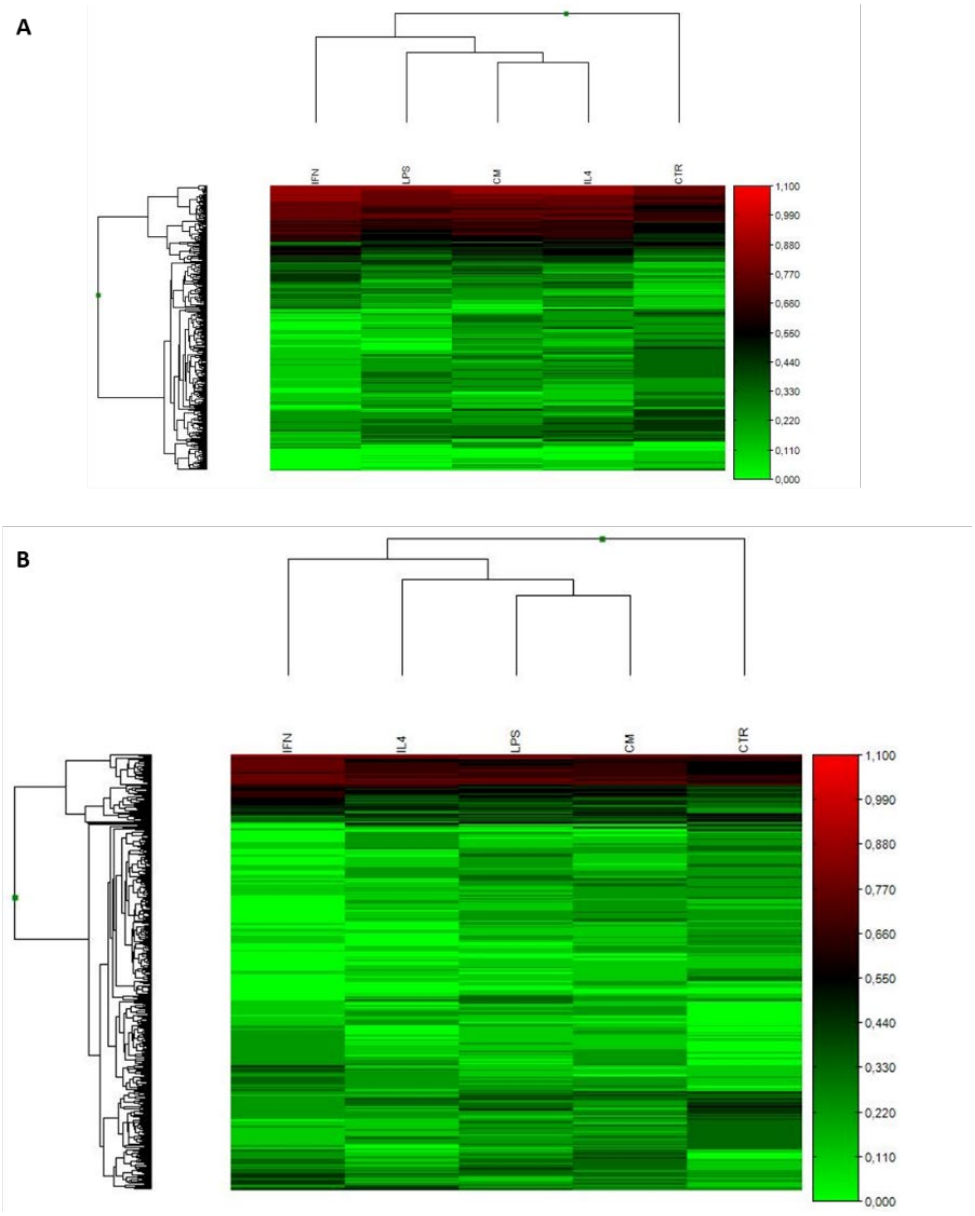

Figure 57. Significant DMS in IFN-γ treated primary microglia exhibit subtle but unique methylation levels amongst treatments:

Effect of 10 ng/mL of LPS, IFN-ɣ, IL-4 and CM-GL261 on the DNA methylation patterns of primary microglial cells. Heatmap displaying the mean methylation values (β-Value) of the significant DMS in IFN-ɣ condition compared to the control, in each treatment condition after one hour (A) and six hours (B). Realized on GenomeStudio. The β-Values are displayed according to a color ranging from light green (0, unmethylated) to deep red (1, fully methylated). Results from three independent experiments.

In A, we observe that, for this set of DMS, the directions of methylation are very similar between control and treatments. Nonetheless, we notice that each treatment exhibits a distinct signature and that the control is clustered alone on the side of all treatments, suggesting that all treatments could

lead to a trend in DNA methylation reorganization after one hour of treatment. In B, we observe an enhancement of the patterns seen after an hour of treatment, the clusters staying the same and the direction of methylation pointing towards hypomethylation in all condition, control included. The similarities seen in the LPS condition before are not found for this set of DMS, suggesting that the sites differentially methylated in the IFN-ɣ condition could be treatments sensitive.

We conclude that primary microglia exposed to IFN-ɣ treatment exhibit significant DMS in all genomic regions with the majority being located in intergenic regions. Those significant DMS displays an overall unique DNA methylation signature after already an hour of exposure, compared to control but also other treatment conditions.

2.8. Primary microglia exposed to IL-4 treatment show significant DNA methylation changes, mostly located in intergenic regions and gene bodies

Figure 58 presents the genetic annotation of the DMS between the IL-4 condition and the untreated control primary microglial cells at one and six hours timepoints.

Similarly to the LPS and IFN-ɣ conditions, most of the DMS induced by IL-4 regardless of the timepoint are located in the intergenic regions and the ratios of hypo- and hypermethylated DMS are similar at the different genetic locations after six hours of treatment. It is worth noting that after an hour of treatment, IL-4 is mostly leading to a hypermethylation of all the genetic localizations. Nevertheless, the amount of DMS between one and six hours of IL-4 exposure remains highly similar.

Concerning the promoter region, encompassing the TSS-200 and the TSS-1500, there is only a slight increase in hypermethylation of those probes from one to six hours (from 10 to 13 and 4 to 7 DMS for TSS-1500 and TSS-200, respectively).

Those results suggest a gradual reorganization of the DNA methylation patterns of primary microglia in reaction to IL-4 exposure between one and six hours.

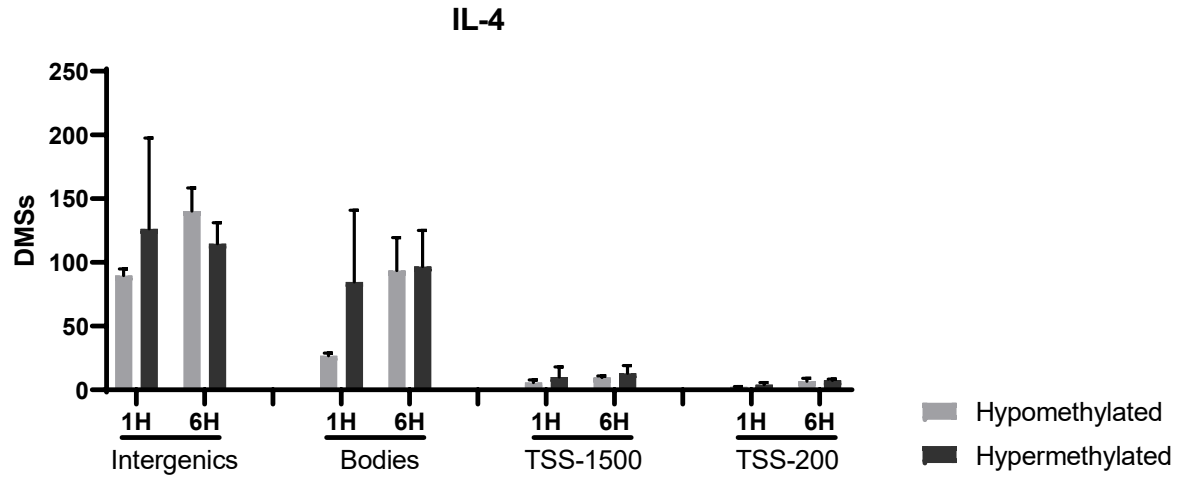

Figure 58. Most of the significant DMS induced by IL-4 treatment are located in intergenic regions and gene bodies in primary microglial cells:

Effect of 10 ng/mL of IL-4 treatment for one or six hours on primary microglial cells DNA methylation patterns. Raw data from MethylMouse arrays were exported into Illumina GenomeStudio software, annotated using Illumina MouseMethylation 12v1 Annotation_Mus_musculus file; and normalized using IlluminCustom method before being compared to the control untreated primary microglial cells in order to obtain a score of methylation (DiffScore). The probes located in the X and Y chromosomes were filtered. The significant DMS were plotted using GraphPad Prism®. Significance was calculated according to the DiffScore, </= 13 or >/= -13 for a P-value < 0.05, FDR adjusted. Significant DMS in IL-4 condition compared to the control: localization according to genetic annotation. TSS200 = 0 to 200 kb upstream the TSS; TSS1500 = 200 to 1500 kb upstream the TSS; Bodies = between the ATG and the stop codon; Intergenics = with no annotated genomic features. Results from three independent experiments.

Figure 59A and B show the significant DMS in the IL-4 condition compared to the control at one and six hours timepoints, respectively. The heatmaps display in rows the mean β-value at each site, ranging from 0 (green) unmethylated to 1 (red) fully methylated. The column displays the treatment conditions.

In A, we find that, for this set of DMS, the direction of methylation is very similar between control and treatments. As seen previously, we observe that each treatment exhibits a distinct signature and that the control is clustered alone on the side of all treatments, suggesting that all treatments could lead to a trend in DNA methylation reorganization after one hour of treatment. In B, we can observe a change within the clustering of the treatment condition, the IL-4 being clustered with the LPS, a cluster that we have observed many times in the BV2 cell model.

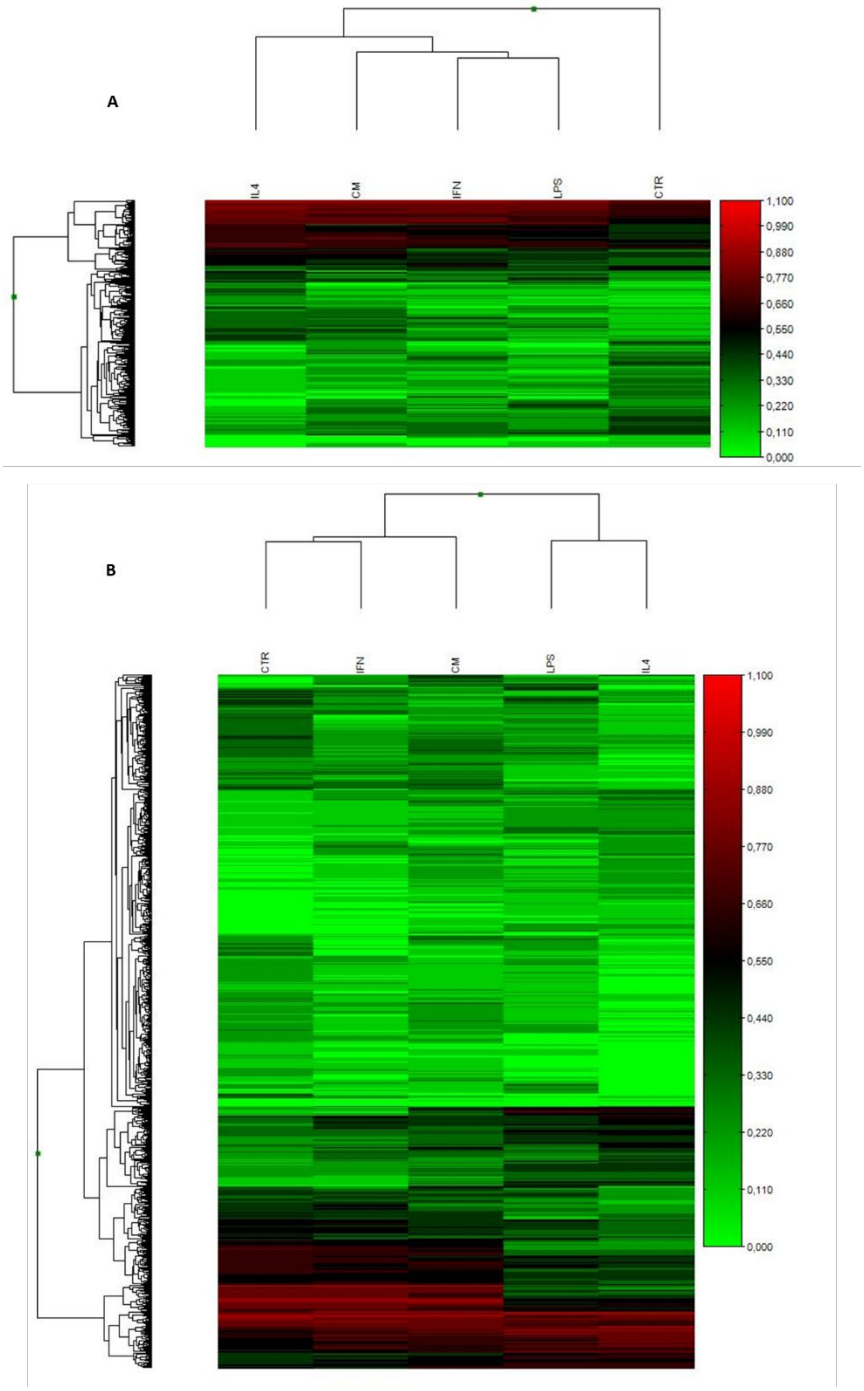

Figure 59. DMS induced by IL-4 related to all treatment conditions:

Effect of 10 ng/mL of LPS, IFN-ɣ, IL-4 and CM-GL261 on the DNA methylation patterns of primary microglial cells. Heatmap displaying the mean methylation values (β-Value) of the significant DMS in IL-4 condition compared to the control, in each treatment condition after one hour (A) and six hours (B). Realized on GenomeStudio. The β-Values are displayed according to a color ranging from light green (0, unmethylated) to deep red (1, fully methylated). Results from three independent experiments.

We conclude that primary microglia exposed to IL-4 treatment exhibit significant DMS in all genomic features with the majority being located in intergenic regions and gene bodies. Those significant DMS display a DNA methylation signature that tends to be higly specific after an hour of treatment but seems to resemble to the one displayed by LPS after six hours of exposure. Even though the underlying mechanisms are not known, this cluster between IL-4 and LPS at the DNA methylation level has been also observed within the BV2 model and suggests a common mechanism of response from microglia to those treatments. Because of the dual phenotypical effects induced by LPS and IL-4, it would be interesting to search for such a common DNA methylation regulation.

2.9. Primary microglia exposed to CM-Gl261 treatment show significant DNA methylation changes, mostly located in intergenic regions

On Figure 60 is presented the genetic annotation of the DMS between the CM-GL261 condition and the untreated control primary microglial cells at the one and six hours timepoints.

Similarly to the all the other conditions, we note that most of the DMS induced by CM-GL261 regardless of the timepoint are located in the intergenic regions, that the ratio of hypo- and hypermethylated DMS are similar at the different genetic locations after one and six hour of treatment and that amount of DMS between one and six hours of CM-GL261 exposure remains highly similar.

Concerning the promoter region, encompassing the TSS-200 and the TSS-1500, we can again notice a very slight increase in hypermethylation of those probes from one to six hours (from 11 to 14 and 4 to 6 DMS for TSS-1500 and TSS-200, respectively).

Those results are suggesting a gradual reorganization of the DNA methylation patterns of primary microglia in reaction to CM-GL261 exposure between one and six hours.

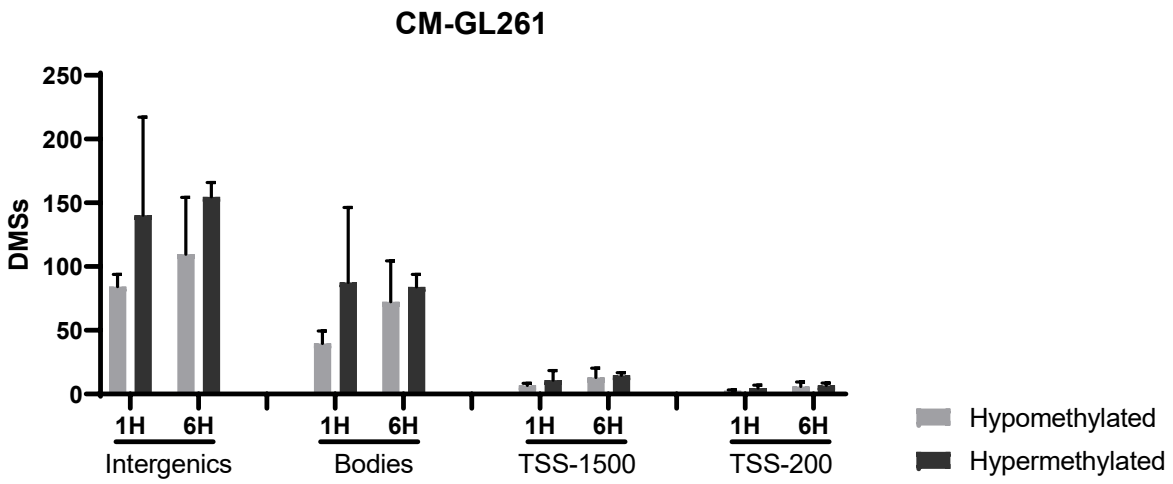

Figure 60. Significant DMS induced by CM-GL261 are mostly located in intergenic regions :

Effect of CM-GL261 treatment for one or six hours on primary microglial cells DNA methylation patterns. Raw data from MethylMouse arrays were exported into Illumina GenomeStudio software, annotated using Illumina MouseMethylation 12v1 Annotation_Mus_musculus file; and normalized using IlluminCustom method before being compared to the control untreated primary microglial cells in order to obtain a score of methylation (DiffScore). The probes located in the X and Y chromosomes were filtered. The significant DMS were plotted using GraphPad Prism®. Significance was calculated according to the DiffScore, </= 13 or >/= -13 for a P-value < 0.05, FDR adjusted. Significant DMS in CM-GL261 condition compared to the control: localization according to genetic annotation. TSS200 = 0 to 200 kb upstream the TSS; TSS1500 = 200 to 1500 kb upstream the TSS; Bodies = between the ATG and the stop codon; Intergenics = with no annotated genomic features. Results from three independent experiments.

Figure 61A and B show the significant DMS in the CM-GL261 condition compared to the control at one and six hours timepoints, respectively. The heatmaps display in rows the mean β-value at each site, ranging from 0 (green) unmethylated to 1 (red) fully methylated. The column displays the treatment conditions.

In A, we see that, for this set of DMS, the direction of methylation is very similar between control and treatments. As seen previously, we observe that each treatment exhibits a distinct signature and that the control is clustered alone on the side of all treatments, suggesting that all treatments could lead to a trend in DNA methylation reorganization after one hour of treatment. In B, we find a change within the clustering of the treatment conditions. Again, we can observe that the IL-4 is clustered with the

LPS, indicating that those treatments, on long term, could lead to similar DNA methylation patterns in primary microglial cells.

We conclude that primary microglia exposed to CM-GL261 treatment exhibit significant DMS in all genomic features with the majority being located in intergenic regions. Those significant DMS displays an overall unique DNA methylation signature after already an hour of exposure, compared to control but also other treatment conditions.

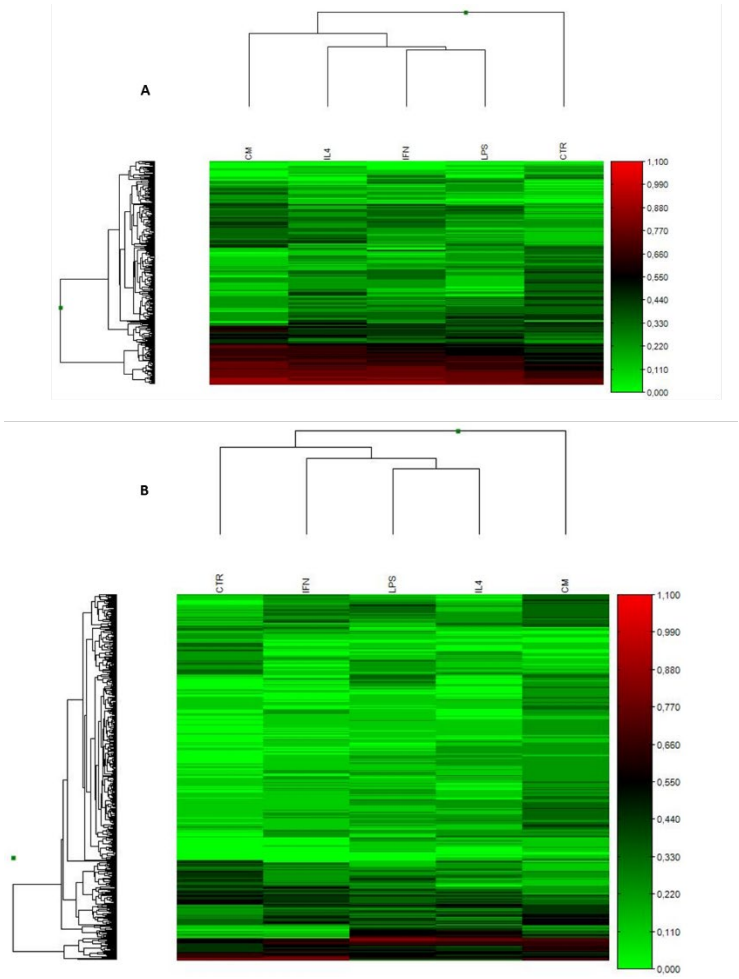

Figure 61. Significant DMS induced by CM-GL261 exhibit similar methylation levels compared to all treatments:

Effect of 10 ng/mL of LPS, IFN-ɣ, IL-4 and CM-GL261 on the DNA methylation patterns of primary microglial cells. Heatmap displaying the mean methylation values (β-Value) of the significant DMS in CM-GL261 condition compared to the control, in each treatment condition after one hour (A) and six hours (B). Realized on GenomeStudio. The β-Values are displayed according to a color ranging from

light green (0, unmethylated) to deep red (1, fully methylated). Results from three independent experiments.

We can conclude that all treatments have an effect on the DNA methylation patterns, impacting greatly intergenic regions and gene bodies, together with few modifications within the promoter regions of genes. Those results could suggest that the methylation outside of gene promoters might represent an underlying mechanism of microglial reactivity to environmental stimulation.

We also notice that even if all treatment seem to induce the same trends in overall methylation profiles, as we have seen in the BV2 cell line model, we observe subtle divergences in each DMS methylation level in primary microglial cells leading to treatment-specific methylation patterns and suggesting an intense DNA methylation plasticity compared to the BV2 cells.

3.0. Primary microglia exposed for one and six hours to LPS, IFN-ɣ, IL-4 and CM-GL261 exhibit few common differentially methylated genes without an associated gene ontology

To understand how gene regulation could be affected by changes in DNA methylation patterns induced by the treatments in primary microglial cells, DMGs were compared in each treatment. Figure 62 presents the overlapping DMGs after an hour (A), six hours (B) and common between one and six hours (C).

On A, we observe that the same 179 genes are differentially methylated in all the treatment conditions, representing ~22% of all the DMGs in the LPS condition and in between ~17% and ~19% for the CM-GL261, IFN-ɣ and IL-4 conditions. We can also notice that the percentage of treatment specific DMGs is quiet low, ~20-25% for IFN-ɣ, IL-4 and LPS and 33% in the CM-GL261 condition, suggesting that most of the DMGs are not specifically differentially methylated in response to one treatment but represent a mechanism of reactivity shared by multiple treatments after one hour.

In B, we find the same trends, 155 genes commonly differentially methylated across treatments, representing at the maximum ~27% of unique DMGs in the IL-4 condition and ~20% in the other treatment conditions. The percentage of shared DMGs across all treatments is lower after six hours, with ~19% for the CM-GL261 and IFN-ɣ conditions and ~7% for the LPS and IL-4 conditions. Those numbers suggest that the initial microglial reactivity could be a DNA methylation common mechanism targeting shared genes in all treatment conditions after one hour and that after six hours then, treatment specific genes are differentially methylated.

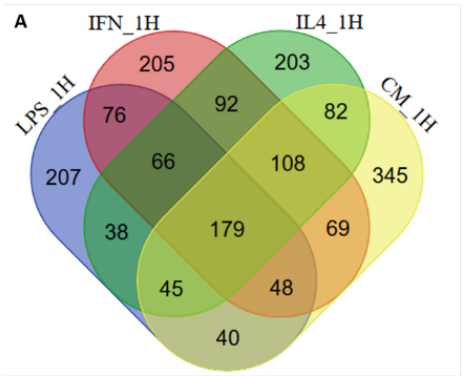

List names	number of elements
CM_1H	1052
IFN_1H	991
IL4_1H	928
LPS_1H	804

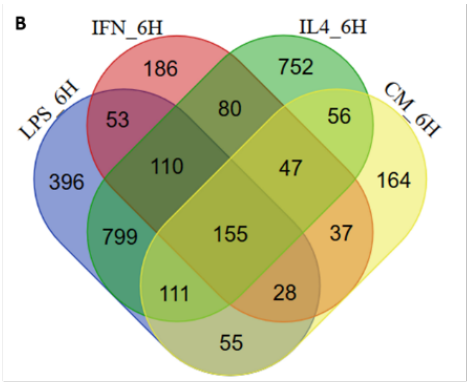

List names	number of elements
CM_6H	795
IFN_6H	827
IL4_6H	2761
LPS_6H	2221

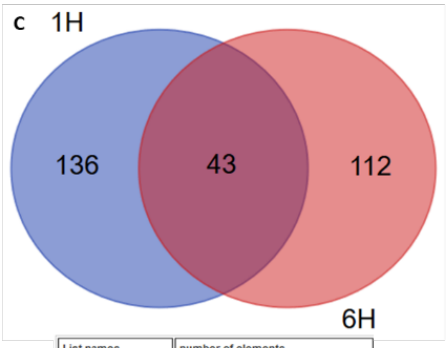

List names	number of elements
1H	179
6H	155

D

Symbol	Ensembl Gene ID	Type	Chr	Description
Ifi202b	ENSMUSG00000026535	protein_coding	1	interferon activated gene 202B [Source:MGI Symbol;Acc:MGI:1347083]
Adal	ENSMUSG00000027259	protein_coding	2	adenosine deaminase-like [Source:MGI Symbol;Acc:MGI:1923144]
Ccl21a	ENSMUSG00000094686	protein_coding	4	chemokine (C-C motif) ligand 21A (serine) [Source:MGI Symbol;Acc:MGI:1349183]
Foxp1	ENSMUSG00000030067	protein_coding	6	forkhead box P1 [Source:MGI Symbol;Acc:MGI:1914004]
Atf7ip	ENSMUSG00000030213	protein_coding	6	activating transcription factor 7 interacting protein [Source:MGI Symbol;Acc:MGI:1858965]
Nipa2	ENSMUSG00000030452	protein_coding	7	non imprinted in Prader-Willi/Angelman syndrome 2 homolog (human) [Source:MGI Symbol;Acc:MGI:1913918]
Sfrp1	ENSMUSG00000031548	protein_coding	8	secreted frizzled-related protein 1 [Source:MGI Symbol;Acc:MGI:892014]
Tns3	ENSMUSG00000020422	protein_coding	11	tensin 3 [Source:MGI Symbol;Acc:MGI:2443012]
Meis1	ENSMUSG00000020160	protein_coding	11	Meis homeobox 1 [Source:MGI Symbol;Acc:MGI:104717]
Adarb2	ENSMUSG00000052551	protein_coding	13	adenosine deaminase, RNA-specific, B2 [Source:MGI Symbol;Acc:MGI:2151118]

Figure 62. Primary microglia exposed for one and six hours to LPS, IFN-ɣ, IL-4 and CM-GL261 show few common differentially methylated genes:

Effect of 10 ng/mL of LPS, IL-4, IFN-ɣ or CM-GL261 treatment for one or six hours on primary microglial cells DNA methylation patterns. Raw data from MethylMouse arrays were exported into Illumina GenomeStudio software, annotated using Illumina MouseMethylation 12v1 Annotation_Mus_musculus file; and normalized using IlluminCustom method before being compared to the control untreated primary microglial cells in order to obtain a score of methylation (DiffScore). The probes located in the X and Y chromosomes were filtered and only the significant DMS were used. The significant DMS located in Intergenic regions were filtered and only the probes located in annotated genes were used. The resulting DMGs within each treatment and timepoint conditions were plotted in a Venn Diagram to highlight the overlapping DMGs between (A) treatments after an hour; (B) treatments after six hours and (C) all treatments-common DMGs between the one and the six hours timepoints. (D) Table of tens of the DMGs common to all treatments and timepoints, generated by ShinyGO v0.80. Significance was calculated according to the DiffScore, </= 13 or >/= -13 for a P-value < 0.05, FDR adjusted. Results from three independent experiments.

Finally, we observe in C, that 43 genes are differentially methylated in all treatments and timepoint conditions, probably constituting the shared DNA methylation response to all treatments in primary microglial cells. No biologically relevant gene ontology analysis could be found. However, few genes could be associated with microglial reactivity. Ten of those genes, coding for TFs and immunomodulatory proteins are detailed in D.

To try to understand the relationship between DNA methylation and gene expression, a gene, *Ifi202b*, significantly differentially methylated in all conditions was selected and its mRNA expression was assessed using RTqPCR.

3.1. No correlation was observed between methylation level of the *Ifi202b* and its mRNA expression

On Figure 63 are displayed the mean methylation level of each probe (targeting each one a CpG site) located within the *Ifi202b* gene after one hour (A) or six hours (B) of treatment with LPS (red squares), IFN-ɣ (green triangles), IL-4 (blue triangles), CM-GL261 (purple losanges) or untreated (orange circles) primary microglial cells.

The probes are annotated on the X-axis while the Y-axis shows the mean methylation of each probe for each treatment, only the cg37797509_TC11 and cg37797509_TC12 are significantly differentially methylated in all treatment conditions compared to the control. On Figure 63C and D, are showed the RTqPCR results for the expression of the *Ifi202b* mRNA expression, in E, the summary of the probes features.

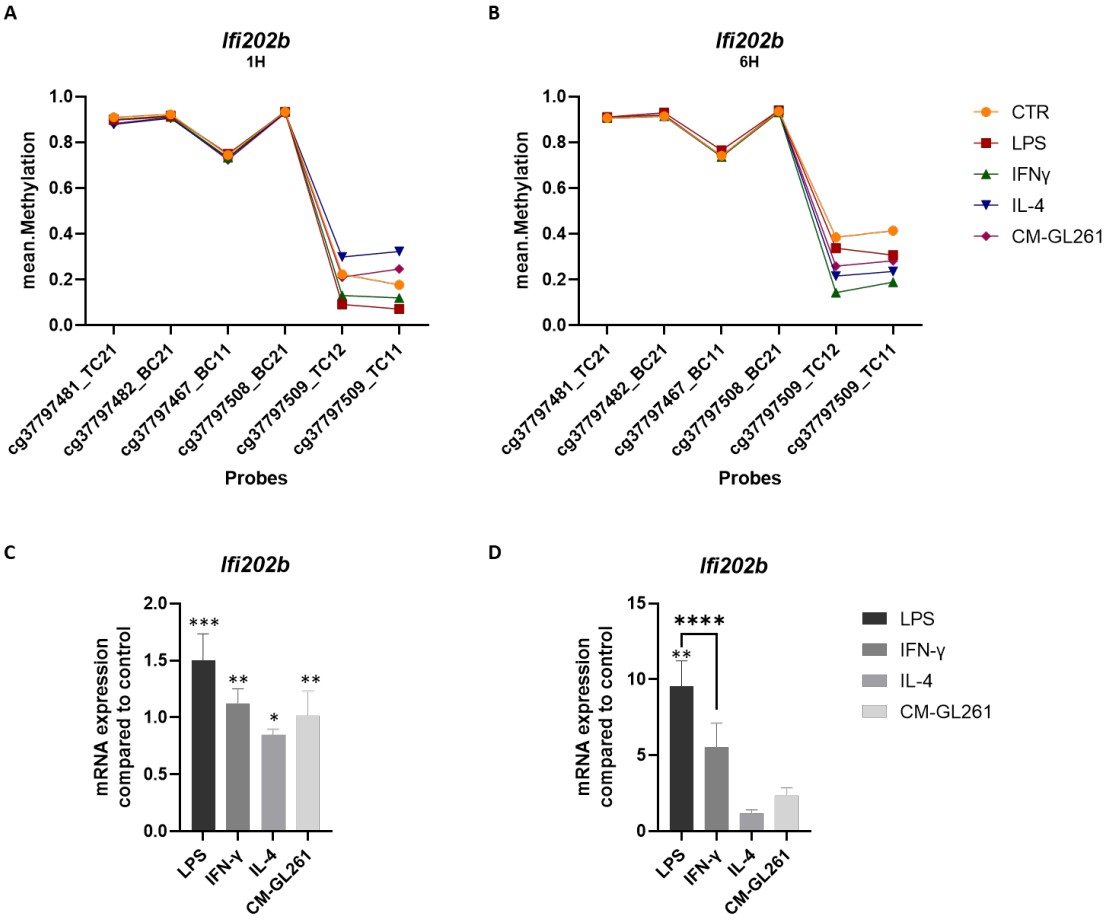

Figure 63. DNA methylation patterns and mRNA expression of *Ifi202b* are not correlated:

Effect of 10 ng/mL of LPS, IL-4, IFN-ɣ or CM-GL261 treatment for one or six hours on the DNA methylation patterns (A and B) and the mRNA expression (C and D) of the *Ifi202b* gene in primary microglial cells. (A and B) Raw data from MethylMouse arrays were exported into Illumina GenomeStudio software, annotated using Illumina MouseMethylation 12v1 Annotation_Mus_musculus file; and normalized using IlluminCustom method. The mean β-value for each probe located within the *Ifi202b* were plotted using GraphPad Prim 9.0. Results from three independent experiments. (C and D) Raw RT-qPCR results targeting *Ifi202b* mRNA were exported into Microsoft Excel and normalized to untreated cells. *Rpl27* was used as a housekeeping gene for normalization of gene expression. Statistical analysis was performed using GraphPadPrism 9 and applying one-way ANOVA with a correction for multiple comparisons between the control and the treatments (Dunnett) and inbetween treatments (Tukey). Data are representative of three independent experiments, each of which done in technical triplicates and are represented as mean ± Standard Error of the Mean (SEM). * indicate a P-value < 0,05; ** indicate a P-value < 0,01; *** indicate a P-value < 0,001; **** indicate a P-value < 0,0001. (E) Illumina annotation file concerning the probes located within the *Ifi202b* gene.

We notice on A and B, that only the probes cg37797509_TC11 and cg37797509_TC12 are significantly differentially methylated between the treatment and the control conditions, the rest of the probes exhibiting similar methylation levels. Indeed, we can see that the methylation levels for those probes are similar inbetween each other at one particular timepoint.

In A, at one hour, those probes show a methylation level of 0.31 for IL-4; 0.23 for CM-GL261; 0.19 for the control; 0.12 for IFN-ɣ and 0.08 for LPS. Those probes being hypomethylated in IFN-ɣ and LPS conditions and hypermethylated in IL-4 and CM-GL261, compared to the control after one hour. In B, at six hours timepoint, those probes being all hypomethylated compared to the control with methylation levels of 0.39 for the control; 0.32 for LPS; 0.27 for CM-GL261; 0.22 for IL-4 and 0.16 for IFN-ɣ.

As the scale of methylation range from 0 being unmethylated to 1 being fully methylated, we find that all conditions, including the control untreated cells, tend to exhibit an hypomethylation for those probes, the hypomethylation just being increased in IFN-ɣ and LPS after one hour and, in all conditions after six hours of treatment.

While we observe in C and D that the mRNA levels of *Ifi202b* are significantly changed by the treatment conditions after an hour and by LPS only after six hours, we can also note that even the trends of expression does not match the DNA methylation patterns.

Indeed, after one hour of treatment, the IL-4 and CM-GL261 shows a hypermethylation compared to control (A) and a trend of upregulation of the mRNA expression (C); while the IFN-ɣ and the LPS shows a hypomethylation (A) and an even more upregulation of *Ifi202b* expression (C). In D, we notice that all treatment are exhibiting a trend of upregulation of *Ifi202b* expression and an hypomethylation compared to control (B) but if we look at the methylation levels, the LPS shows the lowest hypomethylation (B) and the highest upregulation (D) while the IFN-ɣ shows the highest hypomethylation compared to control but an upregulation significantly lower than the LPS one.

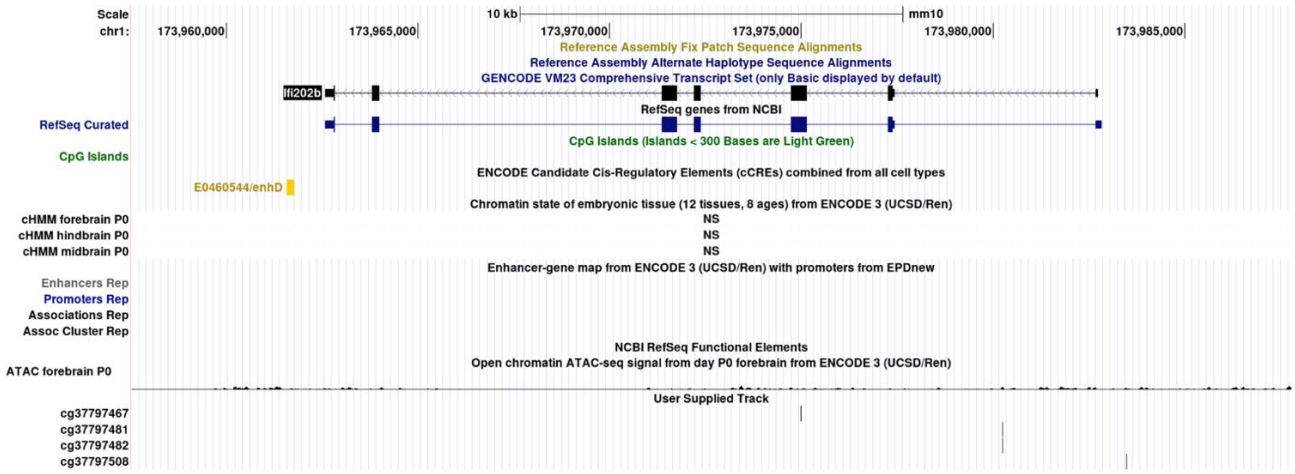

Figure 64. UCSC Genome browser tracks do not provide evidence for a link between DNA methylation and gene expression of *Ifi202b*:

UCSC Genome Browser view of the *Ifi202b* gene from mouse GRCm38/mm10 genome, including tracks (from top to bottom) for CpG islands; ENCODE cis-regulatory elements, chromatin states predicted according to the ChIP-seq databases on forebrain, hindbrain and midbrain of P0 mouse pups; enhancers and promoters functional associations, ATAC-seq database on forebrain of P0 mouse pups and Illumina Mouse Methyl probe localizations.

In addition, Figure 64 shows that no genomic regulatory element is indicated at the position of the probes on UCSC genome browser that could have explained the effect of the DNA methylation level at those positions on the gene expression. We can also observe that no information is available on the predicted chromatin states and the ATAC-seq results tends to exhibit a non accessible chromatin, making it difficult to even hypothesize on the gene expression regulation of *Ifi202b*.

In fine, we can not conclude on the role of DNA methylation in the expression of the *Ifi202b* gene in reactive microglial cells. We can nevertheless hypothesize that other epigenetic mechanisms, like histone modifications, have to be involved in its expression.

3.2. Methylation level of *Ubc* and related mRNA expression do not correlate

To try to understand the relationship between DNA methylation and gene expression, a gene, *Ubc*, only differentially methylated in the IFN-ɣ condition was selected and its mRNA expression was assessed using RTqPCR.

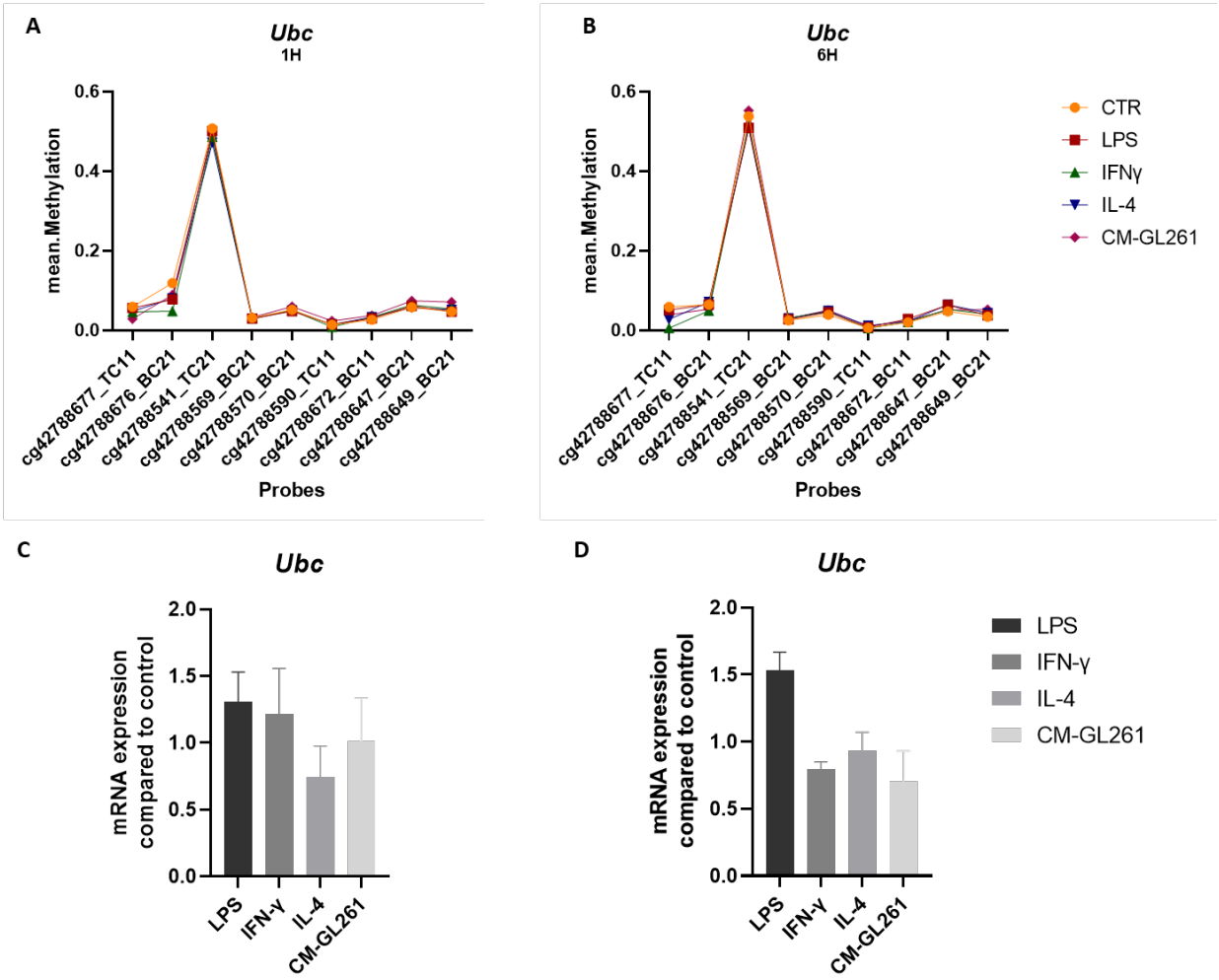

Figure 65. DNA methylation levels and mRNA expression of *Ubc* do not correlate:

Effect of 10 ng/mL of LPS, IL-4, IFN-ɣ or CM-GL261 treatment for one or six hours on the DNA methylation patterns (A and B) and the mRNA expression (C and D) of the *Ubc* gene in primary microglial cells. (A and B) Raw data from MethylMouse arrays were exported into Illumina GenomeStudio software, annotated using Illumina MouseMethylation 12v1 Annotation_Mus_musculus file; and normalized using IlluminCustom method. The mean β-value for each probe located within the *Ubc* were plotted using GraphPad Prim 9.0. Results from three independent experiments. (C and D) Raw RT-qPCR results targeting *Ubc* mRNA were exported into Microsoft Excel and normalized to untreated cells. *Rpl27* was used as a housekeeping gene for normalization of gene expression. Statistical analysis was performed using GraphPadPrism 9 and applying two-way ANOVA with a correction for multiple comparisons (Tukey). Data are representative of three independent experiments, each of which done in technical triplicates and are represented as mean ± Standard Error of the Mean (SEM). **** indicate a P-value < 0,0001.

Figure 65 displays the mean methylation level of each probe (targeting each one a CpG site) located within the *Ubc* gene after one hour (A) or six hours (B) of treatment with LPS (red squares), IFN-ɣ (green triangles), IL-4 (blue triangles), CM-GL261 (purple losanges) or untreated (orange circles) primary microglial cells. The probes are annotated on the X-axis while the Y-axis shows the mean methylation of each probe for each treatment, only the cg42788676_BC21 at one hour and cg42788677_TC11 at six hours in the IFN-ɣ condition are significantly differentially methylated compared to the control. On Figure 65C and D, are showed the RTqPCR results for the expression of the *Ubc* mRNA expression, in E, the summary of the probe features.

Figure 65A shows that only the probe cg42788676_BC21 is significantly differentially methylated when comparing IFN-ɣ treatment with control conditions, while the rest of the probes exhibits similar methylation levels.

Indeed, we see that the methylation levels for this probe at one hour are 0.12 for the control; 0.09 for CM-GL261; 0.08 for IL-4; 0.07 for LPS and 0.05 for IFN-ɣ. This probe remains hypomethylated in all condition compared to the control after one hour.

In B, we can interestingly note that a different probe is significantly differentially methylated between the IFN-ɣ and the control, the probe cg4288677_TC11 with methylation levels of 0.06 for the control; 0.05 for LPS; 0.04 for CM-GL261; 0.03 for IL-4 and 0.006 for IFN-ɣ. This probe remains hypomethylated in all condition compared to the control after six hours.

As the scale of methylation ranges from 0 (unmethylated) to 1 (fully methylated), we observe that all conditions, including the control untreated cells tends to exhibit an hypomethylation for those probes, while the hypomethylation is increased in IFN-ɣ after one and six hours of treatment.

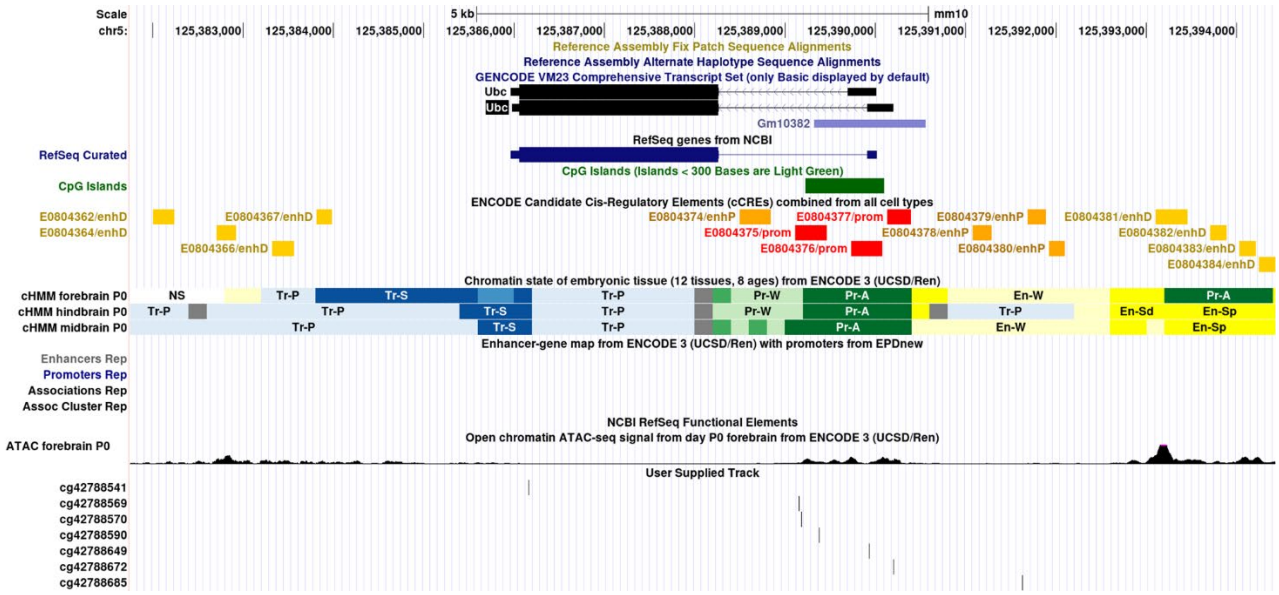

Figure 66. UCSC Genome browser tracks show regulatory elements potentially explaining the gene expression regulation of *Ubc* gene:

UCSC Genome Browser view of the *Ubc* gene from mouse GRCm38/mm10 genome, including tracks (from top to bottom) for CpG islands; ENCODE cis-regulatory elements, chromatin states predicted according to the ChIP-seq databases on forebrain, hindbrain and midbrain of P0 mouse pups; enhancers and promoters functional associations, ATAC-seq database on forebrain of P0 mouse pups and Illumina Mouse Methyl probe localizations.

We notice in Figure 66 that the regulation of *Ubc* gene expression is highly complicated. Indeed, we find the presence of numerous proximal and distal regulatory elements, the presence of a CpG island and chromatin states mostly related to transcriptional activation. We can see that Illumina's probes that are overlapping such regulatory elements are not significantly differentially methylated in our study.

Unfortunately, the two significant probes cg42788676 and cg42788677 were not annotated in UCSC, thus not appearing on Figure 66. Nevertheless, manual interrogation of the UCSC Genome browser database for the localization of significant probes (Mouse GRCm38/mm10 chr5:125,539,217-125,391,517) revealed that two regulatory elements are overlapping the probe. First, the EM10E0804377 promoter, localized on the chromosome 5 from position 125,390,134 to 125,390,399 and second, the EM10E0804378 proximal enhancer, localized from position 125,391,080 to 125,391,285. The presence of those regulatory elements indicates that the differential methylation of the DNA at those positions could have serious effects on the expression of the *Ubc* gene.

However, we can notice in Figure 65C and D, that the mRNA levels of *Ubc* are not significantly changed by the treatment conditions at any timepoint. We can nevertheless note that the trends of mRNA expression tend to be towards upregulation in all conditions at both timepoints compared to the control; and even insignificant, all the conditions tend to show hypomethylation of the regulatory elements of the *Ubc* gene compared to the control.

Thus, we can not conclude about the role of DNA methylation in the regulation of the expression of the *Ubc* gene in reactive microglial cells. As previously mentioned, we can hypothesize that other epigenetic mechanisms are regulating the expression of the *Ubc* gene.

We conclude that the LPS, IFN-ɣ, IL-4 and CM-GL261 treatments are inducing a phenotypical reactivity in primary microglial cells after one and six hours of exposure and that DNA methylation pattern modifications are observed. Those patterns appear to be treatment-specific in primary microglial cells, depicting distinct methylation profiles for each treatment after one and six hours of exposure, with similarities in the direction of methylation but subtle individual CpGs sites differences. Nevertheless, no significant correlation is observed between DNA methylation and gene expression in primary reactive microglial cells. We could hypothesize that other epigenetic mechanisms, such as ncRNAs and histone modifications, are entangled with DNA methylation to regulate gene expression underlying microglial reactivity.

In summary, we observed a phenotypical reprogramming of primary microglial cells upon treatment with LPS, IFN-ɣ, IL-4 and CM-GL261 for one and six hours, characterized by considerable morphological and significant transcriptomic changes. We could also discover significant DNA methylation reorganization at both time points of exposure in all treatment conditions, mostly located in intergenic regions and gene bodies.

It is worth noting that those changes in both epigenetic landscapes and phenotypes were significant at earlier time points of exposure as compared to the BV2 microglia model, suggesting an increased sensitivity exhibited by primary microglia towards stimulation.

3. Primary male and female CD-1 microglial cells exhibit dismorphic DNA methylation reorganization upon treatments

To finalize the project, we wanted to explore if the sexual dimorphism known in microglial cells could be observed in DNA methylation pattern modifications in reaction to LPS and CM-GL261 treatments. Microglial cells from genotyped CD-1 pups were isolated and treated for 24 hours with 10 ng/mL of LPS or CM-GL261. As previously, a Cell Titer Glo assay and an Incucyte® monitoring were performed to make sure the treatments were not affecting significantly the viability and proliferation.

3.1. Treatments significantly affect the viability but not the proliferation of male and female primary microglial cells

Figure 67 exhibits the percentage of viability of the primary microglial cells treated with LPS or CM-GL261, normalized to the control untreated cells. The X-axis shows the treatment conditions, while the Y-axis displays the percentage of viability compared to the control untreated cells set as 100% and the color indicates the sex of the microglial cells.

We observe significant changes between the control group and the treatment groups, regardless of the sex. Indeed, the LPS-treated microglial cells male and female show a significant increase of ~9% of viability compared to the control, while the CM-GL261 condition shows decrease of ~20% of viability for both male and female.

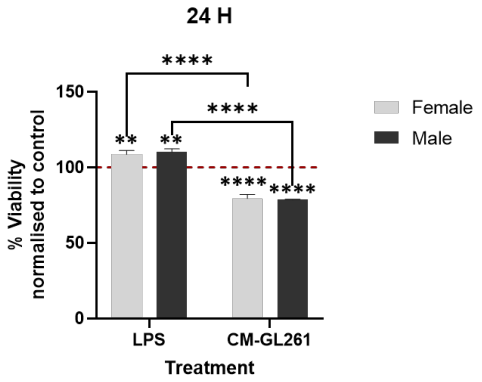

Figure 67. Viability of primary microglial cells is significantly impacted by LPS and CM-GL261:

Effect of 10 ng/mL of LPS or CM-GL261 exposure on the viability of male and female primary microglial cells treated for 24 hours. The cell viability of treated cells was assessed relatively to the control, untreated cells (red line). Statistical analysis by applying a Two-way ANOVA with multiple comparisons between treatments (Tukey) and between treatment and control (Dunnett) GraphPadPrism 9. Data are representative of three independent experiments, each of which done in technical triplicates and are represented as mean ± Standard Error of the Mean (SEM). ** indicate a P-value < 0.001; **** Indicating a P-value < 0.0001.

The significant decrease in microglial viability regarding to the CM-GL261 treatment at 24 hours confirms the trend observed in primary microglial cells treated for six hours (Figure 48). This trend was not observed in BV2 microglial cell line (Figure 23), suggesting a sensitivity of the primary microglial cells to the culture media. Nonetheless, a viability of ~80% is still acceptable to perform experiments.

Figure 68 shows the measure of confluence made by the Incucyte® system on the primary microglial cells treated or not with LPS or CM-GL261 for 24 hours (A, C, E and G) and the cell numbers in each condition counted manually on the Incucyte® pictures (B, D, F and H), normalized to the control untreated cells values. The confluence graphs (A, C, E and G) display the time in hours on X-axis, while the Y-axis presents the percentage of confluence normalized to the control.

We find that no significant change is induced in microglia confluence by LPS and CM-GL261 treatments compared to the control untreated microglia after 24 hours. Despite the absence of significance, we note the same trends in male and female, the LPS is inducing an increase trend (A and C) in confluence compared to the control untreated microglia, while the CM-GL261 inducing a decreased trend (E and G).

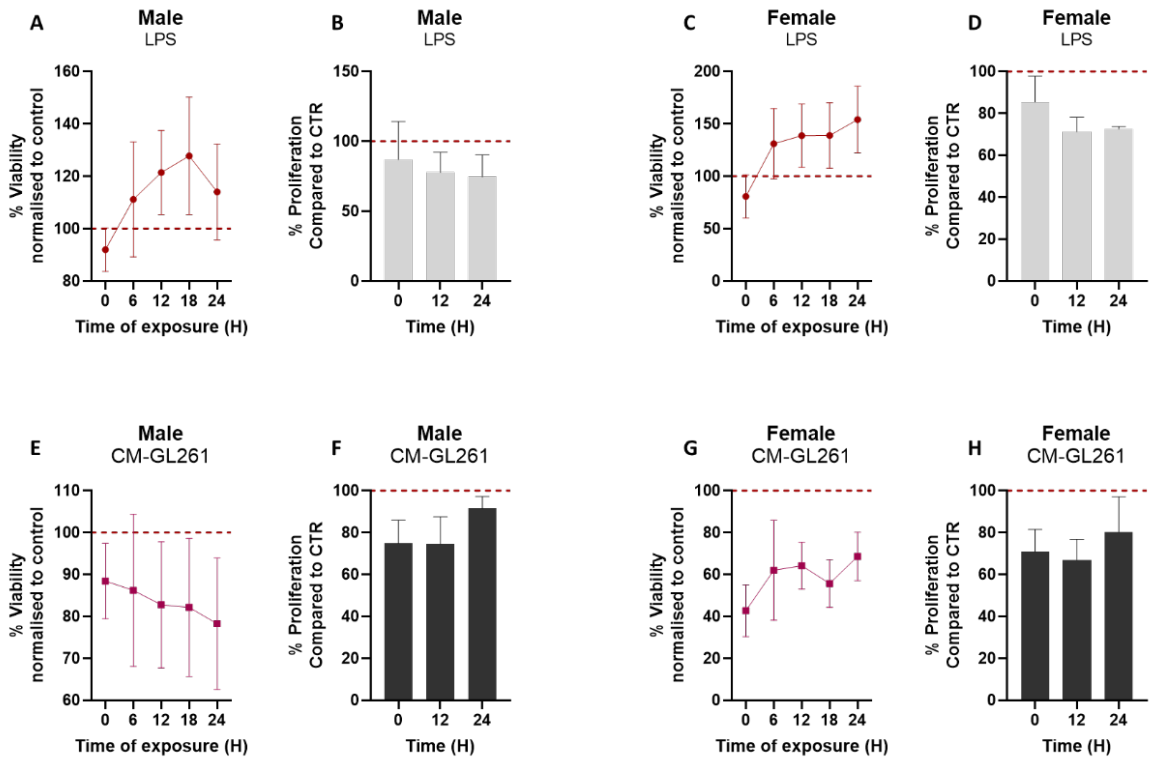

Figure 68. LPS and CM-GL261 do not lead to significant changes in microglial proliferation:

Effect of 10 ng/mL of LPS (top panel) or CM-GL261 (bottom panel) exposure on the confluence and proliferation of male (left panel) and female (right panel) primary microglial cells treated for 24 hours. The cellular confluency of treated cells was monitored and analyzed by the Incucyte® system. Proliferation was assessed by counting of the cells from the pictures generated by the Incucyte system and compared to the control (CTR, red line, untreated cells). Statistical analysis was performed using GraphPadPrism 9 applying a two-way ANOVA with correction for multiple comparisons (Tukey). Data are representative of three independent experiments, each of which done in technical triplicates and are represented as mean ± SEM.

The graphs representing the manual counting of the cell numbers (B, D, F and H) exhibit the timepoints in hours on the X-axis and the percentage of the cell numbers (named proliferation) compared to the control. We notice that no significant change in cell number is induced by the treatments compared to the control untreated microglia.

We can nevertheless observe that the measure of the confluence by measuring the area of the cell *versus* the number of the cells is again, not relevant. Indeed, the number of LPS-treated microglia being decreased while the confluence being increased, suggesting again that for morphologically sensitive cells like microglia, the measure of confluence is not representative of the proliferation rate.

We conclude that the 10 ng/mL LPS and CM-GL261 treatments for 24 hours does impact significantly the viability but not the proliferation of primary microglial cells.

3.2. Morphological changes are induced by LPS and CM-GL261 with slight differences between male and female microglia

To observe if the treatments were inducing phenotypical changes in primary microglia, an IF staining was performed.

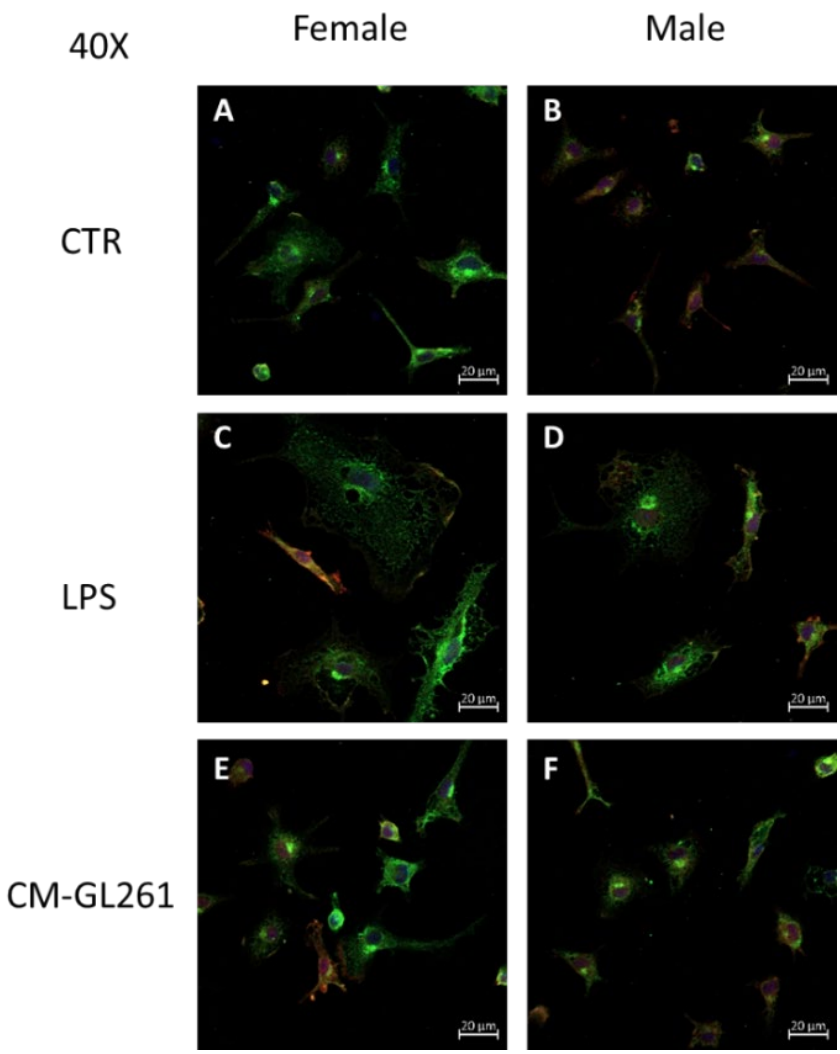

Figure 69. LPS and CM-GL261 lead to morphological changes in primary microglial cells with subtle sex differences:

Morphological assessment of male and female primary microglial cells treated with 10 ng/mL of LPS or CM-GL261 for 24 hours; compared to untreated cells. Confocal images (40X objective) showing the co-labelling of Iba1 (red) and F4/80 (green) in cultured primary microglia. DAPI is shown in blue; scale bar: 20 µm.

On Figure 69 (Annexes 39 and 40 for 20X pictures), we see a change of primary microglia morphology after 24 hours of treatment, especially with LPS.

Compared to the untreated cells and regardless of the sex (CTR, Figure 69A and B), microglia treated with LPS for 24 hours exhibit an important increase in the soma size, with decreased numbers of processes, shorter and thicker (C and D).

On the contrary, we note that compared to control, CM-GL261 treated cells exhibit only a slight difference, the soma of the female microglia is slightly bigger and the processes more elongated (E) but no visible change is seen in the male microglia morphology (F). We cannot observe here the mixed phenotype seen in the previous experiments.

We conclude that the LPS is inducing a morphological change in male and female microglial cells after 24 hours of treatments and that small divergences exist between male and female morphological transformation in response to LPS and CM-GL261 exposure.

3.3. Significant mRNA expression changes are induced by LPS and CM-GL261 treatments, exhibiting differences between male and female microglia

To explore the transcriptomics behind male and female microglial reactivity, RTqPCR were performed on a set of genes known to be part of the pro-inflammatory (*Cxcl10, Tnf, Ccl9, Il-1β*), anti-inflammatory (*Fizz1, Arg1*) and homeostatic (*Cx3cr1, Hexb*) signature of microglial cells.

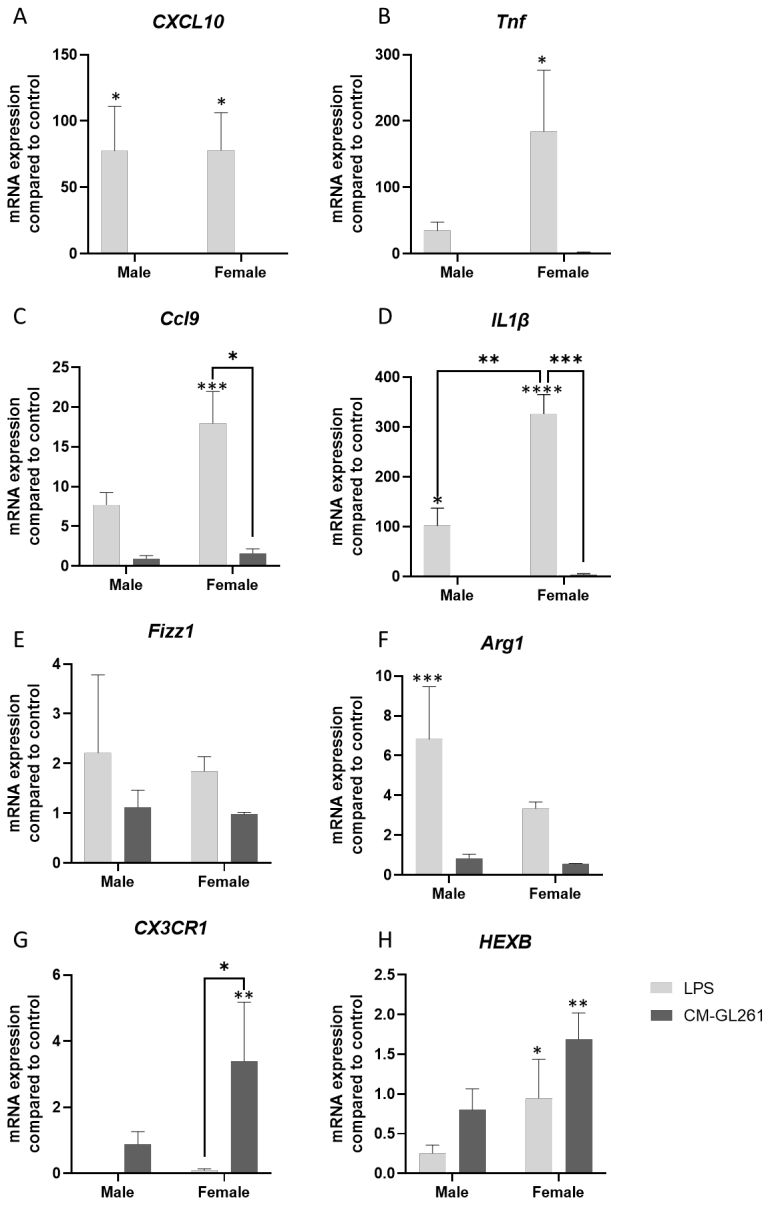

Figure 70. LPS and CM-GL261 lead to significant changes in mRNA expression in primary microglial cells:

Effect of 10 ng/mL of LPS or CM-GL261 exposure on mRNA expression of male and female primary microglial cells treated for 24 hours, normalized to untreated cells. Selected mRNA targets are characteristics of a pro-inflammatory (*Cxcl10*, *Tnf*, *Ccl9* and *IL-1β*), anti-inflammatory (*Arg1* and *Fizz1*) and homeostatic (*Cx3cr1* and *Hexb*) reactivity. Rpl27 was used as a housekeeping gene for normalization of gene expression. Statistical analysis was performed using GraphPadPrism 9 and applying two-way ANOVA with a correction for multiple comparisons for treatments *versus* control (Dunnett) and male versus female or treatment *versus* treatment (Tukey). Data are representative of three independent experiments, each of which done in technical triplicates and are represented as mean ± Standard Error of the Mean (SEM). * indicate a P-value < 0,05; ** indicate a P-value < 0,01; *** indicate a P-value < 0,001.

We decided to measure the quantity of mRNA in primary microglia splitted between male and female treated or not with LPS or CM-GL261 for 24 hours by performing RT-qPCR. We assessed the expression of those mRNA in comparison to the housekeeping gene *Rpl27*. The results, normalized to the control group mRNA counterparts are presented in Figure 70. The top panel of the Figure 70 shows the mRNA expression of pro-inflammatory genes (A, B, C and D), the middle panel the expression of anti-inflammatory associated mRNAs (E and F) and the bottom panel, the expression of homeostatic associated mRNAs (G and H). All the presented graphs X-axis refers to the sex of the microglia; the Y-axis representing the mRNA expression of each gene relative to the control untreated counterpart.

We can see in Figure 70 that the pro-inflammatory associated mRNAs *Cxcl10* (A) and *Il-1β* (D) are significantly induced by the LPS treatment in male and female microglia with values of 77 fold changes for the *Cxcl10* in both male and female; and around 100 and 320 positive fold change for the *Il-1β* mRNA in male and female microglia, respectively compared to the control. The *Tnf* (B) and *Ccl9* (C) mRNAs on the other hand, are only induced by the LPS treatment in female microglial cells with values around 180 and 20 positive fold changes for *Tnf* and *Ccl9*, respectively. The CM-GL261 treatment does not lead to significant change for any of the pro-inflammatory associated mRNA, regardless of the sex.

Concerning the anti-inflammatory associated mRNAs, we find that *Fizz1* (E) expression is not significantly changed by any treatment and regardless of the sex, whereas surprisingly, *Arg1* (F) expression is only significantly induced by the LPS treatment in male microglia with around seven positive fold changes value compared to the control.

Finally, we notice that the homeostatic related mRNAs are significantly induced only in female, LPS leading to nearly one positive fold change increase of *Hexb* expression whereas CM-GL261 leading to nearly 2 positive fold change increase of *Hexb* and around 4 positive fold change increase of *Cx3cr1* expression.

We conclude from Figure 70 that the LPS treatment leads to differential expression of pro- (*Ccl9* and *Tnf*), anti-inflammatory (*Arg1*) and homeostatic (*Hexb*) mRNAs in male and female microglia after 24 hours.

To understand if those phenotypical and transcriptomic changes were related to DNA methylation reorganization, DNA methylation assay using Illumina Methyl Mouse arrays was performed.

3.4. DNA methylation profiles of reactive male and female microglia are clustered by sex and treatments

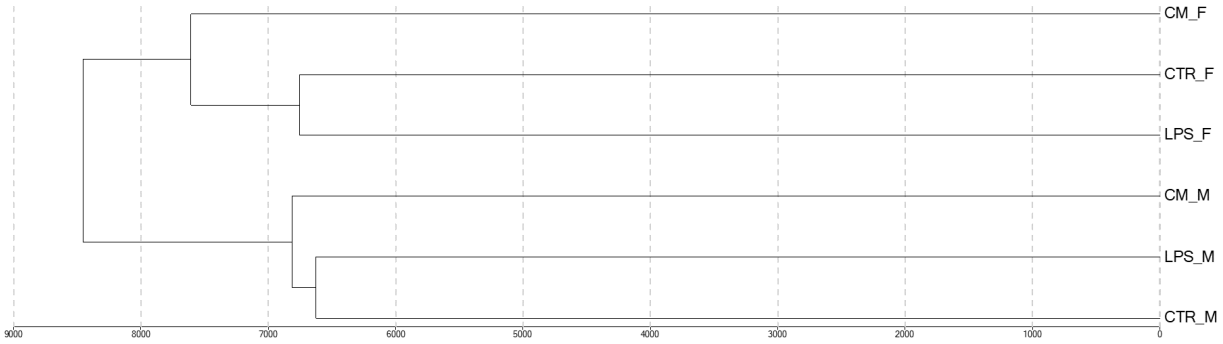

Figure 71. DNA methylation profiles of microglial cells are clustered by sex and treatments:

Effect of 10 ng/mL of LPS or CM-GL261 treatment for 24 hours on male and female primary microglial cells DNA methylation patterns. Raw data from MethylMouse arrays were exported into Illumina GenomeStudio software, annotated using Illumina MouseMethylation 12v1 Annotation_Mus_musculus file; and normalized using IlluminCustom method. The probes located in the X and Y chromosomes were filtered and all the probes left were used in a hierarchical clustering using the Manhattan method. Results from three independent experiments.

Figure 71 shows the hierarchical clustering of the DNA methylation profiles for each sample, the X-axis displays the Manhattan distance between the samples, the Y-axis shows the identification of the sample group. We note a clear separation between male and female regardless of the treatment condition and that the control untreated and LPS microglia are clustered together in both sexes. We can also observe that the LPS and the control conditions are clustered together.

We can already conclude that the DNA methylation profiles of reactive primary microglial cells differ between sexes.

3.5. Primary male and female microglia exhibit significant DMS in reaction to LPS and CM-GL261 exposure for 24 hours

To explore this observation furthermore, the significant DMS between treatment and control in each sex were isolated and plotted in Figure 72, displaying on the Y-axis the number of DMS and in X-axis,

the treatment conditions and the sex of the microglia. The colors used refer as hypomethylated (light grey) and hypermethylated (deep grey) DMS in each condition.

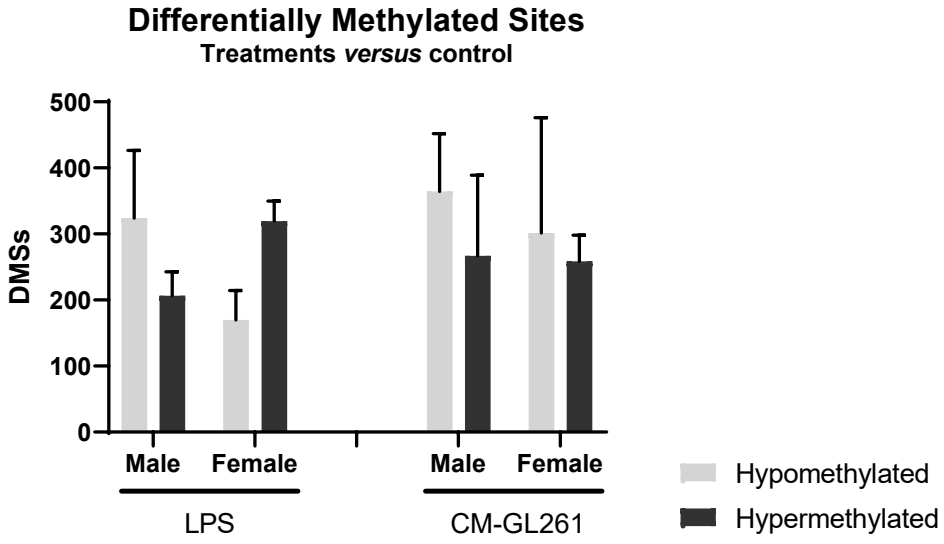

Figure 72. Male and female primary microglia exhibit different DNA methylation reorganization in reaction to LPS and CM-GL261 exposure:

Effect of 10 ng/mL of LPS or CM-GL261 treatment for 24 hours on male and female primary microglial cells DNA methylation patterns. Raw data from MethylMouse arrays were exported into Illumina GenomeStudio software, annotated using Illumina MouseMethylation 12v1 Annotation_Mus_musculus file; and normalized using IlluminCustom method before being compared to the control untreated primary microglial cells in order to obtain a score of methylation (DiffScore). The probes located in the X and Y chromosomes were filtered and only the significant DMS were plotted using GraphPad Prism®. Significance was calculated according to the DiffScore, </= 13 or >/= -13 for a P-value < 0.05, FDR adjusted. Results from three independent experiments.

We notice in Figure 72 that the male microglia display slightly more significant DMS than female in both condition of treatments (average of 550 in CM-GL261; 490 in LPS for female *versus* 630 and 520 for male). We can also observe that the CM-GL261 treatment leads to the same trends in both sexes exhibiting slightly more hypomethylated than hypermethylated DMS. The LPS treatment leads to differential DNA methylation direction mostly towards hypomethylation in male and hypermethylation in female microglia.

We conclude that both treatments lead to significant DMS in male and female microglia compared to control after 24 hours, with different overall methylation between male and female.

3.6. Significant DMS induced by LPS are mostly located in intergenic regions in both male and female microglia but exhibit opposed methylation direction

On Figure 73 are presented the significant DMS between the LPS condition and the untreated control primary male and female microglial cells at the 24 hours timepoint, according to the genetic annotation of the DMS and relative to the distance between the probe and the TSS of the gene.

The terms “TSS-200” refers to a C-G probe located between 0 and 200 base pairs upstream the TSS, “TSS-1500” inbetween 200 and 1500 base pairs and “Bodies” refers to a probe located between the ATG and the stop codon while “Intergenics” means that the probe is found in between coding regions, not associated with any genomic features.

We notice that the treatment with LPS for 24 hours leads to more DMS in male (~530) than in female (~480) and that the DMS in female point mostly toward hypermethylation whereas the DMS in male point mostly towards hypomethylation, highlighting a sex difference reactivity to LPS at the DNA methylation level. Most of the DMS, regardless of the sex of the microglia, are located in intergenic regions.

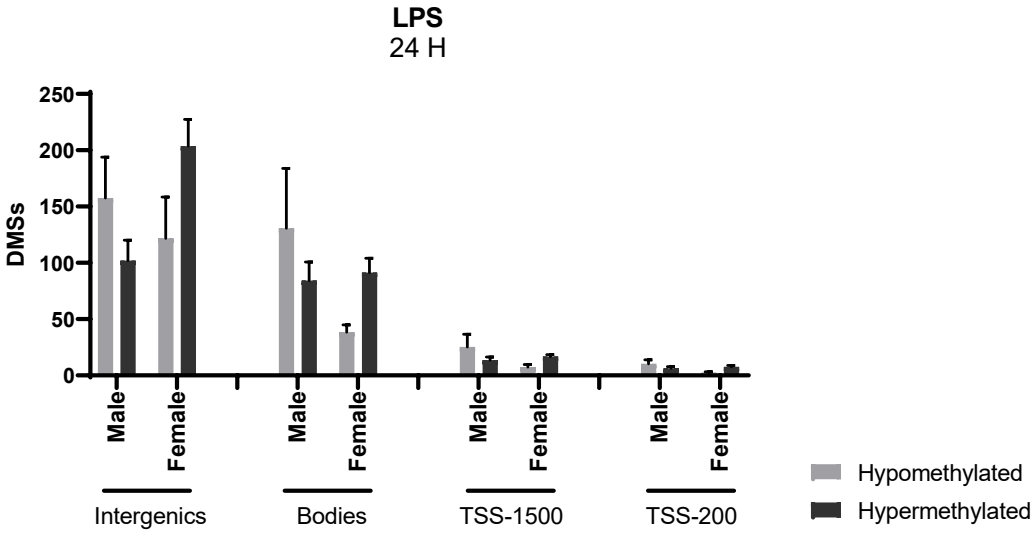

Figure 73. Male and female microglia exposed to LPS for 24 hours exhibit significant DMS in intergenic regions with opposite methylation direction:

Effect of 10 ng/mL of LPS treatment for 24 hours on male and female primary microglial cells DNA methylation patterns. Raw data from MethylMouse arrays were exported into Illumina GenomeStudio software, annotated using Illumina MouseMethylation 12v1 Annotation_Mus_musculus file; and normalized using IlluminCustom method before being compared to the control untreated primary microglial cells in order to obtain a score of methylation (DiffScore). The probes located in the X and Y chromosomes were filtered and only the significant DMS were plotted using GraphPad Prism®. Significance was calculated according to the DiffScore, </= 13 or >/= -13 for a P-value < 0.05, FDR adjusted. Results from three independent experiments.

Figure 74A and B show the significant DMS in the LPS condition compared to the control in male and female microglia, respectively. The heatmaps display in rows the mean β-value at each site, ranging from 0 (green) unmethylated to 1 (red) fully methylated. The columns display the treatment conditions.

In A, we observe that, for this set of DMS in male microglia, the directions of methylation are very similar between control and treatments, mostly towards hypomethylation compared to the control. We can notice slight differences in the methylation profiles of each treatment conditions, the CM-GL261 signature being hypomethylated compared to control but hypermethylated compared to LPS, suggesting the induction of DNA methylation reorganization specific to each treatment after 24 hours in primary male microglial cells. In B, we find that the LPS leads to mostly hypermethylation of DMS in female microglia compared to the control and that the CM-GL261, for this set of DMS, leads to an inbetween control and LPS methylation level.

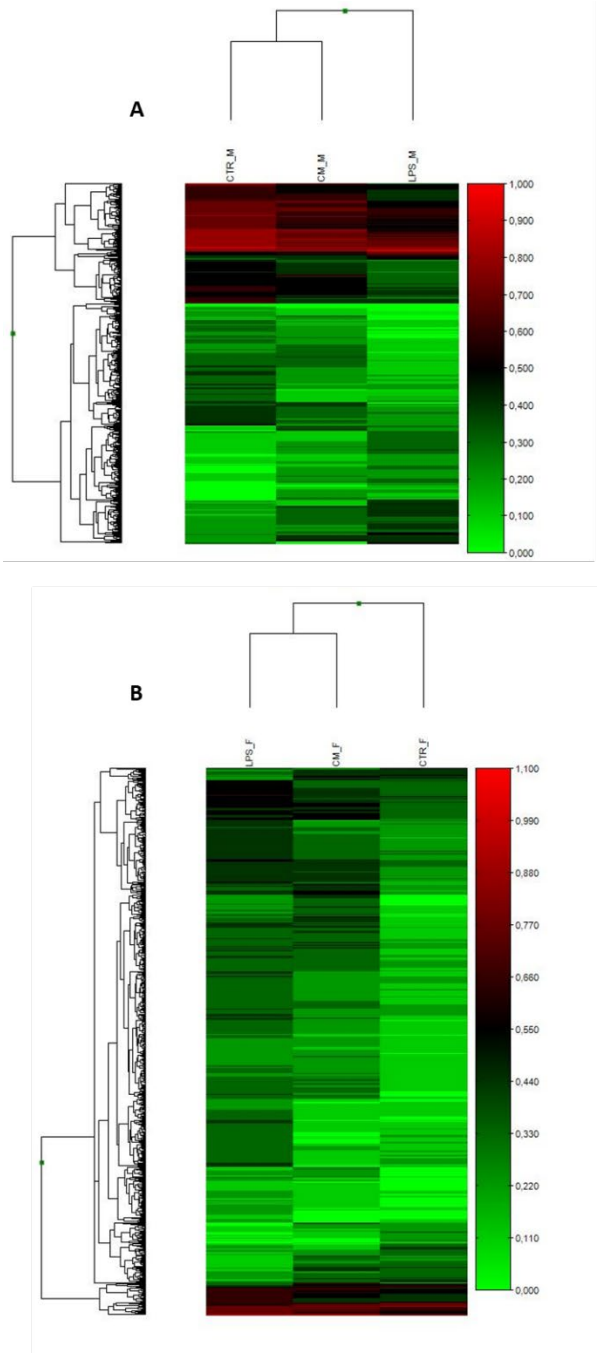

Figure 74. Male and female microglial methylation profiles of LPS-induced significant DMS diverge from CM-GL261:

Effect of 10 ng/mL of LPS on the DNA methylation patterns of male and female primary microglial cells. Heatmap displaying the mean methylation values (β-Value) of the significant DMS in LPS condition compared to the control, in each treatment condition in male (A) and female (B) microglia. Realized on GenomeStudio. The β-Values are displayed according to a color ranging from light green (0, unmethylated) to deep red (1, fully methylated). A hierarchical clustering of the significant DMS and the samples was made using the Manhattan method. Results from three independent experiments.

We can conclude that the LPS treatment is inducing significant DMS in primary microglia, mostly localized in intergenic regions and characterized by hypomethylation in males and hypermethylation in females.

3.7. Significant DMS induced by CM-GL261 are mostly hypermethylated and located in intergenic regions in male and female microglia

On Figure 75 are presented the significant DMS between the CM-GL261 condition and the untreated control primary male and female microglial cells at the 24 hours timepoint, according to the genetic annotation of the DMS and relative to the distance between the probe and the TSS of the gene.

We see that the treatment with CM-GL261 for 24 hours leads to more DMS in male (~620) than in female (~560) and that the DMS in both male and female seem to exhibit a similar ratio between hypo- and hypermethylated DMS, highlighting an homogenous reactivity to CM-GL261 at the DNA methylation level amongst sexes. Most of the DMS, regardless of the sex of the microglia, are located in intergenic regions.

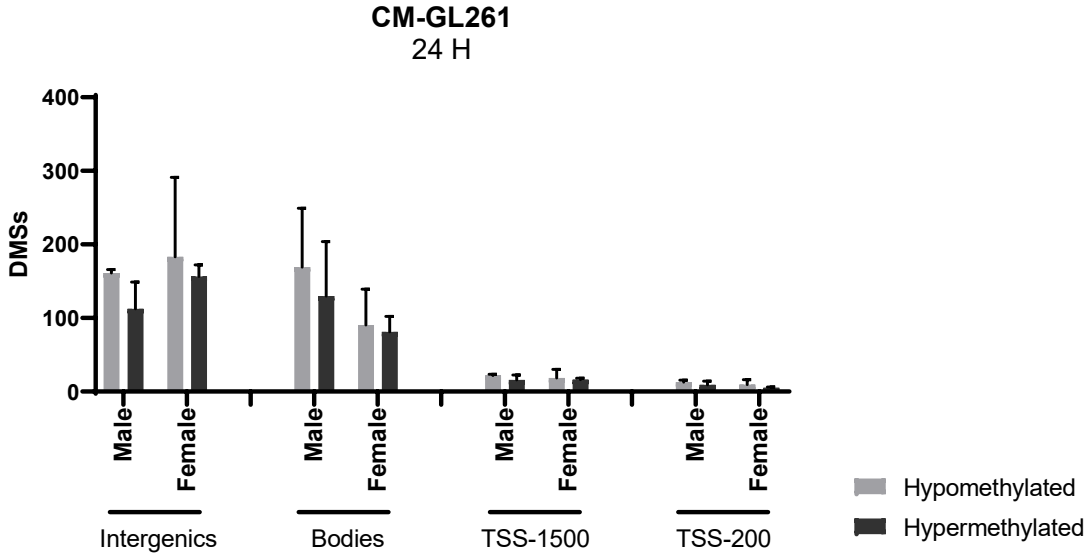

Figure 75. Male and female microglia exposed to CM-GL261 for 24 hours are exhibiting similar ratios of significant hypo- and hypermethylated DMS in intergenic regions and gene bodies:

Effect of CM-GL261 treatment for 24 hours on male and female primary microglial cells DNA methylation patterns. Raw data from MethylMouse arrays were exported into Illumina GenomeStudio software, annotated using Illumina MouseMethylation 12v1 Annotation_Mus_musculus file; and normalized using

IlluminCustom method before being compared to the control untreated primary microglial cells in order to obtain a score of methylation (DiffScore). The probes located in the X and Y chromosomes were filtered and only the significant DMS were plotted using GraphPad Prism®. Significance was calculated according to the DiffScore, </= 13 or >/= -13 for a P-value < 0.05, FDR adjusted. Results from three independent experiments.

We conclude that significant DMS are induced by a 24 hours exposure to CM-GL261 in male and female microglial cells. On the contrary to what was observed with the LPS treatment, those DMS appear to be following the same trend between sexes, suggesting a similar response to the CM-GL261.

Figure 76A and B show the significant DMS in the CM-GL261 condition compared to the control in male and female microglia, respectively. The heatmaps display in rows the mean β-value at each site, ranging from 0 (green) unmethylated to 1 (red) fully methylated. The columns display the treatment conditions.

In A, we find that, for this set of DMS in male microglia, the direction of methylation is very similar between control and treatments. We nevertheless notice slight differences in the methylation profiles of each treatment conditions, suggesting that the induction of DNA methylation reorganization might be specific to each treatment after 24 hours in primary male microglial cells. In B, we note that the CM-GL261 leads to mostly hypermethylation of DMS in female microglia compared to the control and that the LPS, for this set of DMS, leads to an inbetween control and CM-GL261 methylation level.

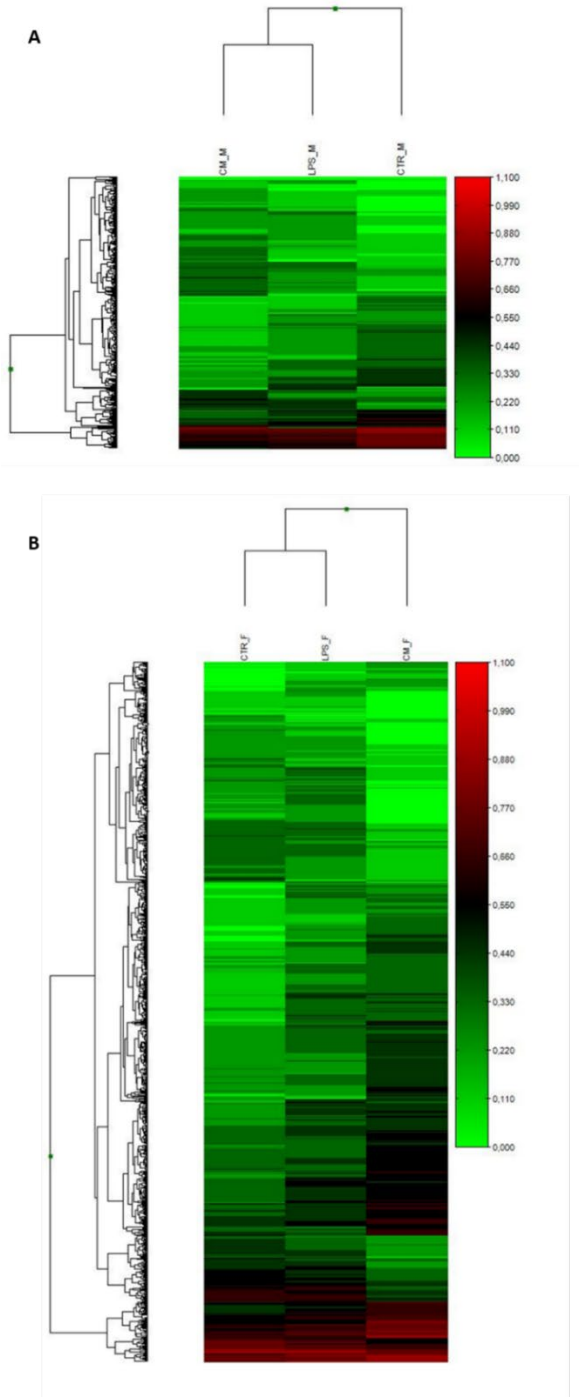

Figure 76. Male and female microglia exposed for 24 hours to CM-GL261 exhibit specific DNA methylation profiles compared to control and LPS:

Effect of CM-GL261 on the DNA methylation patterns of male and female primary microglial cells. Heatmap displaying the mean methylation values (β-Value) of the significant DMS in CM-GL261 condition compared to the control, in each treatment condition in male (A) and female (B) microglia. Realized on GenomeStudio. The β-Values are displayed according to a color ranging from light green (0, unmethylated) to deep red (1, fully methylated). A hierarchical clustering of the significant DMS and the samples was made using the Manhattan method. Results from three independent experiments.

We can conclude that overall, male and female microglial cells exposed to LPS and CM-GL261 for 24 hours lead to DNA methylation reorganization. Those results suggest that, in accordance to what was previously observed in the study, microglial cells DNA methylation patterns are impacted by environmental stimulation and second, that this reactivity is sexually dismorphic at the DNA methylation level.

3.8. Significantly differentially methylated genes seem to be specific to treatments and sexes in primary microglia

To try to understand in more depth the relationship between DNA methylation reorganization in male and female microglia in response to LPS and CM-GL261 after 24 hours, the overlapping DMGs between all conditions were explored. The results are presented in Figure 77.

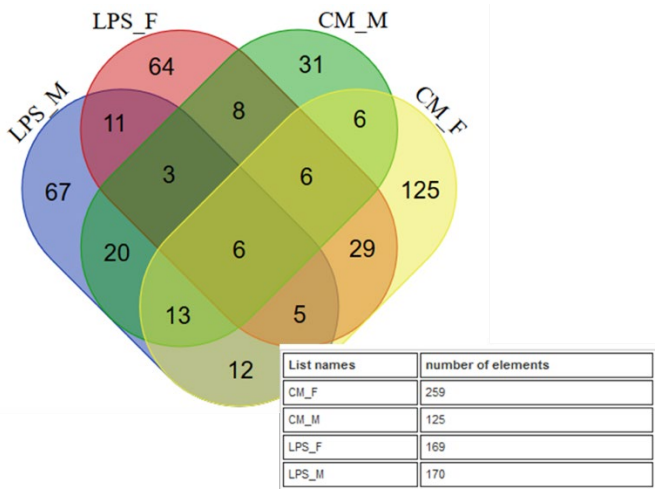

Figure 77. Male and female microglia exposed to LPS and CM-GL261 for 24 hours displays only few common DMGs:

Effect of LPS and CM-GL261 24 hours exposure on the DNA methylation patterns of male and female primary microglial cells. Venn diagram showing the overlapping significant DMGs. Raw data from MethylMouse arrays were exported into Illumina GenomeStudio software, annotated using Illumina MouseMethylation 12v1 Annotation_Mus_musculus file; and normalized using IlluminCustom method before being compared to the control untreated primary microglial cells in order to obtain a score of methylation (DiffScore). The probes located in the X and Y chromosomes were filtered and only the

significant DMS used for further analysis. The non annotated genes were removed and the remaining DMGs were plotted by using the Gent University Venn diagram tool. Significance was calculated according to the DiffScore, </= 13 or >/= -13 for a P-Value < 0.05, FDR adjusted. Results from three independent experiments.

In Figure 77, we observe that each condition exhibits a high percentage of specific DMGs and that only six DMGs are overlapping in all conditions of treatments and sex, the gene ontology made for those condition specific or commons DMGs did not lead to significant pathway or biological function.

Those six DMGs are actually five since one of them is arising from a missing annotation (NA), the remaining *Olfr630*, is coding for an olfactory receptor and *Fra10ac1*, coding for a nuclear phosphoprotein of unknown function and does not seems to have any implication in microglia biology.

Nlrp1, coding for a nucleotide-binding domain and leucine-rich repeat containing protein is implicated in inflammation and has been linked to inflammasome associated microglial reactivity. *Mapkbp1* code for mitogen-activated protein kinase binding protein 1, a scaffold protein that regulate the JNK and NOD2 signaling pathways, known to be important in microglial reactivity. Finally, *Bsx*, coding for the transcriptional activator Brain-specific homeobox TF, has not been linked to microglia.

3.9. The significantly differentially methylated genes in reactive male and female microglia exhibit difference in the methylated probes implicated

To compare the DNA methylation patterns of those five genes according to treatments and sexes, the β-values of each probe within each gene were plotted in Figure 78. On this heatmap, the row represents each probe and the columns represent each condition. The statistical significance of differential methylation between the control and a treatment is represented by a star on the side of the implicated probe, colored with the condition in which it is significant.

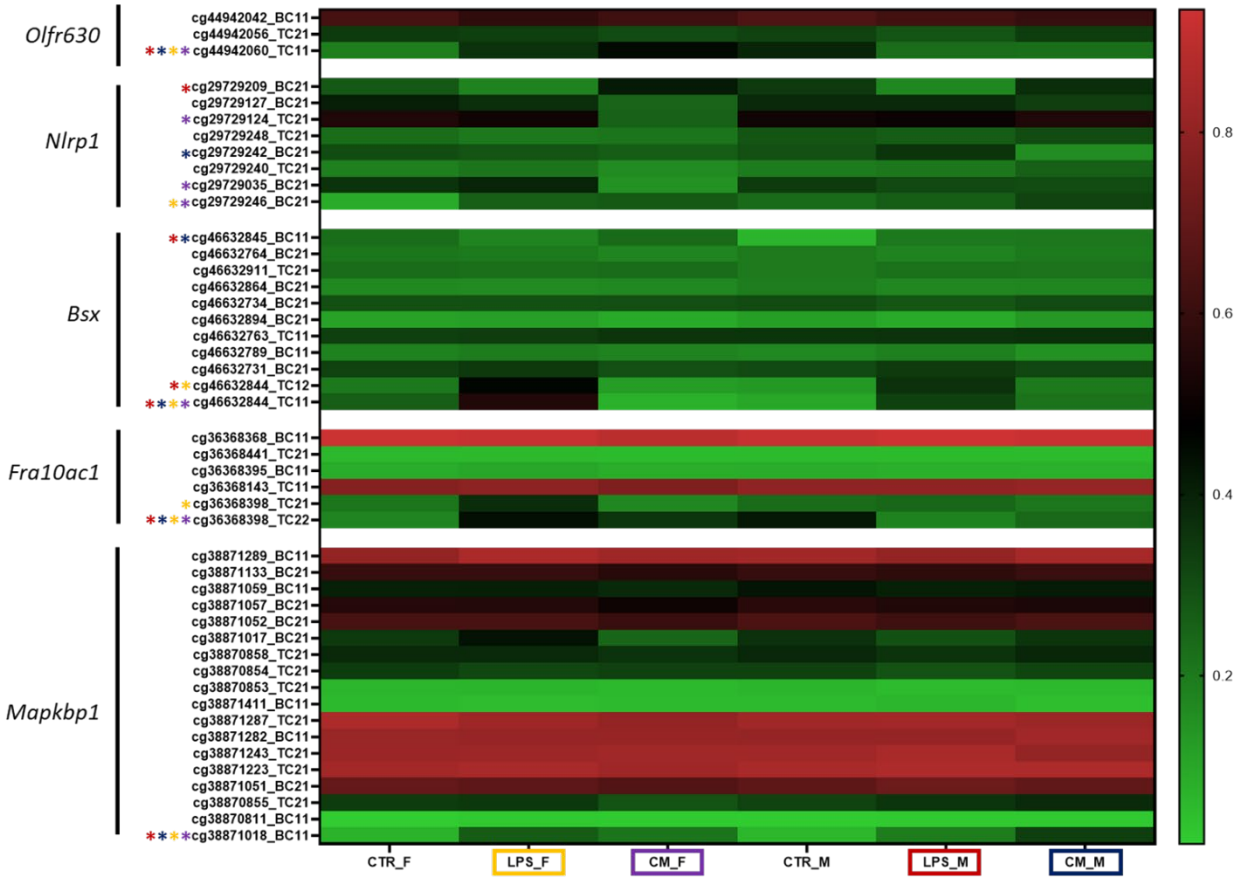

Figure 78. The DMGs common to treatments and sexes exhibit differences in the probes methylated for each gene:

Effect of 10 ng/mL of LPS or CM-GL261 on the DNA methylation patterns of male and female primary microglial cells. Heatmap displaying the mean β-Value of the probes located in the DMGs between control, LPS and CM-GL261 male and female microglia. Raw data from MethylMouse arrays were exported into Illumina GenomeStudio software, annotated using Illumina MouseMethylation 12v1 Annotation_Mus_musculus file; and normalized using IlluminCustom method. The β-Values from the probes located in the *Olfr630*, *Nlrp1*, *Bsx*, *Fra10ac1* and *Mapkbp1* genes of the male and female microglia treated with LPS or CM-GL261 were compared to the control untreated primary microglial cells in order to obtain a score of methylation (DiffScore). The DiffScore allowed the identification of the significant DMS between treatment and control and are presented as star in front of the significant probe. The color of the star represents the condition in which the differential methylation is statistically significant. The β-Values are displayed according to a color ranging from light green (0, unmethylated) to deep red (1, fully methylated). Results from three independent experiments.

We find that overall, the direction of methylation for all the probes are pointing towards the same direction, we only observe few probes that switch from extreme hypomethylation to hypermethylation or *vice versa*, especially in the LPS condition for both male and female.

It is worth noting that, even though the genes differentially methylated are common to all conditions, some of them do not exhibit the same differentially methylated probes in each gene. For instance, *Nlrp1* methylation pattern shows the highest degree of significant divergence in its methylation profiles amongst treatments and sexes, even though the degree of methylation in between all condition are quiet similar. On the contrary, for the *Mapkbp1* gene, all the conditions exhibit the same significant DMS, which is an interesting finding, meaning that DNA methylation could regulate the expression of the same gene in different ways by targeting differents sites.

The different features of the DMS are presented in Figure 79 and we can indeed notice that the distribution of the DMS amongst the DMGs are differents in function of the treatment and the sex of the microglia. For instance, for the *Mapkbp1* gene, all the conditions exhibit an hypermethylated state of the same significant probe; while for the *Olfr630* gene, the same probe is significantly differentially methylated but hypermethylated in female and hypomethylated in male; for both treatments.

Overall, we observed that each condition of treatment related to sex is characterized by a signature of hypo- and hypermethylated probes compared to the control, confirming the hypothesis that DNA methylation profiles are specific to treatments and different in male and in female microglial reactivity.

			LPS_F	CM_F	LPS_M	CM_M
cg36368398_TC21	***Fra10ac1***	tss_body	Hypermethylated	NS	NS	NS
cg36368398_TC22	***Fra10ac1***	tss_body	Hypermethylated	Hypermethylated	Hypomethylated	Hypomethylated
cg46632844_TC12	***Bsx***	tss_body	Hypermethylated	NS	Hypermethylated	NS
cg46632844_TC11	***Bsx***	tss_body	Hypermethylated	Hypomethylated	Hypermethylated	Hypermethylated
cg46632845_BC11	***Bsx***	tss_body	NS	NS	Hypermethylated	Hypermethylated
cg29729124_TC21	***Nlrp1b***	tss_body	NS	Hypomethylated	NS	NS
cg29729035_BC21	***Nlrp1b***	tss_body	NS	Hypomethylated	NS	NS
cg29729246_BC21	***Nlrp1b***	tss_body	Hypermethylated	Hypermethylated	NS	NS
cg29729209_BC21	***Nlrp1b***	tss_body	NS	NS	Hypomethylated	NS
cg29729242_BC21	***Nlrp1b***	tss_body	NS	NS	NS	Hypomethylated
cg44942060_TC11	***Olfr630***	tss_1500	Hypermethylated	Hypermethylated	Hypomethylated	Hypomethylated
cg38871018_BC11	***Mapkbp1***	tss_body	Hypermethylated	Hypermethylated	Hypermethylated	Hypermethylated

Figure 79. Significant DMS common to treatments and sexes show divergence in methylation profile:

Effect of 10 ng/mL of LPS or CM-GL261 on the DNA methylation patterns of male and female primary microglial cells. Features of the significant DMS located in the DMGs between control, LPS and CM-GL261 male and female microglia are displayed. Raw data from MethylMouse arrays were exported into Illumina GenomeStudio software, annotated using Illumina MouseMethylation 12v1

Annotation_Mus_musculus file; and normalized using IlluminCustom method. The β-Values from the probes located in the *Olfr630*, *Nlrp1*, *Bsx*, *Fra10ac1* and *Mapkbp1* genes of the male and female microglia treated with LPS or CM-GL261 were compared to the control untreated primary microglial cells in order to obtain a DiffScore. Results from three independent experiments.

Even though we can not finally conclude about the impact of DNA methylation patterns on gene expression or microglial phenotypes, we can however conclude that treatments of male and female microglial cells with LPS and CM-GL261 for 24 hours lead to significant sexually dysmorphic reactivity with changes in morphology and transcriptomics, together with divergent DNA methylation profiles.

Overall, in conclusion, we have shown that the induction of microglial reactivity, in microglial cell line or primary cells, was characterized by significant changes in morphology and transcriptomics and associated with significant DNA methylation reorganization. The causal link between DNA methylation, gene expression and microglial function remains to be unravelled.

However, we could observe that many of those DMS were located in genomic regions from which the effects on the gene expression are unknown, that only one CpG could be significantly different and that the level of methylation difference could be low, indicating that future research will have to focus in more detail on DNA methylation localization and intensity.

Finally, we could see that the reactivity towards treatment exposure at any levels was not the same between the different models and sex. Those differences were even higher at the DNA methylation level compared to the observed phenotype, highlighting the specificity and sensitivity of epigenetic marks.

This PhD project highlights the crucial need to explore in depth the link between DNA methylation patterns, specific microglial functions and thebiological meaning of DNA methylation all along the genome.

Part V. Discussion

1. Refinement of the experimental design on DNA methylation implication in microglial reactivity

1.1. Techniques used in the present study can be refined to unravel a clearer link between DNA methylation and related microglial functions

As the keystone of the entire project, the induction and characterization of microglial reactivity is the first point that need to be discussed.

Indeed, in our study, no significant changes in microglial functionality have been highlighted between control and treated microglial cells, regardless of the treatment and the time of exposure. This problem might arise from the technical limitations associated with our experimental design and could be overcome by reconducting the experimental plan in the opposite direction, starting by DNA methylation to end with the functionality of microglia.

It could be done with another set of DNA methylation data generated from another model of microglial cells or directly from the large dataset produced in this project, from which significant differentially methylated genes could be used as the base of the project. From the selected genes with its associated DNA methylation levels, one could explore the mRNA expression, the protein secretion and the function modulated by such protein.

For example, from our dataset, the *Cxcl2* gene could be a good candidate, as differentially methylated in promoters and differentially expressed in BV2 exposed to LPS for 24 hours (Figures 38 and 39), compared to the control. As a secreted chemokine, CXCL2 protein can easily be measured and linked to the secretory function of microglia. The expression of *Cxcl2* mRNA could easily be evaluated by RTqPCR while the secretion of CXCL2 could be assessed by ELISA. From this pipeline, the DNA methylation pattern of the *Cxcl2* promoter could be modified by using a CRISPR-Cas9-DNMT3A[410] or a CRISPR-Cas9-TET1[411] and effect of those modulations could be assessed at the DNA methylation, mRNA and protein secretion levels, providing very practical informations about the effect of DNA methylation on the secretory function of microglia.

From this hypothetical pipeline, other genes coding for secreted molecules, with the significant differentially methylated CpGs site located in other regulatory elements could be used to unravel the

effects of single DNA methylation modifications in different part of the genome on the gene expression and the secreted function of microglial cells.

As seen in the introduction, in addition to secretion, the microglial function that appears to be the most detrimental when dysregulated by pathological microenvironment is the phagocytosis and thus, it would be crucial to develop an established protocol for evaluation of phagocytosis to see the potential modulation by DNA methylation changes.

Indeed, if phagocytosis related genes, such as *Flt1*, *Cnn3* or *Igf1*, were found to be differentially methylated, in addition to the mRNA expression and the protein quantification by Western-Blot, the function of phagocytosis would need to be assessed.

This part of our study was higly problematic leading to unconclusive results (Figure 26).

First, the phagocytosis was assessed by manual counting of fluorescent beads present inside BV2 cells stained by IF (Annexe 14) and even though this technique was the one exhibiting the less variation between technical triplicates, it could be influenced by observer bias and was thus abandoned.

Second, the same fluorescent beads were used together with a Clariostar® plate reader but the results were constantly disturbed by a very high fluorescent background regardless of the amount of PBS washes and Trypan Blue quenching realized and the variations between technical replicates was unacceptable.

Finally, the Clariostar plate reader was then used with pH sensitive fluorescent beads but the variation between technical replicates remains leading us to those inconclusive results (Figure 48). Those problems are well discussed in literature and thought to be overcome by using a Fluorescent activated cell sorting (FACS) with pH sensitive dyes for the cargo used, which is the second problem arising from such technologies.

Indeed, as it was shown in the introduction, phagocytic function of microglia can be triggered by a various range of cargoes and the one used in our study was composed of *E.Coli* particles, reflective of bacterial activation of phagocytosis, not relevant in the context of most neuropathological conditions. To overcome this issue, several cargos can be isolated, dyed and exposed to microglial culture, including carboxylate microbeads to mimick phosphatidylserine of apoptotic cells, purified myelin debris or even purified synaptosomes to evaluate synaptic pruning[412].

Even though they might not seem relevant for translational research, other microglial functions should be considered if associated genes are found to be differentially methylated.

Briefly, perception could simply be evaluated by sensome exploration through Mass Spectrometry[413] or co-immunoprecipitation[414]. Concerning the self-maintenance function of microglia, proliferation could be explored by using carboxyfluorescein succinimidyl ester while measure of the apoptosis can be measured by TUNEL assay, ferroptosis by measure of the Fe^{2+} release and necroptosis by measure of the phosphorylation status of MLKL[415]. In addition, motility can be assessed by Transwell assay under the influence of a chemotactic agents or without any influence with the use of highly developed software such as MotiQ[416].

Finally, and even if it is not directly linked to function, morphology assessement still is necessary in microglial research and could be usefull if genes related to cytoskeleton would be found differentially methylated. In that regard, our study could have been improved by the precise measure of important parameters such as processes number, length and thickness while microglial markers could have be quantified, especially Iba1 that has been related to microglial reactivity[80].

However, the techniques used in our study are not the only problematic point of the experimental design, the model, including the cells, the stimulation and the time of exposure, should be discussed.

1.2. The model used needs to be adjusted to have a potential translational application

In order to investigate whether or not DNA methylation patterns could play a role in the modulation of microglial identity, it was necessary to define different phenotypes that could represent clear cut identities possibly acquired by microglial cells amongst their spectrum of activation.

To induce such a reprogramming, we choose to treat the microglial cells with the LPS and the IFN-ɣ, known to induce a microglial reprogramming related to inflammation. Second, to tackle the anti-inflammatory related phenotype, we decided to use IL-4. Finally, to try to investigate the less known microglial identity in brain tumors, we decided to produce media conditioned by the GL261 mouse glioma cell line. The concentrations of products were settep-up on 10 ng/mL final concentration and a 48 hours time of media conditioning by GL261 cells. The cells were treated from one to 48 hours in relation to the model of cells used.

From this experimental design, we could indeed find different phenotypical changes in microglia, accompagnied with significant DMS, suggesting that the stimulation and time of treatment were adapted for such an exploratory project.

Nevertheless, the relevance of such a model for translational purpose remains questionable. Indeed, the proinflammatory treatments used and especially the LPS, is linked to infection stimulation, which are rarely implicated in neurological diseases and could have been replaced by CK mixture such as TNFα and IL-1β, implicated in microglial dysfunction in a wide range of neurological diseases. In addition, mimicking the glioma microenvironment with CM-GL261 might not have been the best option, since its composition during the project could evolve, relative to the GL261 cell culture itself and furthermore, alters the nutrients content of the original media, thus inducing a bias when compared to the control. Finally, concerning the stimulation regarding the time of treatment, as microglia dysfunction seems to arise from accumulation of epigenetic marks along time, it would have been preferable to treat microglia in successive waves prior to experiment instead of exposing it in an acute way.

For the cellular model to explore microglial reactivity, we decided to take advantage of the widely characterized mouse microglia cell line BV2 (Annexe 1), providing enough material to test a considerable amount of parameters in an easy to use culture system; and already available knowledge on the features constituting BV2 identity in different experimental settings.

A trial was made on the human cell line HMC3 but the induction of differential phenotypes was unsuccessful (Annexe 3) and DNA methylation data non significant (Annexe 4), maybe suggesting an absence of epigenetic plasticity that would be in alignment with the lack of phenotypic changes within our cultures. We suspect that the cell line might be corrupted[417], that the stimulations were not strong enough or that the times of exposure were unadapted. A further study with trial of higher concentrations and a panel of time of exposure could overcome this interrogation.

As we are aware that the usage of a cell line did not represent physiological reality and lack the cellular heterogeneity presents within a population of primary isolated microglial cells, we decided to then isolate microglial cells from newborn CD-1 mouse pups. The differences between the BV2 cell line results and the primary microglia are difficult to assess in our study since few timepoints matches, all the experiments have not been tried on primary microglia (CK arrays) and because we obtained less material with less good quality from the genotyped male and female microglia (Part 3 of the results). We can nevertheless observe that primary microglia viability upon LPS and CM-GL261 treatments was significantly affected at 24 hours (Figure 67) while it was not for the BV2 (Figure 23), suggesting an increased sensitivy to the culture conditions. In the same manner, we find that the morphological changes induced by the treatments are already clearly noticeable after six hours in primary microglia (Figure 50), while being very subtle for BV2 (Figure 25), again suggesting an increased sensitivity towards stimulation.

Unfortunately, the differences in DNA methylation modulations between BV2 and primary microglia cannot be clearly established for now, since the raw data from BV2 have been analyzed with R software, while the ones from primary has been realized using GenomeStudio.

For instance, even if we find significant DMS after an hour of treatment of primary microglia (Figure 53) while they only appear after 12 hours for BV2 (Figure 29), we can not conclude about the epigenetic sensitivity of primary microglia since those results could arise from the filtering of the probes that is more stringent with R software (cross-linking probes does not appear to be filtered in GenomeStudio).

Nevertheless, we could observe that for BV2 treated with LPS and IFN-ɣ induced significant DMS were mostly towards hypomethylation of promoters and introns (Figures 30, 31, 36 and 37), while the ones in primary microglia were mostly directed towards hypermethylation of gene bodies and intergenic regions (Figures 54 and 56), when compared to the respective controls, clearly highlighting the different epigenetic landscapes between immortalized and primary cells.

For instance, it is known that cell lines have the tendency to exhibit chromosomal instability[418] along time in culture and this phenomena has actually been linked to genome wide demethylation[419], especially in intergenic regions[420], that could explain part of the differences in DNA methylation that are observed between our models. Even thought such observations render the results on BV2 questionnable, we also know that primary microglial cells lose their microglial homeostatic transcriptomic signature upon culture[421], and can be influenced by a MACS isolation[422], render the primary mouse microglial model also highly questionable.

Finally, the last part of this project, done on separated male and female microglia highlighted the dimorphism of reactivity towards treatment of microglia and thus, interrogate the strength of the results obtained in the bulk primary microglia part of the study. Interestingly, when we compare the BV2 cells treated for 24 hours with LPS with the male and female primary microglia in the same condition, we observe opposite results. Indeed, BV2 are female cells and exhibit mostly hypomethylation of promoters (Figure 36) while female primary microglia exhibit mostly hypermethylation of the intergenic regions (Figure 73) located probes, highlighting a potential effect of alteration by the immortalization process.

In addition, as seen in the introduction and stated by Paolicelli et al., a good model for microglial study should take in account the specie, the sex, the age and the localization, highlighting the inadequacy of our model for translational research.

Indeed, the perfect model for the translational research targeting potential microglial reprogramming based on DNA methylation should be done in humans, both male and female but separated, with a

average age of 40 years old to tackle microglial accumulation of epigenetic marks potentially relevant for neurodegenerative diseases, neuro-immunological diseases and brain tumors with localization from the cortex to specific regions such as the amygdala, the hippocampus or the *substantia nigra*, which seems utopian. A difficult but suitable model between relevant and convenient could be microglia isolated from the cortex of adult mice separated by sexes and freshly isolated.

In any case, it seems highly complicated to have enough material from an adequate model of microglia, without even discussing the widely known problems of microglia isolation and culture. The model to unravel microglia still need further investigation and development to be used for translational research.

Despite those challenges from our experimental settings and the lack of translational relevance, we could still successfully induce microglial reactivity and discover associated differential methylation patterns, which seems crutial for the exploration of the epigenetic code underlying microglia reactivity, a major advance for fundamental research.

2. Understanding the implication of DNA methylation in microglial reactivity

2.1. DNA methylation reorganization is associated to microglial reactivity, but the causal links are missing

As explained above, BV2 cell line model does not fully represents reality, but was a good tool to obtain enough material for realization of different experiments from which we could induce significantly different microglial identities and observe associated DNA methylation reorganization.

For example, we have seen that the pro-inflammatory treatments were leading to an increasing hypomethylation of promoters after 12 and 24 hours of treatments (Figures 30 and 36) and interestingly, those timepoints are related to the progressive acquisition of microglia characteristic morphology (Figure 25).

On the contrary, and even if it is a result of a microglial adaptation to the culture media and not the treatments, the 48 hours timepoint for those conditions leads to hypermethylation of promoters (Figures 42 and 43) and loss of those morphological characteristics (Figure 25). Interestingly, the transcriptomics analysis shows a continual decrease in expression from 12 to 48 hours (Figure 28), that could be related to the small panel of genes explored or a feedback mechanism induced by the very

high expression of pro-inflammatory mRNA at the earliest timepoints. Those observation show that a link seems to exist between the changes happening on the DNA methylation level and the phenotypes observed.

Moreover, we have seen that the IFN-ɣ treatment for 12 and 24 hours in comparison to the control, leads to a progressive hypomethylation of promoters and active genomic regulatory elements of genes implicated in the biological response to interferons through the STAT5 and the P53 TFs, which clearly indicates a modulation of cellular biology by differential methylation of the DNA (Figures 30 to 33).

Similarly, the treatment with LPS for 12 and 24 hours compared to the control condition shows a progressive hypomethylation of promoters and active genomic regulatory elements of genes associated with the TNF signaling pathway through the activation of NFκB TF (Figures 36 to 38).

Unfortunately, the causality between those associations seems to be highly complicated and could not be unraveled in our study.

In addition, the RNAseq results show upregulation of mRNA for which the genes where differentially methylated. In that regard, we could see the hypomethylation of a probe within *Traf1*, *Lcn2* and *Saa3* genes and the upregulation of the related mRNAs in the LPS condition compared to the control (Figures 39, 40 and 41).

Because of the implication of those genes in the immune regulation of microglia, it seems natural to assume that DNA methylation and biological function are related. But when we look closer at the DNA methylation levels of the probes located within those genes, we find that the probes are hypomethylated for both the control and the LPS conditions, the lattest just being more hypomethylated and thus, leading us to question the true biological meaning of DNA methylation and the level of implication on gene expression and by extension, biological functions.

Moreover, regarding of the true biological meaning of DNA methylation, interesting observations can be made from the results on primary microglial cells experiments. Indeed, we can see that the LPS and IFN-ɣ treatments leads to changes in morphology of primary microglial cells after an hour (Figure 50), while only LPS leads to significant changes in the expression of pro-inflammatory associated mRNAs after an hour (Figure 51). Concerning the DNA methylation results, both LPS and IFN-ɣ lead to overall methylation changes equally hypo- and hyper- mostly in the intergenic regions and gene bodies (Figure 54 and 56). Again, even though no causal links can be established here, it is still interesting since gene bodies hypermethylation are thought to be related to transcriptional activation[423] while methylation of intergenic regions is thought to be related to miRNAs regulation and genome stabilization[424].

Finally, when we compare sex-associated reactivity to LPS, we note that female microglia exhibit more intense morphological changes (Figure 69) and transcriptional expression of pro-inflammatory mRNAs (Figure 70) together with an overall hypermethylation of intergenic regions (Figure 73). Those results, that seem contradictory, highlight the crucial need for understanding the interplays of epigenetic mechanisms along the different genomic elements that are responsible for gene expression regulation.

In reality, from our results, there is no way to know if the level of implication of DNA methylation in gene expression regulation since other regulatory elements methylation could have different effects on gene expression, in addition to the histone modifications landscape for those genes and the possible regulation of ncRNA by DNA methylation that could lead further to feedback regulatory mechanisms.

In conclusion, even though causal relationships are missing, we can attest with confidence that DNA methylation reorganization is linked to microenvironment modulation of microglia identity, but additional levels of exploration need to be realized.

2.2. Biological meaning of DNA methylation in the different genomic regulatory elements

As we have seen, the first step towards the understanding of the effects of DNA methylation modulation on gene expression and associated phenotypical changes, is to understand that the genomic localization of the methylated site does not always leads to the same transcriptional effect. Even though this vast topic still needs major exploration, few clues scattered amongst the different biological fields already pave the way to understand the grand scheme of DNA methylation meaning.

Indeed, apart from the now well-established transcriptional silencing by promoter DNA methylation, knowledge are available concerning the DNA methylation of first intron, enhancers, gene bodies and intergenic regions.

Indeed, in promoters, DNA methylation can represents a direct obstacle for TFs to access binding sites *via* steric hindrance altering the DNA shape, even out of the CpG islands, it has been shown that one single methylation at a CpG site in a middle of a TF binding site could inhibit the hybridization and transcriptional activation. In addition, DNA methylation can be recognized by the Methyl-CpG-binding domain (MBD) of proteins leading to the recruitment of chromatin remodelers associated with transcriptional repression, such as MeCP-1 and MeCP-2 recruiting HDACs, or MBD-1 recruiting histone H3K9 methyltransferase[425].

Similarly, DNA methylation of the first intron, associated with gene expression regulation compared to the other introns, has been majoritarly associated with transcriptional repression. Even though the underlying mechanisms are not known, it is though to be a consequence of the close proximity of the first intron to the TSS, exhibiting extension of the CpG rich regions. Interestingly, few genes seem to display the opposite relationship, exhibiting transcriptional activation related to first intron methylation. This contradicting observation might be related to the decreased density of CpG sites along the first intron TF binding sites and the degree of sensitivity from classes of TFs towards DNA methylation interferences[426,427].

In addition, the DNA methylation of genomic regulatory elements such as enhancers has been linked to gene expression regulation. Indeed, enhancers tend to exhibit a low CpG content with incomplete methylation patterns that is thought to be related to a dynamic movement of methylation and demethylation process that could be related to the increased presence of TET enzymes near those sites.

Not approached at all in this project but worth mentioning are another type of regulatory element named insulators, responsible for transcription silencing *via* isolation of promoters from enhancers and known to be DNA methylation sensitive, leading to their inhibition and thus, linked to transcriptional activation[428].

Concerning the DNA methylation of gene bodies, as it has been mentioned above, has been related to transcriptional activation. Even though most gene bodies do not contain high amount of CpG sites, it has been shown that CpG islands still exist in those regions and even though the mechanisms behind transcription stimulation by gene body methylation is not established, it strongly suggests that transcription initiation but not elongation might be sensitive to restriction by DNA methylation[428].

Finally, concerning the effects of DNA methylation in intergenic regions, only few contradictory facts are available in the field. Indeed, both positive and negative correlation have been observed between DNA methylation in intergenic regions and gene expression but no underlying mechanisms have been found yet, only the suggestion that it was linked to miRNAs regulation and genome stabilization[424].

Moreover, it has to be noted that the cytosine derivatives (5hmC, 5fC, 5caC) but also other types of DNA modifications (N6-methyladenine, 5-hydroxymethyluracil) are also thought to have regulatory effects on gene expression that only starts to emerge now[429]. This already highly complicated web of DNA modifications is subjected to a higher level of regulation by the chromatin accessibility modulation from histone modifications.

It is incredibly clear that our study could have not unravel the link between DNA methylation and gene expression regarding all the different layers of epigenetic complexity, but the data produced on different models with different stimulations represent a major asset for the scientific community.

2.3. DNA methylation and histone modification landscape in microglial reactivity

As mentioned above, DNA methylation of specific genomic regions and regulatory elements influence the binding sites accessibility to TFs and transcriptional machinery, thus influencing gene expression. However, as it was also shown in the introduction, regulatory elements accessibility is also governed by chromatin compaction modulation by histone modifications. In addition, it is now known that histone modifications could impact the recruitment of DNMTs enzymes, thus influencing DNA methylation patterns. Finally, it was also shown that DNA methylation could leads to the recruitment of histone modifiers complexs *via* MBD proteins, highlighting the highly complicated cross-talk between the two epigenetic mechanisms[430].

The details of such crosstalks goes beyond the scope of this phD project but is necessary to establish the mechanisms behind microglial reactivity. Exploration of histone marks should be included in such a study in the future since it is clear that both microglial core programs and stimulation related modulations are defined by the histone modifications inducing accessibility to specific enhancers.

In addition to the DNA methylation and gene expression experiments, the use of databases collecting the results of Chip-seq experiments (such as UCSC Genome Browser or Chip Atlas used with IGV software) can already represent a strong asset to explore epigenetic landscapes.

However, it has to be kept in mind that histone modifications vary amongst cell types and are very dynamic and thus, might not be representative. It is thus necessary to include step of Chip-seq experiment in such projects for relevant conclusion on gene expression modulation and further phenotypical modulation.

Part VI. Conclusions and outlook

Microglial cells, the resident immune cells of the brain parenchyma, display an outstanding functional plasticity arising from a dynamic transcriptional regulation that is thought to be under the control of epigenetic mechanisms. It as been shown that microglial behavior was linked to nearly all neurological diseases and associated to pathological environment induced detrimental misuse of microglial functional plasticity. Innovative therapeutic strategies to tackle neurological diseases consist in the reprogramming of microglial towards a beneficial phenotype in function of the state of the pathological environment. In that regard, the goal would be to reprogram microglial cells towards an anti-tumor phenotype in brain tumors and a neurogenic one in neurodegerative diseases. Achieving such a goal would require the deep understanding of the core molecular mechanisms underlying microglial modulation of functions. Latest research has been focusing on the transcriptional regulation through chromatin accessibility orchestrated by histone modifications but DNA methylation implication in microglial reactivity still remains obscure.

In this project, we hypothesize that DNA methylation patterns were implicated into the reprogramming of microglia, regulating gene expression and associated functions.

To address that hypothesis, we treated cell lines and primary microglial cells with pro- and anti-inflammatory stimulations together with a glioma-based mixture, to mimick the extreme phenotypes known to be adopted by microglia in pathological contexts. The microglial cells from each treatment conditions were characterized in terms of phagocytosis, morphological changes, cytokine secretions and transcriptomics and the DNA methylation patterns were explored. The gene expression was then assessed to unravel links between DNA methylation reorganization and transcriptional regulation.

First of all, we showed during the project that exposure with pro- and anti-inflammatory stimulations were leading to significant microglial reactivity especially characterized by changes in morphology and transcriptomics. In addition, the induced phenotypes were slightly different between cell line and primary microglia but also between sexes, showing the different sensitivities towards stimulation in function of the model used.

Secondly, we showed that each treatment induced microglial reactivity was associated with a specific methylation profile characterized by variabilities in the amount, the localization and the direction of methylation of significant differentially methylated genes. Again, differences between the models used could be observed, the primary microglia exhibiting significant methylation changes with lower time of cytokine exposure compared to the cell line. Lastly, a sexual dysmorphism was observed in microglial reactivity towards treatments at the DNA methylation level.

Finally, gene expression could not be correlated to DNA methylation regulation but we showed that the differentially methylated genes were related to microglial biological pathways that are consistent with literature, suggesting that our initial hypothesis might be true but incomplete.

Therefore, we can conclude that DNA methylation patterns are changing in accordance to the reactivity of microglial cells to certain microenvironements. Unfortunately, the causal link between such DNA methylation reorganization and microglial transcriptional regulation and furthermore phenotypical reactivity could not be established.

Nevertheless, such links could be determined by a new set of experimental designs exploring chromatin accessibility (ATAC-seq) and histone modifications (Chip-seq) on well characterized reactive microglial cells; from the functional level (CK secretion by ELISA and phagocytosis assay by FACS), to the proteomic level (mass spectrometry) and finally, the transcriptiomic level (RNA-seq).

Those informations could lead to identify DNA methylation sensitive genes in microglial reactivity that could be further explored as therapeutic candidate for microglial reprogramming.

To do so, a catalytically inactivated Cas9 (dCas9) fused with either DNMT3a or TETs enzymes targeting the candidate genes regulatory elements could be used on the same model of microglial reactivity to see the effects of DNA methylation modulation on the transcriptomic, proteomic and functional behavior in such microglial reactivity.

On top of this highly complex experimental design, the modelling of microglia reactivity remains highly challenging, the best would be to have access to fresh microglia from human suffering from neurodegenerative diseases or brain tumors, which constitute already more than a challenge. But in addition, the culture of such primary human microglial cells is known to impacted the identity of the cells even with the best of care. Finally, even if this condition is met, as microglial cells are exhibiting huge variations between sexes, amongst ages and in different brain areas, it seems utopian to believe that a single DNA methylation sensitive gene could be found and have a meaningful impact on the physiopathology when reprogrammed.

The translational achievement from such an experimental would be difficult and mostly to succeed by focusing on more impactful epigenetic modifications, such as histone modifications reprogramming. However, we are convinced that the fundamental understanding of microglial biology can not be achieved without such an experimental design to understand the true meaning of DNA methylation in microglial identity.

Annexes

A

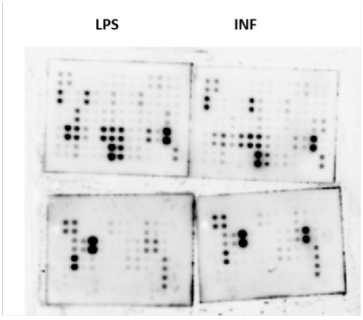

B

	A	B	C	D	E	F	G	H	I	J	K	L	M	N
1	POS	POS	NEG	NEG	BLANK	Axl	BLC	CD30L	CD30	CD40	CRG-2	CTACK	CXCL16	Eotaxin 1
2	POS	POS	NEG	NEG	BLANK	Axl	BLC	CD30L	CD30	CD40	CRG-2	CTACK	CXCL16	Eotaxin 1
3	Eotaxin 2	FasLg	CX3CL1	G-CSF	GM-CSF	IFNγ	IGFBP-3	IGFBP-5	IGFBP-6	IL-1α	IL-1β	IL-2	IL-3	IL-3 Rb
4	Eotaxin 2	FasLg	CX3CL1	G-CSF	GM-CSF	IFNγ	IGFBP-3	IGFBP-5	IGFBP-6	IL-1α	IL-1β	IL-2	IL-3	IL-3 Rb
5	IL-4	IL-5	IL-6	IL-9	IL-10	IL-12 p40/70	IL-12 p70	IL-13	IL-17	KC	Leptin R	Leptin	LIX	L-Selectin
6	IL-4	IL-5	IL-6	IL-9	IL-10	IL-12 p40/70	IL-12 p70	IL-13	IL-17	KC	Leptin R	Leptin	LIX	L-Selectin
7	Ltn/XC1	MCP-1	MCP-5	M-CSF	MIG	MIP-1α	MIP-1γ	MIP-2	MIP-3β	MIP-3α	PF-4	P-Selectin	RANTES	SCF
8	Ltn/Xc1	MCP-1	MCP-5	M-CSF	MIG	MIP-1α	MIP-1γ	MIP-2	MIP-3β	MIP-3α	PF-4	P-Selectin	RANTES	SCF
9	SDF1α	TARC	TCA 3	TECK	TIMP-1	TNFα	sTNFRI	sTNFRII	TPO	VCAM-1	VEGF-A	BLANK	BLANK	POS
10	SDF1α	TARC	TCA 3	TECK	TIMP-1	TNFα	sTNFRI	sTNFRII	TPO	VCAM-1	VEGF-A	BLANK	BLANK	POS

C

	A	B	C	D	E	F	G	H	I	J	K	L
1	POS	POS	NEG	NEG	BLANK	bFGF	CD26	Dtk	E-Selectin	FCγ RIIB	Flt-3 Lg	GITR
2	POS	POS	NEG	NEG	BLANK	bFGF	CD26	Dtk	E-Selectin	FCγ RIIB	Flt-3 Lg	GITR
3	HGF-R	ICAM-1	IGFBP-2	IGF-1	IGF-2	IL-15	IL-17 BR	IL-7	I-TAC	LungKine	MDC	MMP-2
4	HGF-R	ICAM-1	IGFBP-2	IGF-1	IGF-2	IL-15	IL-17 BR	IL-7	I-TAC	LungKine	MDC	MMP-2
5	MMP-3	OPN	OPG	Pro MMP9	Resistin	Shh-N	TCK-1	TIMP-2	TRANCE	TROY	TSLP	VEGF-R1
6	MMP-3	OPN	OPG	Pro MMP9	Resistin	Shh-N	TCK-1	TIMP-2	TRANCE	TROY	TSLP	VEGF-R1
7	VEGF-R2	VEGF-R3	VEGF-D	BLANK	BLANK	BLANK	BLANK	BLANK	BLANK	BLANK	BLANK	POS
8	VEGF-R2	VEGF-R3	VEGF-D	BLANK	BLANK	BLANK	BLANK	BLANK	BLANK	BLANK	BLANK	POS

Annexe 1. Cytokine Arrays used in the BV2 study:

ELISA based membrane CK arrays commercialized by Abcam and targeting 96 mouse CKs. (A) Picture of two of the blots used on the supernatants of BV2 treated with 10 ng/mL of LPS and IFN-γ, treated according to manufacturer's instructions and exposed to chemiluminescence (B and C) Tables representing the different locations of the CKs present on the array.

Axl : AXL receptor tyrosine kinase; bFGF : Basic Fibroblast Growth Factor; BLANK : Blank control; BLC : CXCL13; CD30L :CD30 ligand; CRG2 : CXCL10; CTACK : CCL27; HGFR : Hepatocyte Growth Factor Receptor; ICAM-1 : Intercellular Adhesion Molecule 1; ITAC : Interferon Inducible Tcell Alpha Chemoattractant; KC : CXCL1; LIX : CXCL5; Ltn/XC1 : Lymphotactin; LungKine : CXCL15; MCP : Monocyte Chemattractant Protein; MDC : Macrophage derived chemokine; MIG : CXCL9; MIP : Macrophage Inflammatory Protein; NEG : Negative control; OPG : Osteoprotegerin; OPN : Osteopontin; PF-4 : CXCL4; POS : Positive control; RANTES : CCL5; SCF : Stem Cell Factor; SDF-1 : CXCL12; Shh-N : N-term Sonic Hedgehog; TARC : CCL17; TCA3 : CCL1; TCK-1 : CXCL7; TECK : CCL25; TIMP : Tissue Inhibitors of MMPs; TPO : Thrombopoietin; sTNFR : Soluble TNF Receptor; TSLP : Thymic Stromal Lymphopoietin protein; VCAM1 : Vacsular Cell Adhesion Molecule 1.

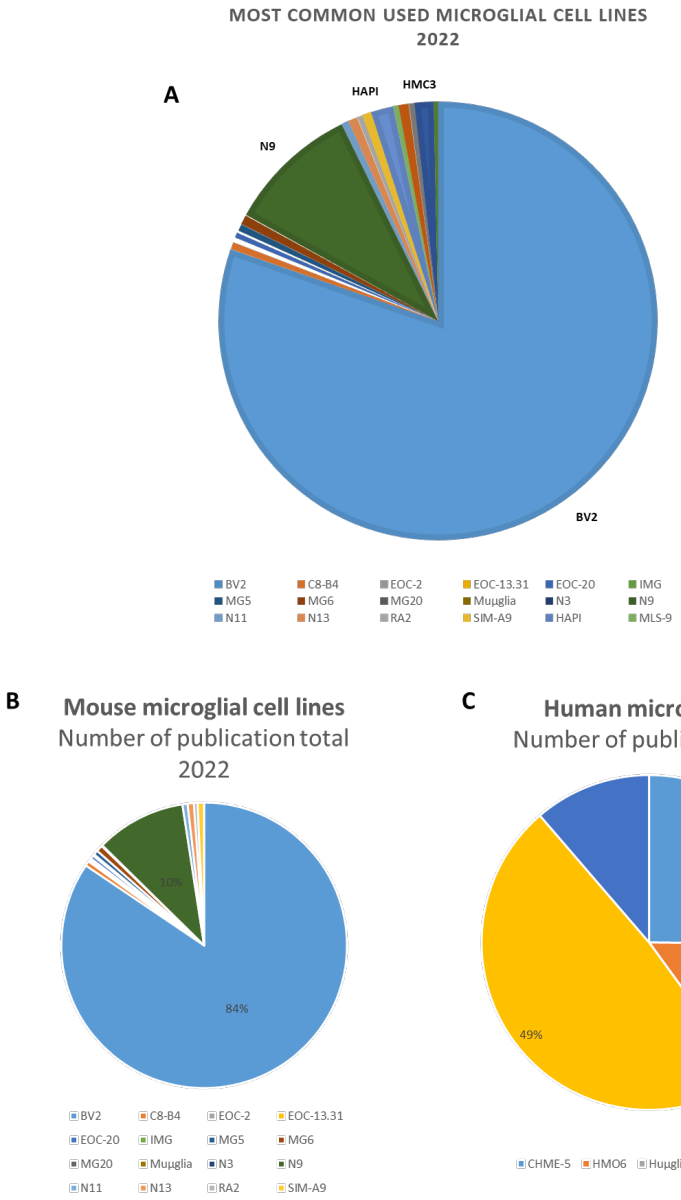

Annexe 2. Most used microglial cell lines worldwide in 2022:

Representation of the microglial cell lines used in 2022 for publications according to a Pubmeb search (database accessed in January 2023 using the keyword “microglia cell line”). In (A) is presented the overall used microglial cell lines, all species considered, only the murine ones in (B) and the human ones in (C).

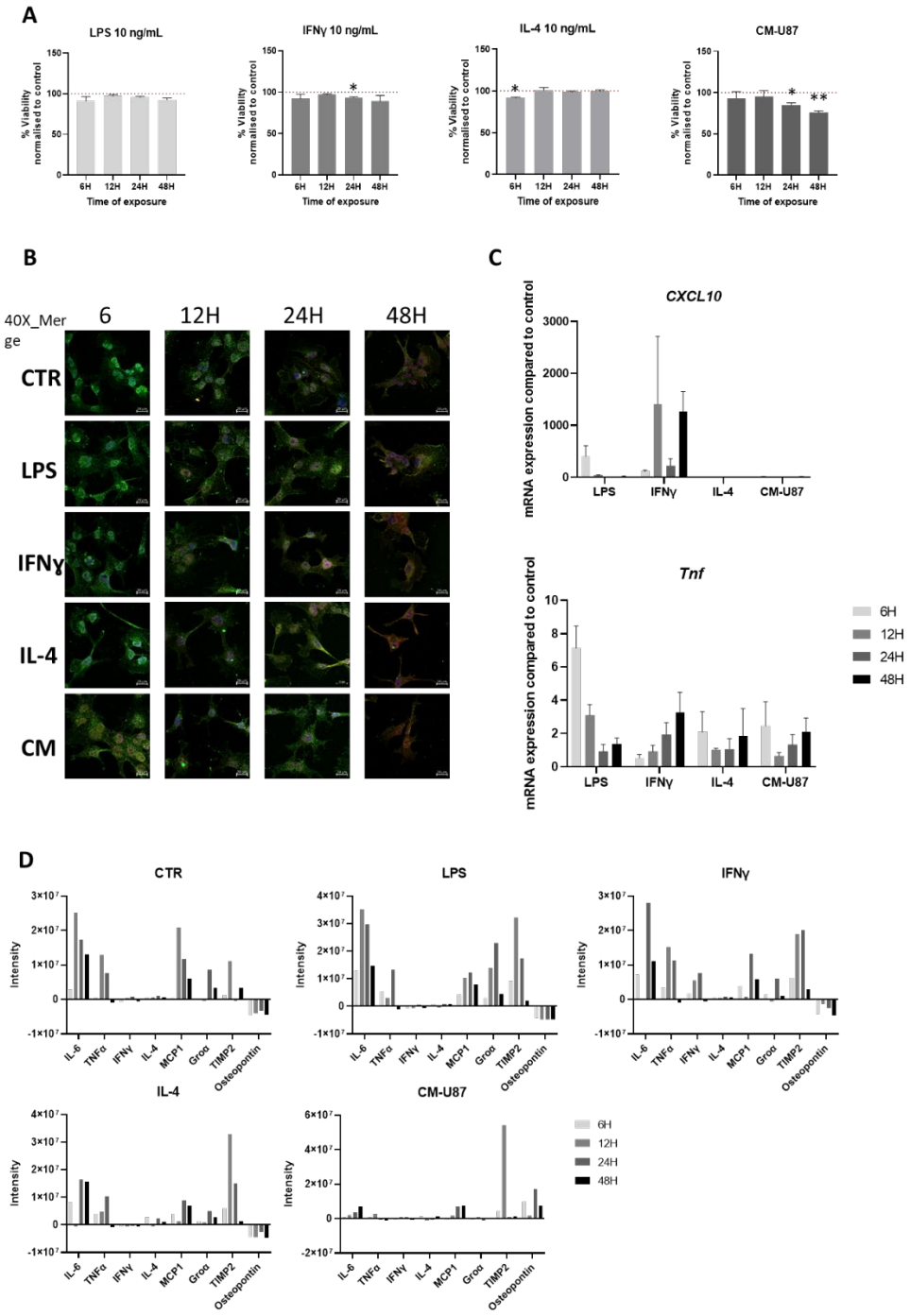

Annexe 3. Pilot study on human microglial cell line HMC3:

Results of a pilot study realized on the HMC3 cell line. The cell line was kindly donated by Dr.Tony Heurtaux, cultured in DMEM Full in standard culture conditions and treated or not with 10 ng/mL of LPS, human recombinant IFN-ɣ and IL-4 and U87 human glioma cells supernatant for 6, 12, 24 and 48 hours. (A) Viability assay using Cell Title Glo according to manufacturer's instructions. Three independent experiments (B) IF with CD11b (green) and Iba1 (red) together with DAPI (blue), imaged with Zeiss confocal microscope and scaled with Zen Blue software. (C) RTqPCR targeting the *Cxcl10* and *Tnf* genes, normalized to the expression of *Gapdh* housekeeping gene and to the control untreated HMC3 gene expression. Three independent experiments (D) Selected results of human Abcam CK arrays realized on HMC3 supernatants according to manufacturer's instructions. One biological replicate, two technical replicates.

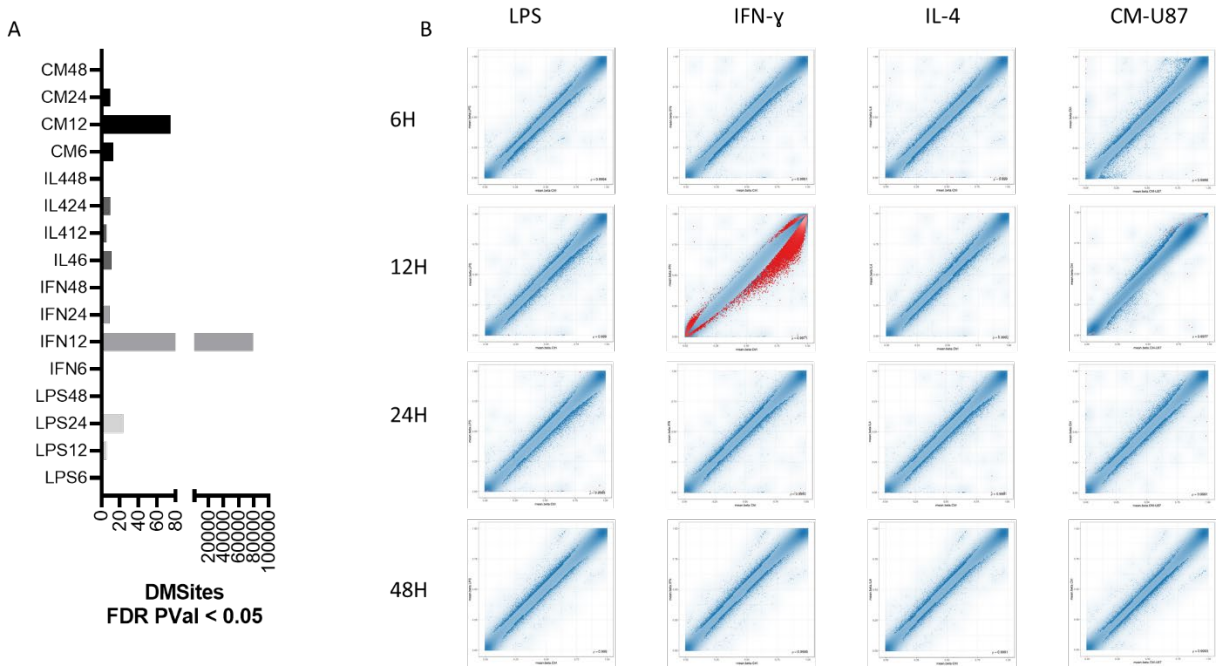

Annexe 4. Preliminary DNA methylation analysis of DMS in treated HMC3 cells:

HMC3 microglial cells were treated with 10 ng/mL of LPS, IFN-ɣ, IL-4 and CM-U87 for 6 to 48 hours of exposure. gDNA was extracted and submitted to Illumina DNA methylation assay and EPIC arrays according to manufacturer's instructions. Raw data were exported into R software and processed through the RnBeads data jungler pipeline. (A) Graph presenting the amount of significant differentially methylated sites between control and treated HMC3. (B) Scatter plot of each comparison between control and treated HMC3. Each dot represent a probe, red highlight a significant FDR adjusted 0.05 Pvalue. Results from three independent experiments.

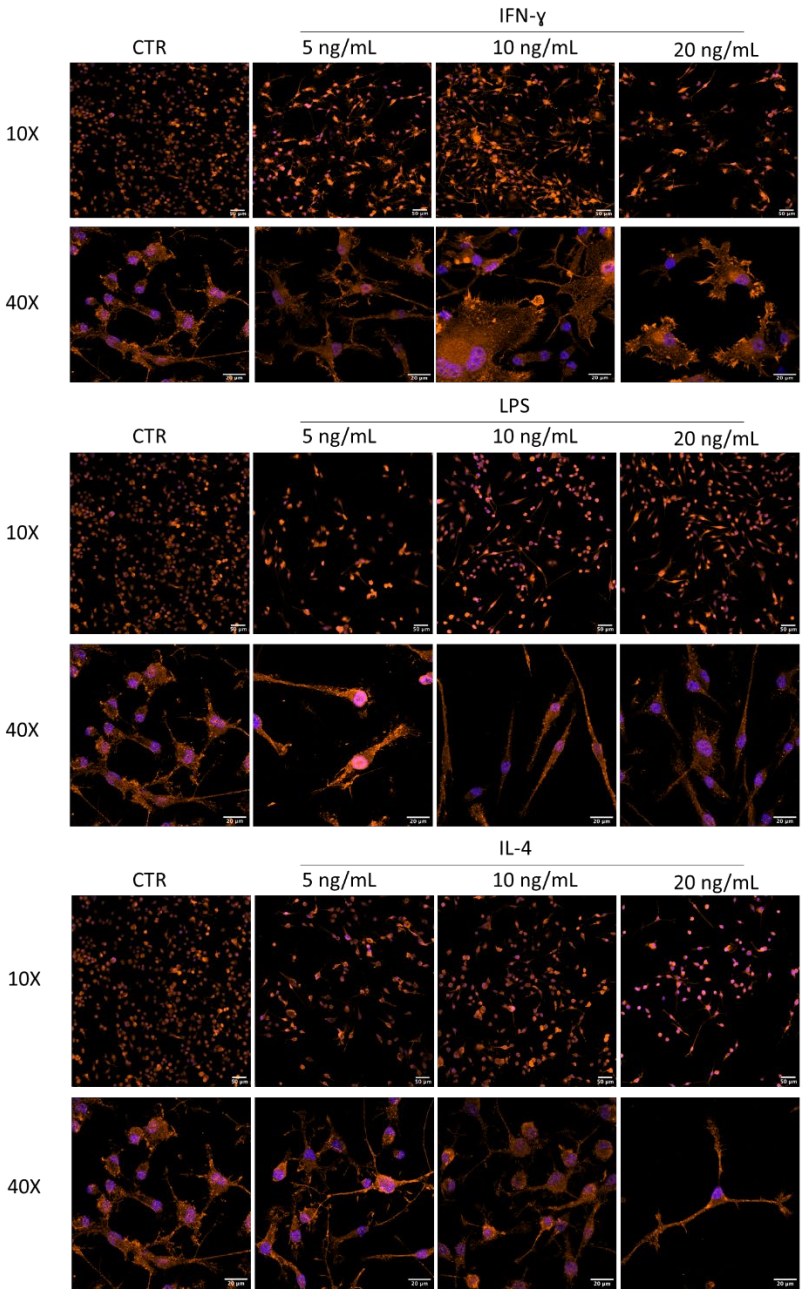

Annexe 5. Pilot study on concentration of IFN-ɣ, LPS and IL-4 on BV2 cells morphology:

BV2 cells were treated for 48 hours with 5, 10 or 20 ng/mL of LPS, IFN-ɣ and IL-4 and an IF staining was realized targeting Iba1 (Orange –Cy3) and DAPI (blue). Pictures were taken using Zeiss confocal microscope and scaled using FIJI software.

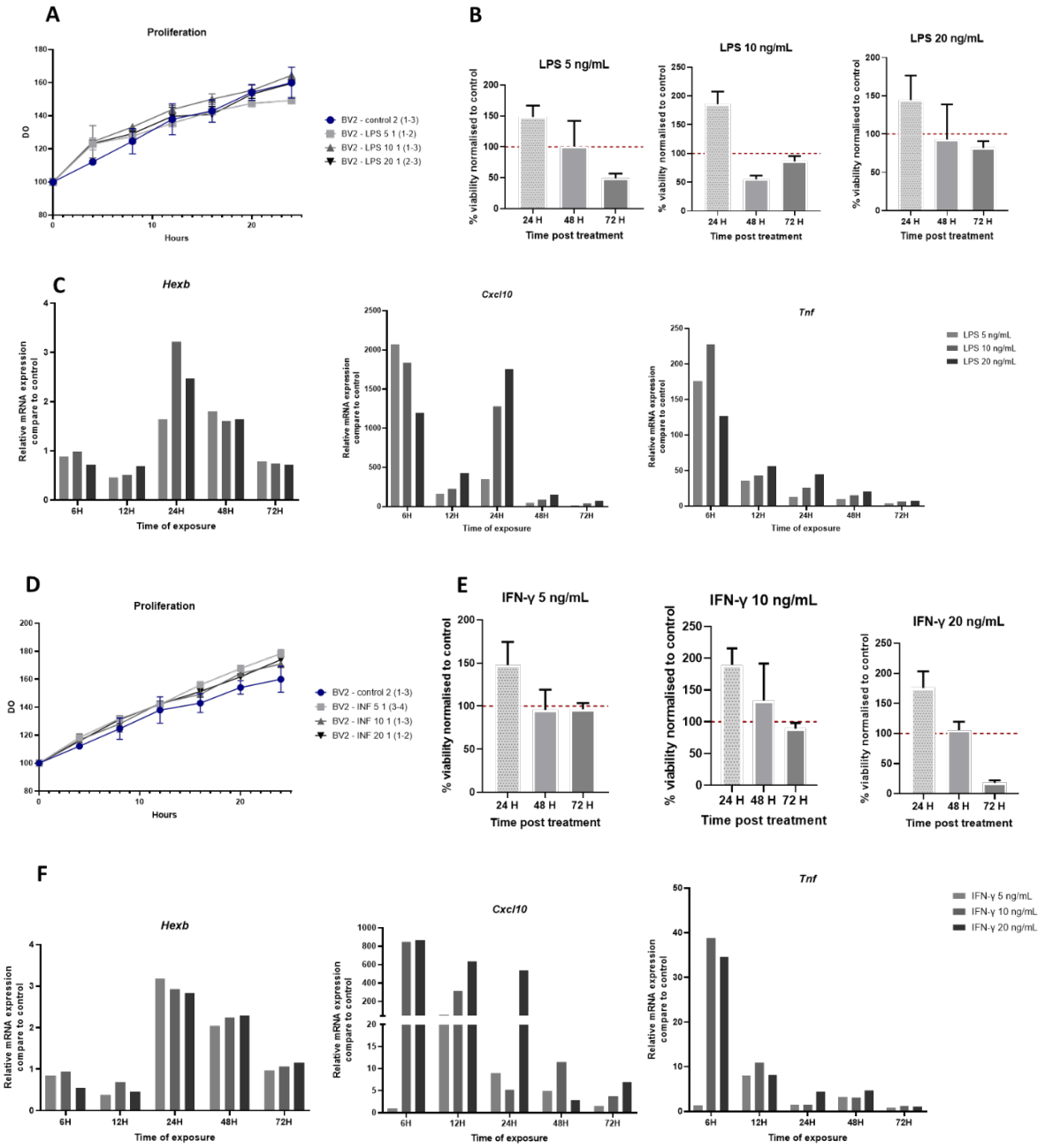

Annexe 6. Pilot study on the effects of concentrations and time of LPS and IFN-ɣ exposure on BV2 cells:

During the pilot study to decide the treatment concentration and time of exposure, the proliferation, viability and mRNA expression were assessed. The LPS (Top panel, A to C) and IFN-ɣ (Bottom panel, D to F) treatments at concentrations of 5, 10 and 20 ng/mL were tested. (A and D) Results of the confluence measure by the Incucyte system® according to the Material and Methods section. Three biological replicates, three technical replicates. (B and E) Results of the viability assessment by Abcam MTT assay (ab211091) according to manufacturer's instructions. Raw data were normalized to the control untreated BV2 values. Three biological replicates, three technical replicates. (C and F) Result of mRNA expression of *Hexb*, *Cxcl10* and *Tnf* realized according to the Material and Methods section. Normalized to the housekeeping gene *Rpl27* and the control values. One biological replicate, three technical replicates.

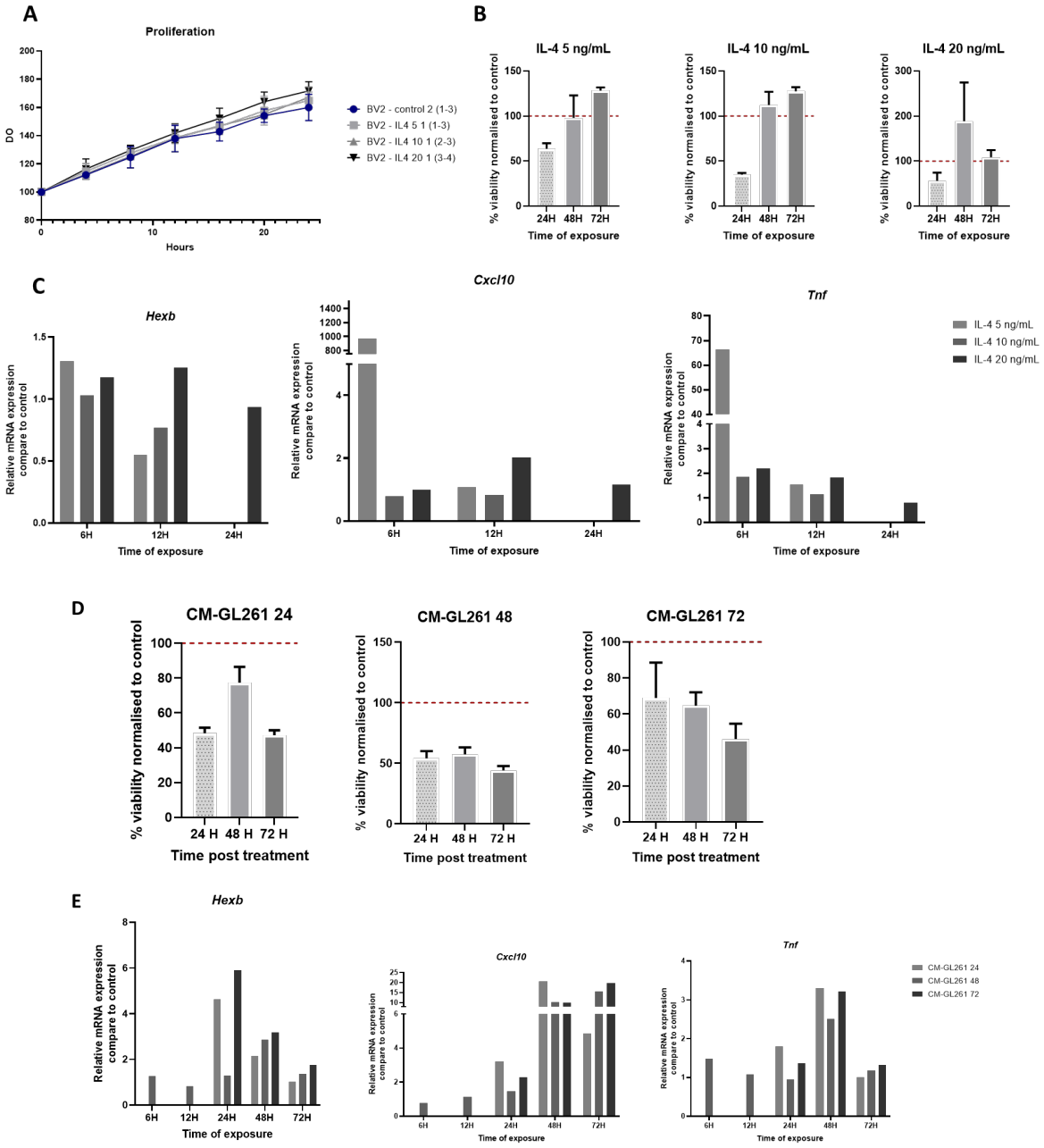

Annexe 7. Pilot study on the effects of concentration and time of IL-4 and CM-GL261 exposure on BV2 cells :

During the pilot study to decide the treatment concentration and time of exposure, the proliferation, viability and mRNA expression were assessed. The IL-4 (Top panel, A to C) treatment at concentrations of 5, 10 and 20 ng/mL and CM-GL261 harvested after 24, 48 or 72 hours (Bottom panel, D to E) were tested. (A) Results of the confluence measure by the Incucyte system® according to the Material and Methods section. Three biological replicates, three technical replicates. (B and D) Results of the viability assessment by Abcam MTT assay (ab211091) according to manufacturer's instructions. Raw data were normalized to the control untreated BV2 values. Three biological replicates, three technical replicates. (C and E) Result of mRNA expression of *Hexb*, *Cxcl10* and *Tnf* realized according to the Material and Methods section. Normalized to the housekeeping gene *Rpl27* and the control values. One biological replicate, three technical replicates.

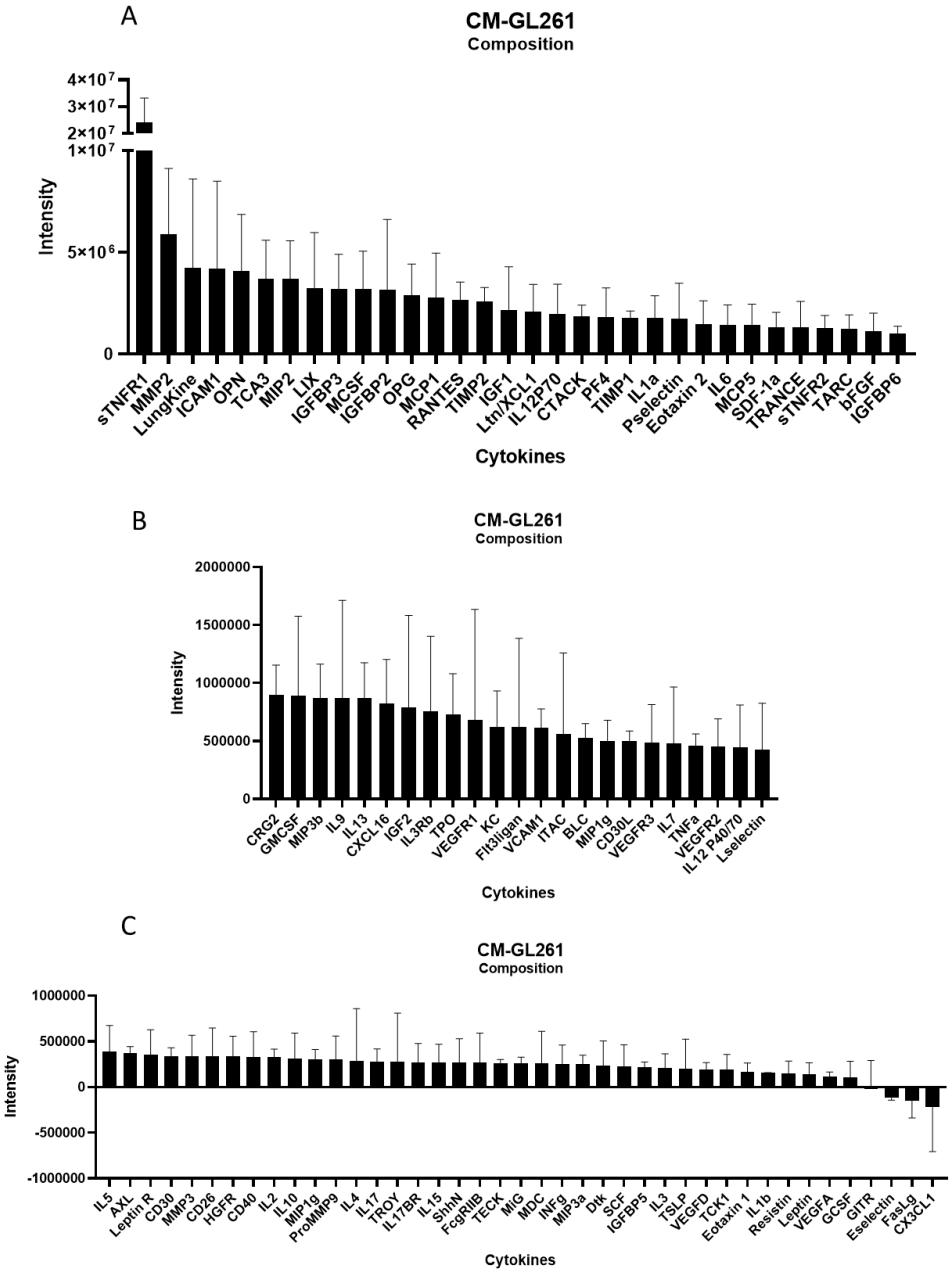

Annexe 8. CM-GL261 composition exploration by CK arrays :

Complementary results from the 96 targets Abcam mouse CK arrays on GL261 supernatant. Briefly, 10^6 GL261 cells were kept in culture for 48 hours in 8 mL of DMEM Full. The supernatant was harvested and used for CK array analysis according to manufacturer's instructions. The raw intensity data were normalized to the DMEM Full. The data were further visualized with GraphPad Prism software. Results from two independent experiments with two technical replicates for each.

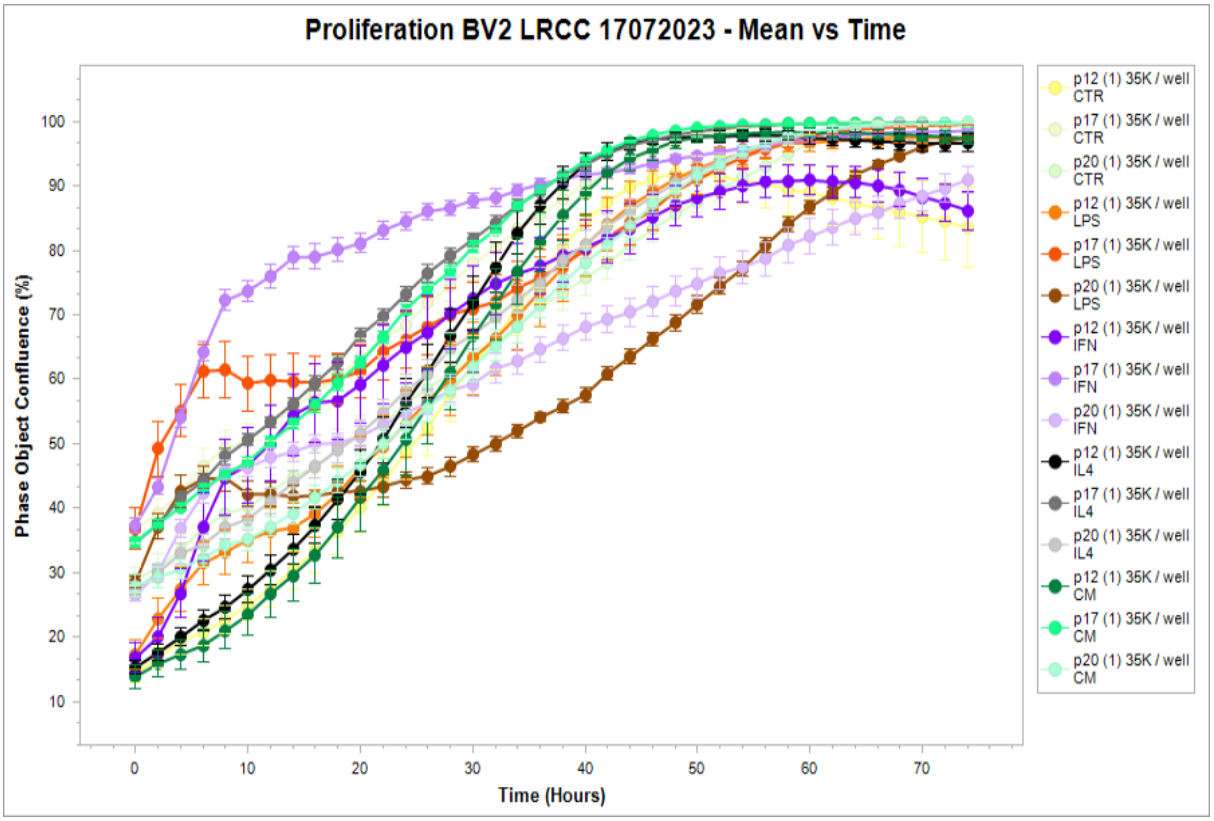

Annexe 9. Confluence data of BV2 cells generated by the Incucyte system:

Results exported from the Incucyte Imaging System showing the confluence of the BV2 cells treated or not with 10 ng/mL of LPS, IFN-ɣ, IL-4 or CM-GL261 for 72 hours. The confluence measure is a estimation based on a predefined area mask applied on the contrast phase pictures made by the system.

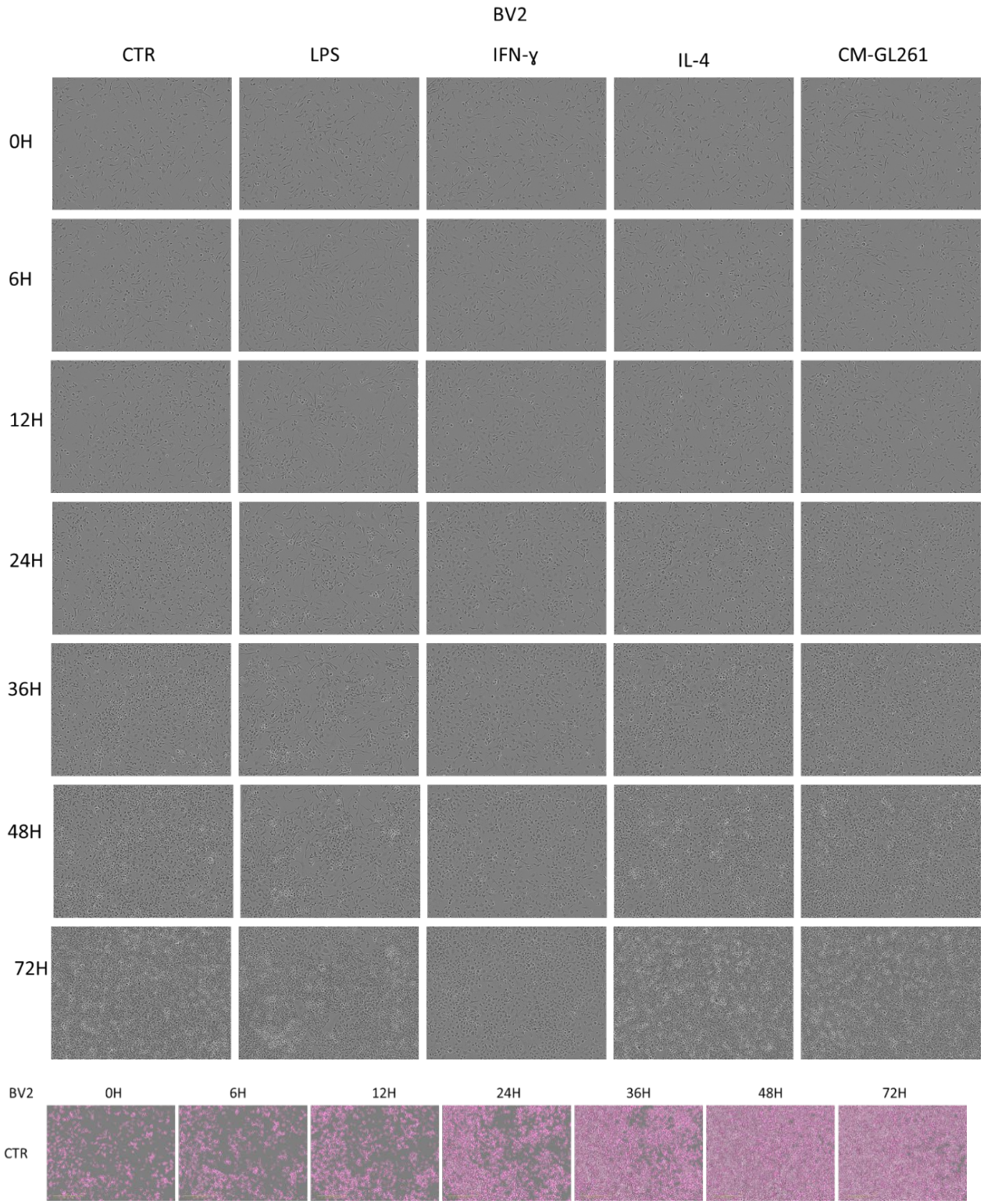

Annexe 10. Selection of Incucyte pictures of the BV2 cells for 72 hours:

Selection of Incucyte brightfield pictures of BV2 cells treated or not with 10 ng/mL of LPS, IFN-ɣ, IL-4 or CM-GL261 for 72 hours. The top panel shows the phase contrast brighfield picture while the bottom panel shows the pictures merged with the phase contrast aera analysis mask (in pink).

	X	A			B			C			D			E		
		CTR			LPS			IFN-γ			IL-4			CM-GL261		
	X	Mean	SD	N	Mean	SD	N	Mean	SD	N	Mean	SD	N	Mean	SD	N
1	0	26.667	11.313	3	27.616	9.815	3	26.878	10.281	3	25.764	9.793	3	25.540	10.662	3
2	6	34.761	13.021	3	45.739	14.918	3	47.909	14.444	3	33.732	10.835	3	31.382	12.209	3
3	12	41.079	13.040	3	46.167	12.230	3	57.979	15.673	3	41.628	11.448	3	38.071	11.835	3
4	18	48.673	12.098	3	48.286	10.208	3	62.280	15.732	3	51.005	10.769	3	46.953	11.482	3
5	24	57.738	10.038	3	54.521	10.994	3	68.094	15.130	3	62.562	9.227	3	58.082	11.075	3
6	30	67.814	8.824	3	60.876	11.567	3	73.202	14.246	3	73.527	7.484	3	69.729	9.644	3
7	36	77.655	7.185	3	67.848	11.989	3	77.490	12.839	3	83.701	7.673	3	80.769	8.876	3
8	42	85.884	7.136	3	75.670	12.828	3	81.117	11.395	3	91.394	6.551	3	89.531	7.693	3
9	48	91.457	5.640	3	83.020	12.376	3	84.963	10.424	3	95.248	4.198	3	94.969	5.009	3
10	54	93.685	4.550	3	88.906	10.167	3	87.758	9.409	3	97.430	2.064	3	97.669	2.089	3
11	60	95.099	5.495	3	93.699	6.053	3	90.062	7.519	3	98.381	1.157	3	98.737	0.812	3
12	66	95.136	7.514	3	96.540	2.951	3	91.349	6.283	3	98.662	1.520	3	99.163	0.889	3
13	72	94.653	8.842	3	97.977	1.333	3	91.801	5.832	3	98.682	1.822	3	99.032	1.228	3

Annexe 11. Row statistics of Incucyte measured BV2 confluence :

Row analysis of BV2 confluence measures from the Incucyte system®. BV2 were treated or not with 10 ng/mL of LPS, IFN-ɣ, IL-4 or CM-GL261 and left in the Incucyte system® for 72 hours according to the Materials and Methods section. Results from three independent experiments, each containing three technical replicates. Row statistics generated on GraphPad Prism software from the raw data. Left axis : time in hours. SD : Standard Deviation; N : Biological replicates.

	X	A			B			C			D		
		LPS			IFN-γ			IL-4			CM-GL261		
	X	Mean	SD	N	Mean	SD	N	Mean	SD	N	Mean	SD	N
1	0	111.979	22.507	3	89.364	12.544	3	91.761	4.730	3	93.664	13.398	3
2	36	88.698	32.435	3	75.873	16.375	3	111.312	18.923	3	115.753	16.050	3
3	72	108.194	14.386	3	86.028	30.586	3	104.092	14.454	3	116.391	27.324	3

Annexe 12. Row statistics of manual countings of BV2 cells from Incucyte generated pictures :

Row analysis of BV2 numbers from Incucyte generated pictures. BV2 were treated or not with 10 ng/mL of LPS, IFN-ɣ, IL-4 or CM-GL261 and left in the Incucyte system® for 72 hours according to the Materials and Methods section. Results from three independent experiments, each containing three technical replicates. Row statistics generated on GraphPad Prism software from the pre-processed data of BV2 numbers. The raw data were generated by a third party to avoid observer bias. The pre-processing was done by normalization to the control untreated BV2 values. Left axis : time in hours. SD : Standard Deviation; N : Biological replicates.

BV2

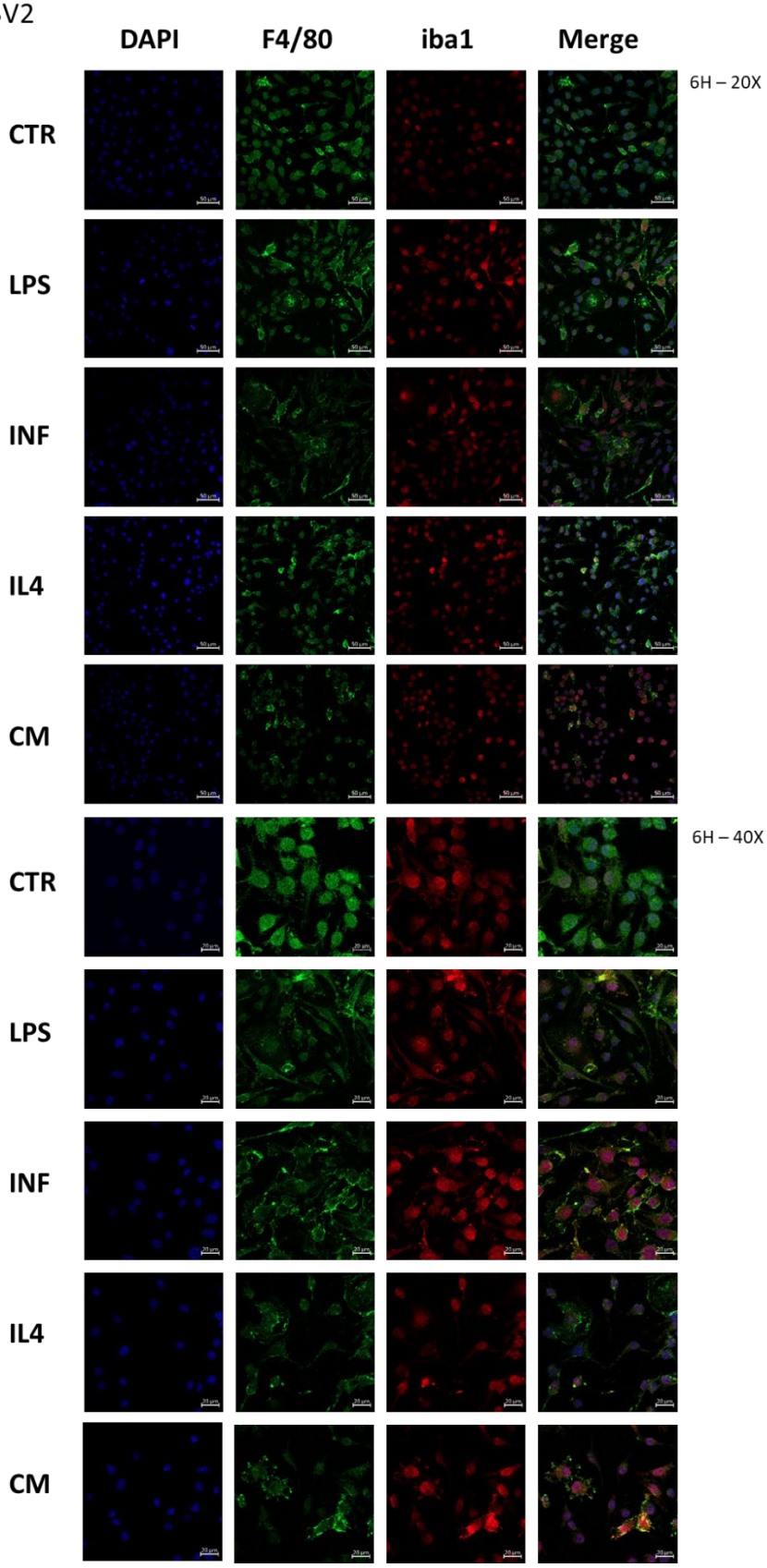
DAPI
F4/80
iba1
Merge
6H – 20X
CTR
LPS
INF
IL4
CM
6H – 40X
CTR
LPS
INF
IL4
CM

BV2

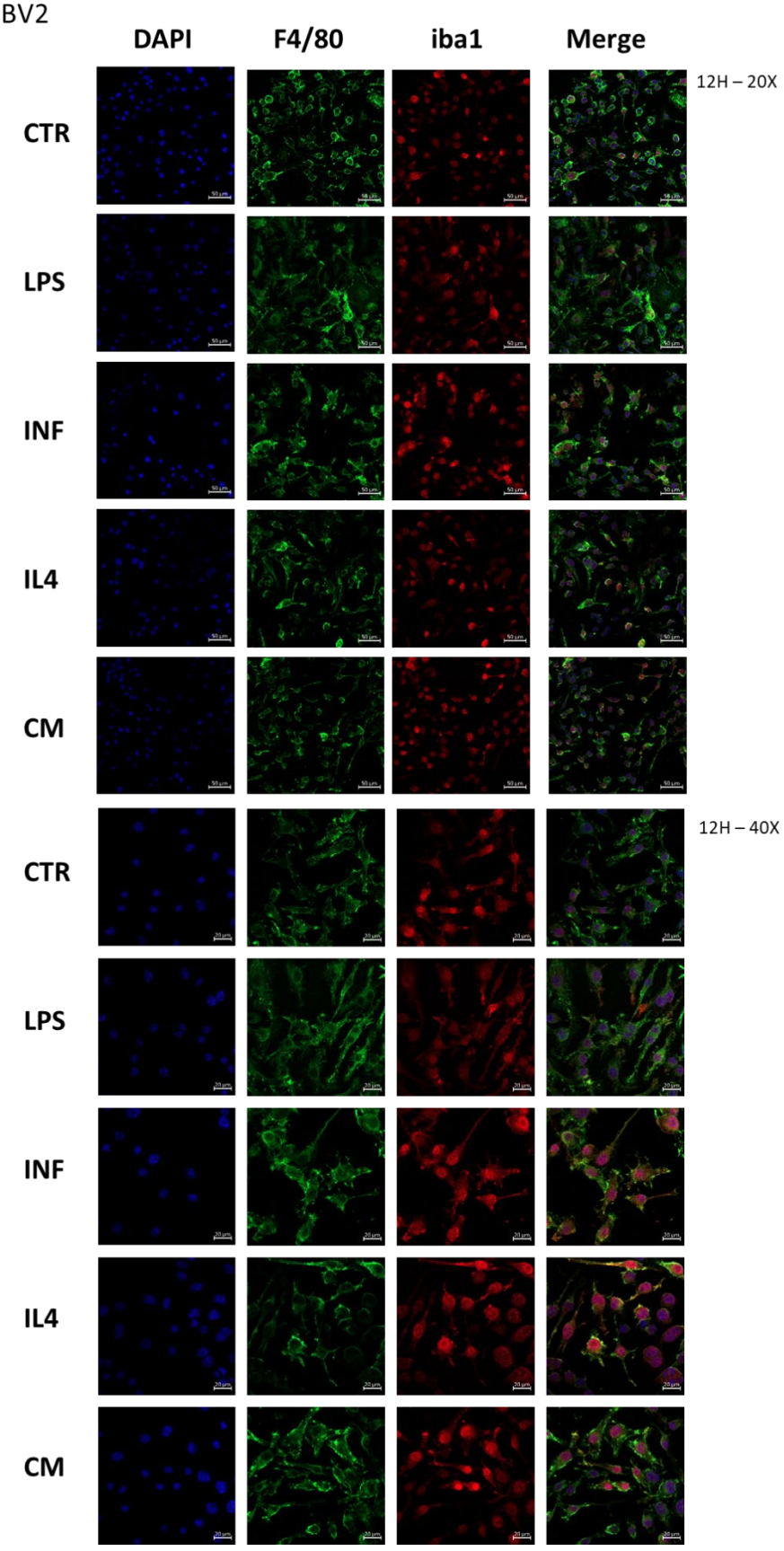
DAPI
F4/80
iba1
Merge
12H – 20X
CTR
LPS
INF
IL4
CM
12H – 40X
CTR
LPS
INF
IL4
CM

BV2

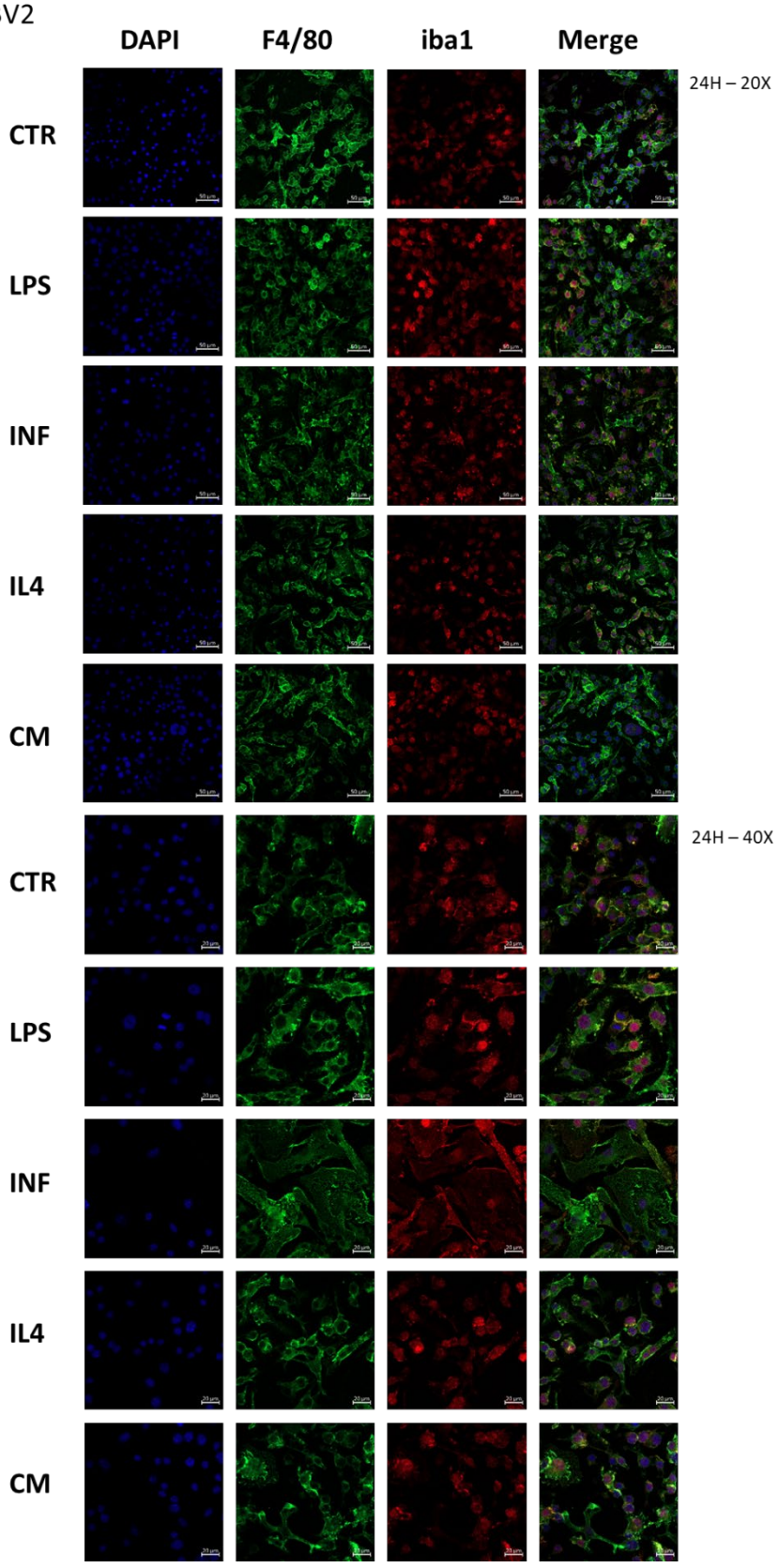
DAPI
F4/80
iba1
Merge
24H – 20X
CTR
LPS
INF
IL4
CM
24H – 40X
CTR
LPS
INF
IL4
CM

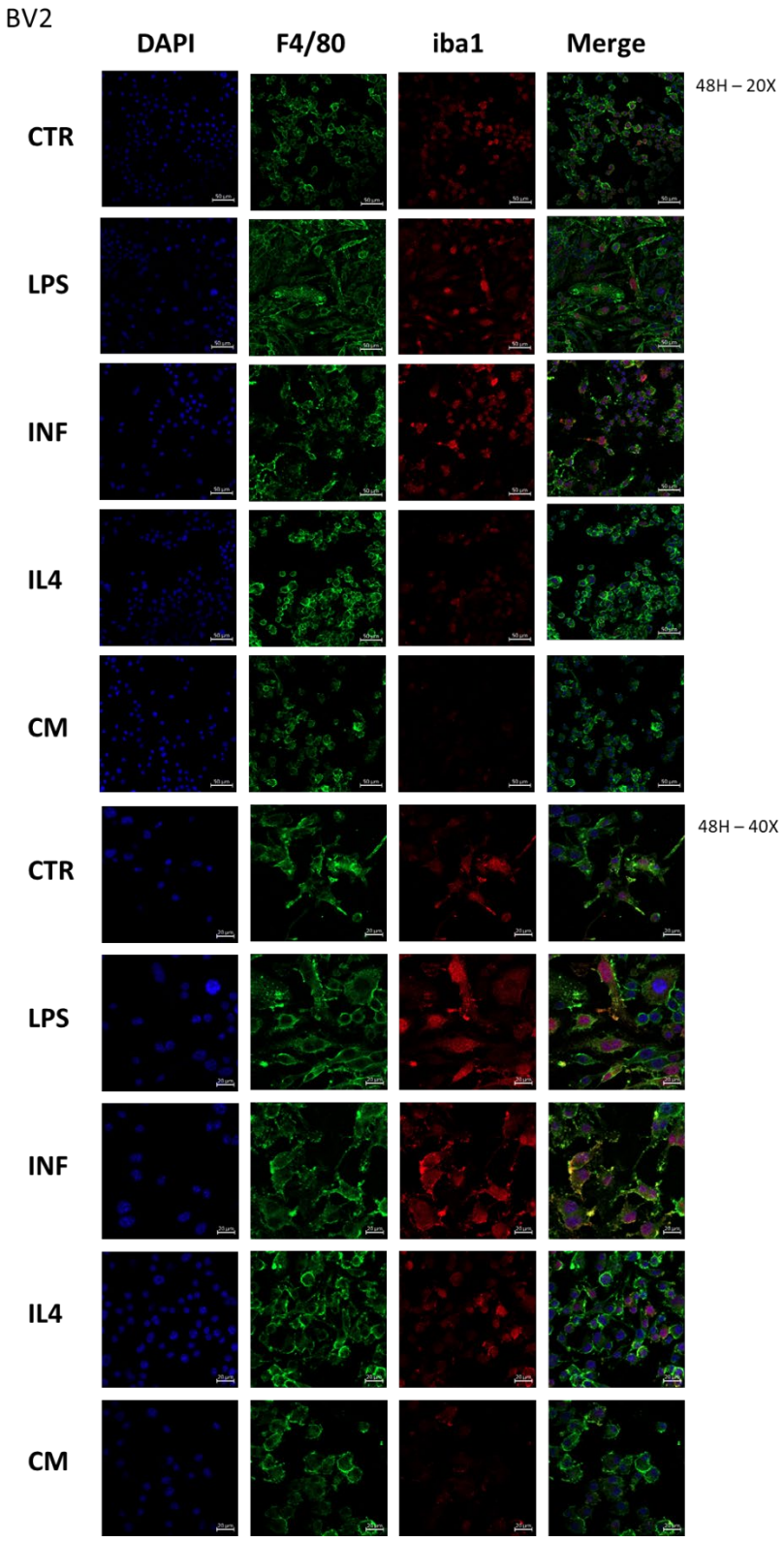

Annexe 13. Individual channels of IF stainings of BV2 cells at 20 and 40X objectives :

Confocal images of BV2 cells, treated or not with 10 ng/mL of LPS, IFN-ɣ, IL-4 or CM-GL261 for 6 to 48 hours and stained for Iba1 (red), F4/80 (green) and counterstained with DAPI (blue). The detailed procedure can be found in the Materials and Methods section.

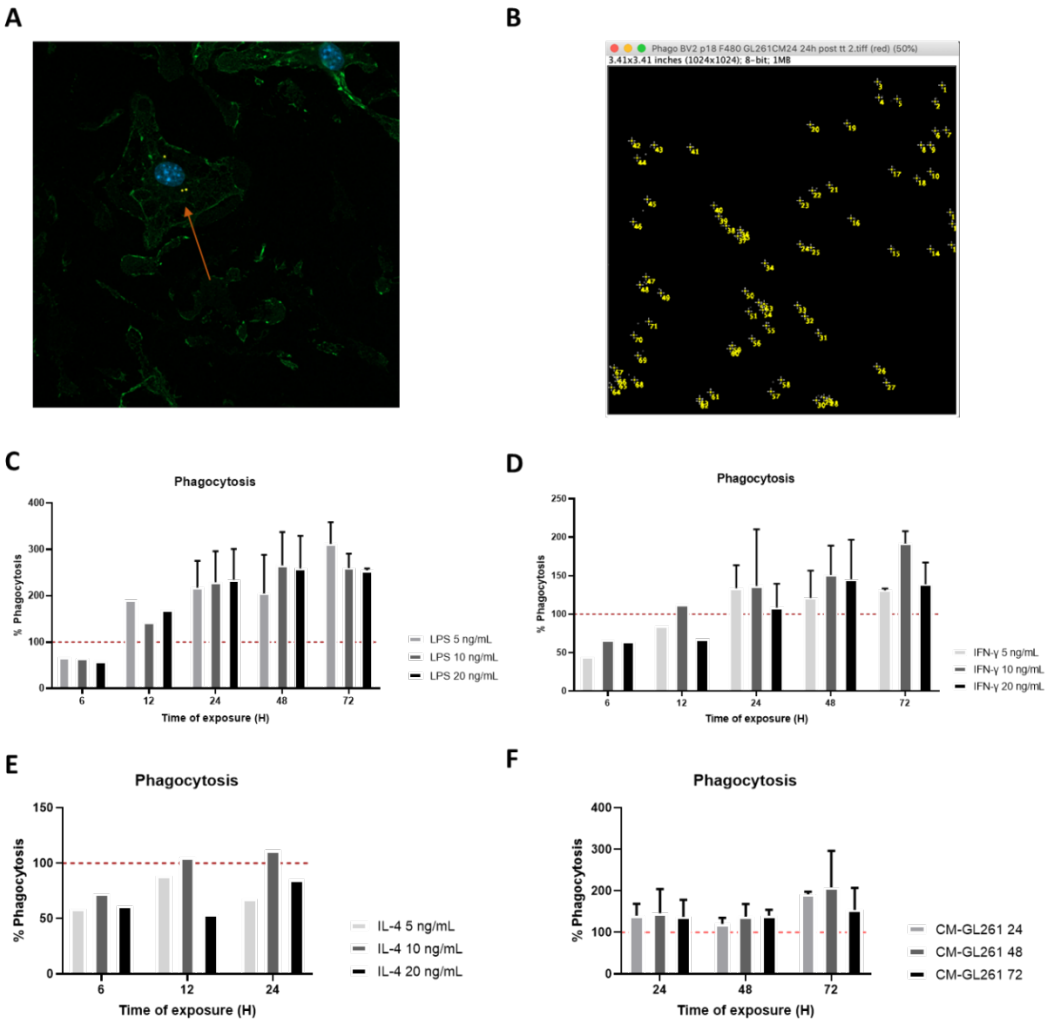

<u>Annexe 14. Phagocytosis assessment by manual counting of fluorescent beads, BV2 cells</u> :

During the pilot study to decide the treatment concentration and time of exposure, the phagocytosis was assessed by manual counting of engulfed fluorescent particles. Those results were later excluded because of the potential observer biais carried out by this method. Briefly, 10^4 BV2 cells were plated in a 24 well plate with 1 mL of DMEM full and were treated or not with 5, 10 and 20 ng/mL of LPS, IFN-ɣ and IL-4 and with different GL261 conditionned media (24, 48 and 72 hours in culture before media harvest) with an exposure time ranging from 6 to 72 hours. Following treatment exposure, sonicated fluorescent microspheres (Caroxylates, 1 µm, Invitrogen) were disposed in the media for 2 hours at 37°C. After three washes of PBS, the cells were fixed with PFA solution and the IF protocol targeting F4/80 couple with DAPI was realized. Using a Zeiss confocal microscope, five pictures at the 20X objective were made and exported into FIJI software with which the beads were counted manually. Data were normalized to the amount of beads within the control untreated BV2, Statistical analysis (2-way ANOVA and multiple comparison with Tukey's) and visualization of the results was made using GraphPad Prism software. (A) Representative 40X of the beads engulfed by a BV2 cell. (B) Representative 20X image in FIJI for manual counting. (C, D, E and F) Graphs showing the percentage of phagocytosis in treated BV2 compared to untreated BV2 cells. Except for the IL-4 condition and the LPS and IFN-ɣ at the 6 and 12 hours timepoints, the results are representative of three independent experiments.

	X	A			B			C			D		
		LPS			IFN-y			IL-4			CM-GL261		
	X	Mean	SD	N	Mean	SD	N	Mean	SD	N	Mean	SD	N
1	0	91.259	28.982	3	99.468	15.520	3	130.088	57.732	3	87.867	8.357	3
2	30	59.314	18.136	3	56.136	54.381	3	90.445	42.794	3	33.287	55.416	3
3	60	29.286	42.014	3	30.427	95.084	3	57.655	71.247	3	-45.285	96.627	3
4	90	-827.386	1456.142	3	-1076.790	2007.760	3	-934.948	1713.988	3	-1745.435	2839.623	3
5	120	-17.198	282.724	3	171.987	262.536	3	103.726	145.391	3	-42.561	407.816	3
6	150	1602.404	2513.953	3	-1313.823	1851.720	3	-155.244	399.186	3	13.731	1865.411	3
7	180	-14.112	207.041	3	52.061	451.177	3	-57.670	313.455	3	-298.005	656.126	3
8	210	67.488	94.732	3	12.520	297.380	3	-17.067	228.939	3	-226.262	569.912	3
9	240	135.238	71.839	3	-30.442	351.710	3	-46.167	286.101	3	-339.925	783.331	3
10	270	168.191	92.715	3	-11.394	290.461	3	-13.285	220.984	3	-292.947	720.769	3
11	300	158.322	64.603	3	60.194	185.931	3	22.852	161.216	3	-109.030	522.329	3
12	330	171.797	60.647	3	97.483	166.758	3	48.851	110.390	3	-9.261	581.503	3
13	360	186.116	72.296	3	246.748	336.741	3	107.523	122.339	3	500.963	1271.201	3
14	390	144.479	55.834	3	2.253	143.624	3	102.142	80.196	3	-481.736	585.132	3
15	420	140.007	69.691	3	72.997	57.620	3	85.739	50.769	3	-199.632	173.376	3
16	450	143.972	37.121	3	85.240	40.007	3	94.943	39.948	3	-139.371	118.503	3
17	480	145.629	26.801	3	92.930	37.673	3	102.001	42.922	3	-92.042	86.218	3

Annexe 15. Row statistics of treated BV2 phagocytosis percentage compare to control :

Phagocytosis assay using pHrodo fluorescent beads was realized on BV2 treated or not with 10 ng/mL of LPS, IFN-ɣ, IL-4 or CM-GL261 according to manufacturer's instructions. Results from three independent experiments. Row statistics generated on GraphPad Prism software from the pre-processed data of phagocytosis experiments. The raw data were generated with a Clariostar plate reader measuring fluorescence intensity. The pre-processing was done by substraction of background fluorescence intensity (wells with BV2 cells but no pHrodo beads) and normalization to the control untreated BV2 phagocytosis values. Left axis : time in minutes. SD : Standard Deviation; N : Biological replicates.

	X	A			B			C			D			E		
		CTR			LPS			IFN-γ			IL-4			CM-GL261		
	X	Mean	SD	N	Mean	SD	N	Mean	SD	N	Mean	SD	N	Mean	SD	N
1	6H	98382.500	1638261.053	2	5177088.500	2305516.710	2	3743885.641	1.003e+007	2	2163259.427	3611786.572	2	3255555.500	2603381.199	2
2	12H	-358746.000	230577.622	2	2361932.500	4224570.573	2	1182523.550	1408954.739	2	2936529.500	4967243.411	2	1512920.500	2580632.160	2
3	24H	5552115.500	3429042.432	2	2159304.000	4126737.400	2	9231556.000	1.423e+007	2	1.803e+007	2.482e+007	2	1.298e+007	1.446e+007	2
4	48H	2.425e+007	3.370e+007	2	3546438.500	1.021e+007	2	3691429.500	1.072e+007	2	5.302e+007	6.066e+007	2	6.118e+007	8.601e+007	2

Annexe 16. Row statistics of the IL-4 measures of intensity (CK arrays, BV2 cells):

CK array row analysis, focusing on IL-4 intensity in BV2 treated or not with 10 ng/mL of LPS, IFN-ɣ, IL-4 or CM-GL261 from 6 to 48 hours, according to manufacturer's instructions. Results from two independent experiments, each containing two technical replicates. Row statistics generated on GraphPad Prism software from the pre-processed data of IL-4 intensity. The raw data were generated with FIJI software from pixel intensity measurement on chemiluminescence exposed arrays. The pre-processing was done by substraction of background intensity (measure of the intensity of negative control on the array). Left axis : time in hours. SD : Standard Deviation; N : Biological replicates.

	X	A			B			C			D			E		
		CTR			LPS			IFN-γ			IL-4			CM-GL261		
	X	Mean	SD	N	Mean	SD	N	Mean	SD	N	Mean	SD	N	Mean	SD	N
1	6H	968633.000	2037416.467	2	3.146e+007	1.369e+007	2	254404.450	655624.387	2	-153860.000	17198.251	2	1031923.250	670218.081	2
2	12H	-788522.000	176288.792	2	4956399.000	4400626.727	2	171785.200	171194.229	2	220478.350	42391.688	2	653909.600	413085.559	2
3	24H	49417.700	209657.161	2	2.160e+007	2329456.517	2	3654228.257	5155945.100	2	1448447.500	3240289.248	2	3043628.500	1904949.204	2
4	48H	2054930.500	2472116.725	2	2.343e+007	2.155e+007	2	5865148.625	3237740.791	2	1553803.850	2016757.848	2	1.439e+007	2.037e+007	2

Annexe 17. Row statistics of the IL-6 measures of intensity (CK arrays, BV2 cells):

CK arrays focusing on IL-6 intensity in BV2 treated or not with 10 ng/mL of LPS, IFN-ɣ, IL-4 or CM-GL261 from 6 to 48 hours, according to manufacturer's instructions. Results from two independent experiments, each containing two technical replicates. Row statistics generated on GraphPad Prism software from the pre-processed data of IL-6 intensity. The raw data were generated with FIJI software from pixel intensity measurement on chemiluminescence exposed arrays. The pre-processing was done by substraction of background intensity (measure of the intensity of negative control on the array). Left axis : time in hours. SD : Standard Deviation; N : Biological replicates.

	X	A			B			C			D			E		
		CTR			LPS			IFN-γ			IL-4			CM-GL261		
	X	Mean	SD	N	Mean	SD	N	Mean	SD	N	Mean	SD	N	Mean	SD	N
1	6H	1841899.500	3112737.084	2	1759283.500	554447.377	2	600389.145	810653.879	2	1062731.000	1889938.034	2	1029883.000	1796113.450	2
2	12H	-118499.200	476350.686	2	485924.000	1232429.137	2	760679.000	1224877.236	2	3775175.600	3143308.439	2	190764.550	81191.061	2
3	24H	990119.050	862607.977	2	956480.150	879861.241	2	2.145e+007	1.234e+007	2	3299249.500	340807.791	2	1214231.400	615139.908	2
4	48H	2160408.350	2151220.566	2	1731415.835	2328399.626	2	9112603.000	1.010e+007	2	526574.450	763813.280	2	4834777.850	3858313.736	2

Annexe 18. Row statistics of the IFN-ɣ measures of intensity (CK arrays, BV2 cells) :

CK arrays focusing on IFN-ɣ intensity in BV2 treated or not with 10 ng/mL of LPS, IFN-ɣ, IL-4 or CM-GL261 from 6 to 48 hours, according to manufacturer's instructions. Results from two independent experiments, each containing two technical replicates. Row statistics generated on GraphPad Prism software from the pre-processed data of IFN-ɣ intensity. The raw data were generated with FIJI software from pixel intensity measurement on chemiluminescence exposed arrays. The pre-processing was done by substraction of background intensity (measure of the intensity of negative control on the array). Left axis : time in hours. SD : Standard Deviation; N : Biological replicates.

	X	A			B			C			D			E		
		CTR			LPS			IFN-γ			IL-4			CM-GL261		
	X	Mean	SD	N	Mean	SD	N	Mean	SD	N	Mean	SD	N	Mean	SD	N
1	6H	-487533.500	1052548.95(	2	1400696.00(	1456477.33	2	705977.500	1158644.66	2	441690.750	311362.945	2	7097272.00(	3134242.32	2
2	12H	592362.850	606819.453	2	451833.000	1034771.57	2	180185.800	272119.862	2	3320282.00(	4868983.14	2	2071266.35(	1755776.75	2
3	24H	948360.350	239843.054	2	163988.800	400058.107	2	865675.000	932497.068	2	201942.750	89816.774	2	1.823e+007	5489847.64	2
4	48H	1988557.85(	2642987.16	2	1233868.50(	552992.151	2	659911.800	0.000	1	1681479.75(	1994748.58	2	9813041.00(	1.034e+007	2

Annexe 19. Row statistics of the MMP2 measures of intensity (CK arrays, BV2 cells):

CK arrays focusing on MMP2 intensity in BV2 treated or not with 10 ng/mL of LPS, IFN-ɣ, IL-4 or CM-GL261 from 6 to 48 hours, according to manufacturer's instructions. Results from two independent experiments, each containing two technical replicates. Row statistics generated on GraphPad Prism software from the pre-processed data of MMP2 intensity. The raw data were generated with FIJI software from pixel intensity measurement on chemiluminescence exposed arrays. The pre-processing was done by substraction of background intensity (measure of the intensity of negative control on the array). Left axis : time in hours. SD : Standard Deviation; N : Biological replicates.

	X	A			B			C			D			E		
		CTR			LPS			IFN-γ			IL-4			CM-GL261		
	X	Mean	SD	N	Mean	SD	N	Mean	SD	N	Mean	SD	N	Mean	SD	N
1	6H	789319.500	1688551.902	2	9475976.500	5516717.706	2	1734364.750	1752082.264	2	3407301.500	1584744.383	2	1443074.400	1691239.049	2
2	12H	328675.900	576913.149	2	1970507.500	1161309.044	2	1589832.350	1947092.980	2	921843.800	178858.701	2	770894.000	223395.397	2
3	24H	4617139.650	5817759.721	2	2528230.000	584221.522	2	4881204.500	3217524.652	2	9800859.000	3829807.707	2	4541076.000	3659437.399	2
4	48H	4273460.500	4157524.123	2	2477603.400	2557808.309	2	3914328.500	9613200.836	2	3030905.000	9696003.747	2	1.569e+007	2.224e+007	2

Annexe 20. Row statistics of the TNFα measures of intensity (CK arrays, BV2 cells):

CK arrays focusing on TNFα intensity in BV2 treated or not with 10 ng/mL of LPS, IFN-ɣ, IL-4 or CM-GL261 from 6 to 48 hours, according to manufacturer's instructions. Results from two independent experiments, each containing two technical replicates. Row statistics generated on GraphPad Prism software from the pre-processed data of TNFα intensity. The raw data were generated with FIJI software from pixel intensity measurement on chemiluminescence exposed arrays. The pre-processing was done by substraction of background intensity (measure of the intensity of negative control on the array). Left axis : time in hours. SD : Standard Deviation; N : Biological replicates.

	X	A			B			C			D			E		
		CTR			LPS			IFN-γ			IL-4			CM-GL261		
	X	Mean	SD	N	Mean	SD	N	Mean	SD	N	Mean	SD	N	Mean	SD	N
1	6H	785139.500	1908554.034	2	1.321e+007	1.147e+007	2	14240.500	476157.928	2	-121766.000	373294.398	2	1005514.500	1708516.354	2
2	12H	-931634.500	69776.590	2	9757218.000	1046304.490	2	-17865.150	695894.684	2	25421.760	136.104	2	169703.150	44634.913	2
3	24H	349079.600	129035.957	2	3.107e+007	1699679.641	2	4371962.500	6578523.391	2	2736751.850	3457241.841	2	1091888.900	883948.672	2
4	48H	1695301.400	1866001.904	2	3.103e+007	1.552e+007	2	7178405.000	1.034e+007	2	953750.350	1411617.986	2	5916831.000	8540633.693	2

Annexe 21. Row statistics of the G-CSF measures of intensity (CK arrays, BV2 cells):

CK arrays focusing on G-CSF intensity in BV2 treated or not with 10 ng/mL of LPS, IFN-ɣ, IL-4 or CM-GL261 from 6 to 48 hours, according to manufacturer's instructions. Results from two independent experiments, each containing two technical replicates. Row statistics generated on GraphPad Prism software from the pre-processed data of G-CSF intensity. The raw data were generated with FIJI software from pixel intensity measurement on chemiluminescence exposed arrays. The pre-processing was done by substraction of background intensity (measure of the intensity of negative control on the array). Left axis : time in hours. SD : Standard Deviation; N : Biological replicates.

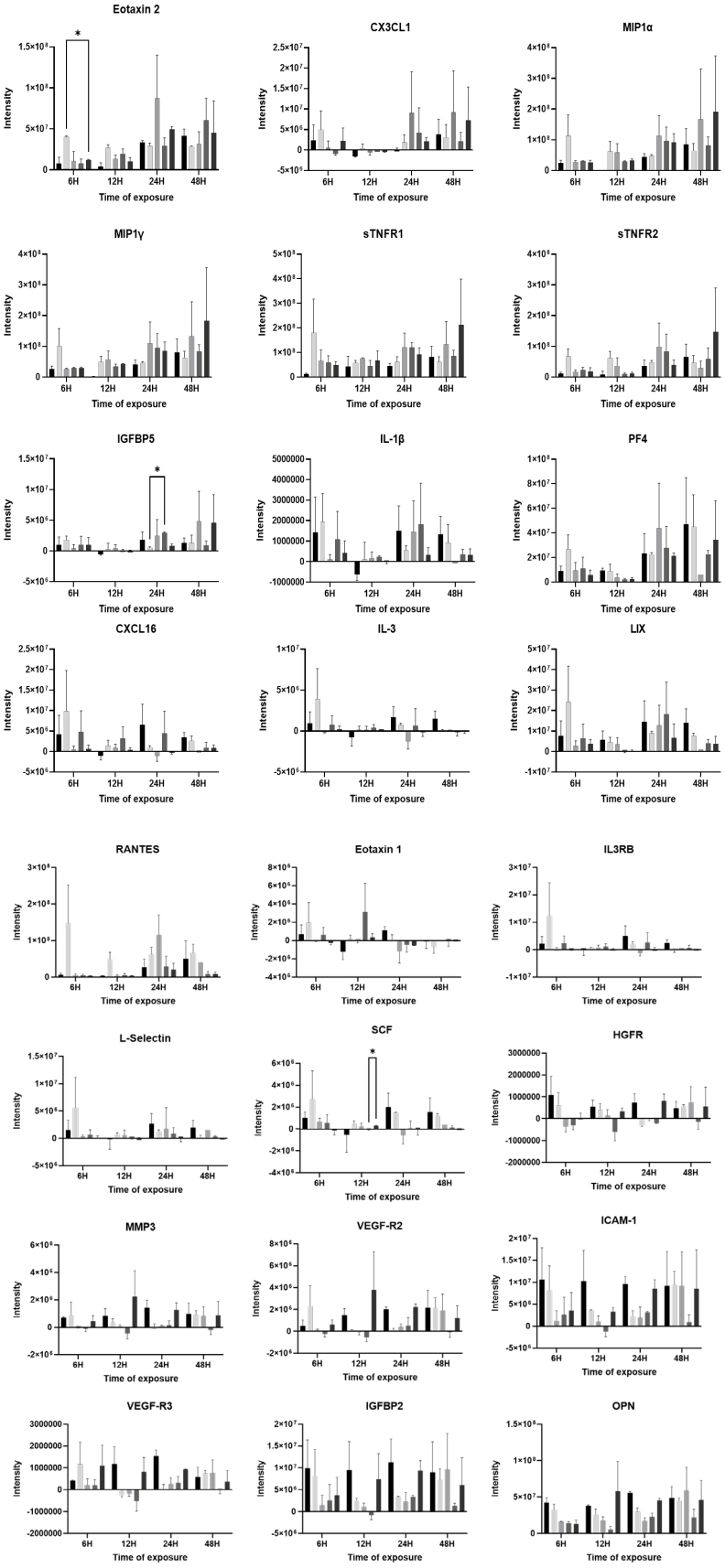
Eotaxin 2
CX3CL1
MIP1α
MIP1γ
sTNFR1
sTNFR2
IGFBP5
IL-1β
PF4
CXCL16
IL-3
LIX
RANTES
Eotaxin 1
IL3RB
L-Selectin
SCF
HGFR
MMP3
VEGF-R2
ICAM-1
VEGF-R3
IGFBP2
OPN
Intensity
Time of exposure
6H
12H
24H
48H
*

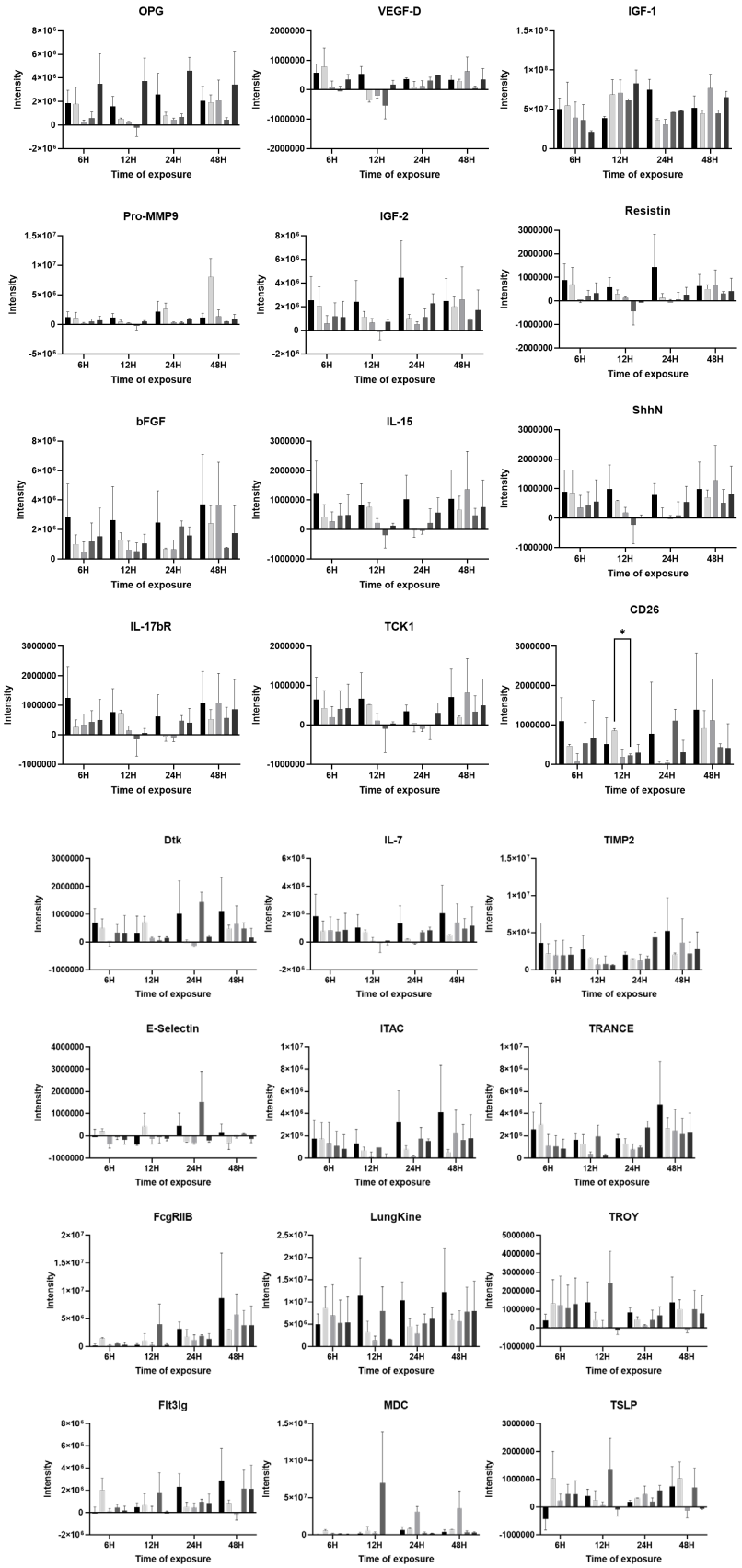
OPG
VEGF-D
IGF-1
Pro-MMP9
IGF-2
Resistin
bFGF
IL-15
ShhN
IL-17bR
TCK1
CD26
Dtk
IL-7
TIMP2
E-Selectin
ITAC
TRANCE
FcgRIIB
LungKine
TROY
Flt3lg
MDC
TSLP
Intensity
Time of exposure
6H
12H
24H
48H
*

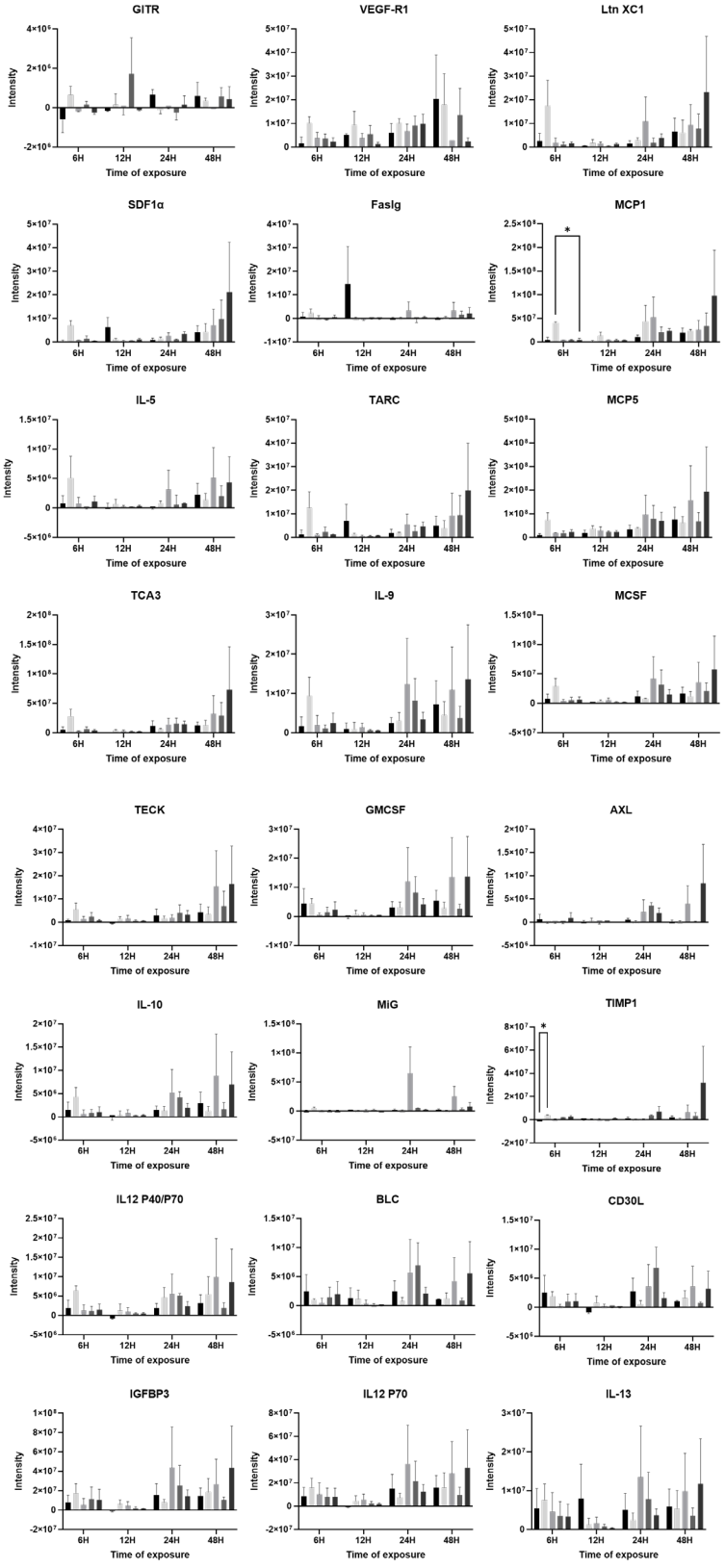
GITR
VEGF-R1
Ltn XC1
SDF1α
FasIg
MCP1
IL-5
TARC
MCP5
TCA3
IL-9
MCSF
TECK
GMCSF
AXL
IL-10
MIG
TIMP1
IL12 P40/P70
BLC
CD30L
IGFBP3
IL12 P70
IL-13
Intensity
Time of exposure
6H
12H
24H
48H
*

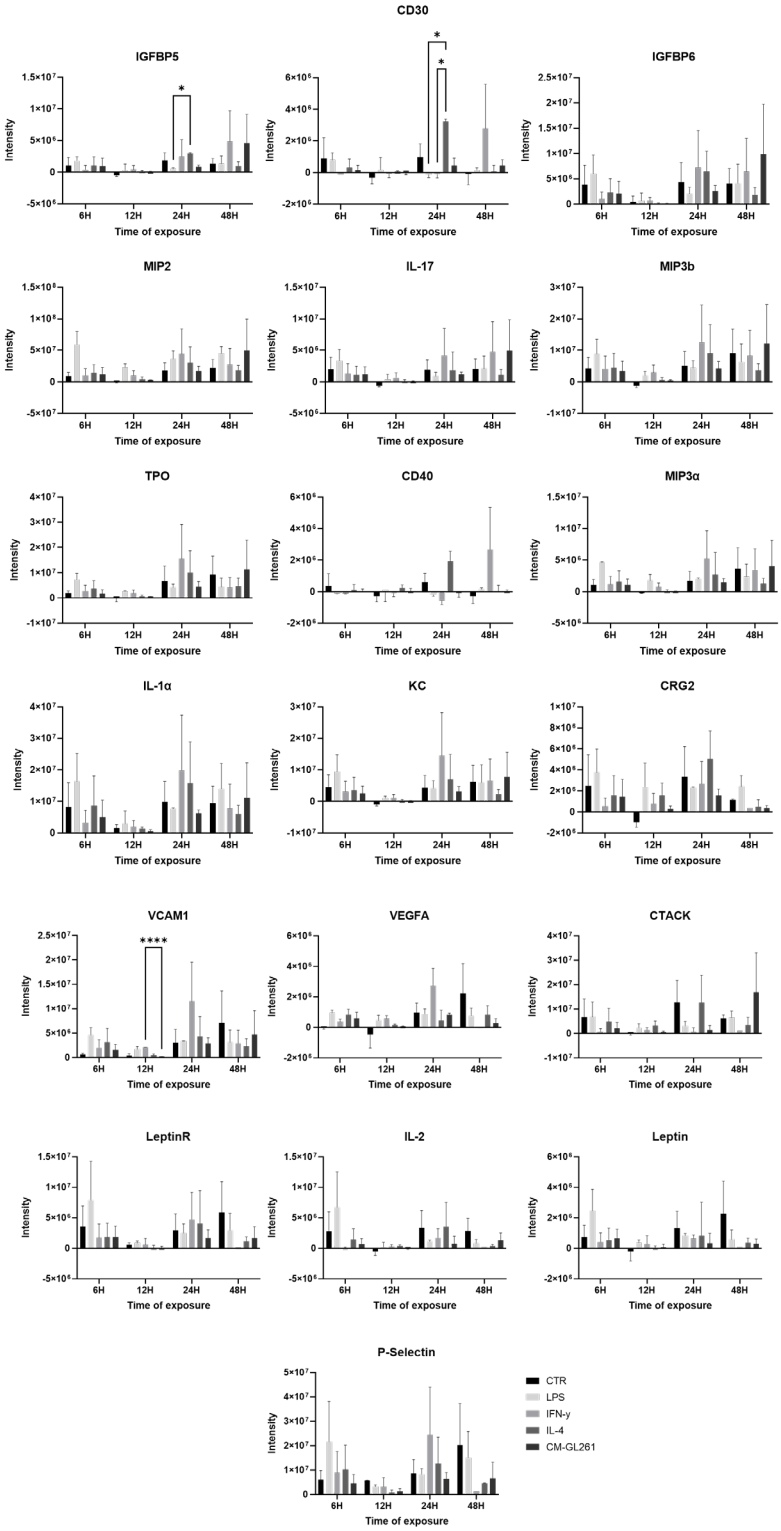

Annexe 22. Additional data from the mouse cytokine arrays in exposed BV2 cells:

Complementary results from the 96 targets Abcam mouse CK arrays on BV2 supernatants. Briefly, BV2 cells were treated or not with 10 ng/mL of LPS, IFN-ɣ, IL-4 or CM-GL261 from 6 to 48 hours. The supernatant was harvested and used for CK array analysis according to manufacturer's instructions. The raw intensity data were normalized to the DMEM Full and to the control untreated BV2 conditionned media. The data were further analysed and visualized with GraphPad Prism software with Dunnett's multiple comparisons in a Mixed analysis frame.

	X	A			B			C			D		
		6H			12H			24H			48H		
	X	Mean	SD	N	Mean	SD	N	Mean	SD	N	Mean	SD	N
1	LPS	103.136	43.036	3	31.400	5.135	3	19.668	6.359	3	5.091	2.672	3
2	IFNγ	28.091	19.988	3	9.247	7.641	3	7.327	5.665	3	2.788	1.988	3
3	IL-4	1.236	0.280	3	1.176	0.127	3	0.744	0.374	3	0.722	0.206	3
4	CM-GL26	1.601	0.305	3	1.905	0.737	3	1.309	0.759	3	1.186	1.033	3

Annexe 23. Row statistics for *Tnf* RT-qPCR data (BV2 cells):

RTqPCR results focusing on *Tnf* mRNA expression in BV2 treated or not with 10 ng/mL of LPS, IFN-ɣ, IL-4 or CM-GL261 from 6 to 48 hours. Results from three independent experiments, each containing three technical replicates. Row statistics generated on GraphPad Prism software from the pre-processed data of *Tnf* mRNA expression. The raw data were generated by QuantStudio software from fluorescence intensity measurements. The pre-processing was done by normalization to the *Rpl27* housekeeping gene expression, together with the untreated BV2 *Tnf* expression values. Top axis : time in hours. SD : Standard Deviation; N : Biological replicates.

	X	A			B			C			D		
		6H			12H			24H			48H		
	X	Mean	SD	N	Mean	SD	N	Mean	SD	N	Mean	SD	N
1	LPS	330.583	183.212	3	382.731	230.607	3	126.078	59.618	3	36.881	14.136	3
2	IFNγ	5.110	3.273	3	1.249	0.915	3	0.955	0.118	3	2.504	1.475	3
3	IL-4	1.108	0.376	3	1.514	0.534	3	1.074	0.453	3	1.274	0.788	3
4	CM-GL26	0.844	0.230	3	1.867	1.177	3	1.281	0.446	3	1.285	0.981	3

Annexe 24. Row statistics for *Il1β* RT-qPCR data (BV2 cells):

RTqPCR results focusing on *Il1ϐ* mRNA expression in BV2 treated or not with 10 ng/mL of LPS, IFN-ɣ, IL-4 or CM-GL261 from 6 to 48 hours. Results from three independent experiments, each containing three technical replicates. Row statistics generated on GraphPad Prism software from the pre-processed data of *Il1ϐ* mRNA expression. The raw data were generated by QuantStudio software from fluorescence intensity measurements. The pre-processing was done by normalization to the *Rpl27* housekeeping gene expression, together with the untreated BV2 *Il1ϐ* expression values. Top axis : time in hours. SD : Standard Deviation; N : Biological replicates.

	X	A			B			C			D		
		6H			12H			24H			48H		
	X	Mean	SD	N	Mean	SD	N	Mean	SD	N	Mean	SD	N
1	LPS	3744.430	1186.911	3	365.427	225.312	3	204.667	79.725	3	32.540	23.356	3
2	IFNγ	2170.170	1759.474	3	1377.183	1390.356	3	478.867	461.716	3	254.613	342.448	3
3	IL-4	0.673	0.291	3	1.447	0.653	3	1.130	0.495	3	2.003	0.777	3
4	CM-GL26	1.827	0.806	3	3.810	2.217	3	2.110	0.494	3	4.630	6.513	3

Annexe 25. Row statistics for *Cxcl10* RT-qPCR data (BV2 cells):

RTqPCR results focusing on *Cxcl10* mRNA expression in BV2 treated or not with 10 ng/mL of LPS, IFN-ɣ, IL-4 or CM-GL261 from 6 to 48 hours. Results from three independent experiments, each containing three technical replicates. Row statistics generated on GraphPad Prism software from the pre-processed data of *Cxcl10* mRNA expression. The raw data were generated by QuantStudio software from fluorescence intensity measurements. The pre-processing was done by normalization to the *Rpl27* housekeeping gene expression, together with the untreated BV2 *Cxcl10* expression values. Top axis : time in hours. SD : Standard Deviation; N : Biological replicates.

	X	A			B			C			D		
		6H			12H			24H			48H		
	X	Mean	SD	N	Mean	SD	N	Mean	SD	N	Mean	SD	N
1	LPS	0.509	0.241	3	0.041	0.026	3	0.016	0.011	3	0.048	0.033	3
2	IFNγ	0.920	0.342	3	0.620	0.313	3	0.383	0.237	3	0.393	0.260	3
3	IL-4	2.472	1.744	3	2.171	1.919	3	1.979	0.773	3	2.058	0.319	3
4	CM-GL26	1.298	0.656	3	1.331	0.356	3	1.249	0.343	3	1.584	0.868	3

Annexe 26. Row statistics for *Arg1* RT-qPCR data (BV2 cells):

RTqPCR results focusing on *Arg1* mRNA expression in BV2 treated or not with 10 ng/mL of LPS, IFN-ɣ, IL-4 or CM-GL261 from 6 to 48 hours. Results from three independent experiments, each containing three technical replicates. Row statistics generated on GraphPad Prism software from the pre-processed data of *Arg1* mRNA expression. The raw data were generated by QuantStudio software from fluorescence intensity measurements. The pre-processing was done by normalization to the *Rpl27* housekeeping gene expression, together with the untreated BV2 *Arg1* expression values. Top axis : time in hours. SD : Standard Deviation; N : Biological replicates.

	X	A			B			C			D		
		6H			12H			24H			48H		
	X	Mean	SD	N	Mean	SD	N	Mean	SD	N	Mean	SD	N
1	LPS	1.412	0.684	3	1.321	1.071	3	0.634	0.303	3	0.354	0.212	3
2	IFNγ	1.309	0.313	3	1.686	1.475	3	0.891	0.523	3	0.536	0.071	3
3	IL-4	0.992	0.516	3	4.832	3.960	3	3.078	1.808	3	5.757	2.152	3
4	CM-GL26	1.368	0.577	3	2.150	2.109	3	0.823	0.447	3	0.553	0.386	3

Annexe 27. Row statistics for *Ym1* RT-qPCR data (BV2 cells):

RTqPCR results focusing on *Ym1* mRNA expression in BV2 treated or not with 10 ng/mL of LPS, IFN-ɣ, IL-4 or CM-GL261 from 6 to 48 hours. Results from three independent experiments, each containing three technical replicates. Row statistics generated on GraphPad Prism software from the pre-processed data of *Ym1* mRNA expression. The raw data were generated by QuantStudio software from fluorescence intensity measurements. The pre-processing was done by normalization to the *Rpl27* housekeeping gene expression, together with the untreated BV2 *Ym1* expression values. Top axis : time in hours. SD : Standard Deviation; N : Biological replicates.

	X	A			B			C			D		
		6H			12H			24H			48H		
	X	Mean	SD	N	Mean	SD	N	Mean	SD	N	Mean	SD	N
1	LPS	0.659	0.265	3	0.753	0.363	3	1.744	1.392	3	0.524	0.331	3
2	IFNγ	0.941	0.204	3	0.641	0.252	3	0.966	0.264	3	2.412	3.626	3
3	IL-4	2.987	2.533	3	2.668	3.047	3	1.212	0.851	3	1.982	2.000	3
4	CM-GL26	1.203	1.054	3	3.198	1.504	3	0.812	0.124	3	0.941	0.720	2

Annexe 28. Row statistics for *Fizz1* RT-qPCR data (BV2 cells):

RTqPCR results focusing on *Fizz1* mRNA expression in BV2 treated or not with 10 ng/mL of LPS, IFN-ɣ, IL-4 or CM-GL261 from 6 to 48 hours. Results from three independent experiments, each containing three technical replicates. Row statistics generated on GraphPad Prism software from the pre-processed data of *Fizz1* mRNA expression. The raw data were generated by QuantStudio software from fluorescence intensity measurements. The pre-processing was done by normalization to the *Rpl27* housekeeping gene expression, together with the untreated BV2 *Fizz1* expression values. Top axis : time in hours. SD : Standard Deviation; N : Biological replicates.

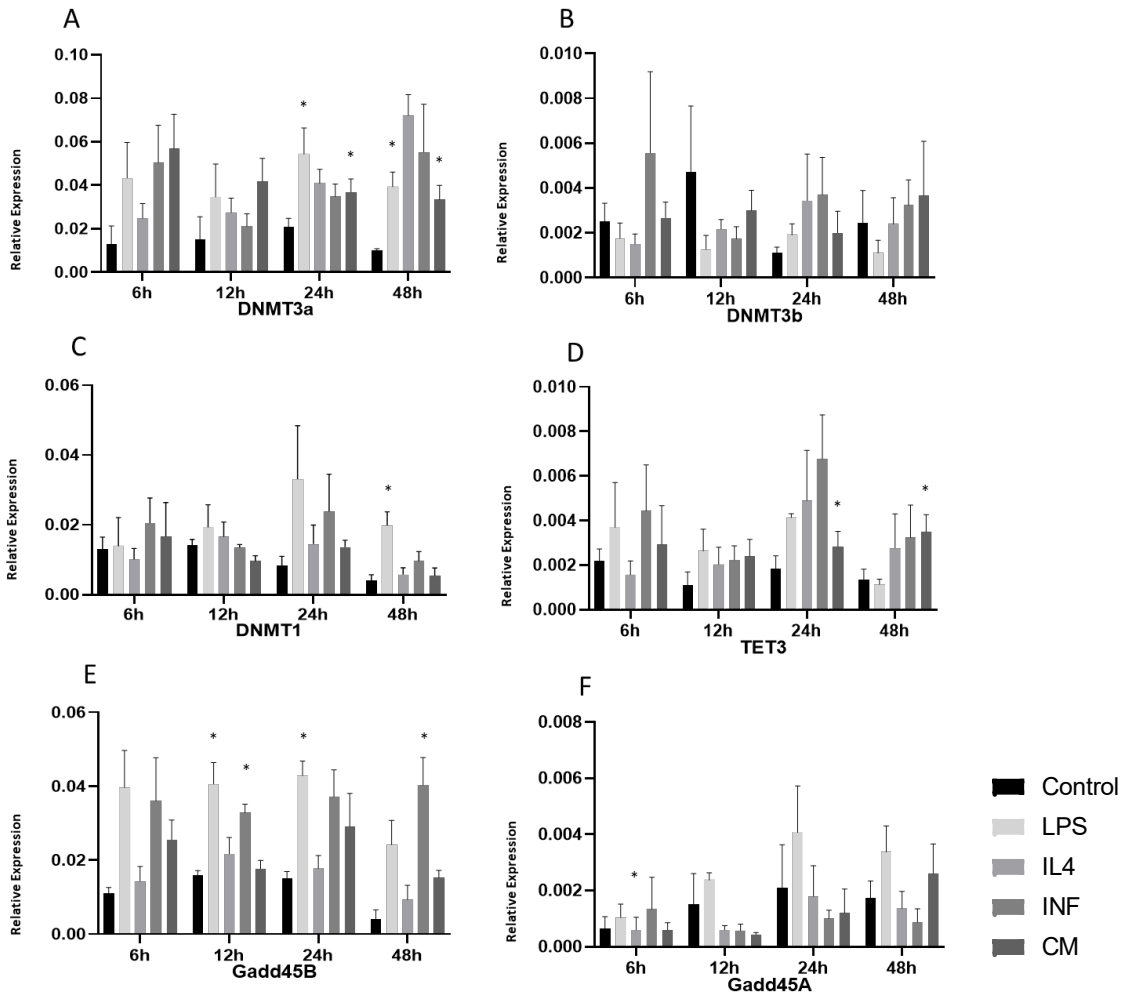

Annexe 29. RTqPCR results targetting DNA methylation actors in treated BV2 cells:

In order to explore the molecular actors responsible for potential changes in DNA methylation patterns reorganization in BV2 cells, the mRNA expression of methylation (*Dnmt1*, *Dnmt3a* and *Dnmt3b*) and demethylation (*Tet3*, *Gadd45a* and *Gadd45b*)involved molecules were realized on the RNA from BV2 treated or not with 10 ng/mL of LPS, IFN-ɣ, IL-4 or CM-GL261 for 6 to 48 hours. The data were normalized to the housekeeping gene *Rpl27* expression and the control untreated BV2 values. The data were further analyzed with GraphPad Prism software by applying a 2-way ANOVA with Dunnett's multiple comparisons. Results from three biological replicates with three technical replicates each.

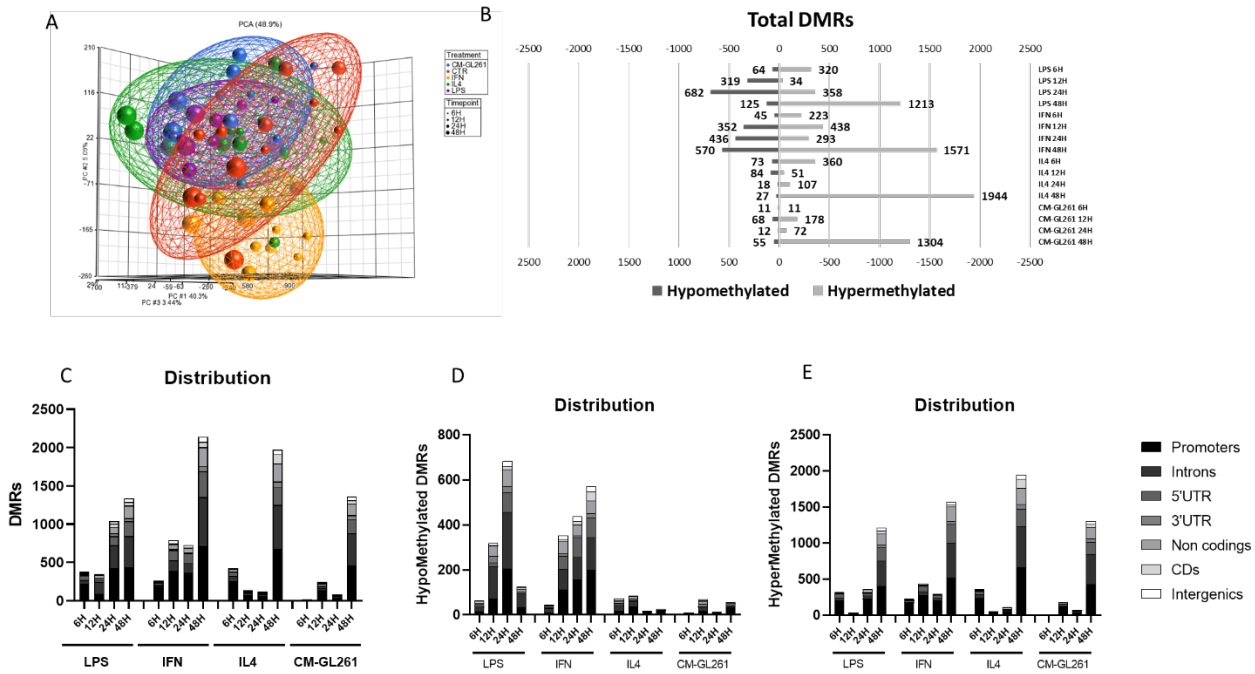

Annexe 30. DNA methylation analysis of treated BV2 cells by using Partek Genomic Suite software :

Before the DNA methylation analysis was done by Dr. Reka Toth, a trial of DNA methylation analysis was made using the free Partek Genomic Suite software trial. The raw data obtained from BV2 methylation assay according to the Materials and Methods section were uploaded into the software and were normalized *via* functional normalization with Noob background correction. (A) PCA plot of all the BV2 samples according to overall methylation profile. (B) Significant hyper- and hypomethylated Differentially Methylated Regions in all the conditions (*versus* control untreated BV2), FDR adjusted 0.05 Pvalue; FC = 1. Distribution according to genomic location of the significant DMRs (C), the hypomethylated ones (D) or the hypermethylated ones (E).

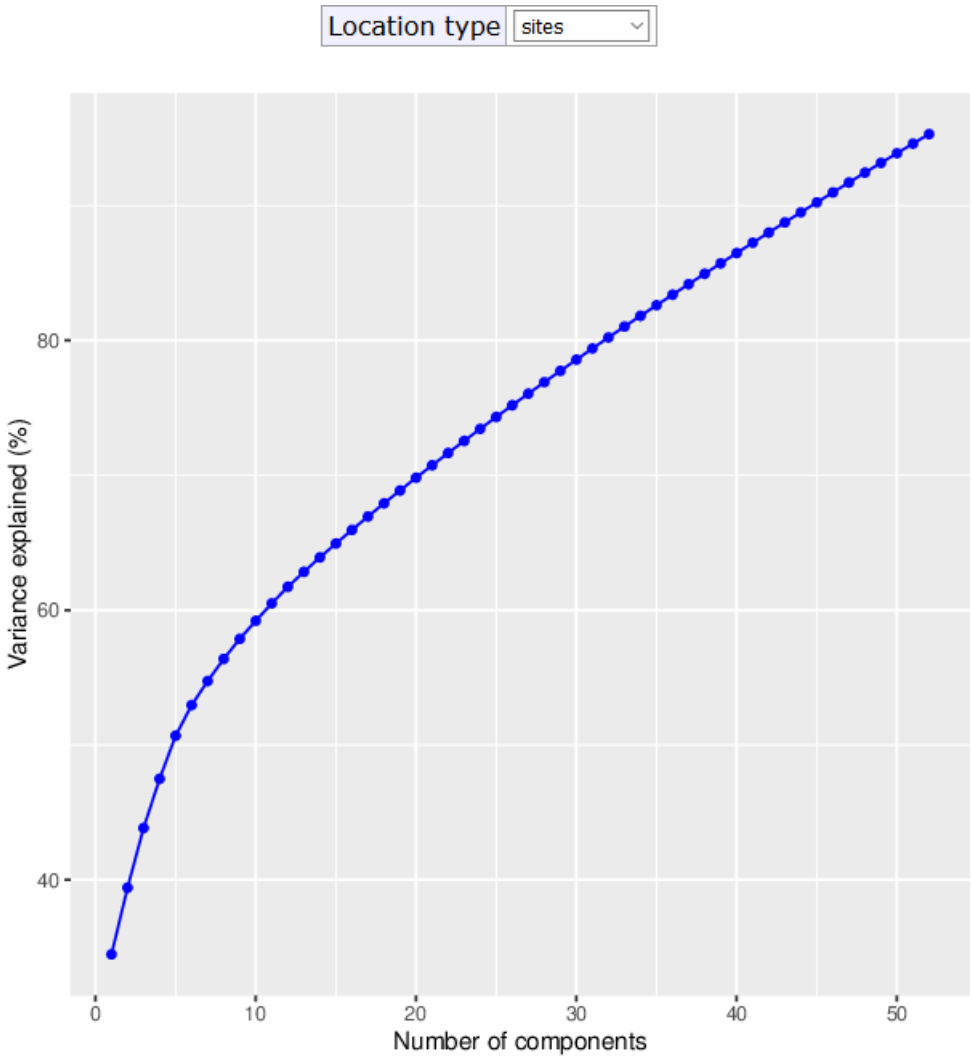

Annexe 31. Cumulative distribution of variances explained by the principal components, BV2, all treatments and timepoints:

The Figure above, from the PCA analysis done on the raw data from the BV2 methylation assay and focusing on the CpG sites, shows the cumulative distribution of functions of variance explained by the principal components.

Annexe 32. Heatmap summarizing the association of variables between each principal component:

Heatmap from the PCA analysis done on the raw data from the BV2 methylation assay and focusing on the CpG sites, summarizing the results of association of variables between principal components. Significant Pvalues (less than 0.01) are displayed in a pink color.

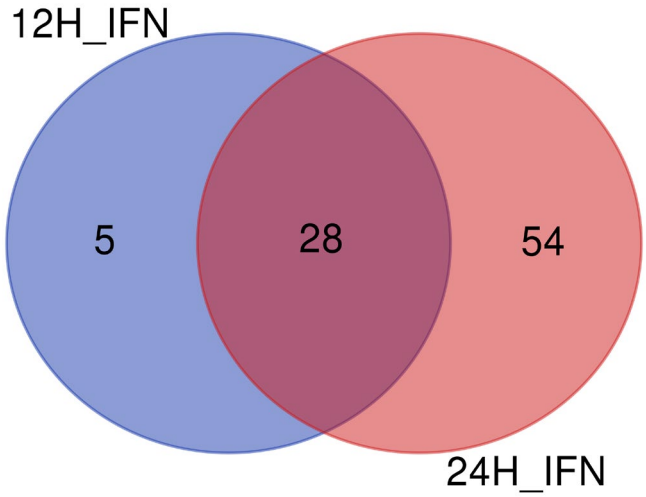

Annexe 33. Common significant DMSs between IFN treated BV2 for 12 and 24 hours:

Common DMSs found in both timepoints of the IFN-ɣ treatment condition (versus control untreated BV2 microglial cells). BV2 treated or not with 10 ng/mL of IFN-ɣ for 12 and 24 hours were used to performed an Illumina Methylation assay according to manufacturer's instructions. Raw data were analyzed by Dr. Reka Toth using Rsoftware according to the Materials and Methods section. The identified significant DMSs were uploaded into an online Venn Diagram generator (http://bioinformatics.psb.ugent.be/webtools/Venn/, link accessed on the 29.05.2024).

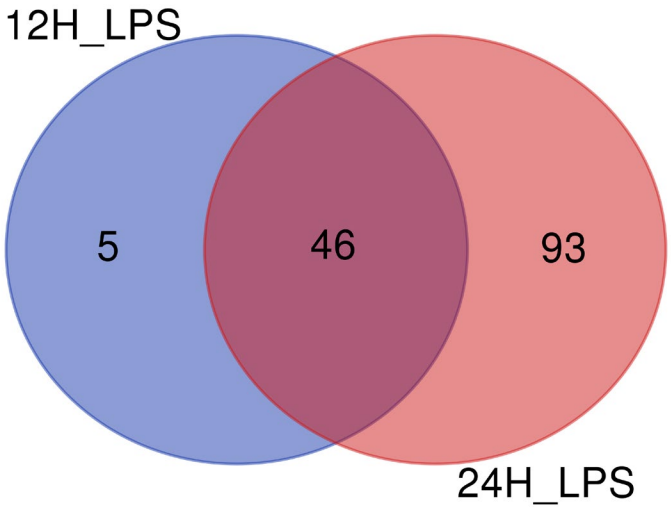

Annexe 34. Common significant DMSs between LPS treated BV2 for 12 and 24 hours:

Common DMSs found in both timepoints of the LPS treatment condition (versus control untreated BV2 microglial cells). BV2 treated or not with 10 ng/mL of LPS for 12 and 24 hours were used to performed an Illumina Methylation assay according to manufacturer's instructions. Raw data were analyzed by Dr. Reka Toth using Rsoftware according to the Materials and Methods section. The identified significant DMSs were uploaded into an online Venn Diagram generator (http://bioinformatics.psb.ugent.be/webtools/Venn/, link accessed on the 29.05.2024).

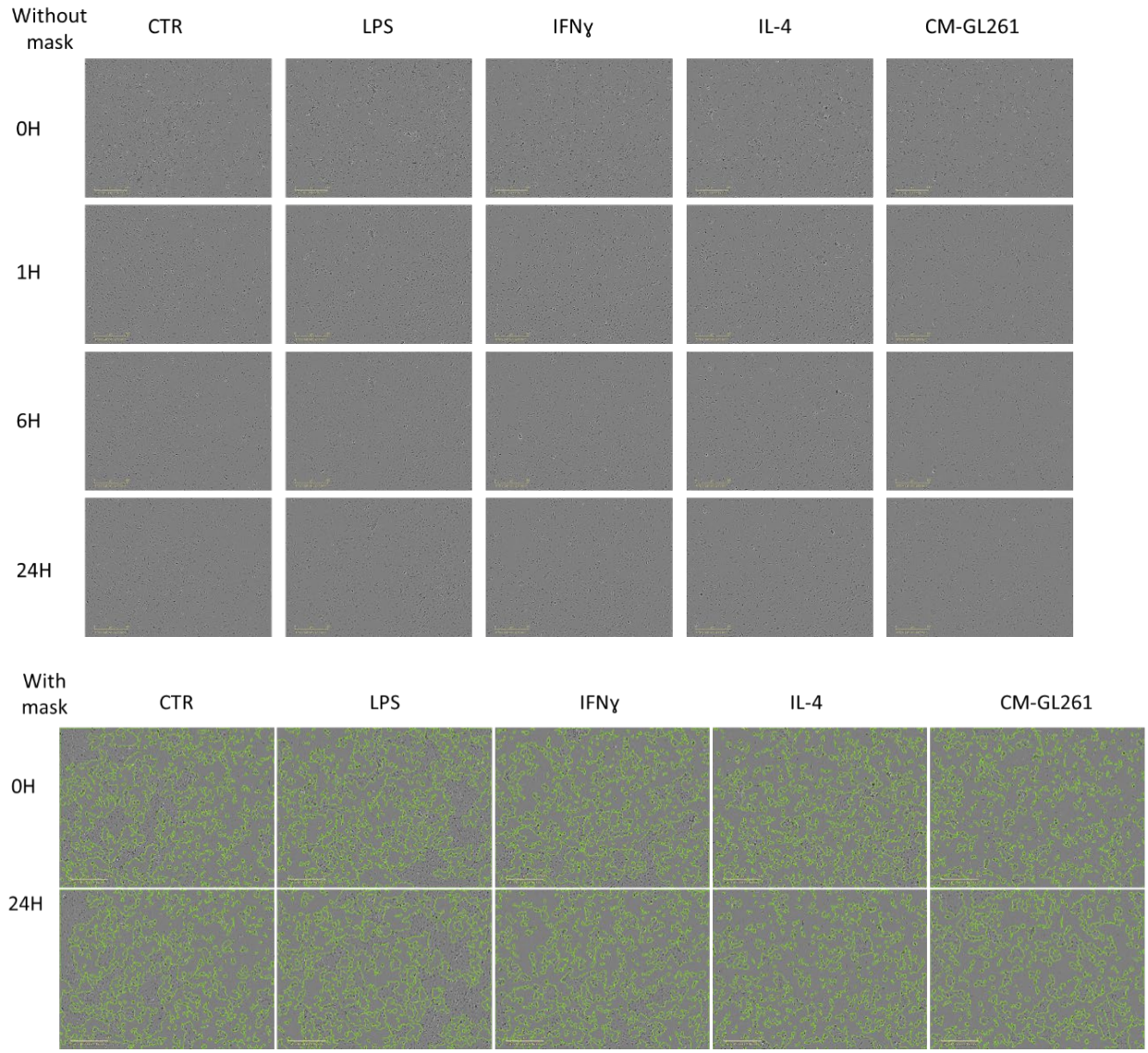

Annexe 35. Selection of Incucyte pictures of primary microglial cells:

Selection of Incucyte brightfield pictures of primary microglial cells treated or not with 10 ng/mL of LPS, IFN-ɣ, IL-4 or CM-GL261 for 24 hours. The top panel shows the phase contrast brighfield picture while the bottom panel shows the pictures merged with the phase contrast aera analysis mask (in yellow).

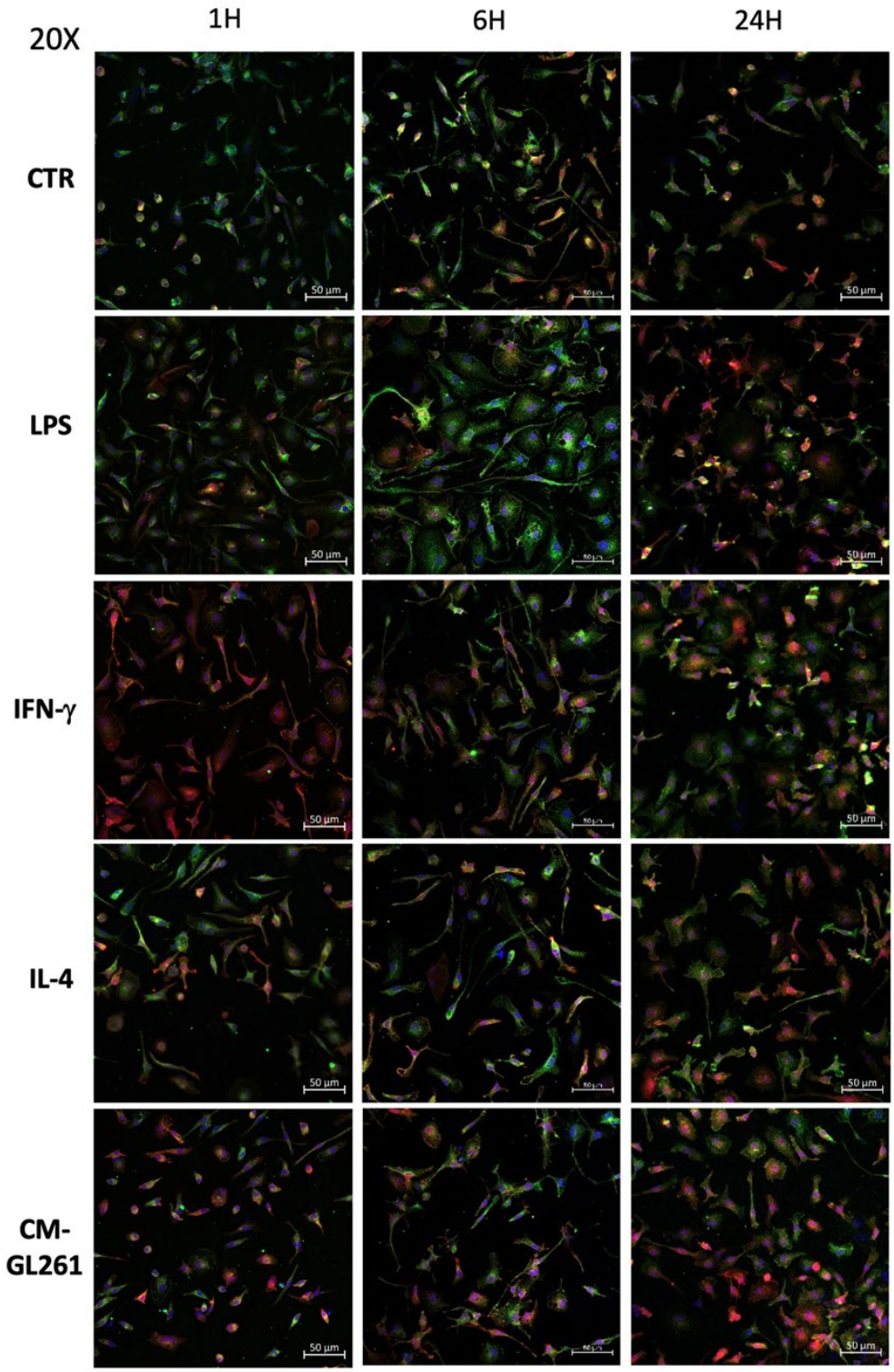

Annexe 36. IF staining of primary microglia at the 20X objective:

Confocal images of primary microglial cells, treated or not with 10 ng/mL of LPS, IFN-ɣ, IL-4 or CM-GL261 for one to 24 hours and stained for Iba1 (red), F4/80 (green) and counterstained with DAPI (blue). The detailed procedure can be found in the Materials and Methods section.

Symbol	Ensembl Gene ID	Type	Chr	Description
4930448I18Rik	ENSMUSG00000104870	lncRNA	5	RIKEN cDNA 4930448I18 gene [Source:MGI Symbol;Acc:MGI:1921215]
1700084F23Rik	ENSMUSG00000099639	lncRNA	13	RIKEN cDNA 1700084F23 gene [Source:MGI Symbol;Acc:MGI:1921530]
Gm3772	ENSMUSG00000113074	lncRNA	13	predicted gene 3772 [Source:MGI Symbol;Acc:MGI:3781946]
Gm30695	ENSMUSG00000116595	lncRNA	16	predicted gene, 30695 [Source:MGI Symbol;Acc:MGI:5589854]
Ifi202b	ENSMUSG00000026535	protein_coding	1	interferon activated gene 202B [Source:MGI Symbol;Acc:MGI:1347083]
Olfr1280	ENSMUSG00000109449	protein_coding	2	olfactory receptor 1280 [Source:MGI Symbol;Acc:MGI:3031114]
Adal	ENSMUSG00000027259	protein_coding	2	adenosine deaminase-like [Source:MGI Symbol;Acc:MGI:1923144]
Slc28a2	ENSMUSG00000027219	protein_coding	2	solute carrier family 28 (sodium-coupled nucleoside transporter), member 2 [Source:MGI Symbol;Acc:MGI:1913105]
H13	ENSMUSG00000019188	protein_coding	2	histocompatibility 13 [Source:MGI Symbol;Acc:MGI:95886]
Ccl21a	ENSMUSG00000094686	protein_coding	4	chemokine (C-C motif) ligand 21A (serine) [Source:MGI Symbol;Acc:MGI:1349183]
Fam205a1	ENSMUSG00000078721	protein_coding	4	family with sequence similarity 205, member A1 [Source:MGI Symbol;Acc:MGI:3651059]
Ttc28	ENSMUSG00000033209	protein_coding	5	tetratricopeptide repeat domain 28 [Source:MGI Symbol;Acc:MGI:2140873]
Foxp1	ENSMUSG00000030067	protein_coding	6	forkhead box P1 [Source:MGI Symbol;Acc:MGI:1914004]
Atf7ip	ENSMUSG00000030213	protein_coding	6	activating transcription factor 7 interacting protein [Source:MGI Symbol;Acc:MGI:1858965]
Gucy2c	ENSMUSG00000042638	protein_coding	6	guanylate cyclase 2c [Source:MGI Symbol;Acc:MGI:106903]
Nipa2	ENSMUSG00000030452	protein_coding	7	non imprinted in Prader-Willi/Angelman syndrome 2 homolog (human) [Source:MGI Symbol;Acc:MGI:1913918]
Myo7a	ENSMUSG00000030761	protein_coding	7	myosin VIIA [Source:MGI Symbol;Acc:MGI:104510]
Trim5	ENSMUSG00000060441	protein_coding	7	tripartite motif-containing 5 [Source:MGI Symbol;Acc:MGI:3646853]
Defb8	ENSMUSG00000031471	protein_coding	8	defensin beta 8 [Source:MGI Symbol;Acc:MGI:2654206]
Nek3	ENSMUSG00000031478	protein_coding	8	NIMA (never in mitosis gene a)-related expressed kinase 3 [Source:MGI Symbol;Acc:MGI:1344371]
Sfrp1	ENSMUSG00000031548	protein_coding	8	secreted frizzled-related protein 1 [Source:MGI Symbol;Acc:MGI:892014]
Tacc1	ENSMUSG00000065954	protein_coding	8	transforming, acidic coiled-coil containing protein 1 [Source:MGI Symbol;Acc:MGI:2443510]
Psd3	ENSMUSG00000030465	protein_coding	8	pleckstrin and Sec7 domain containing 3 [Source:MGI Symbol;Acc:MGI:1918215]
Zfhx3	ENSMUSG00000038872	protein_coding	8	zinc finger homeobox 3 [Source:MGI Symbol;Acc:MGI:99948]
Bsx	ENSMUSG00000054360	protein_coding	9	brain specific homeobox [Source:MGI Symbol;Acc:MGI:2669849]
Nek11	ENSMUSG00000035032	protein_coding	9	NIMA (never in mitosis gene a)-related expressed kinase 11 [Source:MGI Symbol;Acc:MGI:2442276]
Myct1	ENSMUSG00000046916	protein_coding	10	myc target 1 [Source:MGI Symbol;Acc:MGI:1915882]
Tns3	ENSMUSG00000020422	protein_coding	11	tensin 3 [Source:MGI Symbol;Acc:MGI:2443012]
Meis1	ENSMUSG00000020160	protein_coding	11	Meis homeobox 1 [Source:MGI Symbol;Acc:MGI:104717]
Kcnh6	ENSMUSG00000001901	protein_coding	11	potassium voltage-gated channel, subfamily H (eag-related), member 6 [Source:MGI Symbol;Acc:MGI:2684139]
Tex2	ENSMUSG00000040548	protein_coding	11	testis expressed gene 2 [Source:MGI Symbol;Acc:MGI:102465]
Adarb2	ENSMUSG00000052551	protein_coding	13	adenosine deaminase, RNA-specific, B2 [Source:MGI Symbol;Acc:MGI:2151118]
Prl3d2	ENSMUSG00000062737	protein_coding	13	prolactin family 3, subfamily d, member 1 [Source:MGI Symbol;Acc:MGI:2660935]
Uimc1	ENSMUSG00000025878	protein_coding	13	ubiquitin interaction motif containing 1 [Source:MGI Symbol;Acc:MGI:103185]
Ercc6l2	ENSMUSG00000021470	protein_coding	13	excision repair cross-complementing rodent repair deficiency, complementation group 6 like 2 [Source:MGI Symbol;Acc:MGI:1923501]
Slf1	ENSMUSG00000021597	protein_coding	13	SMC5-SMC6 complex localization factor 1 [Source:MGI Symbol;Acc:MGI:2145448]
Zfp943	ENSMUSG00000053347	protein_coding	17	zinc finger prtoein 943 [Source:MGI Symbol;Acc:MGI:1921920]
Aldh7a1	ENSMUSG00000053644	protein_coding	18	aldehyde dehydrogenase family 7, member A1 [Source:MGI Symbol;Acc:MGI:108186]
Zfp950	ENSMUSG00000074733	protein_coding	19	zinc finger protein 950 [Source:MGI Symbol;Acc:MGI:2652824]
D3YZ35	Not mapped	NA	NA	NA
GM37013	Not mapped	NA	NA	NA
GM42185	Not mapped	NA	NA	NA
K7N6B2	Not mapped	NA	NA	NA

Annexe 37. **Differentially Methylated Genes common in all treatment conditions and timepoints in exposed primary microglia compared to control :**

Summary of the DMGs found in all conditions of treatments and timepoints (versus control untreated primary microglial cells). Primary microglial cells treated or not with LPS, IFN-ɣ, IL-4 or CM-GL261 for one or six hours were used to performed an Illumina Methylation assay according to manufacturer's instructions. Raw data were analyzed using GenomeStudio according to the Materials and Methods section. The identified significant DMGs were uploaded into an online Venn Diagram generator (http://bioinformatics.psb.ugent.be/webtools/Venn/, link accessed on the 29.05.2024). The table presented summarized all the DMGs common in all the treatments conditions both timepoints.

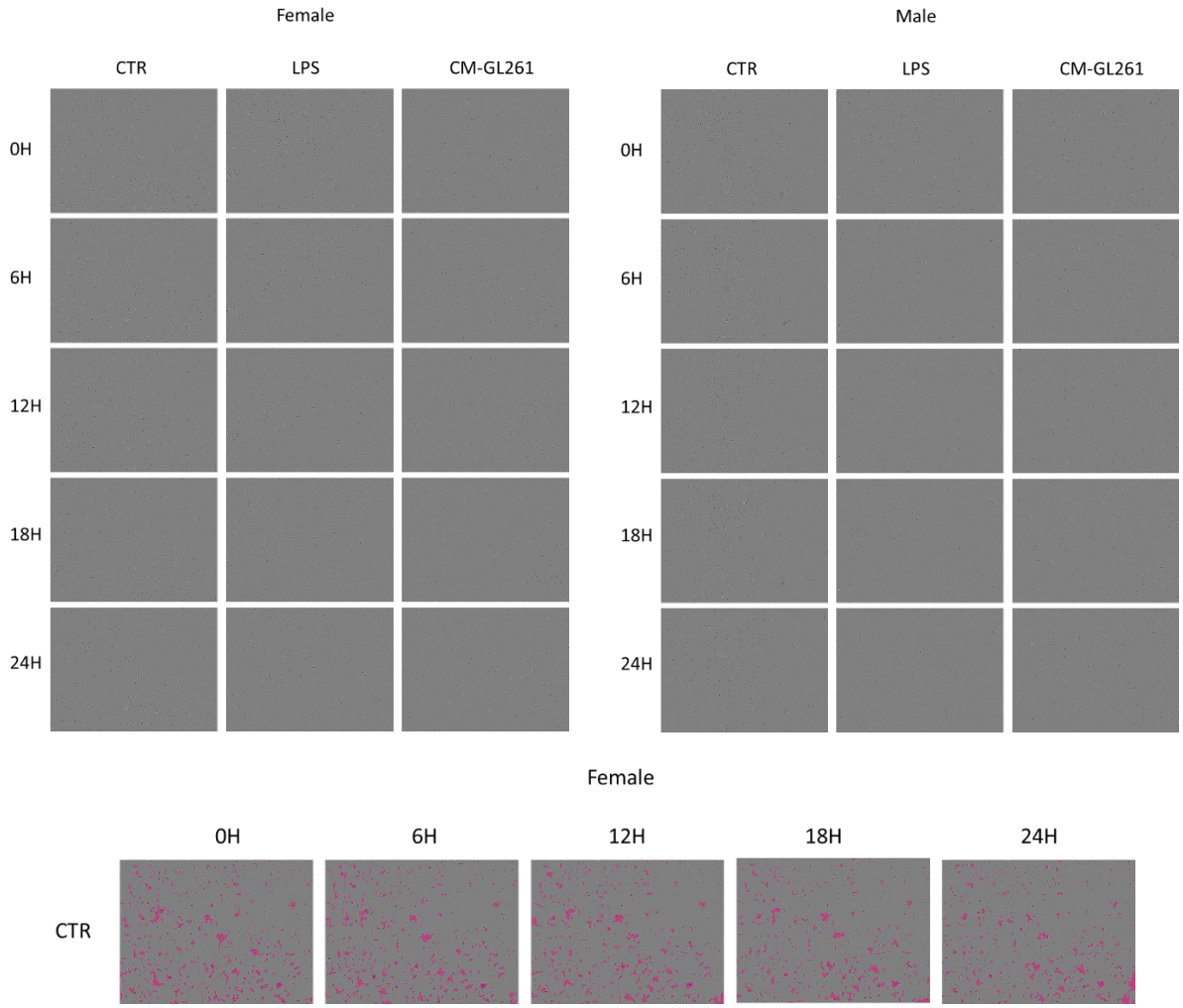

Annexe 38. Incucyte pictures for male and female primary microglial cells culture :

Selection of Incucyte brightfield pictures of male and female primary microglial cells treated or not with 10 ng/mL of LPS or CM-GL261 for 24 hours. The top panel shows the phase contrast brighfield pictures while the bottom panel shows the pictures merged with the phase contrast aera analysis mask (in pink).

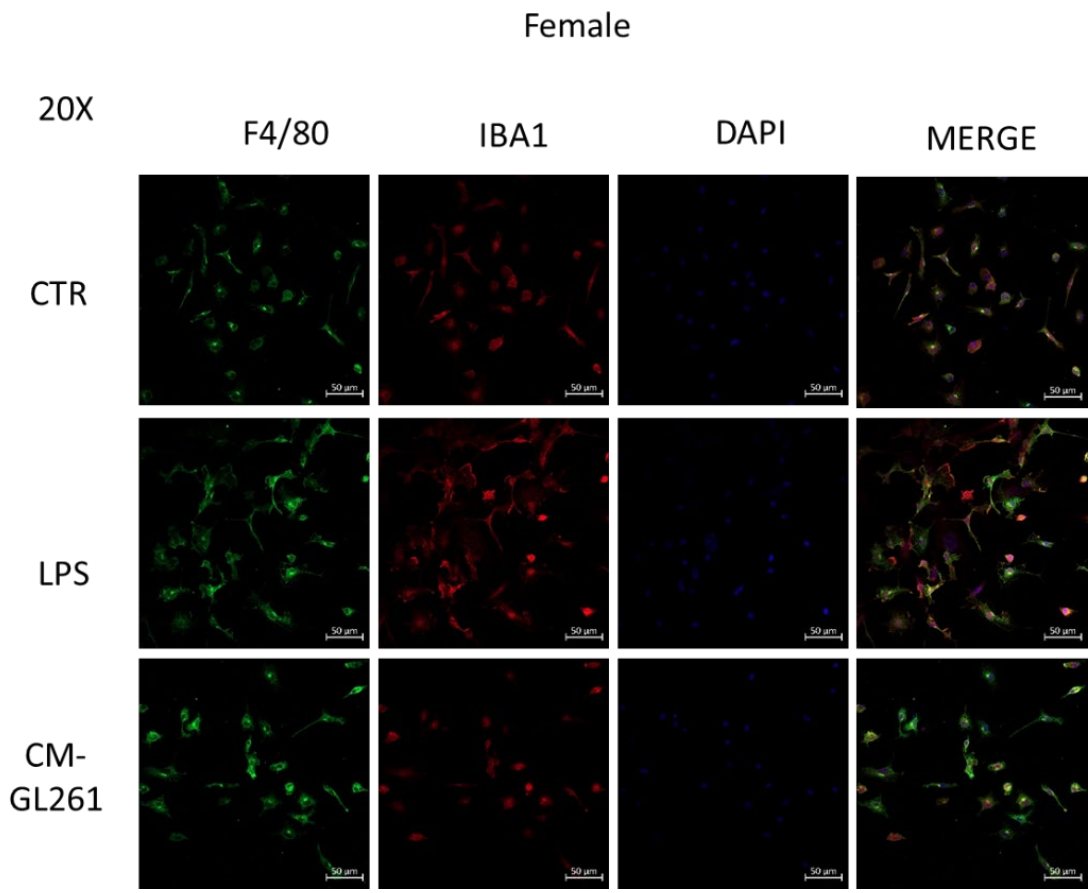

Annexe 39. IF pictures at the 20X objective of the primary female microglia treated or not with LPS or CM-GL261 :

Confocal images of female primary microglial cells, treated or not with 10 ng/mL of LPS or CM-GL261 for 24 hours and stained for Iba1 (red), F4/80 (green) and counterstained with DAPI (blue) at the 20X objectives. The detailed procedure can be found in the Materials and Methods section.

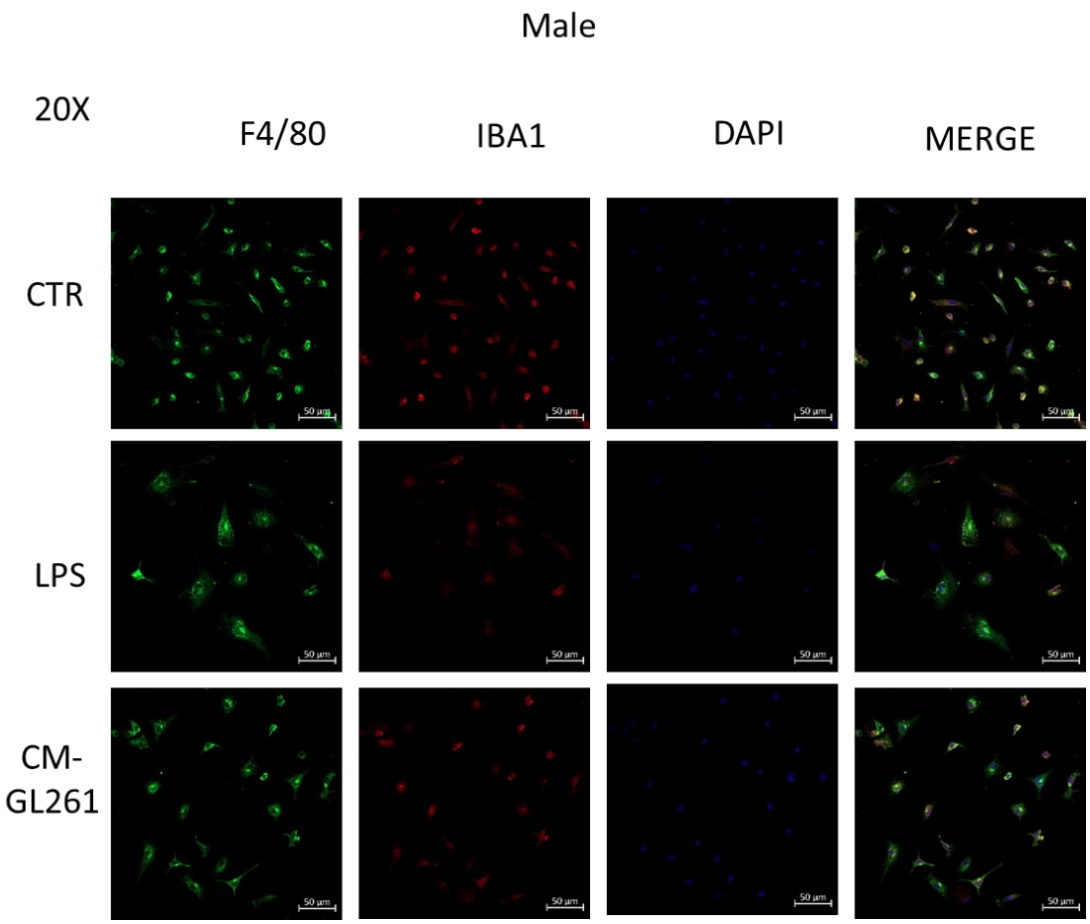

Annexe 40. IF pictures at the 20X objective of the male primary microglia treated or not with LPS or CM-GL261 :

Confocal images of male primary microglial cells, treated or not with 10 ng/mL of LPS or CM-GL261 for 24 hours and stained for Iba1 (red), F4/80 (green) and counterstained with DAPI (blue) at the 20X objectives. The detailed procedure can be found in the Materials and Methods section.

Bibliography

1. Virchow, R. *Gesammelte Abhandlungen Zur Wissenschaftlichen Medicin.* (1856).
2. W Mills, M. V. L. *Der Feinere Bau Des Nervensystems Im Lichte Neuester Forschungen*. (1895).
3. y Cajal, R. Contribución al conocimiento de la neuroglia del cerebro humano. **Trab. Lab. Invest. Biol., 11, 255.**, (1913).
4. Río-Hortega P. El "tercer elemento" de los centros nerviosos. I. La microglía en estado normal. **Bol Soc Esp Biol VIII: 67–82.**, (1919).
5. Río-Hortega P. El "tercer elemento de los centros nerviosos". II. Intervención de la microglía en los procesos patológicos (células en bastoncito y cuerpos gránuloadiposos). **Bol Soc Esp Biol VIII: 91–103.**, (1919).
6. Río-Hortega P. El "tercer elemento" de los centros nerviosos. III. Naturaleza probable de la microglía. **Bol Soc Esp Biol VIII: 108–115.**, (1919).
7. del Río-Hortega P. Estudios sobre la neuroglía.- La glía de escasas radiaciones (oligodendroglía). **Bol. R. Soc. Esp. Hist. Nat. 21: 63-92; also published in: Arch. Neurobiologia. 1921; 2: 16-43**, (1921).
8. Lawson, L. J., Perry, V. H. & Gordon, S. Turnover of resident microglia in the normal adult mouse brain. *Neuroscience* **48**, 405–415 (1992).
9. Blinzinger, K. & Kreutzberg, G. Displacement of synaptic terminals from regenerating motoneurons by microglial cells. *Z. F[?]r Zellforsch. Mikrosk. Anat.* **85**, 145–157 (1968).
10. Ibrahim, M. Z. M., Khreis, Y. & Koshayan, D. S. The histochemical identification of microglia. *J. Neurol. Sci.* **22**, 211–233 (1974).
11. Giulian, D. & Baker, T. Characterization of ameboid microglia isolated from developing mammalian brain. *J. Neurosci.* **6**, 2163–2178 (1986).
12. Blasi, E., Barluzzi, R., Bocchini, V., Mazzolla, R. & Bistoni, F. Immortalization of murine microglial cells by a v-raf / v-myc carrying retrovirus. *J. Neuroimmunol.* **27**, 229–237 (1990).

13. Ito, D. *et al.* Microglia-specific localisation of a novel calcium binding protein, Iba1. *Mol. Brain Res.* **57**, 1–9 (1998).

14. Sierra, A. *et al.* The “Big-Bang” for modern glial biology: Translation and comments on Pío del Río-Hortega 1919 series of papers on microglia: 1919 Río-Hortega Papers on Microglia. *Glia* **64**, 1801–1840 (2016).

15. Sierra, A., Paolicelli, R. C. & Kettenmann, H. Cien Años de Microglía: Milestones in a Century of Microglial Research. *Trends Neurosci.* **42**, 778–792 (2019).

16. Augusto-Oliveira, M. *et al.* Plasticity of microglia. *Biol. Rev.* **97**, 217–250 (2022).

17. Stratoulias, V., Venero, J. L., Tremblay, M. & Joseph, B. Microglial subtypes: diversity within the microglial community. *EMBO J.* **38**, e101997 (2019).

18. Prinz, M., Jung, S. & Priller, J. Microglia Biology: One Century of Evolving Concepts. *Cell* **179**, 292–311 (2019).

19. Provenzano, F., Pérez, M. J. & Deleidi, M. Redefining Microglial Identity in Health and Disease at Single-Cell Resolution. *Trends Mol. Med.* **27**, 47–59 (2021).

20. Oehmichen, M. Are Resting and/or Reactive Microglia Macrophages? *Immunobiology* **161**, 246–254 (1982).

21. Ginhoux, F. *et al.* Fate Mapping Analysis Reveals That Adult Microglia Derive from Primitive Macrophages. *Science* **330**, 841–845 (2010).

22. Kierdorf, K. *et al.* Microglia emerge from erythromyeloid precursors via Pu.1- and Irf8-dependent pathways. *Nat. Neurosci.* **16**, 273–280 (2013).

23. Perry, V. H., Hume, D. A. & Gordon, S. Immunohistochemical localization of macrophages and microglia in the adult and developing mouse brain. *Neuroscience* **15**, 313–326 (1985).

24. De, S. *et al.* Two distinct ontogenies confer heterogeneity to mouse brain microglia. *Development* **145**, dev152306 (2018).

25. Hattori, Y. *et al.* CD206+ macrophages transventricularly infiltrate the early embryonic cerebral wall to differentiate into microglia. *Cell Rep.* **42**, 112092 (2023).

26. Profaci, C. P., Munji, R. N., Pulido, R. S. & Daneman, R. The blood–brain barrier in health and disease: Important unanswered questions. *J. Exp. Med.* **217**, e20190062 (2020).

27. Squarzoni, P. *et al.* Microglia Modulate Wiring of the Embryonic Forebrain. *Cell Rep.* **8**, 1271–1279 (2014).

28. Barry-Carroll, L. *et al.* Microglia colonize the developing brain by clonal expansion of highly proliferative progenitors, following allometric scaling. *Cell Rep.* **42**, 112425 (2023).

29. Mildner, A. *et al.* Microglia in the adult brain arise from Ly-6ChiCCR2+ monocytes only under defined host conditions. *Nat. Neurosci.* **10**, 1544–1553 (2007).

30. Tay, T. L. *et al.* A new fate mapping system reveals context-dependent random or clonal expansion of microglia. *Nat. Neurosci.* **20**, 793–803 (2017).

31. Füger, P. *et al.* Microglia turnover with aging and in an Alzheimer's model via long-term in vivo single-cell imaging. *Nat. Neurosci.* **20**, 1371–1376 (2017).

32. Hugh Perry, V. A revised view of the central nervous system microenvironment and major histocompatibility complex class II antigen presentation. *J. Neuroimmunol.* **90**, 113–121 (1998).

33. Lawson, L. J., Perry, V. H., Dri, P. & Gordon, S. Heterogeneity in the distribution and morphology of microglia in the normal adult mouse brain. *Neuroscience* **39**, 151–170 (1990).

34. Swinnen, N. *et al.* Complex invasion pattern of the cerebral cortex bymicroglial cells during development of the mouse embryo. *Glia* **61**, 150–163 (2013).

35. Madry, C. *et al.* Microglial Ramification, Surveillance, and Interleukin-1β Release Are Regulated by the Two-Pore Domain K+ Channel THIK-1. *Neuron* **97**, 299-312.e6 (2018).

36. Gomez Perdiguero, E. *et al.* Tissue-resident macrophages originate from yolk-sac-derived erythro-myeloid progenitors. *Nature* **518**, 547–551 (2015).

37. Arnò, B. *et al.* Neural progenitor cells orchestrate microglia migration and positioning into the developing cortex. *Nat. Commun.* **5**, 5611 (2014).

38. Truman, L. A. *et al.* CX3CL1/fractalkine is released from apoptotic lymphocytes to stimulate macrophage chemotaxis. *Blood* **112**, 5026–5036 (2008).

39. Wurm, J., Konttinen, H., Andressen, C., Malm, T. & Spittau, B. Microglia Development and Maturation and Its Implications for Induction of Microglia-Like Cells from Human iPSCs. *Int. J. Mol. Sci.* **22**, 3088 (2021).

40. Hattori, Y. *et al.* Transient microglial absence assists postmigratory cortical neurons in proper differentiation. *Nat. Commun.* **11**, 1631 (2020).

41. Matcovitch-Natan, O. *et al.* Microglia development follows a stepwise program to regulate brain homeostasis. *Science* **353**, aad8670 (2016).

42. Greter, M. *et al.* Stroma-Derived Interleukin-34 Controls the Development and Maintenance of Langerhans Cells and the Maintenance of Microglia. *Immunity* **37**, 1050–1060 (2012).

43. Butovsky, O. *et al.* Identification of a unique TGF-β–dependent molecular and functional signature in microglia. *Nat. Neurosci.* **17**, 131–143 (2014).

44. Liddelow, S. A., Marsh, S. E. & Stevens, B. Microglia and Astrocytes in Disease: Dynamic Duo or Partners in Crime? *Trends Immunol.* **41**, 820–835 (2020).

45. Elmore, M. R. P. *et al.* Colony-Stimulating Factor 1 Receptor Signaling Is Necessary for Microglia Viability, Unmasking a Microglia Progenitor Cell in the Adult Brain. *Neuron* **82**, 380–397 (2014).

46. Mosser, C.-A., Baptista, S., Arnoux, I. & Audinat, E. Microglia in CNS development: Shaping the brain for the future. *Prog. Neurobiol.* **149–150**, 1–20 (2017).

47. Thion, M. S. & Garel, S. On place and time: microglia in embryonic and perinatal brain development. *Curr. Opin. Neurobiol.* **47**, 121–130 (2017).

48. Li, Q. & Barres, B. A. Microglia and macrophages in brain homeostasis and disease. *Nat. Rev. Immunol.* **18**, 225–242 (2018).

49. Canfield, John V. The Concept of Function in Biology. **Philosophical Topics 18**, 29–53 (1990).

50. Thomas, P. D. The Gene Ontology and the Meaning of Biological Function. in *The Gene Ontology Handbook* (eds. Dessimoz, C. & Škunca, N.) vol. 1446 15–24 (Springer New York, New York, NY, 2017).

51. Nimmerjahn, A., Kirchhoff, F. & Helmchen, F. Resting Microglial Cells Are Highly Dynamic Surveillants of Brain Parenchyma in Vivo. *Science* **308**, 1314–1318 (2005).

52. Mangale, V. *et al.* Microglia influence host defense, disease, and repair following murine coronavirus infection of the central nervous system. *Glia* **68**, 2345–2360 (2020).

53. Koutsouras, G. W., Ramos, R. L. & Martinez, L. R. Role of microglia in fungal infections of the central nervous system. *Virulence* **8**, 705–718 (2017).

54. Mariani, M. M. & Kielian, T. Microglia in Infectious Diseases of the Central Nervous System. *J. Neuroimmune Pharmacol.* **4**, 448–461 (2009).

55. Otani, K. & Shichita, T. Cerebral sterile inflammation in neurodegenerative diseases. *Inflamm. Regen.* **40**, 28 (2020).

56. Li, Q. & Haney, M. S. The role of glia in protein aggregation. *Neurobiol. Dis.* **143**, 105015 (2020).

57. Haynes, S. E. *et al.* The P2Y12 receptor regulates microglial activation by extracellular nucleotides. *Nat. Neurosci.* **9**, 1512–1519 (2006).

58. Stence, N., Waite, M. & Dailey, M. E. Dynamics of microglial activation: A confocal time-lapse analysis in hippocampal slices. *Glia* **33**, 256–266 (2001).

59. Vidal-Itriago, A. *et al.* Microglia morphophysiological diversity and its implications for the CNS. *Front. Immunol.* **13**, 997786 (2022).

60. Chiang, C.-S., Stalder, A., Samimi, A. & Campbell, I. L. Reactive Gliosis as a Consequence of Interleukin-6 Expression in the Brain: Studies in Transgenic Mice. *Dev. Neurosci.* **16**, 212–221 (1994).

61. Neniskyte, U., Vilalta, A. & Brown, G. C. Tumour necrosis factor alpha-induced neuronal loss is mediated by microglial phagocytosis. *FEBS Lett.* **588**, 2952–2956 (2014).

62. Rogove, A. D., Lu, W. & Tsirka, S. E. Microglial activation and recruitment, but not proliferation, suffice to mediate neurodegeneration. *Cell Death Differ.* **9**, 801–806 (2002).

63. Hickman, S. E. *et al.* The microglial sensome revealed by direct RNA sequencing. *Nat. Neurosci.* **16**, 1896–1905 (2013).

64. Kigerl, K. A., De Rivero Vaccari, J. P., Dietrich, W. D., Popovich, P. G. & Keane, R. W. Pattern recognition receptors and central nervous system repair. *Exp. Neurol.* **258**, 5–16 (2014).

65. Witting, A., Müller, P., Herrmann, A., Kettenmann, H. & Nolte, C. Phagocytic Clearance of Apoptotic Neurons by Microglia/Brain Macrophages In Vitro: Involvement of Lectin-, Integrin-, and Phosphatidylserine-Mediated Recognition. *J. Neurochem.* **75**, 1060–1070 (2002).

66. Galloway, D. A., Phillips, A. E. M., Owen, D. R. J. & Moore, C. S. Phagocytosis in the Brain: Homeostasis and Disease. *Front. Immunol.* **10**, 790 (2019).

67. Aloisi, F. Immune function of microglia. *Glia* **36**, 165–179 (2001).

68. Yang, I., Han, S. J., Kaur, G., Crane, C. & Parsa, A. T. The role of microglia in central nervous system immunity and glioma immunology. *J. Clin. Neurosci.* **17**, 6–10 (2010).

69. Ruan, Z. *et al.* Microglial Activation Damages Dopaminergic Neurons through MMP-2/-9-Mediated Increase of Blood-Brain Barrier Permeability in a Parkinson's Disease Mouse Model. *Int. J. Mol. Sci.* **23**, 2793 (2022).

70. Candelario-Jalil, E., González-Falcón, A., García-Cabrera, M., León, O. S. & Fiebich, B. L. Post-ischaemic treatment with the cyclooxygenase-2 inhibitor nimesulide reduces blood-brain barrier disruption and leukocyte infiltration following transient focal cerebral ischaemia in rats. *J. Neurochem.* **100**, 1108–1120 (2007).

71. D'Mello, C., Le, T. & Swain, M. G. Cerebral Microglia Recruit Monocytes into the Brain in Response to Tumor Necrosis Factorα Signaling during Peripheral Organ Inflammation. *J. Neurosci.* **29**, 2089–2102 (2009).

72. Kremlev, S. Differential expression of chemokines and chemokine receptors during microglial activation and inhibition. *J. Neuroimmunol.* **149**, 1–9 (2004).

73. Sun, X. *et al.* Microglia play an important role in PRV infection-induced immune responses of the central nervous system. *Virol. J.* **20**, 151 (2023).

74. Wang, S., Zhang, H. & Xu, Y. Crosstalk between microglia and T cells contributes to brain damage and recovery after ischemic stroke. *Neurol. Res.* **38**, 495–503 (2016).

75. Fani Maleki, A. & Rivest, S. Innate Immune Cells: Monocytes, Monocyte-Derived Macrophages and Microglia as Therapeutic Targets for Alzheimer's Disease and Multiple Sclerosis. *Front. Cell. Neurosci.* **13**, 355 (2019).

76. Zrzavy, T. *et al.* Pro-inflammatory activation of microglia in the brain of patients with sepsis. *Neuropathol. Appl. Neurobiol.* **45**, 278–290 (2019).

77. Berchtold, D., Priller, J., Meisel, C. & Meisel, A. Interaction of microglia with infiltrating immune cells in the different phases of stroke. *Brain Pathol.* **30**, 1208–1218 (2020).

78. Fu, R., Shen, Q., Xu, P., Luo, J. J. & Tang, Y. Phagocytosis of Microglia in the Central Nervous System Diseases. *Mol. Neurobiol.* **49**, 1422–1434 (2014).

79. Fourgeaud, L. *et al.* TAM receptors regulate multiple features of microglial physiology. *Nature* **532**, 240–244 (2016).

80. Jurga, A. M., Paleczna, M. & Kuter, K. Z. Overview of General and Discriminating Markers of Differential Microglia Phenotypes. *Front. Cell. Neurosci.* **14**, 198 (2020).

81. Smith, A. N., Shaughness, M., Collier, S., Hopkins, D. & Byrnes, K. R. Therapeutic targeting of microglia mediated oxidative stress after neurotrauma. *Front. Med.* **9**, 1034692 (2022).

82. Allagnat, F. *et al.* C/EBP homologous protein contributes to cytokine-induced pro-inflammatory responses and apoptosis in β-cells. *Cell Death Differ.* **19**, 1836–1846 (2012).

83. Weidinger, A. & Kozlov, A. Biological Activities of Reactive Oxygen and Nitrogen Species: Oxidative Stress versus Signal Transduction. *Biomolecules* **5**, 472–484 (2015).

84. Lull, M. E. & Block, M. L. Microglial activation and chronic neurodegeneration. *Neurotherapeutics* **7**, 354–365 (2010).

85. Liddelow, S. A. *et al.* Neurotoxic reactive astrocytes are induced by activated microglia. *Nature* **541**, 481–487 (2017).

86. Garcia, J. M. *et al.* Role of Interleukin-10 in Acute Brain Injuries. *Front. Neurol.* **8**, 244 (2017).

87. Francos-Quijorna, I., Amo-Aparicio, J., Martinez-Muriana, A. & López-Vales, R. IL-4 drives microglia and macrophages toward a phenotype conducive for tissue repair and functional recovery after spinal cord injury: IL-4 in SCI. *Glia* **64**, 2079–2092 (2016).

88. Takahashi, K., Rochford, C. D. P. & Neumann, H. Clearance of apoptotic neurons without inflammation by microglial triggering receptor expressed on myeloid cells-2. *J. Exp. Med.* **201**, 647–657 (2005).

89. Kang, R. *et al.* The Dual Role of Microglia in Blood-Brain Barrier Dysfunction after Stroke. *Curr. Neuropharmacol.* **18**, 1237–1249 (2020).

90. Lively, S., Lam, D., Wong, R. & Schlichter, L. C. Comparing Effects of Transforming Growth Factor β1 on Microglia From Rat and Mouse: Transcriptional Profiles and Potassium Channels. *Front. Cell. Neurosci.* **12**, 115 (2018).

91. Neumann, H., Kotter, M. R. & Franklin, R. J. M. Debris clearance by microglia: an essential link between degeneration and regeneration. *Brain* **132**, 288–295 (2008).

92. Michell-Robinson, M. A. *et al.* Roles of microglia in brain development, tissue maintenance and repair. *Brain* **138**, 1138–1159 (2015).

93. Biber, K., Neumann, H., Inoue, K. & Boddeke, H. W. G. M. Neuronal 'On' and 'Off' signals control microglia. *Trends Neurosci.* **30**, 596–602 (2007).

94. Abutbul, S. *et al.* TGF-β signaling through SMAD2/3 induces the quiescent microglial phenotype within the CNS environment. *Glia* **60**, 1160–1171 (2012).

95. Duan, L. *et al.* PDGFRβ Cells Rapidly Relay Inflammatory Signal from the Circulatory System to Neurons via Chemokine CCL2. *Neuron* **100**, 183-200.e8 (2018).

96. Kovac, A., Erickson, M. A. & Banks, W. A. Brain microvascular pericytes are immunoactive in culture: cytokine, chemokine, nitric oxide, and LRP-1 expression in response to lipopolysaccharide. *J. Neuroinflammation* **8**, 139 (2011).

97. Matsumoto, J. *et al.* TNF-α-sensitive brain pericytes activate microglia by releasing IL-6 through cooperation between IκB-NFκB and JAK-STAT3 pathways. *Brain Res.* **1692**, 34–44 (2018).

98. Recasens, M. *et al.* Chronic exposure to IL-6 induces a desensitized phenotype of the microglia. *J. Neuroinflammation* **18**, 31 (2021).

99. Li, J. *et al.* Microglial Phenotypic Transition: Signaling Pathways and Influencing Modulators Involved in Regulation in Central Nervous System Diseases. *Front. Cell. Neurosci.* **15**, 736310 (2021).

100. Brown, G. C. & Neher, J. J. Microglial phagocytosis of live neurons. *Nat. Rev. Neurosci.* **15**, 209–216 (2014).

101. Wilkinson, K. & El Khoury, J. Microglial Scavenger Receptors and Their Roles in the Pathogenesis of Alzheimer's Disease. *Int. J. Alzheimers Dis.* **2012**, 1–10 (2012).

102. Yang, Y. *et al.* The PDGF-BB-SOX7 axis-modulated IL-33 in pericytes and stromal cells promotes metastasis through tumour-associated macrophages. *Nat. Commun.* **7**, 11385 (2016).

103. Rustenhoven, J., Jansson, D., Smyth, L. C. & Dragunow, M. Brain Pericytes As Mediators of Neuroinflammation. *Trends Pharmacol. Sci.* **38**, 291–304 (2017).

104. Bisht, K. *et al.* Capillary-associated microglia regulate vascular structure and function through PANX1-P2RY12 coupling in mice. *Nat. Commun.* **12**, 5289 (2021).

105. Joost, E. *et al.* Microglia contribute to the glia limitans around arteries, capillaries and veins under physiological conditions, in a model of neuroinflammation and in human brain tissue. *Brain Struct. Funct.* **224**, 1301–1314 (2019).

106. Haruwaka, K. *et al.* Dual microglia effects on blood brain barrier permeability induced by systemic inflammation. *Nat. Commun.* **10**, 5816 (2019).

107. Rock, R. B. *et al.* Role of Microglia in Central Nervous System Infections. *Clin. Microbiol. Rev.* **17**, 942–964 (2004).

108. Mendes, M. S. & Majewska, A. K. An overview of microglia ontogeny and maturation in the homeostatic and pathological brain. *Eur. J. Neurosci.* **53**, 3525–3547 (2021).

109. Carsten Möller, J. *et al.* Regulation of thrombospondin in the regenerating mouse facial motor nucleus. *Glia* **17**, 121–132 (1996).

110. Shigemoto-Mogami, Y., Hoshikawa, K., Goldman, J. E., Sekino, Y. & Sato, K. Microglia Enhance Neurogenesis and Oligodendrogenesis in the Early Postnatal Subventricular Zone. *J. Neurosci.* **34**, 2231–2243 (2014).

111. Stevens, B. *et al.* The Classical Complement Cascade Mediates CNS Synapse Elimination. *Cell* **131**, 1164–1178 (2007).

112. Petry, P., Oschwald, A. & Kierdorf, K. Microglial tissue surveillance: The never-resting gardener in the developing and adult CNS. *Eur. J. Immunol.* **53**, 2250232 (2023).

113. Nemes-Baran, A. D., White, D. R. & DeSilva, T. M. Fractalkine-Dependent Microglial Pruning of Viable Oligodendrocyte Progenitor Cells Regulates Myelination. *Cell Rep.* **32**, 108047 (2020).

114. McNamara, N. B. *et al.* Microglia regulate central nervous system myelin growth and integrity. *Nature* **613**, 120–129 (2023).

115. Fantin, A. *et al.* Tissue macrophages act as cellular chaperones for vascular anastomosis downstream of VEGF-mediated endothelial tip cell induction. *Blood* **116**, 829–840 (2010).

116. Volin, M. V., Huynh, N., Klosowska, K., Reyes, R. D. & Woods, J. M. Fractalkine-Induced Endothelial Cell Migration Requires MAP Kinase Signaling. *Pathobiology* **77**, 7–16 (2010).

117. Lou, N. *et al.* Purinergic receptor P2RY12-dependent microglial closure of the injured blood–brain barrier. *Proc. Natl. Acad. Sci.* **113**, 1074–1079 (2016).

118. Harry, G. J. & Kraft, A. D. Microglia in the developing brain: A potential target with lifetime effects. *NeuroToxicology* **33**, 191–206 (2012).

119. Xavier, A. L., Lima, F. R. S., Nedergaard, M. & Menezes, J. R. L. Ontogeny of CX3CR1-EGFP expressing cells unveil microglia as an integral component of the postnatal subventricular zone. *Front. Cell. Neurosci.* **9**, (2015).

120. Nakajima, K. & Kohsaka, S. Microglia:Neuroprotective and Neurotrophic Cells in the Central Nervous System. *Curr. Drug Target -Cardiovasc. Hematol. Disord.* **4**, 65–84 (2004).

121. Sierra, A. *et al.* Microglia Shape Adult Hippocampal Neurogenesis through Apoptosis-Coupled Phagocytosis. *Cell Stem Cell* **7**, 483–495 (2010).

122. Li, C. *et al.* Regulation of microglia phagocytosis and potential involvement of exercise. *Front. Cell. Neurosci.* **16**, 953534 (2022).

123. Ronzano, R. *et al.* Microglia-neuron interaction at nodes of Ranvier depends on neuronal activity through potassium release and contributes to remyelination. *Nat. Commun.* **12**, 5219 (2021).

124. Hattori, Y. & Miyata, T. Microglia extensively survey the developing cortex via the CXCL12/CXCR4 system to help neural progenitors to acquire differentiated properties. *Genes Cells* **23**, 915–922 (2018).

125. Cunningham, C. L., Martínez-Cerdeño, V. & Noctor, S. C. Microglia Regulate the Number of Neural Precursor Cells in the Developing Cerebral Cortex. *J. Neurosci.* **33**, 4216–4233 (2013).

126. Hattori, Y. The behavior and functions of embryonic microglia. *Anat. Sci. Int.* **97**, 1–14 (2022).

127. Nakanishi, M. *et al.* Microglia-derived interleukin-6 and leukaemia inhibitory factor promote astrocytic differentiation of neural stem/progenitor cells. *Eur. J. Neurosci.* **25**, 649–658 (2007).

128. Paolicelli, R. C. *et al.* Synaptic Pruning by Microglia Is Necessary for Normal Brain Development. *Science* **333**, 1456–1458 (2011).

129. Lehrman, E. K. *et al.* CD47 Protects Synapses from Excess Microglia-Mediated Pruning during Development. *Neuron* **100**, 120-134.e6 (2018).

130. Ucar, H. *et al.* Mechanical actions of dendritic-spine enlargement on presynaptic exocytosis. *Nature* **600**, 686–689 (2021).

131. Sherafat, A., Pfeiffer, F., Reiss, A. M., Wood, W. M. & Nishiyama, A. Microglial neuropilin-1 promotes oligodendrocyte expansion during development and remyelination by trans-activating platelet-derived growth factor receptor. *Nat. Commun.* **12**, 2265 (2021).

132. Christopherson, K. S. *et al.* Thrombospondins Are Astrocyte-Secreted Proteins that Promote CNS Synaptogenesis. *Cell* **120**, 421–433 (2005).

133. Parkhurst, C. N. *et al.* Microglia Promote Learning-Dependent Synapse Formation through Brain-Derived Neurotrophic Factor. *Cell* **155**, 1596–1609 (2013).

134. Li, T. *et al.* A splicing isoform of GPR56 mediates microglial synaptic refinement via phosphatidylserine binding. *EMBO J.* **39**, e104136 (2020).

135. Hsieh, C. L. *et al.* A role for TREM2 ligands in the phagocytosis of apoptotic neuronal cells by microglia. *J. Neurochem.* **109**, 1144–1156 (2009).

136. Nguyen, P. T. *et al.* Microglial Remodeling of the Extracellular Matrix Promotes Synapse Plasticity. *Cell* **182**, 388-403.e15 (2020).

137. Cuanalo-Contreras, K. *et al.* Extensive accumulation of misfolded protein aggregates during natural aging and senescence. *Front. Aging Neurosci.* **14**, 1090109 (2023).

138. Kaya, T. *et al.* CD8+ T cells induce interferon-responsive oligodendrocytes and microglia in white matter aging. *Nat. Neurosci.* **25**, 1446–1457 (2022).

139. Sikora, E. *et al.* Cellular Senescence in Brain Aging. *Front. Aging Neurosci.* **13**, 646924 (2021).

140. Clarke, L. E. *et al.* Normal aging induces A1-like astrocyte reactivity. *Proc. Natl. Acad. Sci.* **115**, (2018).

141. Koellhoffer, E., McCullough, L. & Ritzel, R. Old Maids: Aging and Its Impact on Microglia Function. *Int. J. Mol. Sci.* **18**, 769 (2017).

142. Streit, W. J., Xue, Q.-S., Tischer, J. & Bechmann, I. Microglial pathology. *Acta Neuropathol. Commun.* **2**, 142 (2014).

143. Niraula, A., Sheridan, J. F. & Godbout, J. P. Microglia Priming with Aging and Stress. *Neuropsychopharmacology* **42**, 318–333 (2017).

144. Patterson, S. L. Immune dysregulation and cognitive vulnerability in the aging brain: Interactions of microglia, IL-1β, BDNF and synaptic plasticity. *Neuropharmacology* **96**, 11–18 (2015).

145. Brawek, B., Skok, M. & Garaschuk, O. Changing Functional Signatures of Microglia along the Axis of Brain Aging. *Int. J. Mol. Sci.* **22**, 1091 (2021).

146. Fessel, J. Ineffective levels of transforming growth factors and their receptor account for old age being a risk factor for Alzheimer's disease. *Alzheimers Dement. Transl. Res. Clin. Interv.* **5**, 899–905 (2019).

147. Gabandé-Rodríguez, E., Keane, L. & Capasso, M. Microglial phagocytosis in aging and Alzheimer's disease. *J. Neurosci. Res.* **98**, 284–298 (2020).

148. Mecca, C., Giambanco, I., Donato, R. & Arcuri, C. Microglia and Aging: The Role of the TREM2–DAP12 and CX3CL1-CX3CR1 Axes. *Int. J. Mol. Sci.* **19**, 318 (2018).

149. Aires, V. *et al.* CD22 Blockage Restores Age-Related Impairments of Microglia Surveillance Capacity. *Front. Immunol.* **12**, 684430 (2021).

150. Spittau, B., Rilka, J., Steinfath, E., Zöller, T. & Krieglstein, K. TGFβ1 increases microglia-mediated engulfment of apoptotic cells via upregulation of the milk fat globule-EGF factor 8: TGFβ1 Upregulates Mfge8 Expression. *Glia* **63**, 142–153 (2015).

151. Ogrodnik, M. *et al.* Whole-body senescent cell clearance alleviates age-related brain inflammation and cognitive impairment in mice. *Aging Cell* **20**, e13296 (2021).

152. Victorelli, S. & Passos, J. F. Telomeres and Cell Senescence - Size Matters Not. *EBioMedicine* **21**, 14–20 (2017).

153. Stein, G. H., Drullinger, L. F., Soulard, A. & Dulić, V. Differential Roles for Cyclin-Dependent Kinase Inhibitors p21 and p16 in the Mechanisms of Senescence and Differentiation in Human Fibroblasts. *Mol. Cell. Biol.* **19**, 2109–2117 (1999).

154. Gorgoulis, V. *et al.* Cellular Senescence: Defining a Path Forward. *Cell* **179**, 813–827 (2019).

155. Coppé, J.-P., Desprez, P.-Y., Krtolica, A. & Campisi, J. The Senescence-Associated Secretory Phenotype: The Dark Side of Tumor Suppression. *Annu. Rev. Pathol. Mech. Dis.* **5**, 99–118 (2010).

156. Von Bernhardi, R., Eugenín-von Bernhardi, L. & Eugenín, J. Microglial cell dysregulation in brain aging and neurodegeneration. *Front. Aging Neurosci.* **7**, (2015).

157. Chou, A., Krukowski, K., Morganti, J., Riparip, L.-K. & Rosi, S. Persistent Infiltration and Impaired Response of Peripherally-Derived Monocytes after Traumatic Brain Injury in the Aged Brain. *Int. J. Mol. Sci.* **19**, 1616 (2018).

158. Thomas, A. L., Lehn, M. A., Janssen, E. M., Hildeman, D. A. & Chougnet, C. A. Naturally-aged microglia exhibit phagocytic dysfunction accompanied by gene expression changes reflective of underlying neurologic disease. *Sci. Rep.* **12**, 19471 (2022).

159. Marschallinger, J. *et al.* Lipid-droplet-accumulating microglia represent a dysfunctional and proinflammatory state in the aging brain. *Nat. Neurosci.* **23**, 194–208 (2020).

160. Xu, H., Chen, M., Manivannan, A., Lois, N. & Forrester, J. V. Age-dependent accumulation of lipofuscin in perivascular and subretinal microglia in experimental mice. *Aging Cell* **7**, 58–68 (2008).

161. Ye, S.-M. & Johnson, R. W. An Age-Related Decline in Interleukin-10 May Contribute to the Increased Expression of Interleukin-6 in Brain of Aged Mice. *Neuroimmunomodulation* **9**, 183–192 (2001).

162. Hattori, Y. The multifaceted roles of embryonic microglia in the developing brain. *Front. Cell. Neurosci.* **17**, 988952 (2023).

163. Hickman, S. E. & El Khoury, J. Analysis of the Microglial Sensome. in *Microglia* (eds. Garaschuk, O. & Verkhratsky, A.) vol. 2034 305–323 (Springer New York, New York, NY, 2019).

164. Kettenmann, H., Hanisch, U.-K., Noda, M. & Verkhratsky, A. Physiology of Microglia. *Physiol. Rev.* **91**, 461–553 (2011).

165. Mitchell, A. & Lim, W. Cellular perception and misperception: Internal models for decision-making shaped by evolutionary experience. *BioEssays* **38**, 845–849 (2016).

166. Stalder, D. & Gershlick, D. C. Direct trafficking pathways from the Golgi apparatus to the plasma membrane. *Semin. Cell Dev. Biol.* **107**, 112–125 (2020).

167. Hegde, R. S. & Keenan, R. J. The mechanisms of integral membrane protein biogenesis. *Nat. Rev. Mol. Cell Biol.* **23**, 107–124 (2022).

168. Gómez Morillas, A., Besson, V. C. & Lerouet, D. Microglia and Neuroinflammation: What Place for P2RY12? *Int. J. Mol. Sci.* **22**, 1636 (2021).

169. Chun, B. J. *et al.* Purinoreceptors and ectonucleotidases control ATP-induced calcium waveforms and calcium-dependent responses in microglia: Roles of P2 receptors and CD39 in ATP-stimulated microglia. *Front. Physiol.* **13**, 1037417 (2023).

170. Vénéreau, E., Ceriotti, C. & Bianchi, M. E. DAMPs from Cell Death to New Life. *Front. Immunol.* **6**, (2015).

171. Lin, S.-S., Tang, Y., Illes, P. & Verkhratsky, A. The Safeguarding Microglia: Central Role for P2Y12 Receptors. *Front. Pharmacol.* **11**, 627760 (2021).

172. Iring, A. *et al.* The dualistic role of the purinergic P2Y12-receptor in an in vivo model of Parkinson's disease: Signalling pathway and novel therapeutic targets. *Pharmacol. Res.* **176**, 106045 (2022).

173. Crain, J. M., Nikodemova, M. & Watters, J. J. Expression of P2 nucleotide receptors varies with age and sex in murine brain microglia. *J. Neuroinflammation* **6**, 24 (2009).

174. Zhu, C. *et al.* Expression site of P2RY12 in residential microglial cells in astrocytomas correlates with M1 and M2 marker expression and tumor grade. *Acta Neuropathol. Commun.* **5**, 4 (2017).

175. Masuda, T. *et al.* IRF8 Is a Critical Transcription Factor for Transforming Microglia into a Reactive Phenotype. *Cell Rep.* **1**, 334–340 (2012).

176. Liu, S. *et al. Iterative Transcription Factor Screening Enables Rapid Generation of Microglia-like Cells from Human iPSC*. http://biorxiv.org/lookup/doi/10.1101/2022.06.03.494617 (2022) doi:10.1101/2022.06.03.494617.

177. Das, R. & Chinnathambi, S. Actin-mediated Microglial Chemotaxis via G-Protein Coupled Purinergic Receptor in Alzheimer's Disease. *Neuroscience* **448**, 325–336 (2020).

178. Sikorski, K. *et al.* STAT1 as a central mediator of IFNγ and TLR4 signal integration in vascular dysfunction. *JAK-STAT* **1**, 241–249 (2012).

179. Entsie, P., Kang, Y., Amoafo, E. B., Schöneberg, T. & Liverani, E. The Signaling Pathway of the ADP Receptor P2Y12 in the Immune System: Recent Discoveries and New Challenges. *Int. J. Mol. Sci.* **24**, 6709 (2023).

180. Eishingdrelo, H. Minireview: Targeting GPCR Activated ERK Pathways for Drug Discovery. *Curr. Chem. Genomics Transl. Med.* **7**, 9–15 (2013).

181. Hu, B. *et al.* Insights Into the Role of CSF1R in the Central Nervous System and Neurological Disorders. *Front. Aging Neurosci.* **13**, 789834 (2021).

182. Easley-Neal, C., Foreman, O., Sharma, N., Zarrin, A. A. & Weimer, R. M. CSF1R Ligands IL-34 and CSF1 Are Differentially Required for Microglia Development and Maintenance in White and Gray Matter Brain Regions. *Front. Immunol.* **10**, 2199 (2019).

183. Han, J. *et al.* Inhibition of colony stimulating factor-1 receptor (CSF-1R) as a potential therapeutic strategy for neurodegenerative diseases: opportunities and challenges. *Cell. Mol. Life Sci.* **79**, 219 (2022).

184. Tarale, P. & Alam, M. M. Colony-stimulating factor 1 receptor signaling in the central nervous system and the potential of its pharmacological inhibitors to halt the progression of neurological disorders. *Inflammopharmacology* **30**, 821–842 (2022).

185. Sherr, C. J., Roussel, M. F. & Rettenmier, C. W. Colony-stimulating factor-1 receptor (c- *fms*). *J. Cell. Biochem.* **38**, 179–187 (1988).

186. Yeh, H. & Ikezu, T. Transcriptional and Epigenetic Regulation of Microglia in Health and Disease. *Trends Mol. Med.* **25**, 96–111 (2019).

187. Tamura, A. *et al.* Csf1r Is a Downstream Target of C/EBPβ in Ly6C^{-} Monocytes. *Blood* **126**, 994–994 (2015).

188. Sauter, K. A. *et al.* The Function of the Conserved Regulatory Element within the Second Intron of the Mammalian Csf1r Locus. *PLoS ONE* **8**, e54935 (2013).

189. Akiyama, H. *et al.* Expression of the receptor for macrophage colony stimulating factor by brain microglia and its upregulation in brains of patients with Alzheimer's disease and amyotrophic lateral sclerosis. *Brain Res.* **639**, 171–174 (1994).

190. Baccarini, M., Dello Sbarba, P., Buscher, D., Bartocci, A. & Stanley, E. R. IFN-gamma/lipopolysaccharide activation of macrophages is associated with protein kinase C-dependent down-modulation of the colony-stimulating factor-1 receptor. *J. Immunol. Baltim. Md 1950* **149**, 2656–2661 (1992).

191. Zhou, Y., Chen, Y., Xu, C., Zhang, H. & Lin, C. TLR4 Targeting as a Promising Therapeutic Strategy for Alzheimer Disease Treatment. *Front. Neurosci.* **14**, 602508 (2020).

192. Thomson, A. W. & Lotze, M. T. *The Cytokine Handbook*. (Academic Press, Amsterdam Boston, 2003).

193. Lyons, A. *et al.* Fractalkine-induced activation of the phosphatidylinositol-3 kinase pathway attentuates microglial activation *in vivo* and *in vitro*. *J. Neurochem.* **110**, 1547–1556 (2009).

194. Chen, S., Luo, D., Streit, W. J. & Harrison, J. K. TGF-β1 upregulates CX3CR1 expression and inhibits fractalkine-stimulated signaling in rat microglia. *J. Neuroimmunol.* **133**, 46–55 (2002).

195. Li, X., Ye, Z., Guo, Q., Wang, E. & Pan, Y. PDTC ameliorates neuropathic pain by inhibiting microglial activation via blockage of the TNFα-CX3CR1 pathway. *Eur. J. Histochem.* **65**, (2021).

196. Wang, X. *et al.* CX3CL1/CX3CR1 signal mediates M1-type microglia and accelerates high-altitude-induced forgetting. *Front. Cell. Neurosci.* **17**, 1189348 (2023).

197. Ye, Z. *et al. Nuclear Factor Kappa B Increases CX3CR1 Expression in BV-2 Microglial Cells and Aggravates Neuropathic Pain*. https://www.researchsquare.com/article/rs-4487/v1 (2019) doi:10.21203/rs.2.13783/v1.

198. Xiao, L.-J. *et al.* Hypoxia increases CX3CR1 expression via HIF-1 and NF-κB in androgen-independent prostate cancer cells. *Int. J. Oncol.* **41**, 1827–1836 (2012).

199. Cormican, S. & Griffin, M. D. Fractalkine (CX3CL1) and Its Receptor CX3CR1: A Promising Therapeutic Target in Chronic Kidney Disease? *Front. Immunol.* **12**, 664202 (2021).

200. Xu, S. *et al.* TLR4 promotes microglial pyroptosis via lncRNA-F630028O10Rik by activating PI3K/AKT pathway after spinal cord injury. *Cell Death Dis.* **11**, 693 (2020).

201. Kim, S. *et al.* pKr-2 induces neurodegeneration via upregulation of microglial TLR4 in the hippocampus of AD brain. *Brain Behav. Immun. - Health* **28**, 100593 (2023).

202. Yao, L. *et al.* Toll-like receptor 4 mediates microglial activation and production of inflammatory mediators in neonatal rat brain following hypoxia: role of TLR4 in hypoxic microglia. *J. Neuroinflammation* **10**, 785 (2013).

203. Parajuli, B. *et al.* GM-CSF increases LPS-induced production of proinflammatory mediators via upregulation of TLR4 and CD14 in murine microglia. *J. Neuroinflammation* **9**, 268 (2012).

204. Weinstein, J. R., Koerner, I. P. & Möller, T. Microglia in ischemic brain injury. *Future Neurol.* **5**, 227–246 (2010).

205. Yesudhas, D., Gosu, V., Anwar, M. A. & Choi, S. Multiple Roles of Toll-Like Receptor 4 in Colorectal Cancer. *Front. Immunol.* **5**, (2014).

206. Skjesol, A. *et al.* The TLR4 adaptor TRAM controls the phagocytosis of Gram-negative bacteria by interacting with the Rab11-family interacting protein 2. *PLOS Pathog.* **15**, e1007684 (2019).

207. Souza-Junior, F. J. C., Cunha, L. C. & Lisboa, S. F. Toll-like receptor 4 in the interface between neuroimmune response and behavioral alterations caused by stress. *Explor. Neuroprotective Ther.* 182–209 (2022) doi:10.37349/ent.2022.00028.

208. Hu, Y. *et al.* TREM2, Driving the Microglial Polarization, Has a TLR4 Sensitivity Profile After Subarachnoid Hemorrhage. *Front. Cell Dev. Biol.* **9**, 693342 (2021).

209. Askew, K. *et al.* Coupled Proliferation and Apoptosis Maintain the Rapid Turnover of Microglia in the Adult Brain. *Cell Rep.* **18**, 391–405 (2017).

210. Hammond, B. P., Manek, R., Kerr, B. J., Macauley, M. S. & Plemel, J. R. Regulation of microglia population dynamics throughout development, health, and disease. *Glia* **69**, 2771–2797 (2021).

211. Bellver-Landete, V. *et al.* Microglia are an essential component of the neuroprotective scar that forms after spinal cord injury. *Nat. Commun.* **10**, 518 (2019).

212. Lucas, R. M., Luo, L. & Stow, J. L. ERK1/2 in immune signalling. *Biochem. Soc. Trans.* **50**, 1341–1352 (2022).

213. Zenz, R. *et al.* Activator protein 1 (Fos/Jun) functions in inflammatory bone and skin disease. *Arthritis Res. Ther.* **10**, 201 (2007).

214. Konishi, H. & Kiyama, H. Microglial TREM2/DAP12 Signaling: A Double-Edged Sword in Neural Diseases. *Front. Cell. Neurosci.* **12**, 206 (2018).

215. Gómez-Nicola, D., Schetters, S. T. T. & Hugh Perry, V. Differential role of CCR2 in the dynamics of microglia and perivascular macrophages during prion disease. *Glia* **62**, 1041–1052 (2014).

216. Erta, M., Quintana, A. & Hidalgo, J. Interleukin-6, a Major Cytokine in the Central Nervous System. *Int. J. Biol. Sci.* **8**, 1254–1266 (2012).

217. Gómez-Nicola, D., Schetters, S. T. T. & Hugh Perry, V. Differential role of CCR2 in the dynamics of microglia and perivascular macrophages during prion disease. *Glia* **62**, 1041–1052 (2014).

218. Matsudaira, T. & Prinz, M. Life and death of microglia: Mechanisms governing microglial states and fates. *Immunol. Lett.* **245**, 51–60 (2022).

219. Doonan, F. & Cotter, T. G. Morphological assessment of apoptosis. *Methods* **44**, 200–204 (2008).

220. Lossi, L. The concept of intrinsic versus extrinsic apoptosis. *Biochem. J.* **479**, 357–384 (2022).

221. Pistritto, G., Trisciuoglio, D., Ceci, C., Garufi, A. & D'Orazi, G. Apoptosis as anticancer mechanism: function and dysfunction of its modulators and targeted therapeutic strategies. *Aging* **8**, 603–619 (2016).

222. Dudgeon, C., Qiu, W., Sun, Q., Zhang, L. & Yu, J. Transcriptional Regulation of Apoptosis. in *Essentials of Apoptosis* (eds. Dong, Z. & Yin, X.-M.) 239–260 (Humana Press, Totowa, NJ, 2009). doi:10.1007/978-1-60327-381-7_10.

223. Catz, S. D. & Johnson, J. L. Transcriptional regulation of bcl-2 by nuclear factor κB and its significance in prostate cancer. *Oncogene* **20**, 7342–7351 (2001).

224. the Immunological Genome Consortium *et al.* Gene-expression profiles and transcriptional regulatory pathways that underlie the identity and diversity of mouse tissue macrophages. *Nat. Immunol.* **13**, 1118–1128 (2012).

225. Boehme, S. A., Lio, F. M., Maciejewski-Lenoir, D., Bacon, K. B. & Conlon, P. J. The Chemokine Fractalkine Inhibits Fas-Mediated Cell Death of Brain Microglia. *J. Immunol.* **165**, 397–403 (2000).

226. Liu, B. *et al.* Molecular consequences of activated microglia in the brain: overactivation induces apoptosis. *J. Neurochem.* **77**, 182–189 (2001).

227. Yu, Z., Jiang, N., Su, W. & Zhuo, Y. Necroptosis: A Novel Pathway in Neuroinflammation. *Front. Pharmacol.* **12**, 701564 (2021).

228. Morgan, M. J. & Kim, Y.-S. Roles of RIPK3 in necroptosis, cell signaling, and disease. *Exp. Mol. Med.* **54**, 1695–1704 (2022).

229. Dixon, S. J. *et al.* Ferroptosis: An Iron-Dependent Form of Nonapoptotic Cell Death. *Cell* **149**, 1060–1072 (2012).

230. Possel, H., Noack, H., Putzke, J., Wolf, G. & Sies, H. Selective upregulation of inducible nitric oxide synthase (iNOS) by lipopolysaccharide (LPS) and cytokines in microglia: In vitro and in vivo studies. *Glia* **32**, 51–59 (2000).

231. Walsh, J. G., Muruve, D. A. & Power, C. Inflammasomes in the CNS. *Nat. Rev. Neurosci.* **15**, 84–97 (2014).

232. Ko, C.-J., Gao, S.-L., Lin, T.-K., Chu, P.-Y. & Lin, H.-Y. Ferroptosis as a Major Factor and Therapeutic Target for Neuroinflammation in Parkinson's Disease. *Biomedicines* **9**, 1679 (2021).

233. Li, J. *et al.* Oxidative Stress-Induced Ferroptosis in Cardiovascular Diseases and Epigenetic Mechanisms. *Front. Cell Dev. Biol.* **9**, 685775 (2021).

234. Madry, C. & Attwell, D. Receptors, Ion Channels, and Signaling Mechanisms Underlying Microglial Dynamics. *J. Biol. Chem.* **290**, 12443–12450 (2015).

235. Franco-Bocanegra, McAuley, Nicoll, & Boche. Molecular Mechanisms of Microglial Motility: Changes in Ageing and Alzheimer's Disease. *Cells* **8**, 639 (2019).

236. Khurana, B. Functions of LIM proteins in cell polarity and chemotactic motility. *EMBO J.* **21**, 5331–5342 (2002).

237. Hohmann & Dehghani. The Cytoskeleton—A Complex Interacting Meshwork. *Cells* **8**, 362 (2019).

238. Zierler, S., Frei, E., Grissmer, S. & Kerschbaum, H. H. Chloride Influx Provokes Lamellipodium Formation in Microglial Cells. *Cell. Physiol. Biochem.* **21**, 055–062 (2008).

239. Bernier, L.-P. *et al.* Nanoscale Surveillance of the Brain by Microglia via cAMP-Regulated Filopodia. *Cell Rep.* **27**, 2895-2908.e4 (2019).

240. Siddiqui, T. A., Lively, S., Vincent, C. & Schlichter, L. C. Regulation of podosome formation, microglial migration and invasion by Ca2+-signaling molecules expressed in podosomes. *J. Neuroinflammation* **9**, 250 (2012).

241. Humphries, C. L. *et al.* Direct regulation of Arp2/3 complex activity and function by the actin binding protein coronin. *J. Cell Biol.* **159**, 993–1004 (2002).

242. Ohsawa, K., Imai, Y., Kanazawa, H., Sasaki, Y. & Kohsaka, S. Involvement of Iba1 in membrane ruffling and phagocytosis of macrophages/microglia. *J. Cell Sci.* **113**, 3073–3084 (2000).

243. Arber, S. *et al.* Regulation of actin dynamics through phosphorylation of cofilin by LIM-kinase. *Nature* **393**, 805–809 (1998).

244. Li, N. *et al.* CX3CR1 positively regulates BCR signaling coupled with cell metabolism via negatively controlling actin remodeling. *Cell. Mol. Life Sci.* **77**, 4379–4395 (2020).

245. Liang, K. J. *et al.* Regulation of Dynamic Behavior of Retinal Microglia by CX3CR1 Signaling. *Investig. Opthalmology Vis. Sci.* **50**, 4444 (2009).

246. Pollard, T. D. & Borisy, G. G. Cellular Motility Driven by Assembly and Disassembly of Actin Filaments. *Cell* **112**, 453–465 (2003).

247. Olson, E. N. & Nordheim, A. Linking actin dynamics and gene transcription to drive cellular motile functions. *Nat. Rev. Mol. Cell Biol.* **11**, 353–365 (2010).

248. Sidorenko, E. & Vartiainen, M. K. Nucleoskeletal regulation of transcription: Actin on MRTF. *Exp. Biol. Med.* **244**, 1372–1381 (2019).

249. Franco-Bocanegra, McAuley, Nicoll, & Boche. Molecular Mechanisms of Microglial Motility: Changes in Ageing and Alzheimer's Disease. *Cells* **8**, 639 (2019).

250. Madry, C. & Attwell, D. Receptors, Ion Channels, and Signaling Mechanisms Underlying Microglial Dynamics. *J. Biol. Chem.* **290**, 12443–12450 (2015).

251. Madry, C. *et al.* Microglial Ramification, Surveillance, and Interleukin-1β Release Are Regulated by the Two-Pore Domain K+ Channel THIK-1. *Neuron* **97**, 299-312.e6 (2018).

252. Hanisch, U. Microglia as a source and target of cytokines. *Glia* **40**, 140–155 (2002).

253. Kennedy, R. H. & Silver, R. Neuroimmune Signaling: Cytokines and the CNS. in *Neuroscience in the 21st Century* (eds. Pfaff, D. W. & Volkow, N. D.) 1–41 (Springer New York, New York, NY, 2015). doi:10.1007/978-1-4614-6434-1_174-1.

254. Roberto, M., Patel, R. R. & Bajo, M. Ethanol and Cytokines in the Central Nervous System. in *The Neuropharmacology of Alcohol* (eds. Grant, K. A. & Lovinger, D. M.) vol. 248 397–431 (Springer International Publishing, Cham, 2017).

255. Liu, J. *et al.* Predominant Release of Lysosomal Enzymes by Newborn Rat Microglia After LPS Treatment Revealed by Proteomic Studies. *J. Proteome Res.* **7**, 2033–2049 (2008).

256. Woo, J. *et al.* Quantitative Proteomics Reveals Temporal Proteomic Changes in Signaling Pathways during BV2 Mouse Microglial Cell Activation. *J. Proteome Res.* **16**, 3419–3432 (2017).

257. Lindhout, I. A., Murray, T. E., Richards, C. M. & Klegeris, A. Potential neurotoxic activity of diverse molecules released by microglia. *Neurochem. Int.* **148**, 105117 (2021).

258. Ozaki, K. & Leonard, W. J. Cytokine and Cytokine Receptor Pleiotropy and Redundancy. *J. Biol. Chem.* **277**, 29355–29358 (2002).

259. Ferro, A., Auguste, Y. S. S. & Cheadle, L. Microglia, Cytokines, and Neural Activity: Unexpected Interactions in Brain Development and Function. *Front. Immunol.* **12**, 703527 (2021).

260. Ernst, M. Acquiring signalling specificity from the cytokine receptor gp130. *Trends Genet.* **20**, 23–32 (2004).

261. Brocker, C., Thompson, D., Matsumoto, A., Nebert, D. W. & Vasiliou, V. Evolutionary divergence and functions of the human interleukin (IL) gene family. *Hum. Genomics* **5**, 30 (2010).

262. Lacroix, M. *et al.* Novel Insights into Interleukin 6 (IL-6) Cis- and Trans-signaling Pathways by Differentially Manipulating the Assembly of the IL-6 Signaling Complex. *J. Biol. Chem.* **290**, 26943–26953 (2015).

263. Rose-John, S., Jenkins, B. J., Garbers, C., Moll, J. M. & Scheller, J. Targeting IL-6 trans-signalling: past, present and future prospects. *Nat. Rev. Immunol.* **23**, 666–681 (2023).

264. Gruber, S., Werner, P., Germann, R. & Fraunberger, P. Diagnostic relevance of CSF interleukin-6. *LaboratoriumsMedizin* **39**, 000010151520150111 (2016).

265. Gruol, D. L. IL-6 regulation of synaptic function in the CNS. *Neuropharmacology* **96**, 42–54 (2015).

266. Ishijima, T. & Nakajima, K. Inflammatory cytokines TNFα, IL-1β, and IL-6 are induced in endotoxin- stimulated microglia through different signaling cascades. *Sci. Prog.* **104**, 003685042110549 (2021).

267. Rosenstein, J. M., Krum, J. M. & Ruhrberg, C. VEGF in the nervous system. *Organogenesis* **6**, 107–114 (2010).

268. Rothaug, M., Becker-Pauly, C. & Rose-John, S. The role of interleukin-6 signaling in nervous tissue. *Biochim. Biophys. Acta BBA - Mol. Cell Res.* **1863**, 1218–1227 (2016).

269. Greenhill, C. J. *et al.* IL-6 *Trans* -Signaling Modulates TLR4-Dependent Inflammatory Responses via STAT3. *J. Immunol.* **186**, 1199–1208 (2011).

270. Ozawa, Y., Kurihara, T., Tsubota, K. & Okano, H. Regulation of Posttranscriptional Modification as a Possible Therapeutic Approach for Retinal Neuroprotection. *J. Ophthalmol.* **2011**, 1–8 (2011).

271. Murray, R. Z. & Stow, J. L. Cytokine Secretion in Macrophages: SNAREs, Rabs, and Membrane Trafficking. *Front. Immunol.* **5**, (2014).

272. Kim, M., Song, K. & Kim, Y. S. Alantolactone Improves Prolonged Exposure of Interleukin-6-Induced Skeletal Muscle Inflammation Associated Glucose Intolerance and Insulin Resistance. *Front. Pharmacol.* **8**, 405 (2017).

273. Greenhill, C. J. *et al.* IL-6 *Trans* -Signaling Modulates TLR4-Dependent Inflammatory Responses via STAT3. *J. Immunol.* **186**, 1199–1208 (2011).

274. Pal, S., Nath, P., Biswas, S., Mukherjee, U. & Maitra, S. Nonylphenol attenuates SOCS3 expression and M1 polarization in lipopolysaccharide-treated rat splenic macrophages. *Ecotoxicol. Environ. Saf.* **174**, 574–583 (2019).

275. Qin, H. *et al.* Molecular Mechanism of Lipopolysaccharide-Induced SOCS-3 Gene Expression in Macrophages and Microglia. *J. Immunol.* **179**, 5966–5976 (2007).

276. *Regulation of Cytokine Gene Expression in Immunity and Diseases*. vol. 941 (Springer Netherlands, Dordrecht, 2016).

277. Yu, F. *et al.* Phagocytic microglia and macrophages in brain injury and repair. *CNS Neurosci. Ther.* **28**, 1279–1293 (2022).

278. Sierra, A., Abiega, O., Shahraz, A. & Neumann, H. Janus-faced microglia: beneficial and detrimental consequences of microglial phagocytosis. *Front. Cell. Neurosci.* **7**, (2013).

279. Griffiths, M. R., Gasque, P. & Neal, J. W. The Multiple Roles of the Innate Immune System in the Regulation of Apoptosis and Inflammation in the Brain. *J. Neuropathol. Exp. Neurol.* **68**, 217–226 (2009).

280. Tsai, R. K. & Discher, D. E. Inhibition of “self” engulfment through deactivation of myosin-II at the phagocytic synapse between human cells. *J. Cell Biol.* **180**, 989–1003 (2008).

281. Kelley, S. M. & Ravichandran, K. S. Putting the brakes on phagocytosis: “don’t-eat-me” signaling in physiology and disease. *EMBO Rep.* **22**, e52564 (2021).

282. Andoh, M. & Koyama, R. Comparative Review of Microglia and Monocytes in CNS Phagocytosis. *Cells* **10**, 2555 (2021).

283. Fraser, D. A., Pisalyaput, K. & Tenner, A. J. C1q enhances microglial clearance of apoptotic neurons and neuronal blebs, and modulates subsequent inflammatory cytokine production. *J. Neurochem.* **112**, 733–743 (2010).

284. Gordon, S. Phagocytosis: An Immunobiologic Process. *Immunity* **44**, 463–475 (2016).

285. Mylvaganam, S. M., Grinstein, S. & Freeman, S. A. Picket-fences in the plasma membrane: functions in immune cells and phagocytosis. *Semin. Immunopathol.* **40**, 605–615 (2018).

286. Dustin, M. L. Signaling at neuro/immune synapses. *J. Clin. Invest.* **122**, 1149–1155 (2012).

287. Jaumouillé, V. & Grinstein, S. Molecular Mechanisms of Phagosome Formation. *Microbiol. Spectr.* **4**, 4.3.06 (2016).

288. Freeman, S. A. & Grinstein, S. Phagocytosis: receptors, signal integration, and the cytoskeleton. *Immunol. Rev.* **262**, 193–215 (2014).

289. Mylvaganam, S., Freeman, S. A. & Grinstein, S. The cytoskeleton in phagocytosis and macropinocytosis. *Curr. Biol.* **31**, R619–R632 (2021).

290. Lee, H.-J., Woo, Y., Hahn, T.-W., Jung, Y. M. & Jung, Y.-J. Formation and Maturation of the Phagosome: A Key Mechanism in Innate Immunity against Intracellular Bacterial Infection. *Microorganisms* **8**, 1298 (2020).

291. Nguyen, J. A. & Yates, R. M. Better Together: Current Insights Into Phagosome-Lysosome Fusion. *Front. Immunol.* **12**, 636078 (2021).

292. Kinchen, J. M. & Ravichandran, K. S. Phagosome maturation: going through the acid test. *Nat. Rev. Mol. Cell Biol.* **9**, 781–795 (2008).

293. Castoreno, A. B. *et al.* Transcriptional regulation of phagocytosis-induced membrane biogenesis by sterol regulatory element binding proteins. *Proc. Natl. Acad. Sci.* **102**, 13129–13134 (2005).

294. Morita, T., Mayanagi, T. & Sobue, K. Reorganization of the actin cytoskeleton via transcriptional regulation of cytoskeletal/focal adhesion genes by myocardin-related transcription factors (MRTFs/MAL/MKLs). *Exp. Cell Res.* **313**, 3432–3445 (2007).

295. Sardiello, M. *et al.* A Gene Network Regulating Lysosomal Biogenesis and Function. *Science* **325**, 473–477 (2009).

296. Röszer, T. Transcriptional control of apoptotic cell clearance by macrophage nuclear receptors. *Apoptosis* **22**, 284–294 (2017).

297. Lee, H.-J., Woo, Y., Hahn, T.-W., Jung, Y. M. & Jung, Y.-J. Formation and Maturation of the Phagosome: A Key Mechanism in Innate Immunity against Intracellular Bacterial Infection. *Microorganisms* **8**, 1298 (2020).

298. Mylvaganam, S. M., Grinstein, S. & Freeman, S. A. Picket-fences in the plasma membrane: functions in immune cells and phagocytosis. *Semin. Immunopathol.* **40**, 605–615 (2018).

299. Uribe-Querol, E. & Rosales, C. Control of Phagocytosis by Microbial Pathogens. *Front. Immunol.* **8**, 1368 (2017).

300. Vasek, M. J. *et al. Microglia Perform Local Protein Synthesis at Perisynaptic and Phagocytic Structures*. http://biorxiv.org/lookup/doi/10.1101/2021.01.13.426577 (2021) doi:10.1101/2021.01.13.426577.

301. Liu, W. *et al.* Trem2 *Promotes Anti-Inflammatory Responses in Microglia and Is Suppressed under pro-Inflammatory Conditions*. http://biorxiv.org/lookup/doi/10.1101/449884 (2018) doi:10.1101/449884.

302. Morrison, V. E. & Bix, G. J. The meal Maketh the Microglia: Why studying microglial phagocytosis is critical to stroke research. *Neurochem. Int.* **164**, 105488 (2023).

303. Pishesha, N., Harmand, T. J. & Ploegh, H. L. A guide to antigen processing and presentation. *Nat. Rev. Immunol.* **22**, 751–764 (2022).

304. Hubbard, J. A. & Binder, D. K. Inflammation. in *Astrocytes and Epilepsy* 313–342 (Elsevier, 2016). doi:10.1016/B978-0-12-802401-0.00013-2.

305. Louveau, A. *et al.* Structural and functional features of central nervous system lymphatic vessels. *Nature* **523**, 337–341 (2015).

306. Olah, M. *et al.* Identification of a microglia phenotype supportive of remyelination. *Glia* **60**, 306–321 (2012).

307. Almolda, B. Antigen presentation in EAE: role of microglia, macrophages and dendritic cells. *Front. Biosci.* **16**, 1157 (2011).

308. Wu, G. F. *et al.* Limited sufficiency of antigen presentation by dendritic cells in models of central nervous system autoimmunity. *J. Autoimmun.* **36**, 56–64 (2011).

309. Schetters, S. T. T., Gomez-Nicola, D., Garcia-Vallejo, J. J. & Van Kooyk, Y. Neuroinflammation: Microglia and T Cells Get Ready to Tango. *Front. Immunol.* **8**, 1905 (2018).

310. Eggen, B. J. L., Raj, D., Hanisch, U.-K. & Boddeke, H. W. G. M. Microglial Phenotype and Adaptation. *J. Neuroimmune Pharmacol.* **8**, 807–823 (2013).

311. Uriarte Huarte, O., Richart, L., Mittelbronn, M. & Michelucci, A. Microglia in Health and Disease: The Strength to Be Diverse and Reactive. *Front. Cell. Neurosci.* **15**, 660523 (2021).

312. Streit, W. J. & Graeber, M. B. Heterogeneity of microglial and perivascular cell populations: Insights gained from the facial nucleus paradigm. *Glia* **7**, 68–74 (1993).

313. De Haas, A. H., Boddeke, H. W. G. M. & Biber, K. Region-specific expression of immunoregulatory proteins on microglia in the healthy CNS. *Glia* **56**, 888–894 (2008).

314. Hanisch, U.-K. Functional diversity of microglia – how heterogeneous are they to begin with? *Front. Cell. Neurosci.* **7**, (2013).

315. Nelson, L. H. & Lenz, K. M. Microglia depletion in early life programs persistent changes in social, mood-related, and locomotor behavior in male and female rats. *Behav. Brain Res.* **316**, 279–293 (2017).

316. Antignano, I., Liu, Y., Offermann, N. & Capasso, M. Aging microglia. *Cell. Mol. Life Sci.* **80**, 126 (2023).

317. Murray, P. J. *et al.* Macrophage Activation and Polarization: Nomenclature and Experimental Guidelines. *Immunity* **41**, 14–20 (2014).

318. Mills, C. D., Kincaid, K., Alt, J. M., Heilman, M. J. & Hill, A. M. M-1/M-2 Macrophages and the Th1/Th2 Paradigm. *J. Immunol.* **164**, 6166–6173 (2000).

319. Mosmann, T. R. & Coffman, R. L. TH1 and TH2 Cells: Different Patterns of Lymphokine Secretion Lead to Different Functional Properties. *Annu. Rev. Immunol.* **7**, 145–173 (1989).

320. Cherry, J. D., Olschowka, J. A. & O'Banion, M. K. Neuroinflammation and M2 microglia: the good, the bad, and the inflamed. *J. Neuroinflammation* **11**, 98 (2014).

321. Guo, S., Wang, H. & Yin, Y. Microglia Polarization From M1 to M2 in Neurodegenerative Diseases. *Front. Aging Neurosci.* **14**, 815347 (2022).

322. Paolicelli, R. C. *et al.* Microglia states and nomenclature: A field at its crossroads. *Neuron* **110**, 3458–3483 (2022).

323. Delpech, J.-C. *et al.* Microglia in neuronal plasticity: Influence of stress. *Neuropharmacology* **96**, 19–28 (2015).

324. Orihuela, R., McPherson, C. A. & Harry, G. J. Microglial M1/M2 polarization and metabolic states. *Br. J. Pharmacol.* **173**, 649–665 (2016).

325. Rawlinson, C., Jenkins, S., Thei, L., Dallas, M. L. & Chen, R. Post-Ischaemic Immunological Response in the Brain: Targeting Microglia in Ischaemic Stroke Therapy. *Brain Sci.* **10**, 159 (2020).

326. Wang, Q. *et al.* Microglia Polarization in Alzheimer's Disease: Mechanisms and a Potential Therapeutic Target. *Front. Aging Neurosci.* **13**, 772717 (2021).

327. Isik, S., Yeman Kiyak, B., Akbayir, R., Seyhali, R. & Arpaci, T. Microglia Mediated Neuroinflammation in Parkinson's Disease. *Cells* **12**, 1012 (2023).

328. Tang, Y. & Le, W. Differential Roles of M1 and M2 Microglia in Neurodegenerative Diseases. *Mol. Neurobiol.* **53**, 1181–1194 (2016).

329. Geribaldi-Doldán, N. *et al.* The Role of Microglia in Glioblastoma. *Front. Oncol.* **10**, 603495 (2021).

330. Bolós, M., Perea, J. R. & Avila, J. Alzheimer's disease as an inflammatory disease. *Biomol. Concepts* **8**, 37–43 (2017).

331. Salvi, V., Sozio, F., Sozzani, S. & Del Prete, A. Role of Atypical Chemokine Receptors in Microglial Activation and Polarization. *Front. Aging Neurosci.* **9**, 148 (2017).

332. Beutner, C. *et al.* Unique transcriptome signature of mouse microglia. *Glia* **61**, 1429–1442 (2013).

333. Goldmann, T. *et al.* Origin, fate and dynamics of macrophages at central nervous system interfaces. *Nat. Immunol.* **17**, 797–805 (2016).

334. Geirsdottir, L. *et al.* Cross-Species Single-Cell Analysis Reveals Divergence of the Primate Microglia Program. *Cell* **179**, 1609-1622.e16 (2019).

335. Guneykaya, D. *et al.* Transcriptional and Translational Differences of Microglia from Male and Female Brains. *Cell Rep.* **24**, 2773-2783.e6 (2018).

336. Yaqubi, M. *et al.* Analysis of the microglia transcriptome across the human lifespan using single cell RNA sequencing. *J. Neuroinflammation* **20**, 132 (2023).

337. Sousa, C. *et al.* Single-cell transcriptomics reveals distinct inflammation-induced microglia signatures. *EMBO Rep.* **19**, e46171 (2018).

338. Tan, Y.-L., Yuan, Y. & Tian, L. Microglial regional heterogeneity and its role in the brain. *Mol. Psychiatry* **25**, 351–367 (2020).

339. Huang, Y. *et al.* The gut microbiome modulates the transformation of microglial subtypes. *Mol. Psychiatry* **28**, 1611–1621 (2023).

340. Satoh, J. Gene expression profiles of M1 and M2 microglia characterized by comparative analysis of public datasets. *Clin. Exp. Neuroimmunol.* **9**, 124–138 (2018).

341. Selenica, M.-L. B. *et al.* Diverse activation of microglia by chemokine (C-C motif) ligand 2 overexpression in brain. *J. Neuroinflammation* **10**, 856 (2013).

342. Brian Greene. *The Fabric of the Cosmos: Space, Time and the Texture of Reality.* (2004).

343. Miao, J. *et al.* Microglia in Alzheimer's disease: pathogenesis, mechanisms, and therapeutic potentials. *Front. Aging Neurosci.* **15**, 1201982 (2023).

344. Bianchin, M. M., Martin, K. C., De Souza, A. C., De Oliveira, M. A. & De Mello Rieder, C. R. Nasu–Hakola disease and primary microglial dysfunction. *Nat. Rev. Neurol.* **6**, 523–523 (2010).

345. Talantseva, O. I. *et al.* The global prevalence of autism spectrum disorder: A three-level meta-analysis. *Front. Psychiatry* **14**, 1071181 (2023).

346. Aishworiya, R., Valica, T., Hagerman, R. & Restrepo, B. An Update on Psychopharmacological Treatment of Autism Spectrum Disorder. *Neurotherapeutics* **19**, 248–262 (2022).

347. Chen, J. A., Peñagarikano, O., Belgard, T. G., Swarup, V. & Geschwind, D. H. The Emerging Picture of Autism Spectrum Disorder: Genetics and Pathology. *Annu. Rev. Pathol. Mech. Dis.* **10**, 111–144 (2015).

348. Kalavai, S. & Ikezu, S. Neuritogenic function of microglia in maternal immune activation and autism spectrum disorders. *Neural Regen. Res.* **16**, 1436 (2021).

349. Luo, Y. *et al.* Minocycline improves autism-related behaviors by modulating microglia polarization in a mouse model of autism. *Int. Immunopharmacol.* **122**, 110594 (2023).

350. Ghasemi, N., Razavi, S. & Nikzad, E. Multiple Sclerosis: Pathogenesis, Symptoms, Diagnoses and Cell-Based Therapy. *Cell J Yakhteh* **19**, (2017).

351. Papiri, G. *et al.* Multiple Sclerosis: Inflammatory and Neuroglial Aspects. *Curr. Issues Mol. Biol.* **45**, 1443–1470 (2023).

352. Ross, A. P., Ben-Zacharia, A., Harris, C. & Smrtka, J. Multiple Sclerosis, Relapses, and the Mechanism of Action of Adrenocorticotropic Hormone. *Front. Neurol.* **4**, (2013).

353. Yong, V. W. Microglia in multiple sclerosis: Protectors turn destroyers. *Neuron* **110**, 3534–3548 (2022).

354. Wilson, D. M. *et al.* Hallmarks of neurodegenerative diseases. *Cell* **186**, 693–714 (2023).

355. Yiannopoulou, K. G. & Papageorgiou, S. G. Current and Future Treatments in Alzheimer Disease: An Update. *J. Cent. Nerv. Syst. Dis.* **12**, 117957352090739 (2020).

356. Abubakar, M. B. *et al.* Alzheimer's Disease: An Update and Insights Into Pathophysiology. *Front. Aging Neurosci.* **14**, 742408 (2022).

357. Gao, C., Jiang, J., Tan, Y. & Chen, S. Microglia in neurodegenerative diseases: mechanism and potential therapeutic targets. *Signal Transduct. Target. Ther.* **8**, 359 (2023).

358. Torp, S. H., Solheim, O. & Skjulsvik, A. J. The WHO 2021 Classification of Central Nervous System tumours: a practical update on what neurosurgeons need to know—a minireview. *Acta Neurochir. (Wien)* **164**, 2453–2464 (2022).

359. Oronsky, B., Reid, T. R., Oronsky, A., Sandhu, N. & Knox, S. J. A Review of Newly Diagnosed Glioblastoma. *Front. Oncol.* **10**, 574012 (2021).

360. Grochans, S. *et al.* Epidemiology of Glioblastoma Multiforme–Literature Review. *Cancers* **14**, 2412 (2022).

361. Abels, E. R. *et al.* Glioblastoma-Associated Microglia Reprogramming Is Mediated by Functional Transfer of Extracellular miR-21. *Cell Rep.* **28**, 3105-3119.e7 (2019).

362. Hu, C., Li, H., Li, J., Luo, X. & Hao, Y. Microglia: Synaptic modulator in autism spectrum disorder. *Front. Psychiatry* **13**, 958661 (2022).

363. Leng, F. & Edison, P. Neuroinflammation and microglial activation in Alzheimer disease: where do we go from here? *Nat. Rev. Neurol.* **17**, 157–172 (2021).

364. Lin, C., Wang, N. & Xu, C. Glioma-associated microglia/macrophages (GAMs) in glioblastoma: Immune function in the tumor microenvironment and implications for immunotherapy. *Front. Immunol.* **14**, 1123853 (2023).

365. Perdaens, O. & Van Pesch, V. Molecular Mechanisms of Immunosenescene and Inflammaging: Relevance to the Immunopathogenesis and Treatment of Multiple Sclerosis. *Front. Neurol.* **12**, 811518 (2022).

366. Goldberg, A. D., Allis, C. D. & Bernstein, E. Epigenetics: A Landscape Takes Shape. *Cell* **128**, 635–638 (2007).

367. Hu, Z. & Tee, W.-W. Enhancers and chromatin structures: regulatory hubs in gene expression and diseases. *Biosci. Rep.* **37**, BSR20160183 (2017).

368. Matt, S. M., Lawson, M. A. & Johnson, R. W. Aging and peripheral lipopolysaccharide can modulate epigenetic regulators and decrease IL-1β promoter DNA methylation in microglia. *Neurobiol. Aging* **47**, 1–9 (2016).

369. Peng, Q.-M. *et al.* Apelin-13 ameliorates LPS-induced BV-2 microglia inflammatory response through promoting autophagy and inhibiting H3K9ac enrichment of TNF-α and IL-6 promoter. *Acta Neurobiol. Exp. (Warsz.)* (2022) doi:10.55782/ane-2022-006.

370. Zingale, V. D., Gugliandolo, A. & Mazzon, E. MiR-155: An Important Regulator of Neuroinflammation. *Int. J. Mol. Sci.* **23**, 90 (2021).

371. Holtman, I. R., Skola, D. & Glass, C. K. Transcriptional control of microglia phenotypes in health and disease. *J. Clin. Invest.* **127**, 3220–3229 (2017).

372. Barral, A. & Déjardin, J. The chromatin signatures of enhancers and their dynamic regulation. *Nucleus* **14**, 2160551 (2023).

373. Minderjahn, J. *et al.* Mechanisms governing the pioneering and redistribution capabilities of the non-classical pioneer PU.1. *Nat. Commun.* **11**, 402 (2020).

374. Gosselin, D. *et al.* An environment-dependent transcriptional network specifies human microglia identity. *Science* **356**, eaal3222 (2017).

375. Kurotaki, D. *et al.* Transcription Factor IRF8 Governs Enhancer Landscape Dynamics in Mononuclear Phagocyte Progenitors. *Cell Rep.* **22**, 2628–2641 (2018).

376. Datta, M. *et al.* Histone Deacetylases 1 and 2 Regulate Microglia Function during Development, Homeostasis, and Neurodegeneration in a Context-Dependent Manner. *Immunity* **48**, 514-529.e6 (2018).

377. Gosselin, D. Epigenomic and transcriptional determinants of microglial cell identity. *Glia* **68**, 1643–1654 (2020).

378. Kaminska, B., Mota, M. & Pizzi, M. Signal transduction and epigenetic mechanisms in the control of microglia activation during neuroinflammation. *Biochim. Biophys. Acta BBA - Mol. Basis Dis.* **1862**, 339–351 (2016).

379. Smale, S. T. Hierarchies of NF-κB target-gene regulation. *Nat. Immunol.* **12**, 689–694 (2011).

380. Cheray, M. & Joseph, B. Epigenetics Control Microglia Plasticity. *Front. Cell. Neurosci.* **12**, 243 (2018).

381. Wendeln, A.-C. *et al.* Innate immune memory in the brain shapes neurological disease hallmarks. *Nature* **556**, 332–338 (2018).

382. Schaafsma, W. *et al.* Long-lasting pro-inflammatory suppression of microglia by LPS-preconditioning is mediated by RelB-dependent epigenetic silencing. *Brain. Behav. Immun.* **48**, 205–221 (2015).

383. Huang, M. *et al.* Microglial immune regulation by epigenetic reprogramming through histone H3K27 acetylation in neuroinflammation. *Front. Immunol.* **14**, 1052925 (2023).

384. Schwarz, J. M., Hutchinson, M. R. & Bilbo, S. D. Early-Life Experience Decreases Drug-Induced Reinstatement of Morphine CPP in Adulthood via Microglial-Specific Epigenetic Programming of Anti-Inflammatory IL-10 Expression. *J. Neurosci.* **31**, 17835–17847 (2011).

385. Robertson, K. D. DNA methylation and chromatin – unraveling the tangled web. *Oncogene* **21**, 5361–5379 (2002).

386. Suetake, I., Shinozaki, F., Miyagawa, J., Takeshima, H. & Tajima, S. DNMT3L Stimulates the DNA Methylation Activity of Dnmt3a and Dnmt3b through a Direct Interaction. *J. Biol. Chem.* **279**, 27816–27823 (2004).

387. Qin, W., Scicluna, B. P. & Van Der Poll, T. The Role of Host Cell DNA Methylation in the Immune Response to Bacterial Infection. *Front. Immunol.* **12**, 696280 (2021).

388. An, J., Rao, A. & Ko, M. TET family dioxygenases and DNA demethylation in stem cells and cancers. *Exp. Mol. Med.* **49**, e323–e323 (2017).

389. Moore, L. D., Le, T. & Fan, G. DNA Methylation and Its Basic Function. *Neuropsychopharmacology* **38**, 23–38 (2013).

390. Kreibich, E., Kleinendorst, R., Barzaghi, G., Kaspar, S. & Krebs, A. R. Single-molecule footprinting identifies context-dependent regulation of enhancers by DNA methylation. *Mol. Cell* **83**, 787-802.e9 (2023).

391. Bassal, M. A. The Interplay between Dysregulated Metabolism and Epigenetics in Cancer. *Biomolecules* **13**, 944 (2023).

392. Rechache, N. S. *et al.* DNA Methylation Profiling Identifies Global Methylation Differences and Markers of Adrenocortical Tumors. *J. Clin. Endocrinol. Metab.* **97**, E1004–E1013 (2012).

393. Unnikrishnan, A. *et al.* Revisiting the genomic hypomethylation hypothesis of aging. *Ann. N. Y. Acad. Sci.* **1418**, 69–79 (2018).

394. Martin, L. J. & Wong, M. Aberrant Regulation of DNA Methylation in Amyotrophic Lateral Sclerosis: A New Target of Disease Mechanisms. *Neurotherapeutics* **10**, 722–733 (2013).

395. Henderson-Smith, A. *et al.* DNA methylation changes associated with Parkinson's disease progression: outcomes from the first longitudinal genome-wide methylation analysis in blood. *Epigenetics* **14**, 365–382 (2019).

396. Altuna, M. *et al.* DNA methylation signature of human hippocampus in Alzheimer's disease is linked to neurogenesis. *Clin. Epigenetics* **11**, 91 (2019).

397. Cho, S.-H. *et al.* SIRT1 Deficiency in Microglia Contributes to Cognitive Decline in Aging and Neurodegeneration via Epigenetic Regulation of IL-1β. *J. Neurosci.* **35**, 807–818 (2015).

398. Byun, C. J. *et al.* DNA methylation of the 5′-untranslated region at +298 and +351 represses BACE1 expression in mouse BV-2 microglial cells. *Biochem. Biophys. Res. Commun.* **417**, 387–392 (2012).

399. Lam, D., Lively, S. & Schlichter, L. C. Responses of rat and mouse primary microglia to pro- and anti-inflammatory stimuli: molecular profiles, K+ channels and migration. *J. Neuroinflammation* **14**, 166 (2017).

400. Savage, J. C., Carrier, M. & Tremblay, M.-È. Morphology of Microglia Across Contexts of Health and Disease. in *Microglia* (eds. Garaschuk, O. & Verkhratsky, A.) vol. 2034 13–26 (Springer New York, New York, NY, 2019).

401. Laurenzi, M. A., Arcuri, C., Rossi, R., Marconi, P. & Bocchini, V. [No title found]. *Neurochem. Res.* **26**, 1209–1216 (2001).

402. Sarkar, S. *et al.* Characterization and comparative analysis of a new mouse microglial cell model for studying neuroinflammatory mechanisms during neurotoxic insults. *NeuroToxicology* **67**, 129–140 (2018).

403. Ahmed, Z. *et al.* Actin-binding Proteins Coronin-1a and IBA-1 are Effective Microglial Markers for Immunohistochemistry. *J. Histochem. Cytochem.* **55**, 687–700 (2007).

404. Von Roemeling, C. A. *et al.* Therapeutic modulation of phagocytosis in glioblastoma can activate both innate and adaptive antitumour immunity. *Nat. Commun.* **11**, 1508 (2020).

405. He, Y., Taylor, N., Yao, X. & Bhattacharya, A. Mouse primary microglia respond differently to LPS and poly(I:C) in vitro. *Sci. Rep.* **11**, 10447 (2021).

406. Yi, S. *et al.* IL-4 and IL-10 promotes phagocytic activity of microglia by up-regulation of TREM2. *Cytotechnology* **72**, 589–602 (2020).

407. Moritz, K. E. *et al.* The role of the immunoproteasome in interferon-γ-mediated microglial activation. *Sci. Rep.* **7**, 9365 (2017).

408. Das, A. *et al.* Dual RNA Sequencing Reveals the Expression of Unique Transcriptomic Signatures in Lipopolysaccharide-Induced BV-2 Microglial Cells. *PLOS ONE* **10**, e0121117 (2015).

409. Fennell, L. J. *et al.* Comparative analysis of Illumina Mouse Methylation BeadChip and reduced-representation bisulfite sequencing for routine DNA methylation analysis. *Cell Rep. Methods* **2**, 100323 (2022).

410. Vojta, A. *et al.* Repurposing the CRISPR-Cas9 system for targeted DNA methylation. *Nucleic Acids Res.* **44**, 5615–5628 (2016).

411. Tejedor, J. R. *et al.* CRISPR/dCAS9-mediated DNA demethylation screen identifies functional epigenetic determinants of colorectal cancer. *Clin. Epigenetics* **15**, 133 (2023).

412. Maguire, E. *et al.* Assaying Microglia Functions In Vitro. *Cells* **11**, 3414 (2022).

413. Tüshaus, J. *et al.* An optimized quantitative proteomics method establishes the cell type-resolved mouse brain secretome. *EMBO J.* **39**, e105693 (2020).

414. Avila, J. R., Lee, J. S. & Toriia, K. U. Co-Immunoprecipitation of Membrane-Bound Receptors. *Arab. Book* **13**, e0180 (2015).

415. Hu, X. *et al.* Guidelines for Regulated Cell Death Assays: A Systematic Summary, A Categorical Comparison, A Prospective. *Front. Cell Dev. Biol.* **9**, 634690 (2021).

416. Hansen, J. N. *et al.* MotiQ: an open-source toolbox to quantify the cell motility and morphology of microglia. *Mol. Biol. Cell* **33**, ar99 (2022).

417. Dello Russo, C. *et al.* The human microglial HMC3 cell line: where do we stand? A systematic literature review. *J. Neuroinflammation* **15**, 259 (2018).

418. He, Z. *et al.* Chromosomal instability and its effect on cell lines. *Cancer Rep.* **6**, e1822 (2023).

419. Rodriguez, J. *et al.* Chromosomal Instability Correlates with Genome-wide DNA Demethylation in Human Primary Colorectal Cancers. *Cancer Res.* **66**, 8462–9468 (2006).

420. Acharjee, S., Chauhan, S., Pal, R. & Tomar, R. S. Mechanisms of DNA methylation and histone modifications. in *Progress in Molecular Biology and Translational Science* vol. 197 51–92 (Elsevier, 2023).

421. Cadiz, M. P. *et al.* Culture shock: microglial heterogeneity, activation, and disrupted single-cell microglial networks in vitro. *Mol. Neurodegener.* **17**, 26 (2022).

422. Vijaya, A. K., Iešmantaitė, M., Mela, V., Baltriukienė, D. & Burokas, A. Microglia isolation from aging mice for cell culture: A beginner's guide. *Front. Cell. Neurosci.* **17**, 1082180 (2023).

423. Yang, X. *et al.* Gene Body Methylation Can Alter Gene Expression and Is a Therapeutic Target in Cancer. *Cancer Cell* **26**, 577–590 (2014).

424. Luo, R. *et al.* DNA methylation subpatterns at distinct regulatory regions in human early embryos. *Open Biol.* **8**, 180131 (2018).

425. Du, Q., Luu, P.-L., Stirzaker, C. & Clark, S. J. Methyl-CpG-binding domain proteins: readers of the epigenome. *Epigenomics* **7**, 1051–1073 (2015).

426. Héberlé, É. & Bardet, A. F. Sensitivity of transcription factors to DNA methylation. *Essays Biochem.* **63**, 727–741 (2019).

427. Anastasiadi, D., Esteve-Codina, A. & Piferrer, F. Consistent inverse correlation between DNA methylation of the first intron and gene expression across tissues and species. *Epigenetics Chromatin* **11**, 37 (2018).

428. Jones, P. A. Functions of DNA methylation: islands, start sites, gene bodies and beyond. *Nat. Rev. Genet.* **13**, 484–492 (2012).

429. Breiling, A. & Lyko, F. Epigenetic regulatory functions of DNA modifications: 5-methylcytosine and beyond. *Epigenetics Chromatin* **8**, 24 (2015).

430. Cedar, H. & Bergman, Y. Linking DNA methylation and histone modification: patterns and paradigms. *Nat. Rev. Genet.* **10**, 295–304 (2009).

List of publications

Golebiewska A, Hau AC, Oudin A, Stieber D, Yabo YA, Baus V, Barthelemy V, Klein E, Bougnaud S, Keunen O, Wantz M, Michelucci A, Neirinckx V, Muller A, Kaoma T, Nazarov PV, Azuaje F, De Falco A, Flies B, Richart L, Poovathingal S, Arns T, Grzyb K, Mock A, Herold-Mende C, Steino A, Brown D, May P, Miletic H, Malta TM, Noushmehr H, Kwon YJ, Jahn W, Klink B, Tanner G, Stead LF, Mittelbronn M, Skupin A, Hertel F, Bjerkvig R, Niclou SP. Patient-derived organoids and orthotopic xenografts of primary and recurrent gliomas represent relevant patient avatars for precision oncology. Acta Neuropathol. 2020 Dec;140(6):919-949. doi: 10.1007/s00401-020-02226-7. Epub 2020 Oct 3. PMID: 33009951; PMCID: PMC7666297.

Uriarte Huarte O, Richart L, Mittelbronn M, Michelucci A. Microglia in Health and Disease: The Strength to Be Diverse and Reactive. Front Cell Neurosci. 2021 Mar 31;15:660523. doi: 10.3389/fncel.2021.660523. PMID: 33867943; PMCID: PMC8044310.

Heurtaux T, Kirchmeyer M, Koncina E, Felten P, Richart L, Uriarte Huarte O, Schohn H, Mittelbronn M. Apomorphine Reduces A53T α-Synuclein-Induced Microglial Reactivity Through Activation of NRF2 Signalling Pathway. Cell Mol Neurobiol. 2022 Nov;42(8):2673-2695. doi: 10.1007/s10571-021-01131-1. Epub 2021 Aug 20. PMID: 34415465; PMCID: PMC9560932.

Schleimer, A., Richart, L., Drygala, F. *et al.* Introgressive hybridisation between domestic pigs (*Sus scrofa domesticus*) and endemic Corsican wild boars (*S. s. meridionalis*): effects of human-mediated interventions. *Heredity* **128**, 279–290 (2022). https://doi.org/10.1038/s41437-022-00517-1

Schleimer, A., Frantz, A. C., Richart, L., Mehnert, J., Semiadi, G., Wirdateti, Rode-Margono, J., Mittelbronn, M., Young, S., & Drygala, F. (2023). Conservation prioritisation through genomic reconstruction of demographic histories applied to two endangered suids in the Malay Archipelago. *Diversity and Distributions*, 29, 713–726. https://doi.org/10.1111/ddi.13689